Report on THMC Modeling of the Near Field Evolution of a Generic Clay Repository: Model Validation and Demonstration

Fuel Cycle Research & Development

Prepared for

U.S. Department of Energy
Used Fuel Disposition

H.H. Liu, Jim Houseworth, Jonny Rutqvist, Liange Zheng, Daisuke Asahina, Lianchong Li, Victor Vilarrasa, Fei Chen, Seiji Nakagawa, Stefan Finsterle, Christine Doughty, Timothy Kneafsey, and Jens Birkholzer

Lawrence Berkeley National Laboratory

August, 2013

FCRD-UFD-2013-000244

DISCLAIMER

This information was prepared as an account of work sponsored by an agency of the U.S. Government. Neither the U.S. Government nor any agency thereof, nor any of their employees, makes any warranty, expressed or implied, or assumes any legal liability or responsibility for the accuracy, completeness, or usefulness, of any information, apparatus, product, or process disclosed, or represents that its use would not infringe privately owned rights. References herein to any specific commercial product, process, or service by trade name, trade mark, manufacturer, or otherwise, does not necessarily constitute or imply its endorsement, recommendation, or favoring by the U.S. Government or any agency thereof. The views and opinions of authors expressed herein do not necessarily state or reflect those of the U.S. Government or any agency thereof.

Revision 2
12/20/2012

APPENDIX E
FCT DOCUMENT COVER SHEET [1]

Name/Title of Deliverable/Milestone/Revision No.	Report on THMC Modeling of the Near Field Evolution of a Generic Clay Repository: Model Validation and Demonstration
Work Package Title and Number	Generic Natural Systems Evaluations – LBNL FT-13LB080705
Work Package WBS Number	1.02.08.07
Responsible Work Package Manager	Hui-Hai Liu (Name/Signature)

Date Submitted 8/15/2013

Quality Rigor Level for Deliverable/Milestone[2]	☒ QRL-3	☐ QRL-2	☐ QRL-1 ☐ Nuclear Data	☐ Lab/Participant QA Program (no additional FCT QA requirements)

This deliverable was prepared in accordance with Lawrence Berkeley National Laboratory
(Participant/National Laboratory Name)

QA program which meets the requirements of
☒ DOE Order 414.1 ☐ NQA-1-2000 ☐ Other

This Deliverable was subjected to:

☒ Technical Review ☐ Peer Review

Technical Review (TR)

Review Documentation Provided

☐ Signed TR Report or,
☐ Signed TR Concurrence Sheet or,
☒ Signature of TR Reviewer(s) below

Peer Review (PR)

Review Documentation Provided

☐ Signed PR Report or,
☐ Signed PR Concurrence Sheet or,
☐ Signature of PR Reviewer(s) below

Name and Signature of Reviewers

Marco Bianchi Marco Bianchi

NOTE 1: *Appendix E should be filled out and submitted with the deliverable. Or, if the PICS:NE system permits, completely enter all applicable information in the PICS:NE Deliverable Form. The requirement is to ensure that all applicable information is entered either in the PICS:NE system or by using the FCT Document Cover Sheet.*

NOTE 2: *In some cases there may be a milestone where an item is being fabricated, maintenance is being performed on a facility, or a document is being issued through a formal document control process where it specifically calls out a formal review of the document. In these cases, documentation (e.g., inspection report, maintenance request, work planning package documentation or the documented review of the issued document through the document control process) of the completion of the activity along with the Document Cover Sheet is sufficient to demonstrate achieving the milestone. If QRL 1, 2, or 3 is not assigned, then the Lab/Participant QA Program (no additional FCT QA requirements box must be checked, and the work is understood to be performed, and any deliverable developed, in conformance with the respective National Laboratory/Participant, DOE- or NNSA-approved QA Program..*

This page is intentionally blank.

Table of Contents

Executive Summary 1
1. Introduction 3
2. Development and Validation of the Constitutive Relationships 5
2.1 Background 5
2.2 The Two-Part Hooke's Model (TPHM) 6
2.3 Mine-by (MB) Experiment at the Mont Terri Site 8
2.4 Three-Dimensional Numerical Model for the MB Experiment 12
2.5 Simulated Results and Discussion 17
2.5.1 Simulated damage zone and pore-pressure distributions 17
2.5.2 Comparisons between TPHM and SPHM simulation results 21
2.5.3 Comparisons between simulation results and experimental observations 24
2.6 Conclusions 32
3. Discrete Fracture Network (DFN) Approach for Fractures in Argillaceous Rock 33
3.1 Mechanical Damage Model Using RBSN 33
3.1.1 Background 33
3.1.2 Modeling of elastic continua using RBSN 35
3.2 Coupling of Hydraulic and Mechanical Damage Codes 39
3.3 Simulation of Desiccation Cracking of a Mining Waste 42
3.3.1 Experimental program of Rodríguez et al. (2007) 42
3.3.2 Model description 44
3.3.3 Simulation results 46
3.4 Analysis of the HG-A Test at Mont Terri 48
3.4.1 Location and description of the HG-A microtunnel test 48
3.4.2 Observations of rock features and EDZ damage 50
3.4.3 Water and gas injection testing 52
3.4.4 Scoping analysis of rock failure along the drift wall 54
3.5 An Analytical Model for Solute Transport through a Water-Saturated Single Fracture and Permeable Rock Matrix 58
3.5.1 Review of existing analytical models for solute transport in fracture-matrix systems 59
3.5.2 Flow model 61
3.5.3 Transport model 63
3.5.4 Solution behavior without longitudinal diffusion/dispersion 70

3.5.5 Longitudinal diffusion and dispersion 79
3.5.6 Solution behavior including longitudinal diffusion/dispersion 84
3.5.7 Evaluation of longitudinal diffusion and dispersion 90
3.5.8 Results for cumulative arrivals at a downstream location from an instantaneous point source 92
3.6 A Potential Approach to Compute Fracture-Matrix Interaction for Solute Transport in a Discrete Fracture Models 98
3.6.1 Concept for fracture-matrix interaction 98
3.6.2 Partial demonstration of the approach 99
3.7 Conclusions 103
4. THM Modeling of the FE Experiment at the Mont Terri Site 105
4.1 FE Experiment at the Mont Terri Site 105
4.2 Modeling Approach 108
4.3 FE Model Setup 110
4.4 3D TH Simulation with Comparison to 2D Results 113
4.5 3D Peak Temperature Considering Thermal Diffusion in the Buffer 116
4.6 3D THM Simulation Results using the BBM 117
4.7 Conclusions 121
5. Investigation of the Impacts of High Temperature Limits 122
5.1 Background 122
5.2 Detailed Mechanistic Modeling of THMC Alterations 124
5.2.1 Technical approach 128
5.2.2 Technical results 134
5.2.3 Summary 168
5.3 Impact of High-Temperature THMC Changes on Radionuclide Transport and Other PA Drivers 169
5.3.1 Introduction 169
5.3.2 Background 171
5.3.3 Physical processes in near field 173
5.3.4 Conceptual model 173
5.3.5 Performance metrics 178
5.3.6 Base-case scenario and variations 178
5.3.7 Global sensitivity analysis 181
5.3.8 Uncertainty quantification 186

5.3.9 Summary and future work 188
5.4 Laboratory Tests 189
5.4.1 Tested samples 190
5.4.2 Fabrication of miniature inert reaction vessels for clay heating tests 192
5.4.3 Summary and future work 194
5.5 Conclusions 195
6. Overall Summary 197
References 201

Figures

Figure 1-1. Clay/shale-formation distribution in the USA (Gonzales and Johnson, 1984). 3
Figure 2-1. A composite spring system consisting of two springs. The hard and soft springs follow engineering-strain-based and natural-strain-based Hooke's law, respectively (Liu et al., 2009). 6
Figure 2-2. Vertical cross-section of the Mont Terri anticline along the motorway tunnel (a) and the layout of the Mont Terri rock laboratory (b) (Bossart and Thury, 2008). 9
Figure 2-3. Gallery 08 as planned (status Nov 2008) (Vietor, 2011). 10
Figure 2-4. MB Niche 2 in construction: (a) the excavation advancing face, and (b) the view of the niche after reinforcement with shotcrete. 10
Figure 2-5. The instrumentation near MB Niche2. 12
Figure 2-6. The mesh of the numerical model. 14
Figure 2-7. The excavation chronology of MB niche2. 16
Figure 2-8. Simulated results based on TPHM for horizontal cross-section along MB niche 2: (a) pore pressure contours (Pa) and (b) the damage zone (and mode). 19
Figure 2-9. Simulation results based on TPHM for a vertical cross-section along MB niche 2: (a) pore pressure contours (Pa) and (b) the damage zone (and mode). 20
Figure 2-10. The TPHM-based simulation results for the damage zone and deformation around MB niche2 after construction for a vertical cross-section at Y = 12 m and perpendicular to the MB niche2: (a) displacement distribution and (b) the damage zone (and mode). 21
Figure 2-11. Simulation results based on SPHM for a horizontal cross-section along MB niche2: (a) pore pressure contours (Pa) and (b) the damage zone (and mode). 22
Figure 2-12. Simulation results based on SPHM for a vertical cross-section along MB niche2: (a) pore pressure contours (Pa) and (b) the damage zone (and mode). 23
Figure 2-13. The SPHM-based simulation results for the damage zone and deformation around MB niche2 after construction for a vertical cross-section at Y = 12 m and perpendicular to the MB niche2: (a) displacement distribution and (b) the damage zone (and mode). 24
Figure 2-14. Excavation advancing and (simulated and observed) inward displacements as a function of time. 25
Figure 2-15. Excavation advancing and (simulated and observed) pore pressures as a function of time. 27

Figure 2-16. The TPHM-based simulation results for damage zone and deformation around MB niche2 after construction for a vertical cross-section at Y = 12 m and perpendicular to the MB niche2: (a) the damage zone (and mode) and (b) displacement distribution. Note that in this case, the elastic modulus used in modeling is 7GPa. 29

Figure 2-17. The SPHM-based simulation results for the damage zone and deformation around MB niche2 after construction for a vertical cross-section at Y = 12 m and perpendicular to the MB niche2: (a) the damage zone (and mode) and (b) displacement distribution. Note that in this case, the elastic modulus used in modeling is 7GPa. 29

Figure 2-18. Excavation advancing and (simulated and observed) inward displacements as a function of time for two values of elastic modulus. 30

Figure 2-19. Excavation advancing and (simulated and observed) pore pressures as a function of time for two values of elastic modulus. 31

Figure 3-1. Typical lattice element *ij*: a) within a Voronoi grid; b) isolated from the network; and c) a zero-size spring set (referenced to local coordinate axes *n*-*s*-*t*) located at centroid *C* of Voronoi cell boundary area A_{ij}. 34

Figure 3-2. Stress tensor at Voronoi cell node: a) components of spring force local coordinates; b) a set of forces obtained by equilibrium; and c) complete stress tensor at Voronoi cell node. Adapted from Yip et al. (2005). 35

Figure 3-3. Internal reactions under vertical compression: a) a regular network of truss element, and b) homogeneous continua and normalized normal-shear stress condition. 35

Figure 3-4. Modeling procedure to achieve homogenous continua under uniaxial compression using RBSN. 37

Figure 3-5. (a) Regular discretization of a 2-D domain, and (b) Mohr's circle representation of stress state under uniaxial compressive loading. 38

Figure 3-6. Nodal displacements proportion to associated node coordinates in corresponding direction: (a) adjusted spring constant by Equation (3-2 and 3-3), and (b) the RBSN model. 38

Figure 3-7. Flow diagram of TOUGH2-RBSN linkages for a coupled THM simulation. Note that additional nodes and connections are introduced in TOUGH2 to activate flow pathways associated with fracture. 40

Figure 3-8. Nodal connectivity in the TOUGH2 simulator: (a) ordinary matrix nodes and connections; (b) newly established fracture nodes and connections. 41

Figure 3-9. Experimental data (after Rodríguez et al., 2007) and fitted polynomial curves of: (a) Young's modulus, and (b) tensile strength with degree of saturation. 43

Figure 3-10. Evolution of gravimetric moisture content of sample with thickness of 16mm. 43

Figure 3-11. Voronoi discretization of the mining waste sample with 16 mm thickness. 45

Figure 3-12. Dependence of crack patterns on nodal density for sample thicknesses of: (a), (b) 8 mm; and (c), (d) 16 mm. 46

Figure 3-13. Crack patterns for different sample thicknesses: (a) experimental results of Rodríguez et al. (2007), and (b) plan view of 3-D simulation results of the TOUGH-RBSN simulator. 47

Figure 3-14. Variation of mean spacing of cracks with sample thickness. The additional test results are also taken from Rodríguez et al. (2007), but for different drying conditions. 48

Figure 3-15. The Mont Terri underground rock laboratory: (a) geological profile of the site after Freivogel and Huggenberger (2003), (b) site map showing the underground facilities of the laboratory. The HG-A microtunnel is located in the New Gallery 04. (source: Marschall et al., 2006), (c) map view of the HG-A microtunnel and adjacent excavations; structural map

of tunnel surface shown in Figure 3-17 is the area highlighted in yellow (source: Nussbaum and Bossart, 2006). 49

Figure 3-16. HG-A test configuration: (a) schematic drawing of the microtunnel and the site instrumentation. Color coding refers to the steel liner (red), the packer seat (green) and the backfilled test section (orange) (source: Marschall et al., 2008); (b) detail of tunnel showing packer piezometers and test section for fluid injection. 50

Figure 3-17. Structural Mapping of the HG-A microtunnel (source: Nussbaum and Bossart, 2006) 51

Figure 3-18. Excavation damage. (a) Breakouts along microtunnel walls, with an orientation looking from the HG-A Niche towards back end of microtunnel (source: Marschall et al., 2006); (b) Conceptual diagram of the damage zone with the same orientation as in (a). (source: Lanyon et al., 2009; Marschall et al., 2006) 52

Figure 3-19. Fluid pressure response along packer section; (a) piezometer ring furthest from test section; (b) intermediate piezometer ring; (c) piezometer ring nearest to test section. 53

Figure 3-20. Sealing index as a function of time over a 2-year period. (source: Lanyon et al., 2009) 54

Figure 3-21. Definition diagram for plane stress around a circular hole. 55

Figure 3-22. Comparison of effective stress and tensile strength to identify tensile failure: (a) radial direction; (b) circumferential direction. 57

Figure 3-23. Results for shear failure. 57

Figure 3-24. Results for failure analysis, with an orientation looking from the HG-A Niche towards back end of microtunnel. 58

Figure 3-25. Steady-state flow field for single fracture in permeable rock matrix. 62

Figure 3-26. Rotated steady-state flow field for single fracture in permeable rock matrix, equivalent to that shown in Figure 3-25. 63

Figure 3-27. Solute transport mechanisms for single-fracture in permeable rock matrix. 64

Figure 3-28. Case 1: transport results for matrix flow parallel to the fracture and solute release in the fracture. (a) concentration contours at 200 days; (b) cumulative mass arrivals at 100 m; (c) mass arrival rates at 100 m. 72

Figure 3-29. Case 2: Same as case 1 but with the hydraulic gradient at a 45°angle to the fracture. (a) concentration contours at 200 days; (b) cumulative mass arrivals at 100 m; (c) mass arrival rates at 100 m. 73

Figure 3-30. Case 3: Same as case 1 but with the hydraulic gradient at an 84.4° angle to the fracture. (a) concentration contours at 200 days; (b) concentration at 6,000 days – note expanded y-axis scale; (c) cumulative mass arrivals at 100 m; (d) mass arrival rates at 100 m. Note that the transverse scale is expanded for this high cross-flow velocity case. 75

Figure 3-31. Case 4: Same as Case 1 but with source located in matrix 0.5 m from fracture. (a) concentration contours at 2000 days; (b) cumulative mass arrivals at 100 m; (c) mass arrival rates at 100 m. 76

Figure 3-32. Case 5: Same as Case 2 but with source located in matrix 0.5 m from fracture. (a) concentration contours at 2000 days; (b) cumulative mass arrivals at 100 m; (c) mass arrival rates at 100 m. 77

Figure 3-33. Case 6: Same as Case 3 but with source located in matrix 0.5 m from fracture. (a) concentration contours at 2000 days; (b) concentration contours at 40,000 days; (c) cumulative mass arrivals at 100 m; (d) mass arrival rates at 100 m. 79

Figure 3-34. Exact solution including longitudinal dispersion for fracture concentration from Tang et al. (1981) compared with the superposition of instantaneous point-source solutions using Equation (3-78); Tang et al. (1981) solution without dispersion is also shown. 84

Figure 3-35. Cases 7, 8, and 9: Concentration contours at 200 days using Case 1 parameters but with a matrix longitudinal diffusion coefficient of 10^{-10} m^2/s and fracture longitudinal dispersion coefficient of (a) 7×10^{-8} m^2/s ; (b)1.16×10^{-4} m^2/s; (c) 1.16×10^{-3} m^2/s; (d) centerline concentration profiles for cases 1, 7, 8, and 9. 87

Figure 3-36. Case 10: Concentration contours at 2000 days using Case 4 parameters but with a matrix longitudinal diffusion coefficient of 10^{-10} m^2/s and fracture longitudinal dispersion coefficient of 7×10^{-8} m^2/s, (a) full-scale version; contour lines are marked with concentrations in kg/m^3; (b) detail of contours near the source; (c) centerline concentration profiles for cases 4, 10, 11, and 12. 89

Figure 3-37. Comparison of Equation (3-114), preferred for $D_m t_s / \ell^2$ small, with Equation (3-113), preferred for $D_m t_s / \ell^2$ large. 102

Figure 3-38. Comparison of computational approaches (1) re-initializing solution from previous time step (dashed lines) with (2) computing solution for entire time starting from initial concentration of 0 in the LIC. 103

Figure 4-1. Summary schematic of the Mont Terri URL with side galleries and drifts for testing. Three specific experiments of relevance to UFDC are highlighted (based on Garitte and Gens, 2012). 106

Figure 4-2. Plan view of experiment setup and borehole layout (from Garitte and Gens, 2012). 106

Figure 4-3. Side view of experiment setup and borehole layout (from Garitte and Gens, 2012). 107

Figure 4-4. FE experiment time frame. Phases 16 to 20 refer to Mont Terri project phases (Vietor, 2012). 107

Figure 4-5. View of FE tunnel face from the FE niche showing beddings dipping 45° (Vietor, 2012). 110

Figure 4-6. TOUGH-FLAC 3D numerical grid of the FE experiment. 111

Figure 4-7. Capillary curves for Bentonite and Opalinus clays 113

Figure 4-8. New 3D simulation results related to the evolution of TH processes in the buffer and host rock: (a) temperature, (b) liquid saturation. 114

Figure 4-9. Comparison of previous 2D and new 3D simulation results: (a) temperature, (b) liquid saturation, (c) fluid pressure. 115

Figure 4-10. Simulation results considering drying induced by diffusion of water vapor within the buffer: (a) temperature, (b) liquid saturation. 117

Figure 4-11. Simulated stress evolution within the bentonite buffer. 119

Figure 4-12. Simulated evolution of mean stress and bulk modulus within the buffer. 120

Figure 4-13. Simulated stress evolution within the Opalinus Clay. 120

Figure 5-1. Swelling pressure versus mass fraction of smectite for various bentonites. ▲, FEBEX bentonite (ENRESA, 2000); ●, Montigel bentonite (Bucher and Muller-Vonmoos, 1989); □, Kunigel VI bentonite (JNC, 1999); ○, Kunigel bentonite (Konime and Ogata, 1996), ♦ are data for reference material from Czech, Danish, Friedland, Milos Deponit CA-N, Kutch (Indian) and Wyoming MX-80 (Karnland et al., 2006). 131

Figure 5-2. Domain for the test example of a bentonite back-filled horizontal emplacement drift at 500 m (Rutqvist et al., 2009). 135
Figure 5-3. Mesh for modeling of horizontal emplacement drift at 500 m depth. 135
Figure 5-4. Location of key points for monitoring parameter variations in numerical simulations. 136
Figure 5-5. The temporal evolution of temperature at point A (near the canister), point B (inside the bentonite and near the EBS-NS interface), point C (inside the clay formation and near the EBS-NS interface), and point D (in the far field with a distance from canister of 10 m). 137
Figure 5-6. The temporal evolution of water saturation at point A (near the canister), point B (inside the bentonite and near the EBS-NS interface), point C (inside the clay formation and near the EBS-NS interface), and point D (in the far field with a distance from canister of 10 m). 138
Figure 5-7. The Kinnekulle strata (left) and detailed stratigraphy of the about 2 m thick bentonite bed and adjacent strata (right). Scale denotes stratigraphic distance in meters from top of exposure (from Pusch and Madsen, 1995). 139
Figure 5-8. Measured illite percentage (I%) in the Kinnekulle bentonite layer (Pusch and Madsen, 1995) and model results with difference illitization rate. 141
Figure 5-9. The temporal evolution of smectite volume fraction at point A (near the canister), point B (inside the bentonite and near the EBS-NS interface), point C (inside the clay formation and near the EBS-NS interface), and point D (in the far field with a distance of canister of 10 m). 142
Figure 5-10. The temporal evolution of illite volume fraction at point A (near the canister), point B (inside the bentonite and near the EBS-NS interface), point C (inside the clay formation and near the EBS-NS interface), and point D (in the far field with a distance of canister of 10 m). 143
Figure 5-11. The temporal evolution of Al and K concentration at point A (near the canister). 144
Figure 5-12. The temporal evolution of Na and Mg concentration at point A (near the canister). 145
Figure 5-13. The temporal evolution of calcite volume fraction at point A (near the canister), point B (inside the bentonite and near the EBS-NS interface), point C (inside the clay formation and near the EBS-NS interface), and point D (in the far field with a distance of canister of 10 m). 146
Figure 5-14. The temporal evolution of illite volume fraction at s A, B, C, and D for base and sensitivity case with K concentration in the NS clay formation equal to 0.01 mol/L. 147
Figure 5-15. The temporal evolution of smectite volume fraction at points A, B, C, and D for base and sensitivity case with K concentration in the NS clay formation equal to 0.01 mol/L. 148
Figure 5-16. The temporal evolution of K concentration at points A, B, C, and D for base and sensitivity case with initial K concentration in the NS clay formation equal to 0.01 mol/L. 149
Figure 5-17. The temporal evolution of smectite volume fraction at points A, B, C, and D for base and sensitivity case with K concentration in bentonite increased by one order of magnitude. 150
Figure 5-18. The temporal evolution of illite volume fraction at points A, B, C, and D for base and sensitivity case with K concentration in bentonite increased by one order of magnitude. 151
Figure 5-19. The temporal evolution of quartz volume fraction at points A and B, for base and sensitivity case with K concentration in bentonite increased by one order of magnitude. 152
Figure 5-20. The temporal evolution of smectite volume fraction at points A and B, for base and sensitivity case with K concentration in bentonite increased by one order of magnitude. 152
Figure 5-21. The temporal evolution of smectite volume fraction at points A and B, for base and sensitivity case with K concentration in bentonite increased by one order of magnitude. 153

Figure 5-22. The temporal evolution of smectite volume fraction at points A, B, C, and D for base and sensitivity case that there is no K-feldspar dissolution. 154
Figure 5-23. The temporal evolution of illite volume fraction at points A, B, C, and D for base and sensitivity case that there is no K-feldspar dissolution. 155
Figure 5-24. The temporal evolution of smectite volume fraction at points A, B, C, and D for base and sensitivity case that k-feldspar dissolution rate is two orders of magnitude higher. 156
Figure 5-25. The temporal evolution of illite volume fraction at points A, B, C, and D for base and sensitivity case that k-feldspar dissolution rate is two orders of magnitude higher. 157
Figure 5-26. The temporal evolution of quartz volume fraction at points B and C, for base and sensitivity case that quartz dissolution rate is two orders of magnitude higher. 158
Figure 5-27. The temporal evolution of smectite volume fraction at points A, B, C, and D for base and sensitivity case that quartz dissolution rate is two orders of magnitude higher. 159
Figure 5-28. The temporal evolution of illite volume fraction at points A, B, C, and D for base and sensitivity case that quartz dissolution rate is two orders of magnitude higher. 160
Figure 5-29. Simulation results of maximum and minimum principal compressive effective stresses ($\sigma_1^{'}$ and $\sigma_3^{'}$) at point A for the "low T" scenario. The right figure shows the same data as the left figure, but focuses on a shorter time window to illustrate the difference between different cases. 161
Figure 5-30. Simulation results of maximum and minimum principal compressive effective stresses ($\sigma_1^{'}$ and $\sigma_3^{'}$) at point B for the "low T" scenario. The right figure shows the same data as the left figure, but focuses on a shorter time window to illustrate the difference between different cases. 162
Figure 5-31. Simulation results of maximum and minimum principal compressive effective stresses ($\sigma_1^{'}$ and $\sigma_3^{'}$) at point A for the "high T" scenario. The right figure shows the same data as the left figure, but focuses on a shorter time window to illustrate the difference between different cases. 163
Figure 5-32. Simulation results of maximum and minimum principal compressive effective stresses ($\sigma_1^{'}$ and $\sigma_3^{'}$) at point B for "high T" scenario. The right figure shows the same data as the left figure, but focuses on a shorter time window to illustrate the difference between different cases. 163
Figure 5-33. Porosity changes due to mineral precipitation/dissolution at point A (near the canister), point B (inside the bentonite and near the EBS-NS interface) for "high T" and "low T" scenarios. 164
Figure 5-34. Porosity changes due to stress changes at point A (near the canister) for "high T" and "low T" scenarios. 165
Figure 5-35. Porosity changes due to stress changes at point B (near the canister) for "high T" and "low T" scenarios. 165
Figure 5-36. Simulation results of maximum and minimum principal compressive effective stresses ($\sigma_1^{'}$ and $\sigma_3^{'}$) at point C for "low T' and "high T' scenarios. 166
Figure 5-37. Simulation results of maximum and minimum principal compressive effective stresses ($\sigma_1^{'}$ and $\sigma_3^{'}$) at point D for "low T' and "high T' scenarios. 166

Figure 5-38. Simulation results of maximum principal compressive effective stresses ($\sigma_3^{'}$) at point A for "S=f(Sl,C,Sc)" scenario. 167

Figure 5-39. Simulation results of maximum principal compressive effective stresses ($\sigma_3^{'}$) at point B for "S=f(Sl,C,Sc)" scenario. 167

Figure 5-40. Porosity changes due to stress changes at point A for "high T" and "low T" base case and a "high T" case with K-feldspar dissolution rate two orders of magnitude higher. 168

Figure 5-41. Porosity changes due to stress changes at point B for "high T" and "low T" base case and a "high T" case with K-feldspar dissolution rate two orders of magnitude higher. 168

Figure 5-42. Schematic diagram of 1D radial model, showing different materials and locations of potential axial flow paths. 174

Figure 5-43. Heat source strength per meter of waste package as a function of time for the base case. 175

Figure 5-44. Simplified temperature-dependent properties to represent the effects of illitization: (a) permeability increases, (b) swelling ability decreases, and (c) sorptivity decreases. 177

Figure 5-45. Temperature as a function of time at key locations for the base case (a) and cases in which the heat source strength shown in Figure 5.4.2 is doubled (b) and tripled (c). 179

Figure 5-46. Radionuclide concentration as a function of time at key locations for the base case (strongly sorbing radionuclide) and for a non-sorbing radionuclide. 180

Figure 5-47. Temperature as a function of time at key locations for a case with high-thermal conductivity material in place of inner bentonite: (a) heat source strength as shown in Figure 5-43, (b) heat source strength is doubled, and (c) heat source strength is tripled. 181

Figure 5-48. Temperature as a function of time at key locations for a case with low-thermal conductivity material in place of inner bentonite: (a) heat source strength as shown in Figure 5-43, (b) heat source strength is doubled, and (c) heat source strength is tripled. 181

Figure 5-49. Maximum temperature at (a) canister surface and (b) interface between bentonite buffer and host formation as a function of thermal conductivity of the two materials (the heat load corresponds to the 400 W/m scenario). 184

Figure 5-50. Morris global sensitivity analysis of surrogate repository performance metric: absolute elementary effect and coefficient of variation, indicating relative influence and effects of nonlinearity and parameter interdependence. 186

Figure 5-51. Range of predicted maximum temperature as a function of radial distance. 187

Figure 5-52. Histogram of maximum temperature at canister surface, with (red) and without (green) accounting for uncertainty in the heat load factor. 187

Figure 5-53. Results of Monte Carlo uncertainty propagation analysis, showing spread of predicted repository performance metric due to uncertainties in select input parameters (see Table 5-11), (a) including, and (b) excluding uncertainty in heat load factor. 188

Figure 5-54. Mont Terri clay cores acquired through collaboration with NAGRA 190

Figure 5-55. CT cross section of Core 11_12. Dark linear features appear to be dessication fractures. Bright high density features are also present (discussed below). 191

Figure 5-56. A 20 cm section of Core 11_12 with the one-dimensional high-density features highlighted. 192

Figure 5-57. Same as Figure 5-56, but reoriented identifying the orientation of the high-density features. 192

Figure 5-58. Miniature reactor vessels used for clay rock heat treatment 193
Figure 5-59. Sample holder with internal loading system which is inserted in the miniature reactor (sample diameter =1.40 cm) 194

Tables

Table 3-1. Summary of material properties of the mining waste used for TOUGH-RBSN simulator. The values are obtained from Rodríguez et al. (2007). 44
Table 3-2. Sample geometries and results of drying test..... 44
Table 3-3. Hydrogeologic parameters and domain investigated. 70
Table 3-4. Flow and transport parameters varied. 71
Table 3-5. Parameters used for all cases. 71
Table 3-6. Fracture longitudinal dispersion coefficients 85
Table 4-1. Parameters for the Opalinus and Bentonite clay 112
Table 4-2. BBM material parameter values for the bentonite buffer (Gens et al., 2009)..... 118
Table 5-1. Thermal constraints on EBS in different disposal concepts (based on Hicks et al., 2009)..... 123
Table 5-2. List of studies on illitization in clay formation and bentonite 125
Table 5-3. Swelling pressures in the Czech reference materials. The first column shows clay dry density (D_d) in kg/m^3 and the following columns show the $CaCl_2$ concentrations (moles/L) in the test solutions successively in contact with the samples. Pressure values in kPa (Karnland et al., 2006). 130
Table 5-4. Mineral volume fraction (dimensionless, ratio of the volume for a mineral to the total volume of medium) of the bentonite (Ochs et al., 2004) and the clay formation (Bossart, 2011; Lauber et al., 2000) used in the model. 132
Table 5-5. Pore-water composition of EBS bentonite and host clay rock..... 132
Table 5-6. Kinetic properties for minerals considered in the model (Xu et al., 2006). 133
Table 5-7. Thermal and hydrodynamic parameters..... 134
Table 5-8. Mineral content in the < 1/~m fraction (evaluated from Brusevitz, 1986, cited in Pusch and Madsen, 1995). 140
Table 5-9. Saturation indexes of initial pore water in bentonite with respect to the minerals considered in the model 144
Table 5-10. Material properties used for the base case simulation (fluid remains single-phase liquid) 178
Table 5-11. Parameters subjected to global sensitivity and uncertainty propagation analyses 183

Acronyms

BBM	Basic Barcelona Model
BExM	Barcelona Expansive Model
CIEMAT	Centro de Investigaciones Energéticas, Medioambientales y Tecnológicas
CODE-BRIGHT	COupled DEformation, BRIne, Gas and Heat Transport
DFN	Discrete Fracture Network
DRZ	Disturbed Rock Zone
EBS	Engineered Barrier System
EDZ	Excavation-Damaged Zone
FE	Full-Scale Emplacement Experiment
FEBEX	Full-scale Engineered Barriers Experiment
FEM	Finite Element Method
FEPs	Features, Events, and Processes
FLAC	Fast Lagrangian Analysis of Continua
GIC	Globally-Interacting Compartment
HM	Hydrological-Mechanical
LANL	Los Alamos National Laboratory
LBNL	Lawrence Berkeley National Laboratory
LIC	Locally-Interacting Compartment
MB	Mine-by
NAGRA	Nationale Genossenschaft für die Lagerung radioaktiver Abfälle
NBS	Natural Barrier System
NRC	National Research Council
NS	Natural System
RBSN	Rigid Body Spring Network
SPHM	Single-part Hooke's Model
THM	Thermal-Hydrological-Mechanical
THMC	Thermal-Hydrological-Mechanical-Chemical
TOUGH	Transport of Unsaturated Groundwater and Heat
TPHM	Two-part Hooke's Model
UFDC	Used Fuel Disposition Campaign
UPC	Universitat Politècnica de Catalunya
URL	Underground Research Laboratory

This page is intentionally blank.

Executive Summary

Objective

Shale and clay-rich rock formations have been considered as potential host rocks for geological disposal of high-level radioactive waste throughout the world. Coupled thermal, hydrological, mechanical, and chemical (THMC) processes have a significant impact on the long-term safety of a repository in this type of rocks. For example, the excavation damaged zone (EDZ) near repository tunnels can modify local permeability (resulting from induced fractures), potentially leading to less confinement capability. Maximum allowable temperature is one of the most important design variables for a geological repository, because it determines waste package spacing, distance between disposal galleries, and therefore the overall size (and cost) of the repository for a given amount of waste. This report documents results from four R&D activities to address the above concerns: (1) development and validation of constitutive relationships (Chapter 2); (2) development of a discrete fracture network (DFN) model for investigating coupled processes in the EDZ (Chapter 3); (3) development and validation of a THM model for the Full-Scale Emplacement Experiment (FE) tests at Mont Terri, Switzerland (Chapter 4); and (4) investigation of high-temperature impacts, including both laboratory and modeling studies (Chapter 5). The overall objectives of these activities are to provide an improved understanding of and advanced modeling capabilities for EDZ evolution in clay repositories and the associated coupled processes, and to develop a technical basis for the maximum allowable temperature for a clay repository.

The R&D activities documented in this report are part of the work package of natural system evaluation and tool development that directly supports the following Used Fuel Disposition Campaign (UFDC) objectives:

- Develop a fundamental understanding of disposal-system performance in a range of environments for potential wastes that could arise from future nuclear-fuel-cycle alternatives through theory, simulation, testing, and experimentation.

- Develop a computational modeling capability for the performance of storage and disposal options for a range of fuel-cycle alternatives, evolving from generic models to more robust models of performance assessment.

These activities address key Features, Events and Processes (FEPs), which have been ranked in importance from medium to high in the *Used Fuel Disposition Campaign Disposal Research and Development Roadmap* (FCR&D-USED-2011-000065 REV0) (Nutt, 2011). They also address a number of research topics identified in *Research & Development (R&D) Plan for Used Fuel Disposition Campaign (UFDC) Natural System Evaluation and Tool Development* (Wang, 2011), including Topics S3, Disposal system modeling – Natural system; P1, Development of discrete fracture network (DFN) model; P14, Technical basis for thermal loading limits; and P15 Modeling of disturbed rock zone (DRZ) evolution (clay repository).

Major FY13 Accomplishments

- Constitutive relationships are key elements for modeling coupled THMC processes. The validity of the two-part Hooke's model (TPHM), a new constitutive relationship, and associated formulations regarding rock hydraulic/mechanical properties is demonstrated by the consistency between observations from a mine-by test at the Mont Terri site in Switzerland and the predictions from a three-dimensional model for the test. However, the predicted results based on the traditional constitutive model considerably underestimate the observed hydro-mechanical

responses to the tunnel excavation for the mine-by test (including the EDZ size).

- A three-dimensional computational method capable of addressing fracture initiation and propagation as a THM coupled process has been further developed and tested. The hydrogeologic model implements a discrete fracture approach in TOUGH2 code. Geomechanics and fracture damage are computed using the Rigid-Body-Spring-Network (RBSN) modeling method. Initial scoping analyses for the HG-A test being conducted at the Mont Terri site have shown that fracture damage in the EDZ is likely to be a result of both shear and tensile failure, and that these failures are linked to the anisotropic strength in the Opalinus Clay. An analytical model for transport in a single fracture through a porous and permeable rock matrix has also been extended to include additional process capability for longitudinal diffusion/dispersion.

- The Full-Scale Emplacement Experiment (FE) at the Mont Terri site, Switzerland will be one of the largest and longest-duration heater tests worldwide. It will provide data useful for the validation of THM coupling effects regarding the processes in the host rock while correctly accounting for (and examining) the conditions in the emplacement tunnel (temperature, saturation, and swelling pressure). For the purpose of validating modeling capabilities for THM processes, we developed a three-dimensional model for the FE test that gives satisfactory temperature evolution near the heater. We also conducted for the first time a THM analysis involving the Barcelona Basic Model (BBM) in a full three-dimensional field setting for modeling the geomechanical behavior of the buffer. The analysis highlights the complex coupled geomechanical behavior in the buffer and its interaction with the surrounding rock.

- The maximum allowable temperature is one of the most important design variables for a geological repository. Both laboratory tests and numerical modeling studies were conducted on the impact of high temperature on parameters/processes that are relevant to the performance of a clay repository. A fully coupled THMC model for a clay repository with a bentonite engineered barrier system (EBS) was developed with TOUGHREACT-FLAC3D, and model results indicate that the major chemical alteration to the EBS bentonite and clay formation is illitization (dissolution of smectite and precipitation of illite), along with dissolution of K-feldspar and calcite, as well as precipitation of quartz. A high temperature laboratory experiment for bentonite and a sample of Opalinus Clay from Mont Terri is ongoing. We have finished the initial sample characterization and fabrication of special miniature pressure (reactor) vessels. Finally, an approach was outlined showing how the complex THMC process simulation may be incorporated into a highly simplified model that can be used for initial sensitivity and uncertainty analyses.

Suggested Future Work

In FY14, we will continue the current R&D activities. Constitutive relationships will be further developed to include bedding effects and impact of fracture formation on hydraulic properties within the context of the continuum modeling approach. The DFN capability will be improved by testing the approach for capturing the Poisson effect in the RBSN method and by refining the methods for dealing with shearing damage. It will be used for modeling the HG-A test. The FE test model will be further evaluated by modeling the related laboratory tests and a benchmark test, and then used for final prediction of the FE heater experiment. We will continue our THMC modeling study and laboratory experiments regarding the impact of high temperature on hydro-mechanical properties/processes relevant to the performance of a clay repository.

1. Introduction

Shale and clay-rich geological formations have been considered as potential host rock for geological disposal of high-level radioactive waste throughout the world, because of their low permeability, low diffusion coefficient, high retention capacity for radionuclides, and capability to self-seal fractures. For example, Callovo-Oxfordian argillites at the Bure site, France (Fouche et al., 2004), Toarcian argillites at the Tournemire site, France (Patriarche et al., 2004), Opalinus Clay at the Mont Terri site, Switzerland (Meier et al., 2000), and Boom Clay at the Mol site, Belgium (Barnichon and Volckaert, 2003) have all been under intensive scientific investigation (at both field and laboratory scales) for understanding a variety of rock properties and their relationships to flow and transport processes associated with geological disposal of radioactive waste. Figure 1-1 presents the distribution of clay/shale formations within the USA.

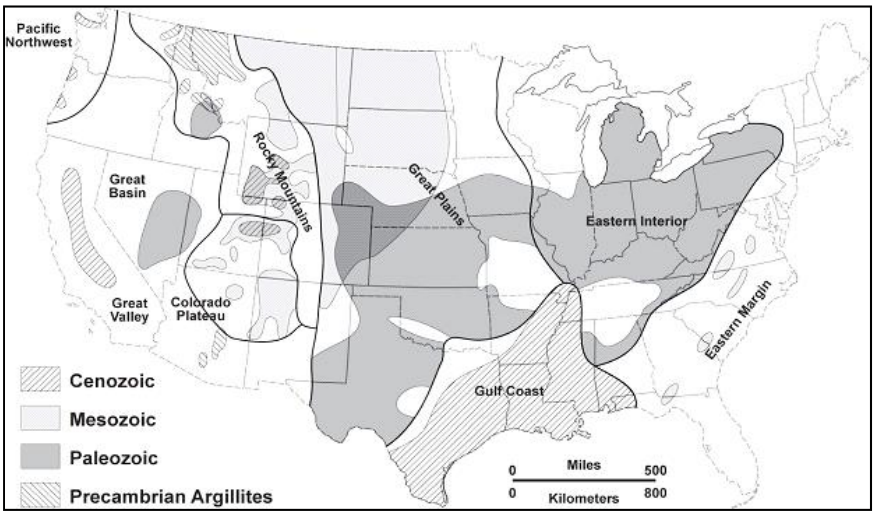

Figure 1-1. Clay/shale-formation distribution in the USA (Gonzales and Johnson, 1984).

Clay-rich rocks may be generally classified as indurated or plastic clays (Tsang et al., 2005). The latter (including Boom Clay, for example) is a softer material without high cohesion, and its deformation is predominantly plastic. For clay/shale formations, coupled thermal, hydrological, mechanical, and chemical (THMC) processes are expected to have a significant impact on the long-term safety of a clay repository. For example, the excavation damaged zone (EDZ) near repository tunnels can modify local permeability (resulting from induced fractures), potentially leading to less confinement capability (Tsang et al., 2005). Because of clay minerals tendency to swell or shrink (depending on whether the clay is in imbibition or drainage processes), fracture properties in the EDZ are quite dynamic and evolve over time as hydromechanical conditions change. Understanding and modeling the coupled processes and their impact on repository performance are critical for any defensible performance assessment of a radioactive waste repository in clay/shale host rock.

Maximum allowable temperature is one of the most important design variables for a geological repository, because it determines waste package spacing, distance between disposal galleries, and therefore the overall size (and cost) of the repository for a given amount of waste. This is especially

important for a clay repository, because clay rock has relatively low heat conductivities. However, data and knowledge gaps exist for establishing a scientific basis for determining this temperature for a clay repository.

Within the Natural Barrier System (NBS) group of the Used Fuel Disposition (UFD) Campaign at DOE's Office of Nuclear Energy, LBNL's research activities have focused on understanding and modeling EDZ evolution and the associated coupled processes, and impacts of high-temperature on parameters and processes relevant to performance of a clay repository to establish the technical base for the maximum allowable temperature. This report documents results from some of these activities. These activities address key Features, Events and Processes (FEPs), which have been ranked in importance from medium to high, as listed in Table 7 of the *Used Fuel Disposition Campaign Disposal Research and Development Roadmap* (FCR&D-USED-2011-000065 REV0) (Nutt, 2011). Specifically, they address FEP 2.2.01, Excavation Disturbed Zone, for shale, by investigating how coupled processes affect EDZ evolution; FEP 2.2.05, Flow and Transport Pathways; and FEP 2.2.08, Hydrologic Processes, and FEP 2.2.07, Mechanical Processes and FEP 2.2.09, Chemical Process—Transport, by studying near-field coupled THMC processes in clay/shale repositories. The activities documented in this report also address a number of research topics identified in *Research & Development (R&D) Plan for Used Fuel Disposition Campaign (UFDC) Natural System Evaluation and Tool Development* (Wang, 2011), including Topics S3, Disposal system modeling – Natural system; P1, Development of discrete fracture network (DFN) model; P14, Technical basis for thermal loading limits; and P15 Modeling of disturbed rock zone (DRZ) evolution (clay repository).

This report documents progress made in LBNL's FY13 research activities, including validation of the two-part Hooke's model, a new constitutive relationship for couple hydro-mechanical processes (Chapter 2), development of a DFN model for investigating coupled processes in the EDZ (Chapter 3), development and validation of a THM model for FE tests at Mont Terri, Switzerland (Chapter 4), and investigation of high-temperature impacts, including both laboratory and modeling studies (Chapter 5). A summary and discussion of future work activities are given in Chapter 6.

2. Development and Validation of the Constitutive Relationships

2.1 Background

Constitutive relationships refer to relationships among hydraulic, mechanical, thermal, and mechanical properties. This chapter documents the validation of a constitutive model using data from the Mont Terri rock laboratory (Switzerland) within an Opalinus Clay. The laboratory started operation in January 1996 as part of the international Mont Terri project. Research there is carried out in an underground facility, located adjacent to the security gallery of the Mont Terri motorway tunnel (Bossart and Thury, 2008). The aim of the project is the geological, hydrogeological, geochemical and geotechnical characterization of argillaceous formations, specifically the Opalinus Clay. The mine-by (MB) test is one of the most important tests in the project to investigate the deformation and the coupled hydro-mechanical (HM) behavior of the Opalinus Clay near excavations (Bossart and Thury, 2008; Vietor, 2011). The generated data sets from the MB test provide a unique opportunity for validating HM models.

Accuracy in modeling coupled processes in a clay/shale repository is largely determined by the validity of the corresponding constitutive relationships and related parameter values. The stress–strain relationship is the most fundamental part of constitutive relationships. Hooke's law has been generally used to describe this stress–strain relationship for elastic mechanical processes. According to Hooke's law, for elastic material, the proportionality in the stress-strain relationship should be constant; the conventional Hooke's law is called as single-part Hooke's model (SPHM) in this study. However, this proportionality is in fact not always constant in many cases, but rather stress-dependent (e.g., Cazacu, 1999; Lionço and Assis, 2000; Brown et al., 1989; Johnson and Rasolofosaon, 1996; Brady, 1969). A number of efforts have been made to relate this stress-dependent behavior to the microstructures of "cracks" in porous rock (Walsh, 1965; Nur, 1971; Mavko and Nur, 1978). An excellent review of these efforts is provided in a chapter entitled "Micromechanical Models" in Jaeger et al. (2007). Because it is generally difficult to characterize small-scale structures accurately, and then relate their properties to large-scale mechanical properties that are of practical interest, it is desirable to have a macroscopic-scale theory that does not rely on the detailed description of small-scale structures, and that can physically incorporate the stress-dependent behavior of relevant mechanical properties. A theory of this kind was developed within the framework of Hooke's law by Liu et al. (2009) and is referred to the two-part Hooke's model (TPHM) in this study.

Liu et al. (2009) argued that different varieties of Hooke's law should be applied within regions of the rock having significantly different stress–strain behavior, and that a rock body could be conceptualized into two distinct parts: a "hard part" that only experiences small deformation and a "soft part" that experiences large deformation. The two parts follows the different forms of Hooke's Law. This approach permits the derivation of constitutive relations between stress and a variety of mechanical and hydraulic rock properties. These theoretically derived relations are generally consistent with empirical expressions and also laboratory experimental data for different rock types (Liu et al., 2009, 2012; Zhao and Liu, 2012). While a number of empirical relationships are available in the literature for describing stress-dependence of different rock properties, the TPHM provides a single coherent framework that can be applied to different rock types and properties and to both rock matrix and fractures.

The focus of this study is on further evaluation of the TPHM using the MB test data. In FY12, the TPHM was implemented into the TOUGH2-FLAC3D simulator (Liu et al., 2009; Liu et al., 2012). In FY13, we have developed a three-dimensional model for the MB test that uses the TPHM as the constitutive model for elastic deformation. Modeling results are compared with available MB test data to demonstrate the usefulness of the TPHM in capturing field-scale HM behavior associated with tunnel excavation.

2.2 The Two-Part Hooke's Model (TPHM)

While the TPHM has been documented in a previous milestone report (Liu et al., 2012), it is briefly reviewed here for completeness. The major reasoning of the TPHM is that the two kinds of strains (natural and engineering) should be carefully distinguished, and the natural (or true) strain should be used in Hooke's law for accurately describing material deformation. When a uniformly distributed force is imposed on the surface of a homogeneous and isotropic material body subject to elastic deformation, the natural (or true)-strain-based Hooke's law can be expressed as (in terms of volumetric strains):

$$d\sigma = -K\frac{dV}{V} = Kd\varepsilon_{v,t} \tag{2-1}$$

where V is the total volume of the material body under the current stress state, σ is the hydrostatic stress for this equation, K is the bulk modulus, and $\varepsilon_{v,t}$ is the natural volumetric strain. The engineering-strain-based Hooke's law can be expressed as

$$d\sigma = -K\frac{dV}{V_0} = Kd\varepsilon_{v,e} \tag{2-2}$$

where V_0 is the unstressed bulk volume, and $\varepsilon_{v,e}$ is the engineering volumetric strain. Note that the two strains are practically identical for small mechanical deformations.

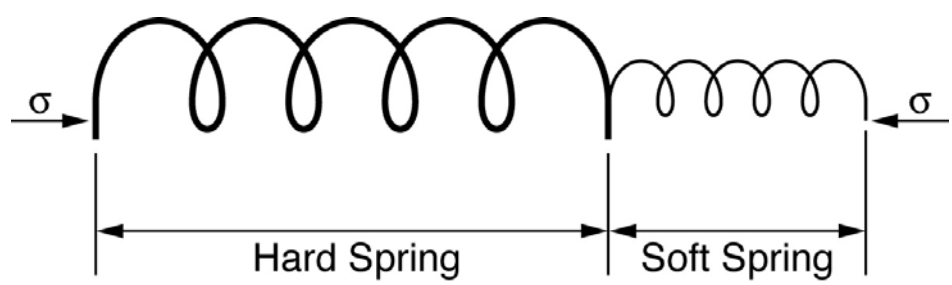

Figure 2-1. A composite spring system consisting of two springs. The hard and soft springs follow engineering-strain-based and natural-strain-based Hooke's law, respectively (Liu et al., 2009).

Engineering strain has been exclusively used in the literature of rock mechanics, considering that the elastic strain is generally small. However, Liu et al. (2009) indicated that the strain could be considerably larger within some portion of a rock body, because of its inherent heterogeneity, and they divide rock mass into two parts to consider the impact of heterogeneity (Figure 2-1). For the soft part, the natural (or true)-strain-based Hooke's law is applied. For the hard part, the engineering-strain-based Hooke's law is applied as a result of small deformation. In this work, we use subscripts *0, e*, and *t* to denote the unstressed state, the hard part, and the soft part, respectively. According to Liu et al. (2009), the stress-strain relationship for porous and fractured rock under the hydrostatic stress state can be expressed as:

$$-\frac{dV}{V_0} = \gamma_e \frac{d\sigma_h}{K_e} + \gamma_t \exp(-\frac{\sigma_h}{K_t}) \frac{d\sigma_h}{K_t} \tag{2-3}$$

$$dV = dV_e + dV_t \tag{2-4}$$

$$V_0 = V_{0,e} + V_{0,t} \tag{2-5}$$

$$\gamma_t = \frac{V_{0,t}}{V_0} \tag{2-6}$$

$$\gamma_e = 1 - \gamma_t \tag{2-7}$$

where K_e and K_t refer to bulk modulus for the hard and soft parts, respectively.

Note that for the zero volumetric fraction of the soft part ($\gamma_t = 0$), Equation (2-3) is reduced to the traditional Hooke's law (SPHM); thus, the TPHM is a generalization of the Hooke's law. The unique aspect of natural rock, compared with other solids (e.g., metals), is its large degree of material heterogeneities characterized by features with different mechanical responses to stress. Consequently, it should not be surprising that natural rocks follow different stress-strain relationships from those for more homogeneous solids. While the TPHM deals with a relatively simple heterogeneous system (a two-part system as shown in Figure 2-1), its usefulness for practical applications is evaluated and demonstrated in this study as well as in previous ones.

The above discussion is limited to isotropic (hydrostatic) stress conditions. A clay repository is generally subject to complex, anisotropic stress conditions. In FY11, we extended the TPHM to such conditions (Zhao and Liu, 2012). Based on the assumption that the principal strain resulting from the soft part is a function of the principal stress along the same direction only (and has nothing to do with any other principal stresses), and the soft part in each principal orientation occupies the same portion of the entire soft part, the stress-strain relations are given by:

$$\left.\begin{aligned}
\varepsilon_1 &= \frac{(3-\gamma_t)}{3E_e}\left[\sigma_1 - \nu(\sigma_2+\sigma_3)\right] + \frac{\gamma_t}{3}\left[1-\exp\left(-\frac{\sigma_1}{E_t}\right)\right] \\
\varepsilon_2 &= \frac{(3-\gamma_t)}{3E_e}\left[\sigma_2 - \nu(\sigma_1+\sigma_3)\right] + \frac{\gamma_t}{3}\left[1-\exp\left(-\frac{\sigma_2}{E_t}\right)\right] \\
\varepsilon_3 &= \frac{(3-\gamma_t)}{3E_e}\left[\sigma_3 - \nu(\sigma_2+\sigma_1)\right] + \frac{\gamma_t}{3}\left[1-\exp\left(-\frac{\sigma_3}{E_t}\right)\right]
\end{aligned}\right\} \tag{2-8}$$

where $\sigma_1, \sigma_2, \sigma_3$ are effective principal stresses, $\varepsilon_1, \varepsilon_2, \varepsilon_3$ are principal engineering strains, ν is Poisson ratio for the hard part, γ_t is the ratio of the soft part to the entire rock body in one principal orientation and has a value, obtained through experimental tests, on the order 10^{-1}~10^{-2}, and E_e and E_t refer to Young's (elastic) modulus for the hard and soft part, respectively. Note that for the same stress values for the three principal stress directions 2, Equation (2-8) is reduced to Equation (2-3).

2.3 Mine-by (MB) Experiment at the Mont Terri Site

The Mont Terri rock laboratory is located near the town of St. Ursanne in the Jura Mountains of northwestern Switzerland. The Reconnaissance Gallery (or Security Gallery) was originally constructed as part of a motorway tunnel; the underground laboratory has been developed over the last decade. Figure 2-2 shows the layout of the Mont Terri rock laboratory. Experiments were initially performed in eight niches in the security gallery. The first dedicated research gallery was excavated in 1998 and is called Gallery 98. Gallery 98 was then extended in 2004 and the extension is called Gallery 04. At the end of 2006, it was decided to expand the Mont Terri rock research laboratory by adding another gallery (called Gallery 08) of 165 m length and 4 niches (called MB niche). The plan view of Gallery 08 and MB niches are shown in Figure 2-3. An experiment team consisting of Nagra, Andra, GRS, BRG, and Obayashi took the opportunity to investigate the deformation and the coupled HM behavior of the Opalinus Clay around such bedding parallel excavations and set up the MB test (Bossart and Thury, 2008; Vietor, 2011). Before the MB Niche was drilled, sensors of different types were installed. The sensor arrangement around the MB Niche 2 was intended to capture the hydraulic and mechanical effects of the excavation over an extensive region (Vietor, 2011).The excavation of the Niche 2 was carried over in 2008 and the resulting data are now available for modeling the niche deformation in order to improve the understanding of HM coupled processes around excavations in clay rich formations.

The aims of this test accompanying the excavation are to collect data for understanding (1) the evolution of the deformation during excavation with particular emphasis on the tunnel face processes; (2) the hydraulic response to excavation in the excavation near field; (3) the influence of different support strategies on the long term deformation of the tunnels; (4) the far field hydraulics (HM coupling: total stress changes versus pore pressure changes); and (5) the far field deformation (e.g., reaction of faults).

In this study, we focus on one of the MB niches, the MB niche 2. The near field response of MB niche 2, including deformation and hydraulic response to excavation, is the main concern here. The MB niche 2 was excavated from 10/13/2008 to 11/07/2008 as a 24 m long dead-end side niche, SSW of Gallery 08. The niche with a diameter of 4.5 m was excavated by a road header; anchors and light shotcrete were chosen as permanent support (as shown in Figure 2-4). In order to maximize the transferability of the results to a high-level waste emplacement tunnel, the niche was constructed in a similar manner for constructing the waste tunnel using the circular geometry of the niche section, small deviations from intended face geometry (vertical, without rounded corners), a constant excavation rate of 1.3 m/day with small variations, full-face excavation, and the same activity pattern every day.

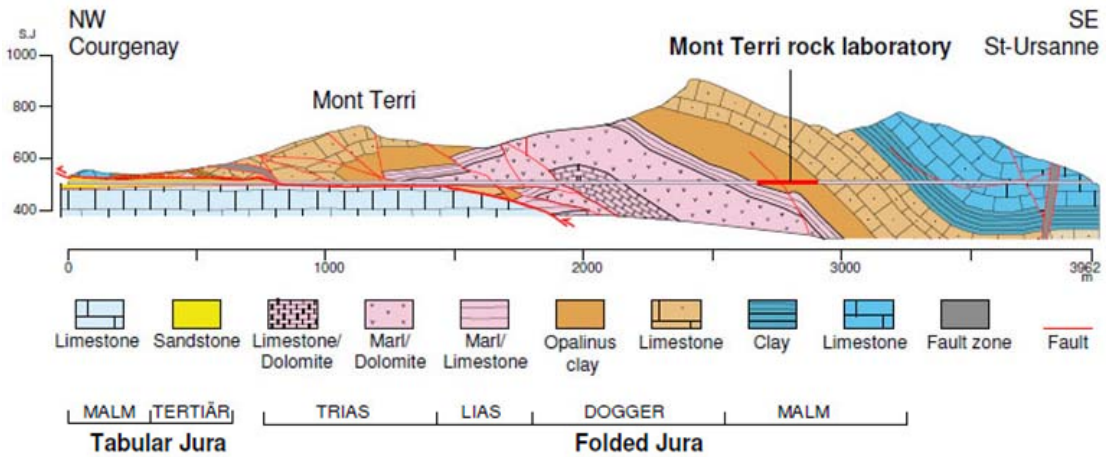

(a)

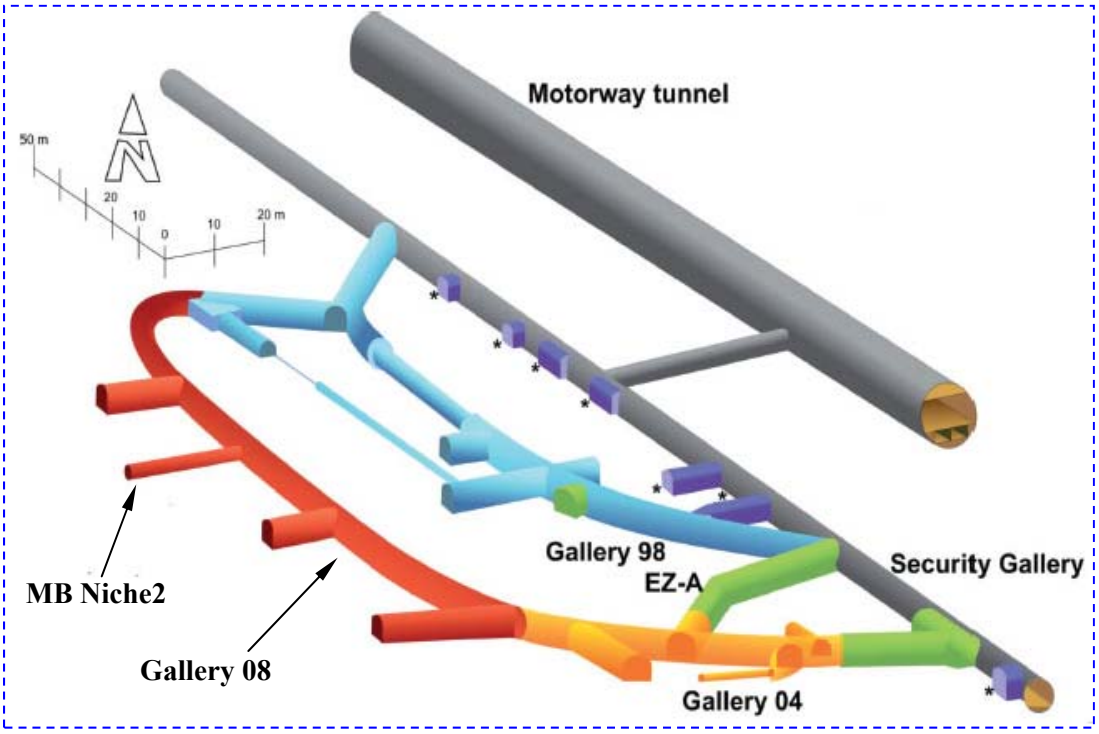

(b)

Figure 2-2. Vertical cross-section of the Mont Terri anticline along the motorway tunnel (a) and the layout of the Mont Terri rock laboratory (b) (Bossart and Thury, 2008).

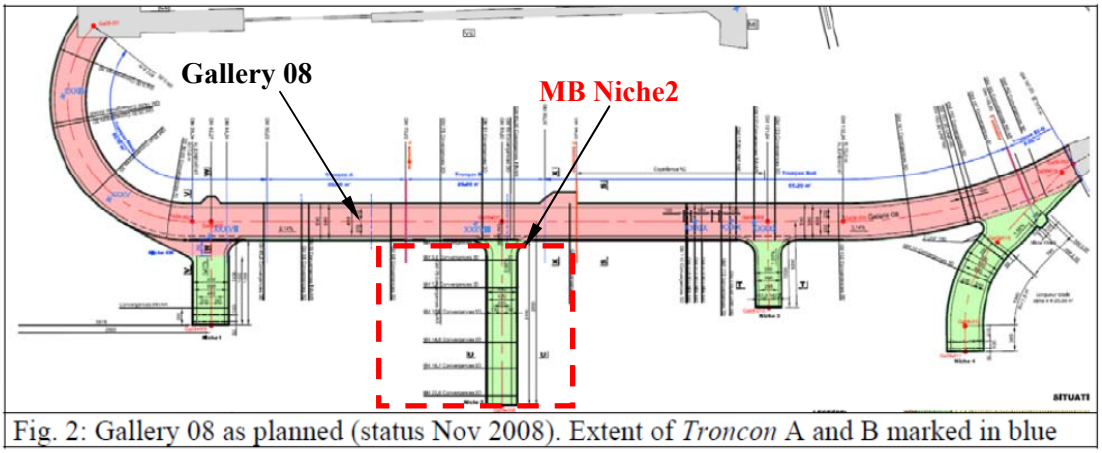

Figure 2-3. Gallery 08 as planned (status Nov 2008) (Vietor, 2011).

(a) (b)

Figure 2-4. MB Niche 2 in construction: (a) the excavation advancing face, and (b) the view of the niche after reinforcement with shotcrete.

Sensors of different types were installed around MB Niche 2 (as shown in Figure 2-5) to capture the hydraulic and mechanical effects of the excavation over an extensive region. The focus was to acquire data on deformation and pressure evolution in the near field in order to improve the understanding of the processes which lead to permanent damage of the clay rock. Note that the excavation damage zone (EDZ) is an important feature impacting a clay-repository performance, because the EDZ, with a much higher permeability than the undisturbed clay rock, may serve as a fast radionuclide-transport path. Thus, the MB test resulted in very valuable data sets associated with the EDZ evolution that are critical for evaluating the capability of an HM model (including constitutive relationships) to capture this evolution.

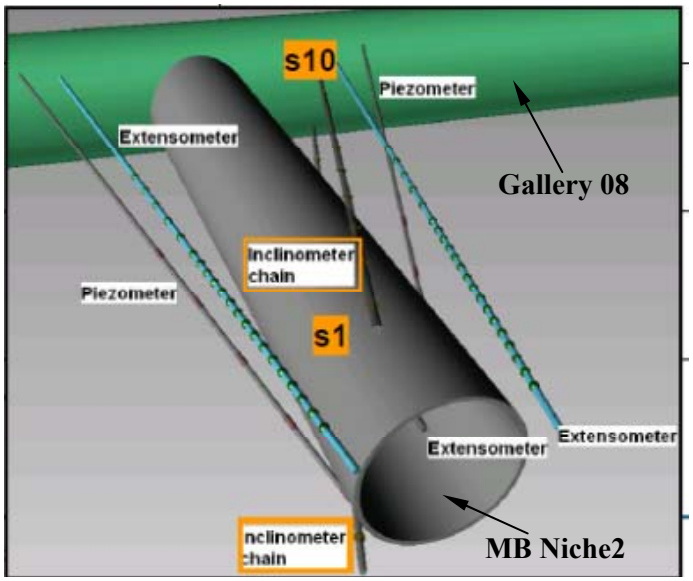

(a) 3D view of MB Niche2

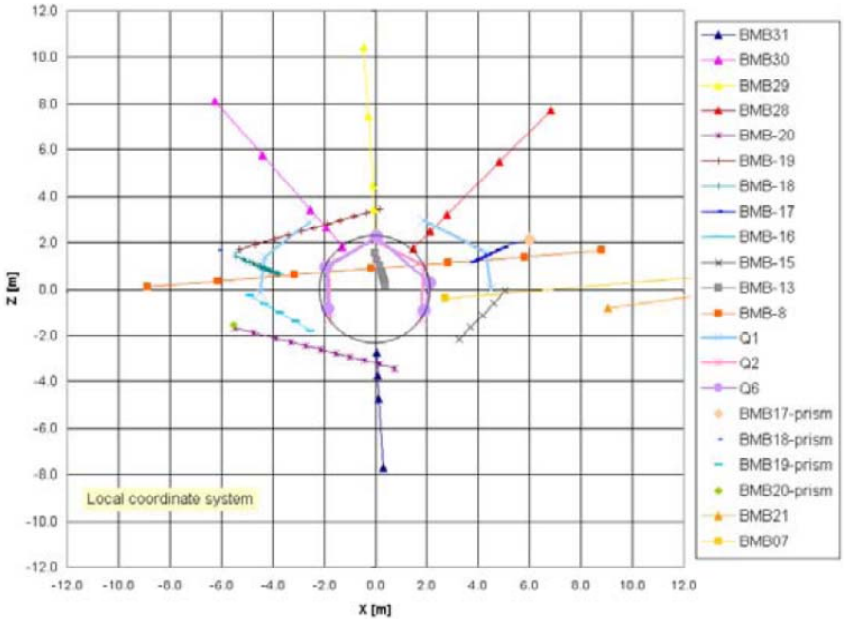

(b) the view from Ga08

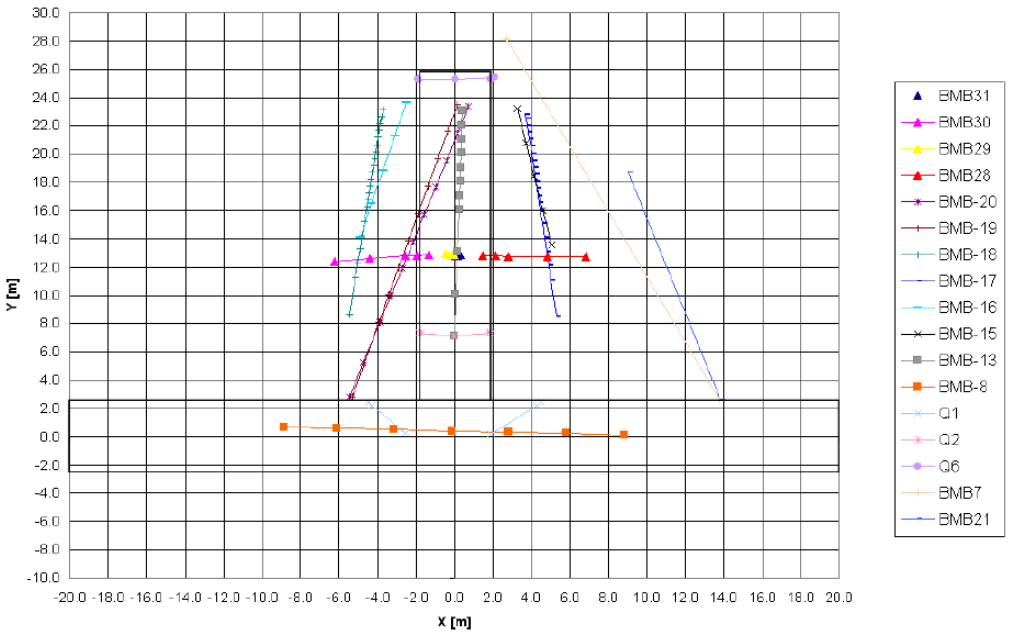

(c) the view from above

Figure 2-5. The instrumentation near MB Niche2.

2.4 Three-Dimensional Numerical Model for the MB Experiment

In this study, numerical simulations were conducted using the geomechanical simulator FLAC3D (Itasca Consulting Group, 2005) into which the TPHM was implemented. The FLAC3D model for MB niche 2 has dimensions 40 m × 46 m × 44 m. The grid has a total of 100,256 zones (grid cells). The MB niche 2 is located in the center of the model. A 24 m length of the tunnel is modeled to represent the niche 2; the axis of the niche is located 22.0 m below the upper surface of the model. A system of coordinate axes is defined with the origin at the center of the tunnel; the z-axis points upward and the y-axis points along the axis of the niche. The FLAC3D grid is shown in Figure 2-6. The niche is constructed in clay rock that is modeled as an isotropic Mohr-Coulomb material.

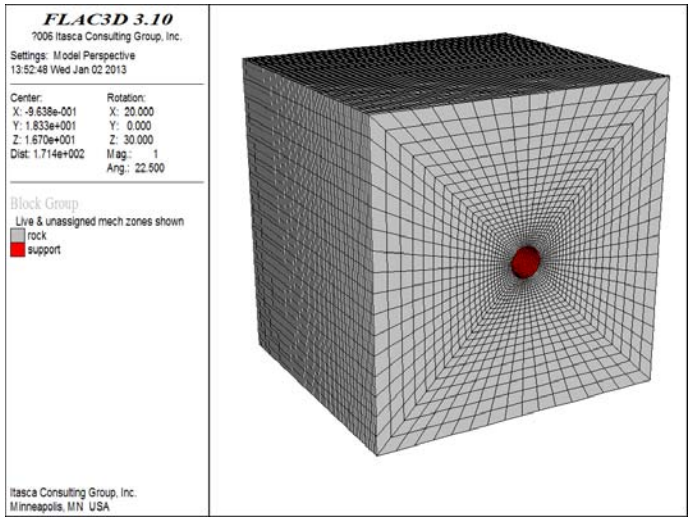

(a) the overview of the model mesh

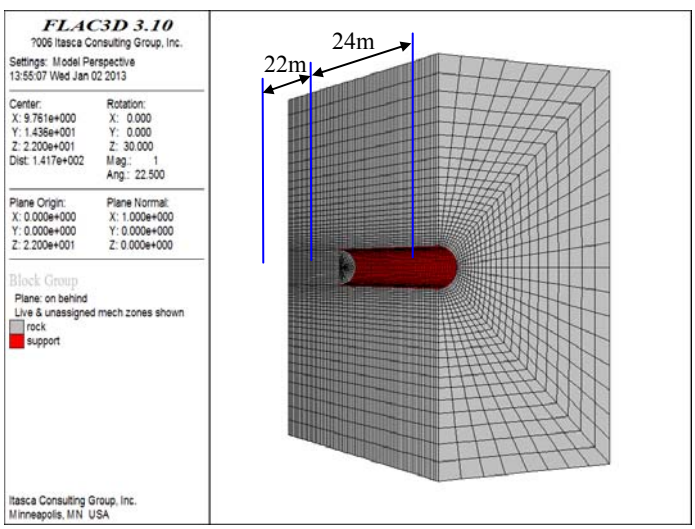

(b) a section plane along Y-axis

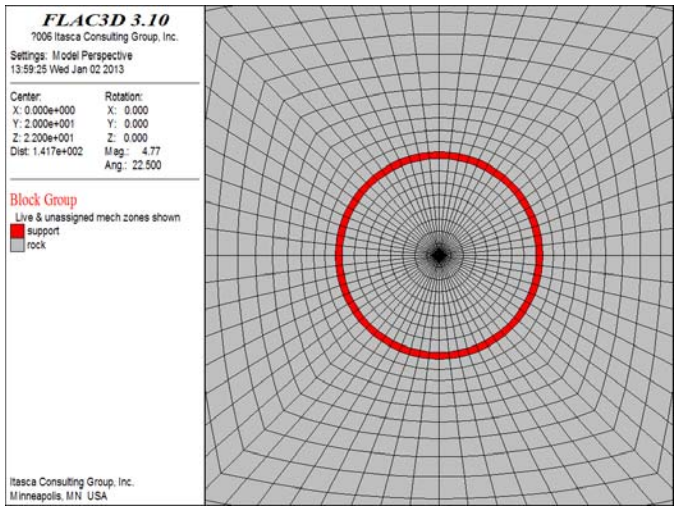

(c) the view from Ga 08

Figure 2-6. The mesh of the numerical model.

Opalinus Clay is of interest not only as a host formation for radioactive waste repositories, but also as a formation through which new transportation tunnels have been constructed. For this reason, a number of investigations have been published. The mechanical parameter values employed in this study are obtained from laboratory experiments and field research (Corkum and Martin, 2007; Bock, 2009; Bock et al., 2010; Zhang et al., 2008; Jobmann et al., 2010), as shown in Table 2-1.

Table 2-1. Physico-mechanical parameters employed in simulations

Parameter	Value	Unit
Bulk density(ρ_m)	2450	kg/m^3
Young's modulus(E_e)	4.0	GPa
Poisson's ratio(v)	0.27	
Tensional strength(σ^t)	1.2	MPa
Cohesion(c)	4.0	MPa
Friction angle(φ)	24.0	°
Young's modulus for the soft parts (E_t)	2.0	MPa
γ_t	0.02	
Initial porosity(ϕ_0)	0.137	
Permeability(k)	2e-20	m^2
Biot coefficient(α)	0.6	
Fluid bulk modulus(K_f)	1000	MPa
Fluid density (ρ_f)	1000	kg/m^3
Fluid viscosity(μ)	1e-3	kg/(m·s)

The concrete tunnel lining (15 cm in thickness as shown in Figure 2-6(c)) is modeled with zones to which we assigned the properties of the lining material. The shotcrete properties of the concrete have been investigated and defined by the Mont Terri consortium (Mont Terri Consortium, 2009). In the modeling, the hydration of shotcrete is not taken into account (no time-dependent evolution of stiffness and strength) and the shotcrete is modeled as an elastic material. The Young's modulus (E_s), compressive strength (σ_s) and Poisson's ratio (ν_s) for the shotcrete are E_s = 10 GPa, σ_s = 10 MPa, ν_s = 0.35, respectively. Other supports, such as anchors, are not considered in this model.

The initial state of stress is assumed to be S1 = 6.5 MPa (vertical), S2 = 4.0 MPa (strike along Ga08) and S3 = 2.5 MPa (strike along Niche2) (Bossart and Thury, 2008). These stresses are applied on the outer boundaries of the model.

The clay matrix is assumed to be a homogenous porous medium and fully saturated. The pore pressure is 2 MPa in the undisturbed state. The fluid in the clay matrix is assumed to be single-phase fluid flow after Darcy's law with isotropic hydraulic conductivity. The coupled process between stress/strain and fluid flow in the deforming rock mass is governed by Biot's consolidation theory (Biot, 1941). The constitutive relationships of a porous medium can be expressed in terms of the stress σ_{ij} (positive for tension), strain ε_{ij} and pore fluid pressure change p as follows:

$$\Delta\sigma_{ij} + \alpha\Delta P\delta_{ij} = H(\sigma_{ij}, \Delta\varepsilon_{ij}), \tag{2-9}$$

where $\Delta\sigma_{ij}$ is the stress increment, the parameter α (≤ 1) is Biot's coefficient, H is the functional form of the constitutive law, δ_{ij} is the Kronecker delta defined as 1 for $i = j$ and 0 for $i \neq j$, and $\Delta\varepsilon_{ij}$ is the strain rate. In this study, the stress-strain in Equation (2-9) is calculated based on Equation (2-8).

Changes in the variation of fluid content are related to changes in pore pressure, p, and mechanical volumetric strain, ε_v. The response Equation for the pore pressure changes is formulated as:

$$\frac{\partial\zeta}{\partial t} = \frac{1}{M}\cdot\frac{\partial p}{\partial t} + \alpha\frac{\partial\varepsilon_v}{\partial t}, \tag{2-10}$$

where ζ is the variation in fluid content or variation in fluid volume per unit volume of porous material due to diffusive fluid mass transport, as introduced by Biot (1956), and M is Biot modulus.

For an ideal porous material, the Biot modulus, M, is related to the fluid bulk modulus K_f:

$$M = \frac{K_f}{\phi + (\alpha - \phi)(1-\alpha)K_f / K} \tag{2-11}$$

where ϕ is the porosity and K is the bulk modulus of solid skeleton.

Based on TPHM, the porosity is related to principal stresses by (Zhao and Liu, 2012):

$$\phi = \phi_0 - \gamma_t - (\phi_0 - \gamma_t) C_e (\sigma_1 + \sigma_2 + \sigma_3) + \frac{\gamma_t}{3}\left[\exp\left(-\frac{\sigma_1}{E_t}\right) + \exp\left(-\frac{\sigma_2}{E_t}\right) + \exp\left(-\frac{\sigma_3}{E_t}\right)\right] \quad (2\text{-}12)$$

where ϕ_0 is the porosity under unstressed conditions, and C_e is the compressibility for the hard fraction of pore volume. In this study, the value of C_e is selected as 2.0×10^{-9} Pa^{-1}. (Nagra, 2002). The rock permeability value given in Table 2-1 is used for the intact rock mass. The impact of porosity change on permeability change is not considered here, because the impact is small (Liu et al., 2012). After rock failure, the permeability is increased by a factor of 100; this will be further discussed in Section 2.5.1. A larger permeability gives rise to quicker pore pressure dissipation.

The excavation chronology of MB niche 2 in the field experiment is shown in Figure 2-7. The total excavation period lasted over four weeks. For each sequential excavation and support step, support measures were usually installed in the morning, followed by renewed excavation in the afternoon.

To model the excavation process, the excavation period is divided into 20 steps. For each step, the excavation is advanced about 1 m and the thick concrete liner is installed simultaneously. In the modeling procedure for a given excavation step, the analysis is divided into two stages. In the first stage, the tunnel is excavated and supported. The excavation and support installation for the first stage are conducted incrementally. The model is run to mechanical equilibrium to simulate a rapid (undrained) excavation process for the given excavation step. In the second stage, a constant pore pressure (atmospheric pressure) is fixed at the excavation surface, and transient water flow is simulated for the time period of the corresponding excavation step. This treatment is based on the fact that mechanical deformation occurs much more quickly than water flow process in a clay formation. Then the pore pressure and deformation around the niche are monitored at locations of selected sensors (Figure 2-5).

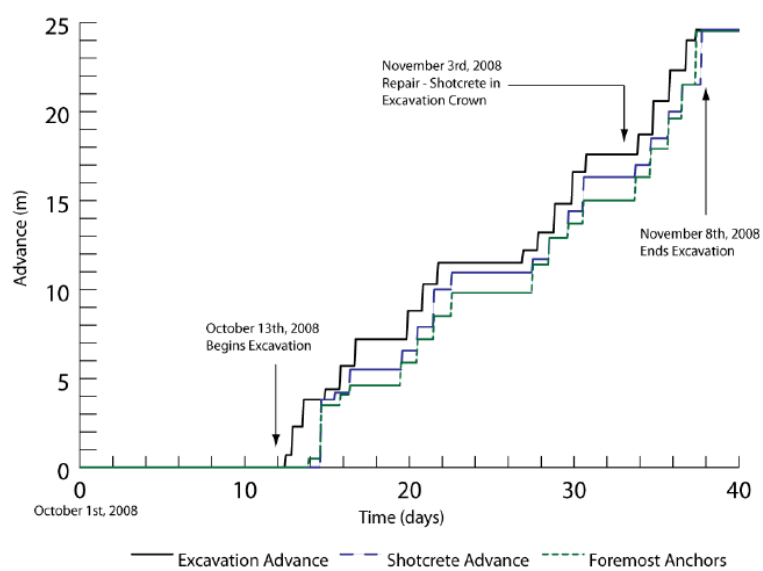

Figure 2-7. The excavation chronology of MB niche2.

In this model study, we used the parameter values given in Table 2-1, which are measured values, as direct inputs into the model for the mine-by test, and performed model predictions of MB test results without any further adjustment of parameter values (or model calibration). This is based on a consideration that a direct comparison between model prediction results and experiment observations allows for a straightforward evaluation of the predictive capability of the corresponding model within the range of parameter uncertainties that always exist for a practical application. The satisfactory matches between data and model results, obtained through model calibration, is not necessarily a good indicator of model predictive capability beyond the range of observations used for calibration, because a good match can be the result of over parameterization of the model, rather than the ability of the model to capture the essence of the physical mechanisms.

2.5 Simulated Results and Discussion

2.5.1 Simulated damage zone and pore-pressure distributions

The simulated extent of the plastic (damage) zone around the niche after 1.5 days, 18 days and 25 days since excavation is shown in Figure 2-8(b) and Figure 2-9(b). The grayscale shades distinguish between shear and tensile failure modes. The letter *n* indicates that the zone is now at active failure; the letter *p* indicates that the zone has failed during a previous excavation step. The creation of the damage zone is dominated by redistribution of the stress around the niche caused by mechanical unloading (excavation). Near the excavation advancing face, tension is the major form of failure with maximum damage zone depth about 2.0 m. In addition to the advancing face area, tensile failure is observed in the roof and floor of the niche, and shear failure is observed at the sidewalls. Near the roof and floor, the damage zone develops up to an average distance of ~0.72 m into the rock matrix, while near sidewalls, the damage zone develops up to an average distance of ~1.4 m into the rock matrix. Figure 2-10(b) shows the plasticity zone in a vertical cross-section at Y = 12 m and perpendicular to the MB niche 2. Based on the in-situ resin impregnation technique, in-situ experimental investigation revealed a dense, interconnected EDZ-fracture pattern down to a maximum depth of 1.1 m from the tunnel wall. The deepest impregnated EDZ-fracture recorded was found at a depth of 2.0 m (Bossart et al., 2002; Bossart et al., 2004; Jaeggi et al., 2012). The numerical result is generally consistent with the reported data. Instrumentation test in field shows an extremely coherent sensor response outside the EDZ that pre-existing faults do not lead to localized deformation outside the EDZ. This finding and the observed dense fractures within the EDZ justify the use of the continuum modeling in this study (Vietor, 2011).

The corresponding pore-pressure distributions around the niche at 1.5 days, 18 days and 25 days after excavation are shown in Figure 2-8(a) and Figure 2-9(a). The pore pressure shows a very sharp gradient at the edge of the damage zone adjacent to the niche walls. Just at the niche walls, the value of pore pressure is 0.1 MPa, equal to the atmospheric pressure in the niche. Beyond a certain distance from the niche walls in rock matrix, the pore pressure evolution shows a tendency to stabilize at a constant value (2.0 MPa). The pore pressure evolution is thus a relatively sensitive response to the excavation progress. Pore pressure increase becomes visible at about 11 m (2.5 diameters of the MB niche2) ahead of the mine-by excavation face. With niche advancement, the zones with higher pore pressure are mainly found near the edge of the damage zones. Particularly near the excavation advancing face, the maximum pore water overpressure is about 3.3 MPa (as shown in Figure 2-9(a)).

As previously indicated, there is a very good correlation between the simulated damage zone and the low pore-pressure zone with pressure values similar to the niche wall pressure (0.1 MPa). This is because the

assigned permeability for the damage zone is two orders of magnitude higher than the undisturbed rock. The observed permeability in the damage zone is generally several orders of magnitude higher than the undisturbed rock (Bossart et al., 2004). As a result, pore pressure within the damage zone becomes equilibrium with the niche wall pressure rapidly. Further increases in damage zone permeability do not change the simulation results significantly. Furthermore, because rock matrix permeability is very low, water flow from the matrix does not have enough time to fill in the new fractures created in the EDZ during the test. It is very likely that air flow from niches to the damage zone occurred during the time that the damage zone was formed, such that approximately pore-pressure equilibrium between damage zone and the niche wall took place quickly. For a given permeability, the mobility of air flow is much higher than that for water flow because air has much smaller viscosity; it is the mobility that controls the flow processes. Note that the two-phase flow process in fractures is complex (Liu et al., 2002) and the simplification is practically needed for this application. The good correlation between damage zone and the low pore-pressure zone also has important practical applications for monitoring EDZ evolution with pore-pressure sensors; this will be further discussed later.

The simulated pore pressure distributions exhibit three distinguishable zones. In addition to the low-pressure zone corresponding to the damage zone and undisturbed zone away from the damage zone, there exists an elevated pore-pressure zone at the edge of the damage zone (Figures 2-8 and 2-9), as previously indicated. This is because the stress at the edge of the EDZ needs to be increased to compensate for the fact that the damage zone is not effective in supporting the overburden. Beyond this high pore-pressure zone into the rock, the unloading effects due to excavation and the associated damage zone disappears.

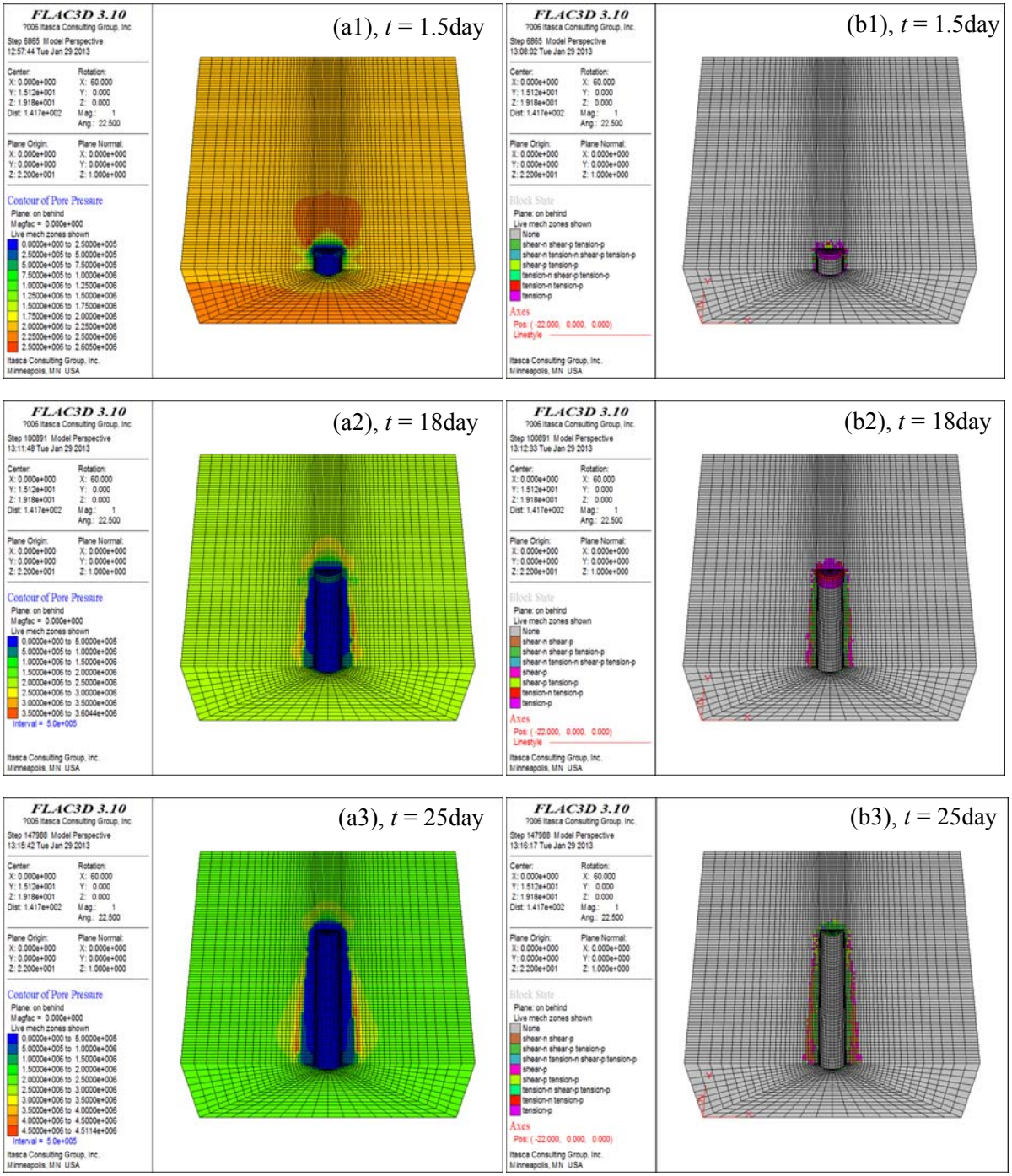

Figure 2-8. Simulated results based on TPHM for horizontal cross-section along MB niche 2: (a) pore pressure contours (Pa) and (b) the damage zone (and mode).

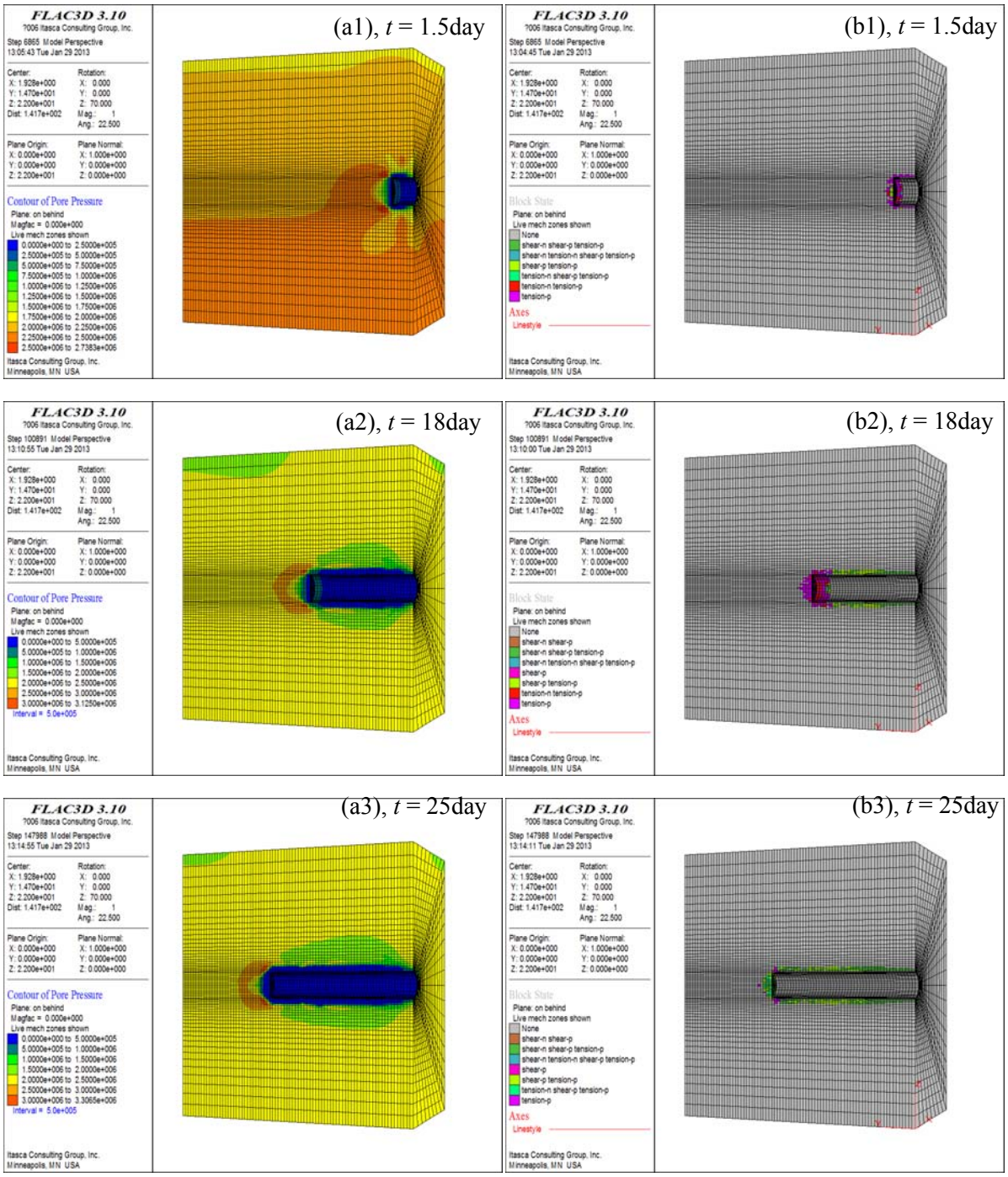

Figure 2-9. Simulation results based on TPHM for a vertical cross-section along MB niche 2: (a) pore pressure contours (Pa) and (b) the damage zone (and mode).

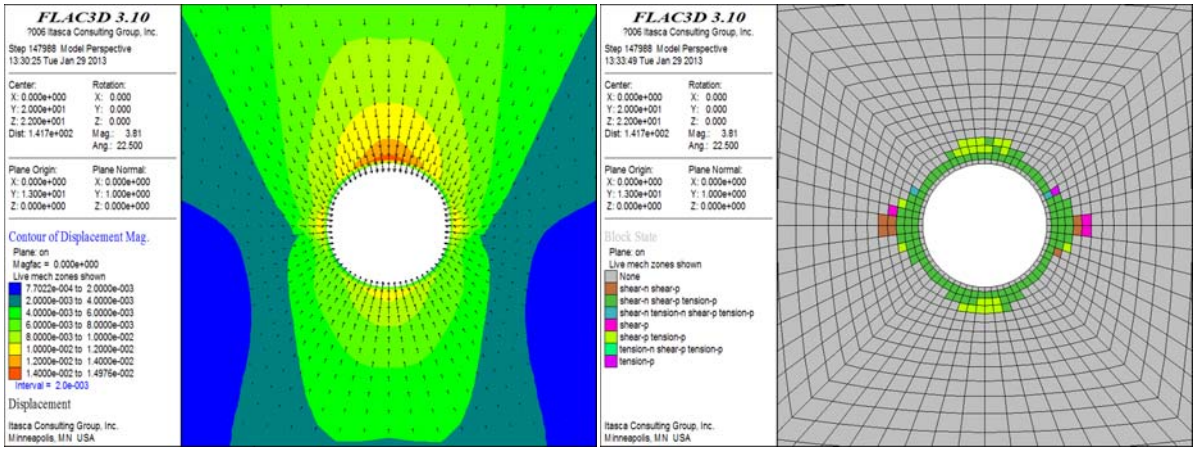

(a) (b)

Figure 2-10. The TPHM-based simulation results for the damage zone and deformation around MB niche2 after construction for a vertical cross-section at Y = 12 m and perpendicular to the MB niche2: (a) displacement distribution and (b) the damage zone (and mode).

2.5.2 Comparisons between TPHM and SPHM simulation results

As a comparison, the simulated damage zone (and mode) and pore pressure distributions based on the conventional Hooke's law (SPHM) are also obtained and shown in Figures 2-10, 2-12 and 2-13. The overall damage patterns are similar to those in Figures 2-8, 2-9 and 2- 10 obtained with the TPHM. The simulated damage zones are characterized by shear failure at sidewalls and tension failure at roof and floor. The SPHM-based results show that near the roof and floor, the damage zone develops up to an average distance of ~0.16 m into the rock, while near the sidewalls it develops up to an average distance of ~0.44 m into the rock. Clearly, the damage zone size modeled with TPHM is larger than that obtained with SPHM and more consistent with field observations, as discussed in the previous subsection. Figure 2-10 and 2-13 also demonstrate deformation distributions simulated with TPHM and SPHM, respectively. While the general distribution patterns of displacement are similar for both models, the magnitudes are clearly different.

The differences in EDZ sizes obtained with TPHM and SPHM can be explained as follows. During the excavation, near-field unloading process occurs, resulting in a low stress in the rock mass near the tunnel. As discussed in Section 2.2, the "soft" part of the rock becomes important in low-stress regions. In other words, rock mass surrounding the tunnel becomes much softer during excavation than it is under the ambient conditions corresponding to higher stresses. In the latter case, the "hard" part plays a more important role. Because of this softening effect, a relatively larger region of rock mass surrounding the tunnel can mechanically feel the unloading effects due to excavation, compared with the region simulated with SPHM that does not consider the "soft" part. This results in a relatively large EDZ size. This does highlight the needs to use the TPHM for modeling the EDZ evolution, a critical feature determining the performance of a clay repository.

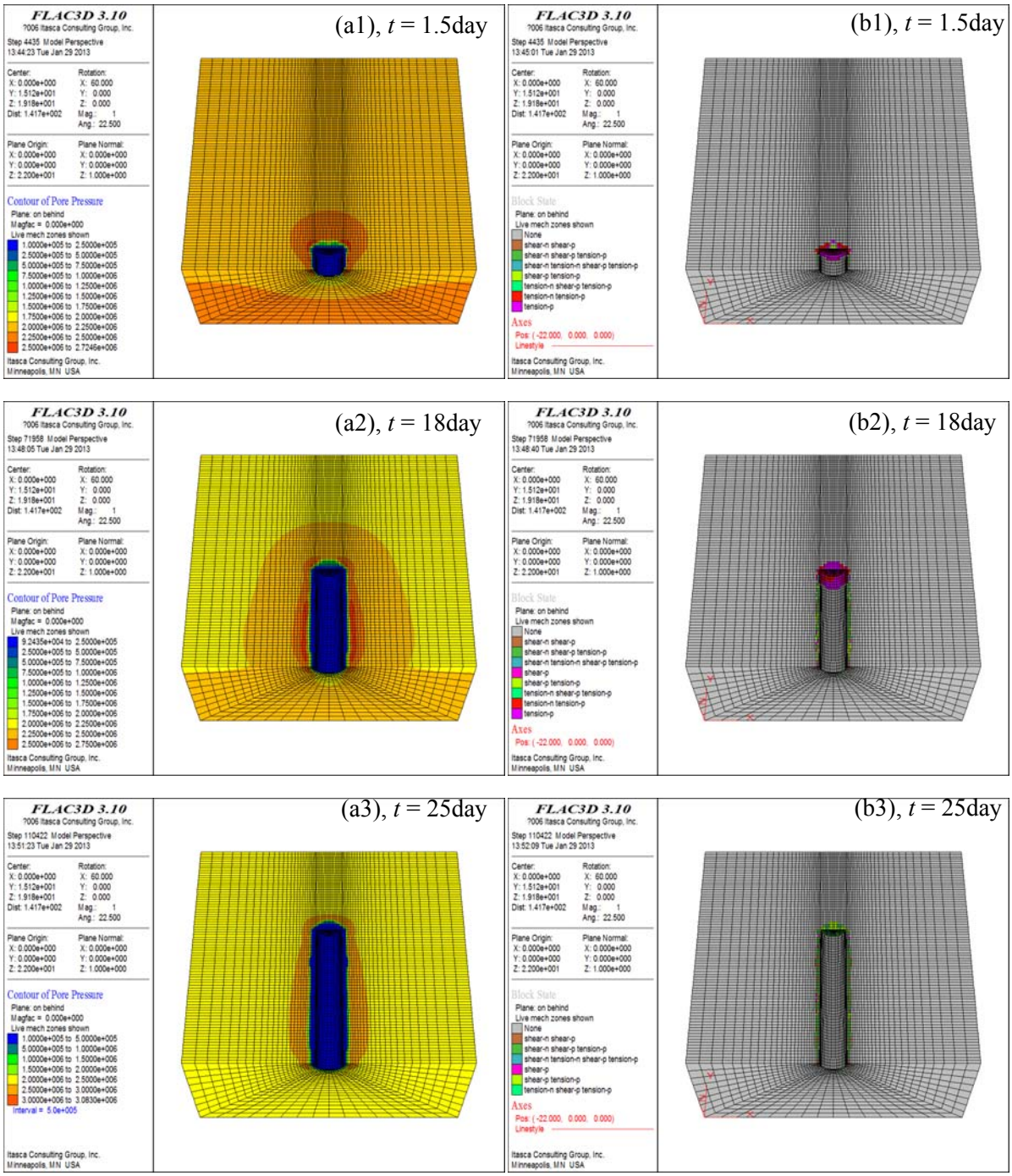

Figure 2-11. Simulation results based on SPHM for a horizontal cross-section along MB niche2: (a) pore pressure contours (Pa) and (b) the damage zone (and mode).

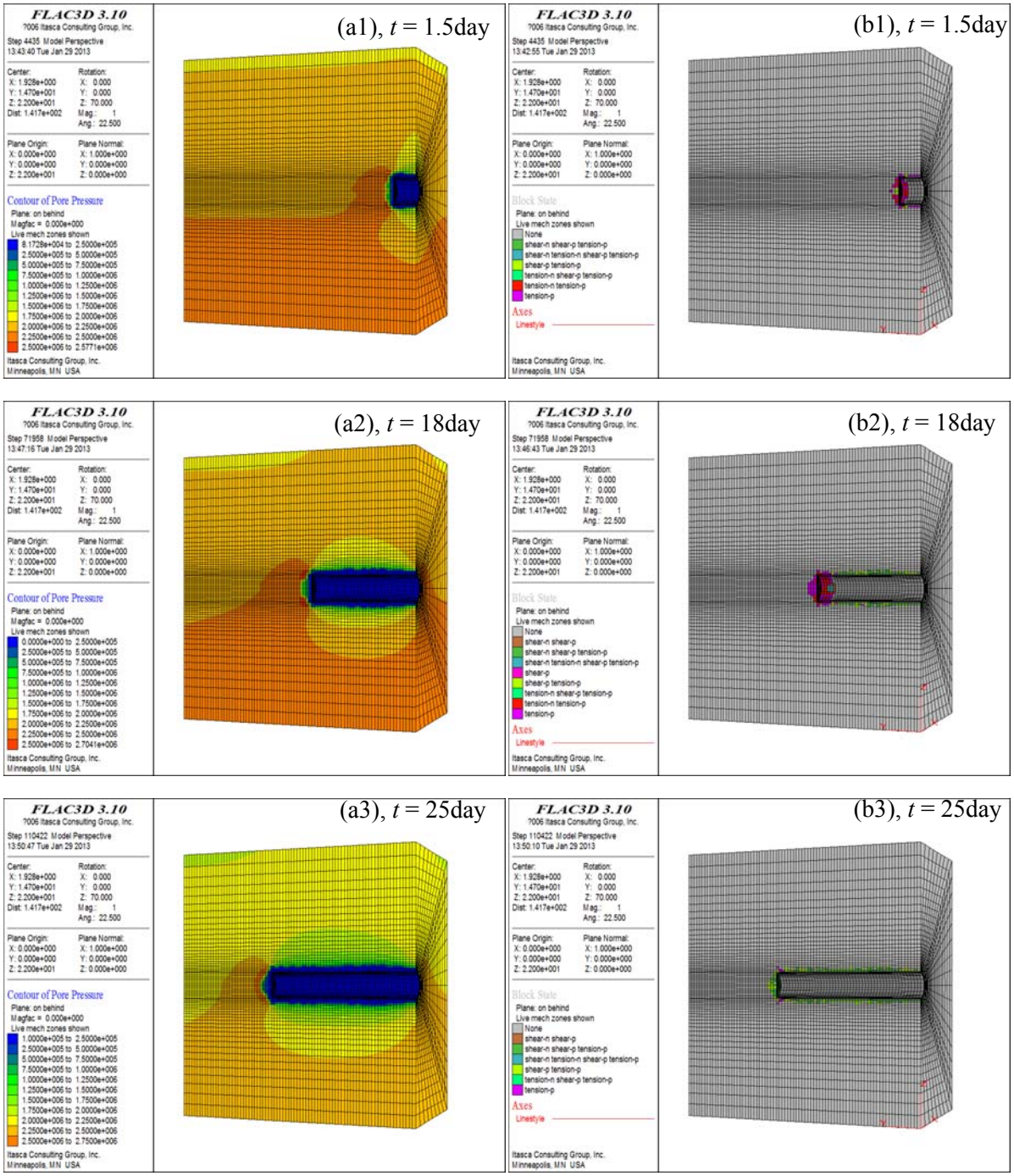

Figure 2-12. Simulation results based on SPHM for a vertical cross-section along MB niche2: (a) pore pressure contours (Pa) and (b) the damage zone (and mode).

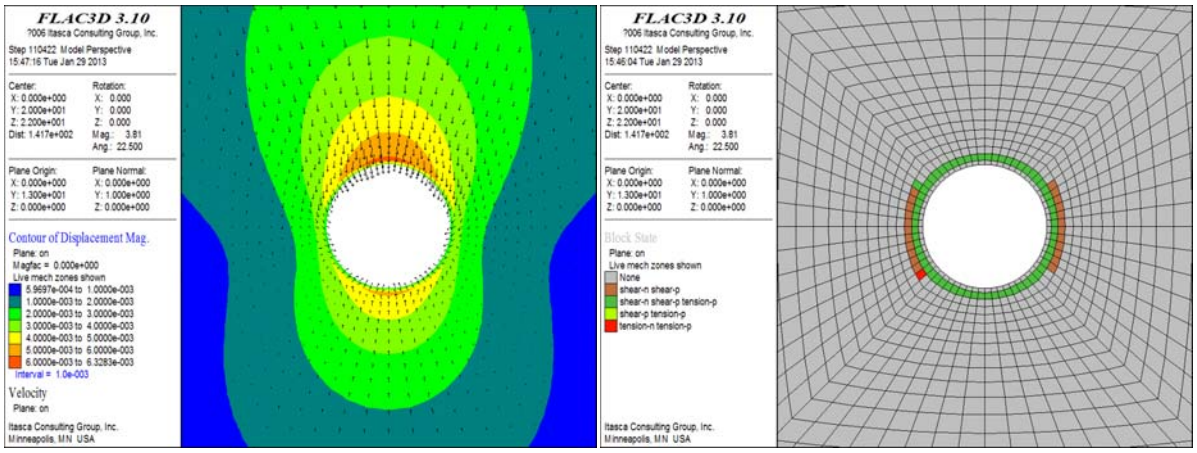

(a) (b)

Figure 2-13. The SPHM-based simulation results for the damage zone and deformation around MB niche2 after construction for a vertical cross-section at Y = 12 m and perpendicular to the MB niche2: (a) displacement distribution and (b) the damage zone (and mode).

2.5.3 Comparisons between simulation results and experimental observations

To further evaluate the TPHM, Figure 2-14 presents comparisons between simulated results from both the TPHM and SPHM and observed radial displacement histories at two selected monitoring locations at inclinometer chains BMB30 as shown in Figure 2-5. These two locations near the central part of the model are selected here to eliminate the influence of boundary effects on the numerical result. The deformation of surrounding rock matrix becomes visible at about 12 m before the mine-by excavation front. The calculated inward displacements based on the TPHM are larger than those predicted with SPHM. Clearly, the TPHM model results represent a better match to measured data. These results show that the TPHM model provides a more realistic representation of the deformation pattern because it takes into account the mechanical behavior of “soft’ features within the rock mass.

Note that the current version of the TPHM is not able to capture the bedding effects of the rock, because it does not consider anisotropic distributions of mechanical properties. The development of the capability to capture the anisotropic effects within the TPHM framework is under way. However, this is not a trivial task because of the non-linear relationship between stress and strain in TPHM. Therefore, the relative importance of the bedding impact on the mechanical deformation near the niche is not conclusive from the current study. However, one speculation, based on the good agreement between simulated and observed displacements (Figure 2-14), is that the bedding may not have a significant effect at least during the test period; this hypothesis needs further evaluation. Also, only a quasi-static analysis was performed and the long-term response (creep or delayed plastic response) was not considered here. This is considered reasonable given the fact the MB experiment only lasted a relatively short time period.

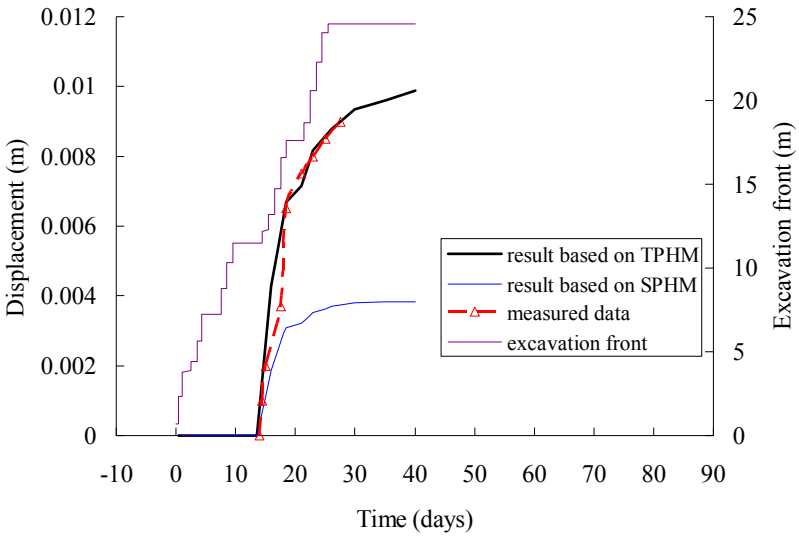

(a) displacement at sensor BMB30_4

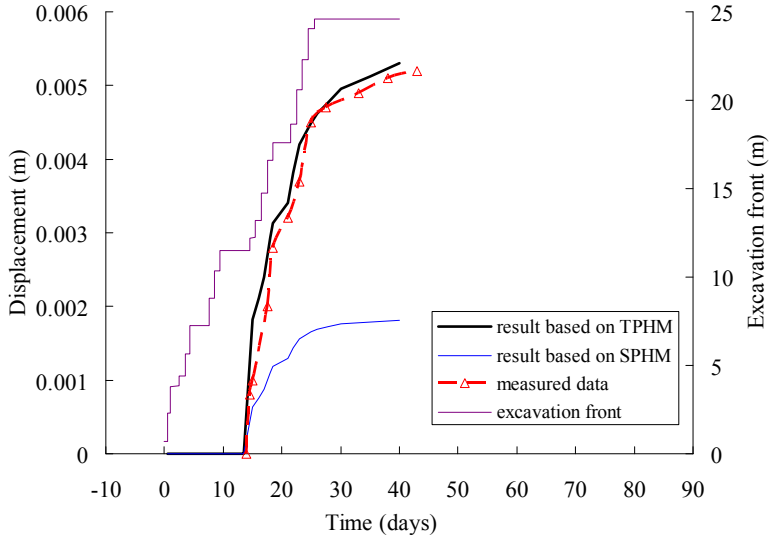

(b) displacement at sensor BMB30_1

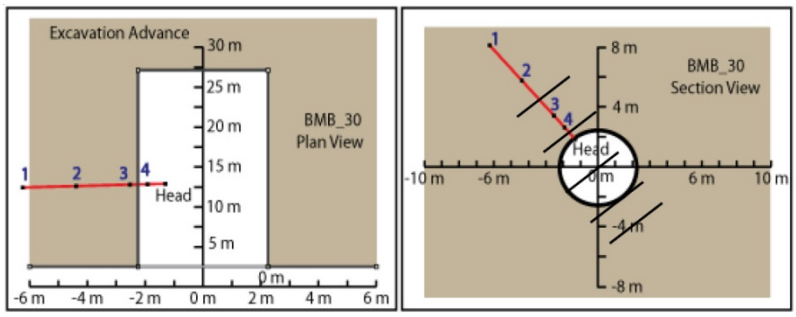

(c) the locations of displacement monitoring sensors (BMB30)

Figure 2-14. Excavation advancing and (simulated and observed) inward displacements as a function of time.

Figure 2-15 shows comparisons between simulated and observed pore pressure histories at two locations corresponding to sensors BMB-15 and BMB-16 (Figure 2-5), 16.0 m and 23.0 m distant (along the niche) from the beginning of the niche, respectively. The observations are consistent with the evolution of three pore-pressure zones discussed in Section 5.2.1. The sensors locations were initially within the undisturbed rock mass and therefore had flat pore pressure distributions corresponding to the ambient conditions. With the excavation advancing, the locations became closer to the EDZ and reached an elevated pressure zone where the stress at the edge of EDZ needs to be increased to compensate for the fact that the damage zone is not effective in supporting the overburden. Then, the pore pressures started to decline with time when the sensor locations were close to or within the EDZ because the EDZ has a relatively large permeability that allows for quick pore-pressure dissipation. The observed pore-pressure histories at two sensor locations are generally predicted by TPHM simulation results. The SPHM results do a good job as well for sensor BMB-16 (Figure 2-15 b), but considerably underestimate pore pressure decline for BMB-15. This is because SPHM underestimates the EDZ size and consequently underestimates the pore-pressure dissipation rate at the location for sensor BMB-15.

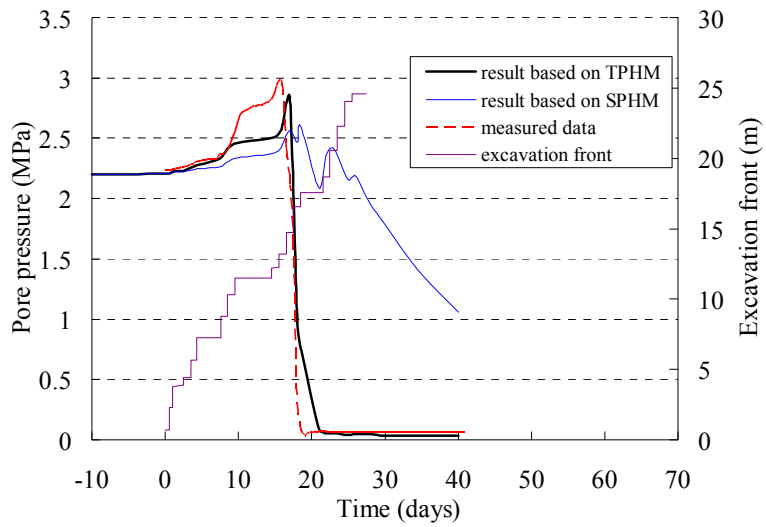

(a) pore pressure at sensor BMB15_I3

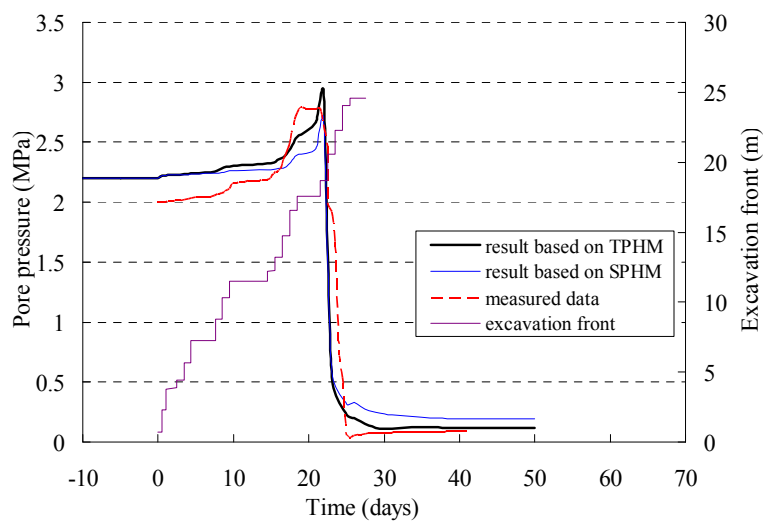

(b) pore pressure at sensor BMB16_I1

Figure 2-15. Excavation advancing and (simulated and observed) pore pressures as a function of time.

2.5.4 Simulation results with an alternative value for Young's modulus (E_e)

As previously demonstrated, the TPHM-based model results are significantly different from those obtained from the traditional approach (SPHM) and agree better with field observations. Also, in this study, we emphasize the usefulness of a direct comparison between predicted and observed results in evaluating the constitutive model. Our predictions are obtained with parameter values given in Table 2-1 that are representative of property measurements and consistent with those used in previous studies in the Opalinus Clay (Corkum and Martin, 2007; Zhang et al., 2008; Jobmann et al., 2010). However, uncertainty exists in these parameter values. Due to the presence of a large number of natural defects, the experimental data on the mechanical properties of the Opalinus Clay are subject to considerable variations (Bock, 2009; Gräsle and Plischke, 2010). To investigate the influence of the variation in stiffness of clay

rock on the deformation and pore pressure, we re-ran some simulations with both the THPM and the SPHM by increasing the elastic modulus from 4.0 to 7.0 GPa, while holding all of the other material parameters and boundary conditions constant (Table 2-1). The latter value of the elastic modulus was suggested for the Opalinus Clay by Bock (2009).

The simulated EDZ size and deformation mode are presented in Figures 2-16 and 2-17. The displacement histories at two points on inclinometer chains BMB30 are plotted in Figure 2-18, and pore-pressure histories for sensors BMB-15 and BMB-16 are given in Figure 2-19. Simulated EDZ sizes are generally similar for the two values of the elastic modulus, as shown in Figures 2-10 and 2-13 compared with Figures 2-16 and 2-17, respectively. The larger elastic modulus results in underestimation of displacements, but the TPHM-based results are much closer to the observations (Figure 2-18). Again, the TPHM-based results reasonably capture the pore-pressure evolutions at locations for sensors BMB-15 and BMB-16, while the SPHM does a poor job for BMB-15.

In summary, this sensitivity study indicates that for the alternative value of elastic modulus, the TPHM still outperforms the SPHM in terms of comparisons between simulated and observed results, and the value of 4.0 GPa seems to be more reasonable for the elastic modulus than 7.0 GPa.

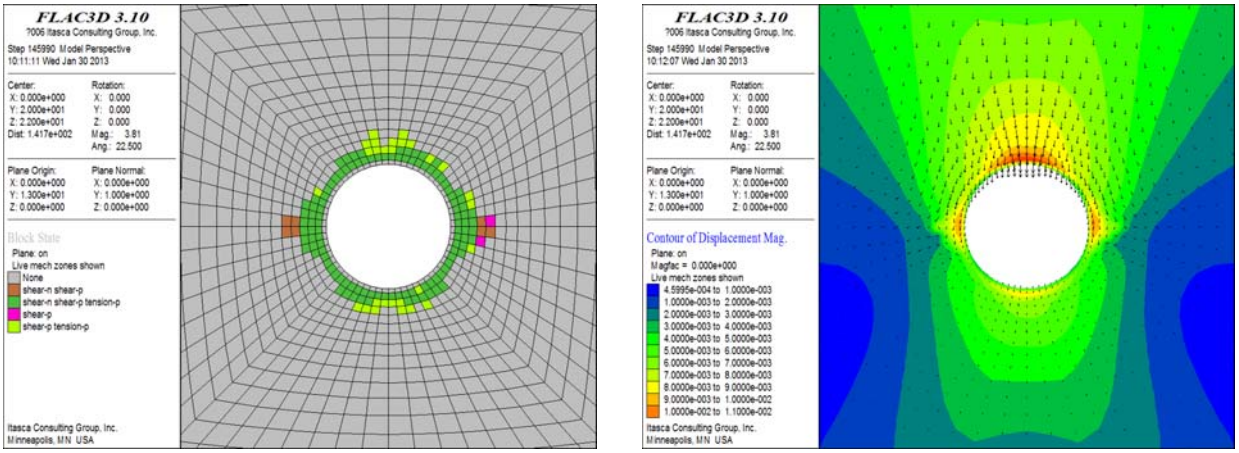

(a) (b)

Figure 2-16. The TPHM-based simulation results for damage zone and deformation around MB niche2 after construction for a vertical cross-section at Y = 12 m and perpendicular to the MB niche2: (a) the damage zone (and mode) and (b) displacement distribution. Note that in this case, the elastic modulus used in modeling is 7GPa.

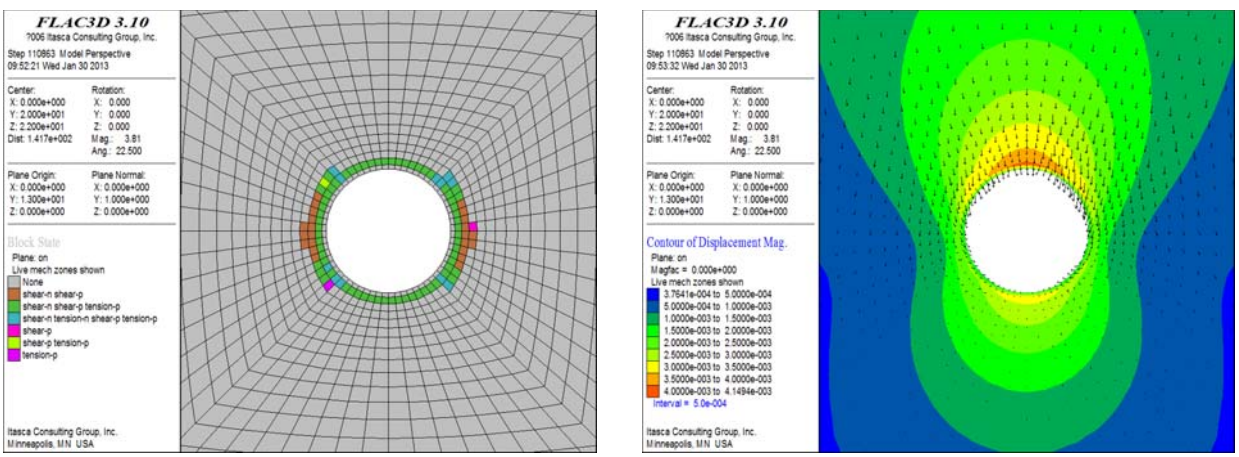

(a) (b)

Figure 2-17. The SPHM-based simulation results for the damage zone and deformation around MB niche2 after construction for a vertical cross-section at Y = 12 m and perpendicular to the MB niche2: (a) the damage zone (and mode) and (b) displacement distribution. Note that in this case, the elastic modulus used in modeling is 7GPa.

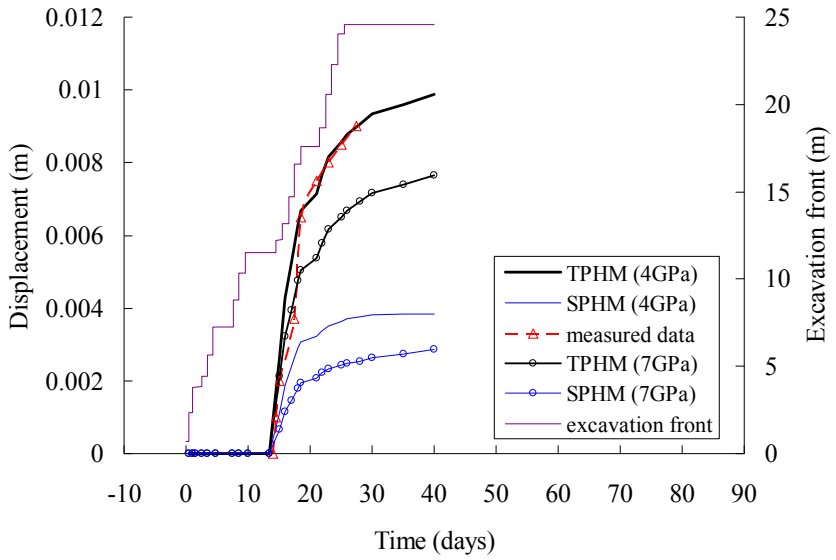

(a) displacement at sensor BMB30_4

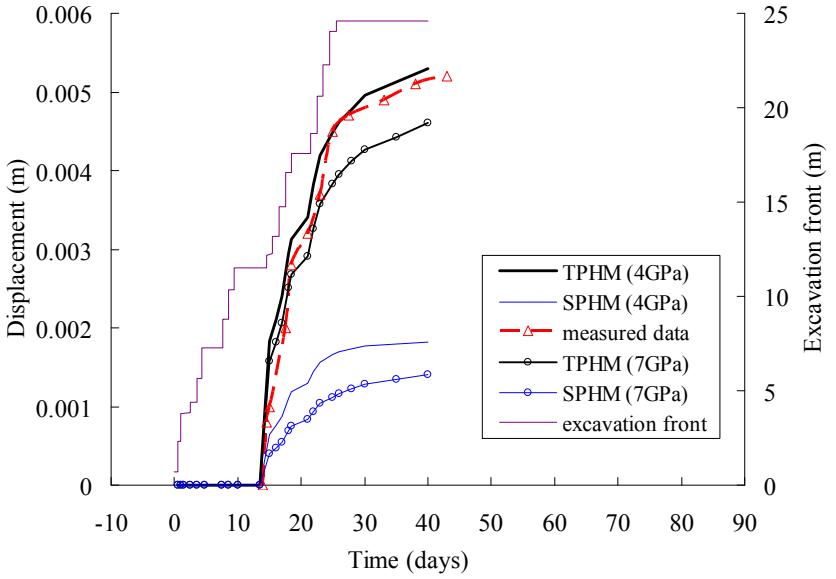

(b) displacement at sensor BMB30_1

Figure 2-18. Excavation advancing and (simulated and observed) inward displacements as a function of time for two values of elastic modulus.

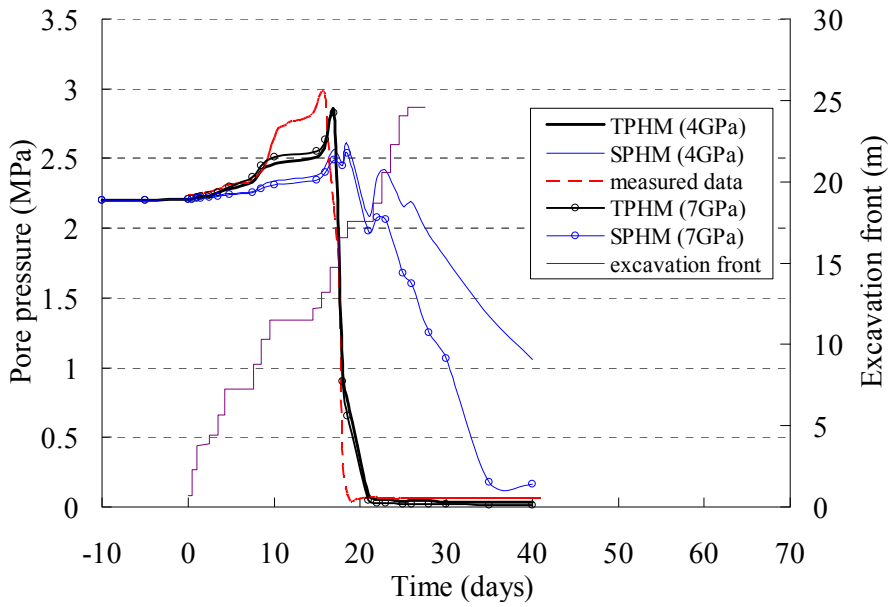

(a) pore pressure at sensor BMB15_I3

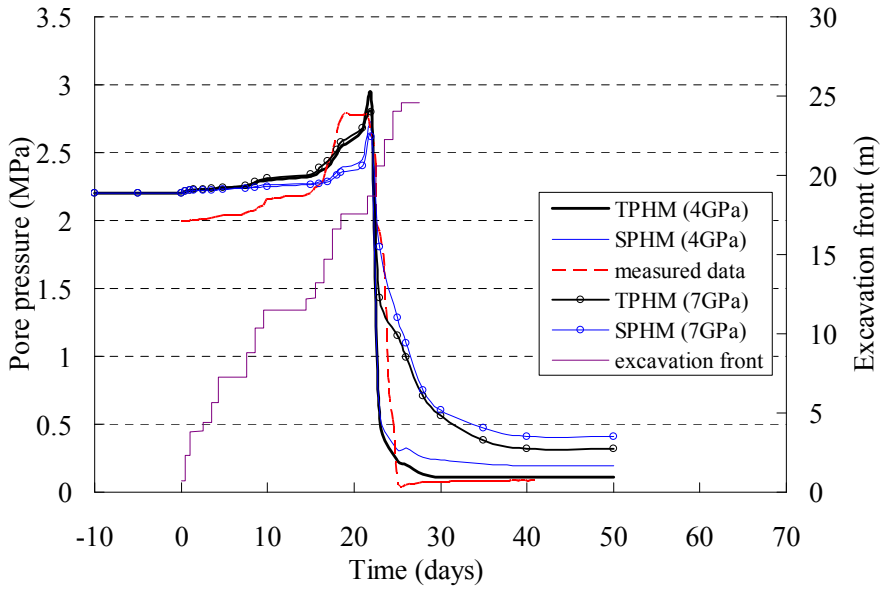

(b) pore pressure at sensor BMB16_I1

Figure 2-19. Excavation advancing and (simulated and observed) pore pressures as a function of time for two values of elastic modulus.

2.6 Conclusions

The MB test in the Mont Terri underground research laboratory has generated valuable data for understanding mechanical and hydraulic processes during tunnel excavation necessary to the construction of a clay repository. In particular, this data set allows for validating THM models including the constitutive relationship. This study documents our progress in validating a new constitutive relationship, represented by the two-part Hooke's model (TPHM), with the field data from the MB test while previous evaluations of the TPHM have been largely done with laboratory-scale data and related empirical relationships available in the literature.

A three-dimensional model based on the TPHM was developed to predict the deformation and pore pressure responses in the near field of MB Niche 2. Simulation results show that the pore pressure disturbance becomes visible at about 11 m ahead of the mine-by excavation advancing face (along the longitudinal direction of the niche). The results also demonstrate that there exists a good correlation between the EDZ and pore-pressure evolution, which may have important practical applications for monitoring EDZ evolution with pore-pressure sensors. The excellent agreement between observed displacement and pore-pressure histories at several locations and those predicted with TPHM clearly indicate that TPHM captures the complex hydro-mechanical responses to the excavation during the MB test.

To further demonstrate the usefulness of the TPHM and associated formulations, we also compared simulation results based on TPHM and the conventional Hooke's law (SPHM). The TPHM results are significantly different from those obtained with the SPHM and much closer to experiment observations. This highlights the need to use TPHM, rather than SPHM, in practical applications, including those associated with construction of a clay repository.

3. Discrete Fracture Network (DFN) Approach for Fractures in Argillaceous Rock

Although clay-rich formations are usually characterized by low intrinsic rock permeability and very limited fracture permeability, observations indicate that permeable fracture networks can form for limited times (e.g., Bossart et al., 2004; Cosgrove, 2001) There are two classes of fracturing that require investigation: (1) fracturing around an excavation in the excavation damaged zone (EDZ) and (2) natural fracturing.

Fractures in the EDZ have been routinely observed in clay-rock underground research laboratories (URL) in Europe, including the Opalinus Clay in Switzerland, Boom Clay in Belgium, and the Callovo-Oxfordian Clay in France (Volckaert et al., 2004). These fractures are a result of mechanical stress resulting from excavation and shrinkage caused by ventilation dryout, conditions that are expected during the pre-closure phase of a repository; however, post-closure effects, such as thermal pressuring and gas evolution may also result in fracturing (Blümling et al., 2007). The EDZ not only shows fracturing along tunnel surfaces, but measurements of permeability also verify that in thin zones (<~1 m) around drifts there can be fracture damage (Bossart et al., 2004). Finally, fractures in clay-rich formations also show significant self-sealing over a three-year period (Bossart et al., 2004). The connectivity of fractures along a tunnel has been observed in the HG-A test at Mont Terri, Switzerland, where a test tunnel section, sealed by a packer, was injected with fluid that showed preferential pressure increases along the packer where the most severe EDZ damage was observed (Lanyon et al., 2009).

Fracturing has also been observed in clay-rich formations as a result of natural processes, often associated with abnormal pore-pressure conditions. These can lead to fault reactivation and hydraulic fracturing. Geologic evidence suggests that the Mercia Mudstone within the Bristol Channel Basin in the UK was subject to repeated episodes of natural hydraulic fracturing over its 250 million year history (Cosgrove, 2001). This mudstone underwent 150 M years of burial followed by 100 million years of uplift. Outcrop evidence shows that natural fractures formed, conducted fluids, and then sealed at various points in time both during burial and uplift.

The main conclusion to be drawn from these observations is that fractures in argillaceous rocks are transient features that require a dynamic modeling approach. In this section we discuss various technical developments related to the TOUGH-RBSN model. This model is capable of computing coupled thermal-hydrological-mechanical processes including fracture initiation, propagation, and evolution in rock.

3.1 Mechanical Damage Model Using RBSN

3.1.1 Background

Various numerical models have been developed to simulate the fracture behavior of geomaterials. Those models can be widely categorized by the representation of the domain of interest: continuum or discrete elements. Discrete models have become popular as computational tools for studying the heterogeneous characteristics of geomaterials. This category includes the Rigid-Body-Spring network (RBSN), in which system behavior is represented by primitive two-node elements interconnected on a set of nodal points. The approach considered here is based on the Rigid-Body-Spring concept of Kawai (1978).

To provide a basic overview of this modeling approach, an overview of the element formulation is given here. Topology of the RBSN is defined by the dual Delaunay tessellation of the nodal points. The basic unit of RBSN is a 1-D lattice element consisting of a zero-size spring set located at the centroid of the

Voronoi boundary (Figure 3-1). Each node has six degrees of freedom for the 3D case. The spring set is formed from three axial springs and three rotational springs. The local spring coefficients are assigned according to:

$$k_s = k_t = \alpha_1 k_n = \alpha_1 \alpha_2 E \frac{A_{ij}}{h_{ij}}, \quad k_{\phi n} = E \frac{J_p}{h_{ij}}, \quad k_{\phi s} = E \frac{I_{ss}}{h_{ij}}, \quad k_{\phi t} = E \frac{I_{tt}}{h_{ij}} \tag{3-1}$$

in which E is the Young modulus, J_p, I_{ss}, and I_{tt} are the polar and two principal moments of inertia of the Voronoi cell boundary with respect to the centroid, respectively. The axial and rotational springs are scaled in proportion to the distance between the element length, h_{ij}, and the area of the Voronoi cell boundary, A_{ij}. For the special case of $\alpha_1 = \alpha_2 = 1$, the Voronoi scaling of the spring constants, A_{ij}/h_{ij}, enables the method to be elastically homogeneous under uniform modes of straining, albeit without proper modeling of the Poisson effect. Such Voronoi scaling also serves energy-conserving, grid-size insensitive representations of tensile fracture. Details regarding the RBSN are given elsewhere (Bolander and Saito, 1998; Asahina et al., 2011).

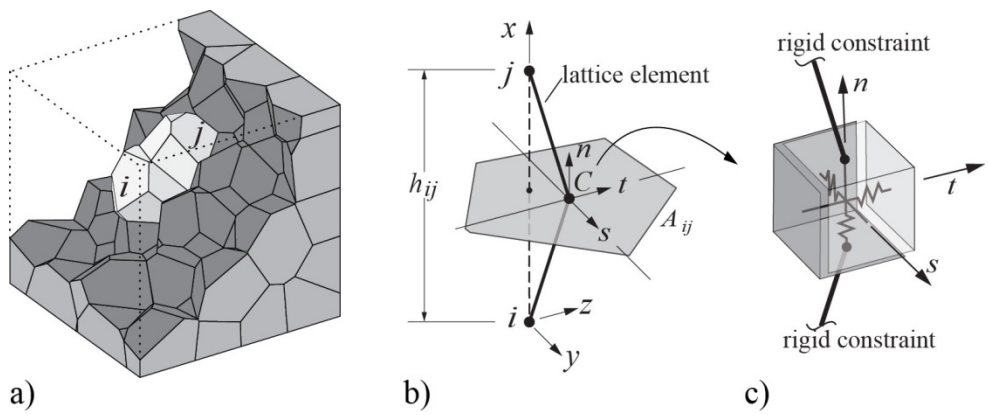

Figure 3-1. Typical lattice element *ij*: a) within a Voronoi grid; b) isolated from the network; and c) a zero-size spring set (referenced to local coordinate axes *n-s-t*) located at centroid *C* of Voronoi cell boundary area A_{ij}.

The stress tensor at the Voronoi cell nodes can be calculated by considering the equilibrium conditions of the spring force. After solving the system equation (i.e., the global system stiffness matrix), components of the spring force at the centroid of a Voronoi cell boundary can be obtained (Figure 3-2a). Figure 3-2b shows local force components F_{nn}, F_{ns}, and F_{nt} for an arbitrary section of the cell (passing through the associated Voronoi cell node) with its corresponding local coordinates, *n-s-t*. Such local force components acting on the cell node can be calculated to satisfy equilibrium with the forces acting on all remaining cell boundaries. By dividing these force components by the cut-face area, the corresponding stress components σ_n, σ_s, and σ_t can be obtained. By repeating this process for three mutually perpendicular sections, the full stress tensor is obtained (Figure 3-2c). Moment contributions to equilibrium are not considered here. Details are given by Yip et al. (2005).

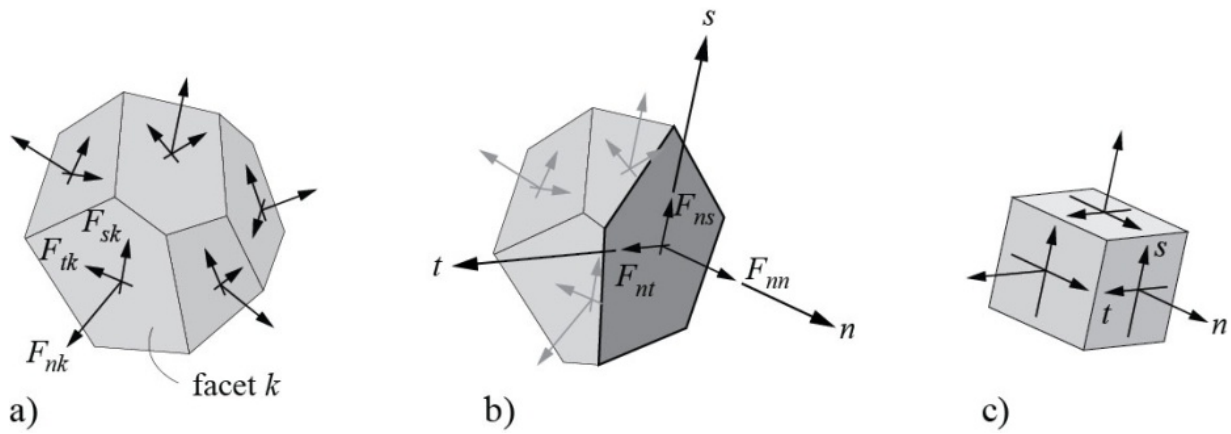

Figure 3-2. Stress tensor at Voronoi cell node: a) components of spring force local coordinates; b) a set of forces obtained by equilibrium; and c) complete stress tensor at Voronoi cell node. Adapted from Yip et al. (2005).

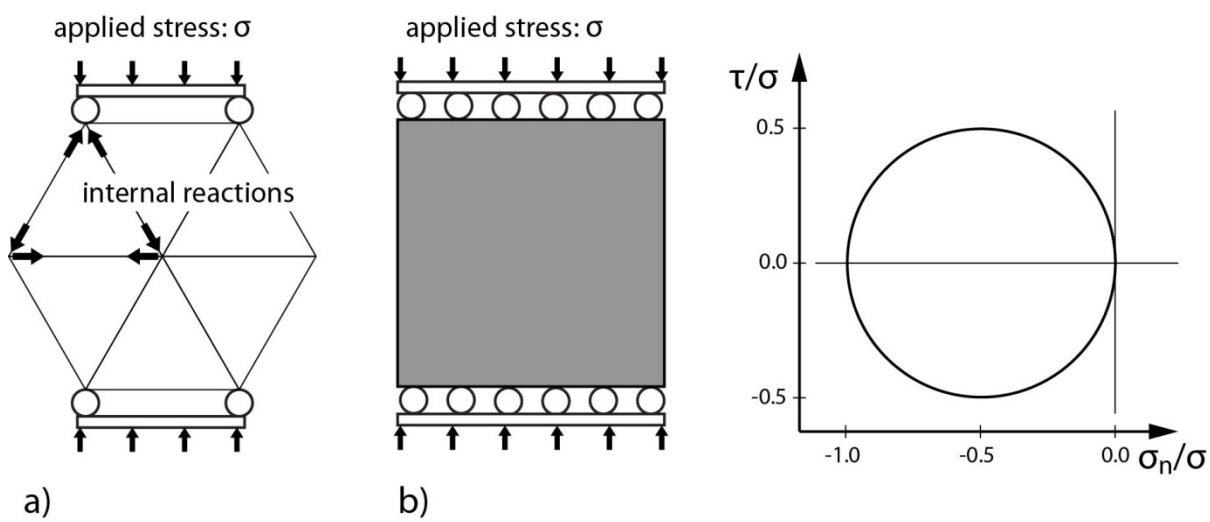

Figure 3-3. Internal reactions under vertical compression: a) a regular network of truss element, and b) homogeneous continua and normalized normal-shear stress condition.

3.1.2 Modeling of elastic continua using RBSN

3.1.2.1 Issue of modeling elastic continua with discrete approaches

When discrete models are used to simulate fracture behavior under compressive loading of an isotropic homogenous medium (in the absence of lateral constraint), they tend to show vertical cracking. Theoretically, if simulated by a continuum model, tensile stress, which could possibly trigger vertical cracking, would not occur (Figure 3-3b). And yet vertical cracking is observed experimentally,

presumably due to heterogeneity at fine scale and non-uniform loading conditions. Ideally, a model should account for both continuous and discontinuous conditions.

Discrete models are based on discontinuous approximation of the field variable over the computational domain. This makes it appropriate for modeling fractures and other discontinuous phenomena. However, as noted above, there are significant differences between discrete models and continuum models in the local stress and force conditions. For example, a discrete regular truss network under uniaxial compression contains lateral tensile reaction, as shown in Figure 3-3a, whereas in homogenous continua, tensile stress cannot exist, as shown in Figure 3-3b.

Because of the discontinuous representation of the displacement field, ordinary discrete models, including the RBSN approach, cannot simulate Poisson effect in a local (intra-element) sense. Macroscopic representation of the Poisson effect can be controlled by adjusting the spring constants of the discrete elements. For the RBSN, macroscopic Poisson effect can be obtained by adjusting the values of α_1 and α_2 in Equation (3-1). Such adjustment, however, introduces an artificial heterogeneity.

This shortcoming can be remedied by combining RBSN with a finite element method that contributes only a Poisson effect (Bolander et al., 2001). This combined RBSN and FEM approach, with the introduction of continuum elements, complicates the modeling of fracture, but it is accurate for linear problems and demonstrates the significant weakness of ordinary discrete element modeling of the local stress fields.

3.1.2.2 Practical relationship of spring constants

For a 2-D regular triangular mesh, Griffiths and Mustoe (2001) and Jagota and Bennison (1994) developed a relation between k_n and k_s from the strain energy density function. The strain energies as approximated by the discrete approximation and continuum expression are set equal to each other, leading to a practical relationship between effective Young's modulus E and Poisson's ratio ν, in which the spring constants are expressed as

$$k_n = E/(\sqrt{3}(1-\nu)) \tag{3-2}$$

$$k_s = E(1-3\nu)/(\sqrt{3}(1-\nu^2)) \tag{3-3}$$

This relationship is limited to the range $-1 < \nu < 1/3$. For an elastic continuum, these equations are accurate for strain; however, the stress at the nodal sites is not accurately represented, as shown in following section.

3.1.2.3 An approach to model elastic continua using RBSN

In this section, we propose a new approach to model homogeneous continua with $\nu \neq 0$ in both local and global perspective using RBSN. The basic idea of this approach is to solve the system equation twice for each computational cycle (i.e., loading step) with different prescribed strain configurations. For the 2-D regular grid under uniaxial compression as shown in Figure 3-4, the simulation procedure is as follows:

Step 1: The system equation is solved as the ordinary RBSN manner for the case of $\alpha_1 = \alpha_2 = 1$ (Equation 3-1), for which the model is elastically homogeneous with $\nu = 0$.

Step 2: Principal stresses and strains, σ_p and ε_p, are calculated at each nodal site based on the stress tensor calculations mentioned in Section 3.1.1. Then, an orthogonal strain is obtained by

$$\varepsilon_{ort} = -\nu\, \varepsilon_p \tag{3-4}$$

Step 3: The force vector used in the system equation of Step1 is recalculated based on the additional prescribed strain, ε_{ort}. The system equation is solved with this updated force vector.

In this way, the orthogonal strain from Step 2 contributes only the Poisson effect, in which the network has no change in the stress field but provides lateral volumetric change. Since the element-stiffness matrix remains the same for both system equations (Step 1 and Step 2), only the back substitution of Crout elimination (Hughes, 2000) is required to solve for the second system equation; therefore, reduced computational cost can be expected for the additional solution procedure (Step 3). Although only the elasticity is considered without modeling the fracture, same rules to determine the critical (e.g., fracturing) elements can be applicable here. The accuracy of this approach is demonstrated in the following section.

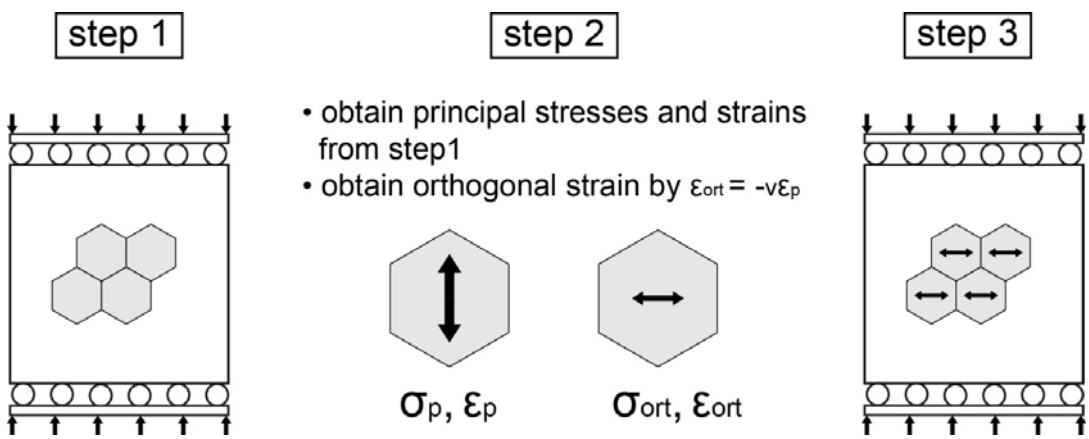

Figure 3-4. Modeling procedure to achieve homogenous continua under uniaxial compression using RBSN.

3.1.2.4 Numerical study

Consider a nearly square domain having constant thickness of a homogeneous and isotropic elastic material subjected to uniform compressive loading, σ, in the vertical direction. The domain is discretized by a regular mesh, as depicted in Figure 3-5a. Appropriate boundary conditions are applied to ensure uniform compressive loading. Using the nodal stress tensor calculations described in Section 3.1.1, a Mohr's circle representation of the stress state at each node can be plotted, as shown in Figure 3-5b, for *n*-*t* stress components. For the case of $\alpha_1 = \alpha_2 = 1$, the model is elastically homogenous with ν = 0. The blue dots shown in Figure 3-5b are the results of a new RBSN approach with ν = 0.2. The results agree well with theory. On the other hand, a discrepancy with the theoretical results is introduced for the case with adjusted spring constants (the red dots). This discrepancy in stress configuration strongly affects the stress-based fracture criteria.

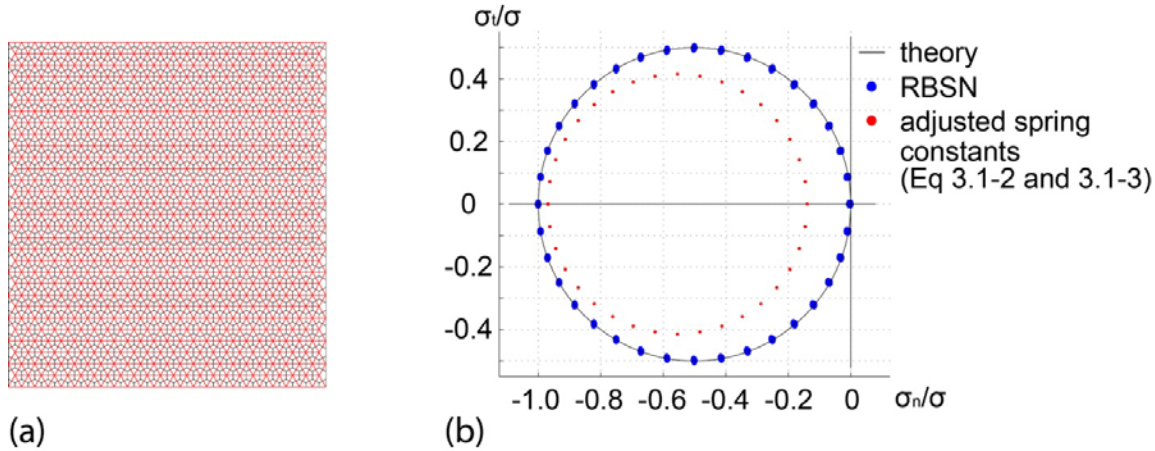

Figure 3-5. (a) Regular discretization of a 2-D domain, and (b) Mohr's circle representation of stress state under uniaxial compressive loading.

The nodal displacements, proportion to the nodal coordinate in the corresponding direction (e.g., vertical or lateral), are given in Figure 3-6. As mentioned above, the approach with adjusted spring constant serves the elastically uniform in the strain (Figure 3-6a). Figure 3-6b shows the results of the new RBSN approach, which accurately represents uniform strain as well. The good agreement between the theory and numerical results with the proposed approach (with respect to representing elastic continua with discrete approximation) is notable. Future work will involve a large range of material behavior with more complicated factors, such as multiaxial loading conditions, nonlinear behavior including fracturing, and 3-D unstructured grid.

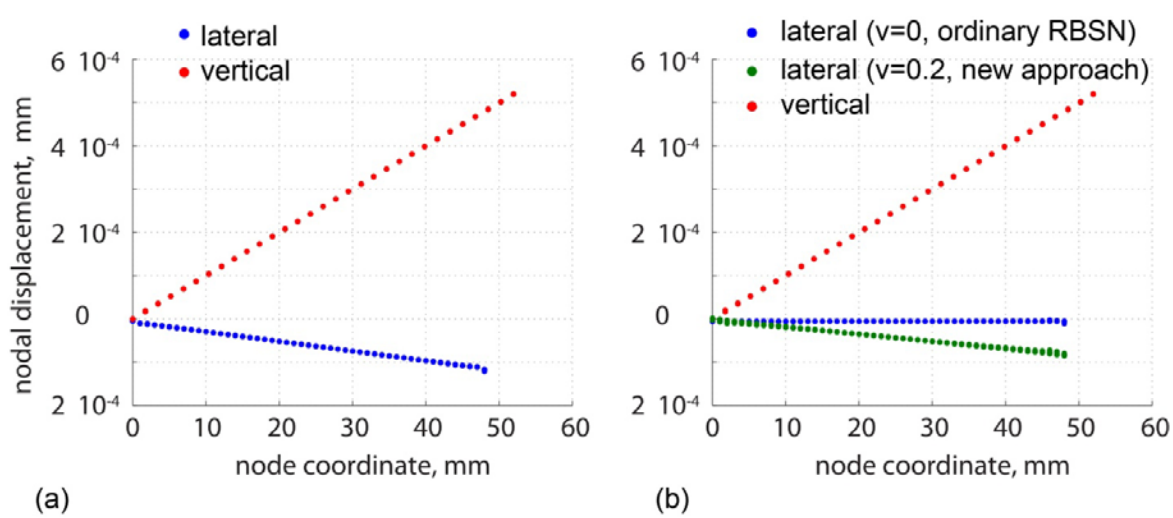

Figure 3-6. Nodal displacements proportion to associated node coordinates in corresponding direction: (a) adjusted spring constant by Equation (3-2 and 3-3), and (b) the RBSN model.

3.2 Coupling of Hydraulic and Mechanical Damage Codes

This section described the linking between the multiphase flow simulator TOUGH2 and RSBN. Several advantages of the coupled TOUGH-RBSN simulator stem from its use of Voronoi-based discretization techniques (Okabe et al., 2000), which allow discretization of dynamically changing discrete fracture networks (DFNs) with embedded matrix in a simple and straightforward manner.

Rutqvist et al. (2002) have coupled TOUGH2 to a commercial continuum-mechanics simulator, FLAC3D. The general procedure for coupling TOUGH2 and RBSN is similar, but substantially modified and extended for modeling discrete fracture propagation. Figure 3-7 shows a schematic flowchart of the linking process between TOUGH2 and RBSN. Here, TOUGH2 is used to simulate the scalar quantities (*e.g.*, temperature, pressure, and degree of saturation) associated with fluid flow and heat transport, whereas RBSN accounts for the mechanical quantities (*e.g.*, displacement, strain, and stress) of interest. Such primary variables are coupled through simplified linear relationships or through nonlinear empirical expressions, which could be estimated by laboratory experiments with appropriate calibration. An advantage of coupling TOUGH2 and RBSN is that both models share the same unstructured, 3-D Voronoi grid and the same set of nodes, which simplifies their data exchange. TOUGH2 and RBSN are currently linked through an external module, which handles two-way transfer of the relevant quantities at each time step. First, a TOUGH2 to RBSN link supplies multiphase temperature, pressure, and degree of saturation to update the mechanical quantities. The general conventional effective stress law of Biot's theory for a fully saturated media is (Biot and Willis, 1957)

$$\boldsymbol{\sigma} = \boldsymbol{\sigma}' - \alpha_p P \mathbf{I} \tag{3-5}$$

where $\boldsymbol{\sigma}$ is total stress tensors, $\boldsymbol{\sigma}'$ is the effective stress tensors, α_p is a Biot effective stress parameter, P is pore fluid pressure, and $\mathbf{I}$ is the identity tensor. Note that tensile stress is positive. In incremental form, Equation (3-1) becomes

$$\Delta\sigma_n = \Delta\sigma_n' - \alpha_p(\Delta P_i + \Delta P_j)/2 \tag{3-6}$$

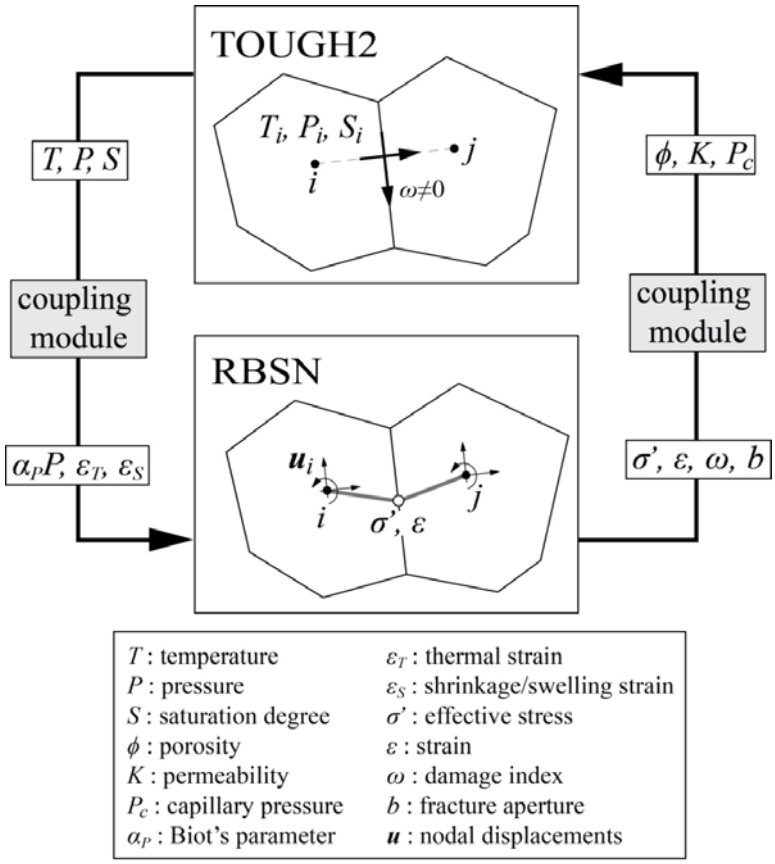

Figure 3-7. Flow diagram of TOUGH2-RBSN linkages for a coupled THM simulation. Note that additional nodes and connections are introduced in TOUGH2 to activate flow pathways associated with fracture.

where σ_n is the stress normal to lattice element *ij*, and ΔP_i and ΔP_j are the changes in pore pressures over the time step at neighboring nodes *i* and *j*. Note that the pore pressure only affects the spring in the normal direction. It is assumed that the local changes of temperature and liquid saturation induce strain as follows:

$$\Delta\varepsilon_T = \alpha_T(\Delta T_i + \Delta T_j)/2 \tag{3-7}$$

$$\Delta\varepsilon_s = \alpha_s(\Delta S_i + \Delta S_j)/2 \tag{3-8}$$

where ε_T is thermal strain; ε_s is shrinkage/swelling strain; ΔT and ΔS are the change in temperature and saturation over the time step in one lattice element, respectively; α_T is the coefficient of linear thermal expansion; and α_s is the hydraulic shrinkage coefficient. ΔT and ΔS are taken as the average of two neighboring nodes *i* and *j*. For an expansive soil material, the effective stress can be affected by both thermal and swelling/shrinking strain as

$$\Delta\sigma_n' = (\Delta\varepsilon_T + \Delta\varepsilon_s)E \tag{3-9}$$

Thereafter, a RBSN-to-TOUGH2 link supplies the stress and strain values from the lattice elements to update the hydrogeological property values associated with each Voronoi cell in the TOUGH2 model (Figure 3-7). The following general relations are considered (Rutqvist and Tsang, 2002):

$$\phi = \phi(\sigma', \varepsilon) \tag{3-10}$$

$$K = K(\sigma', \varepsilon) \tag{3-11}$$

$$P_c = P_c(\sigma', \varepsilon) \tag{3-12}$$

where ϕ is porosity, K is permeability, and P_c is capillary pressure. The permeability of an individual fracture depends on its aperture, b. Herein, a parallel-plate model is used in which permeability is set equal to $b^2/12$ (Bear, 1972). The example application presented later (in Section 3.3) demonstrates the coupling shown on the left side of Figure 3-7 (*i.e.*, the use of temperature, pressure, and degree of saturation supplied by TOUGH2 to drive the mechanical-damage model).

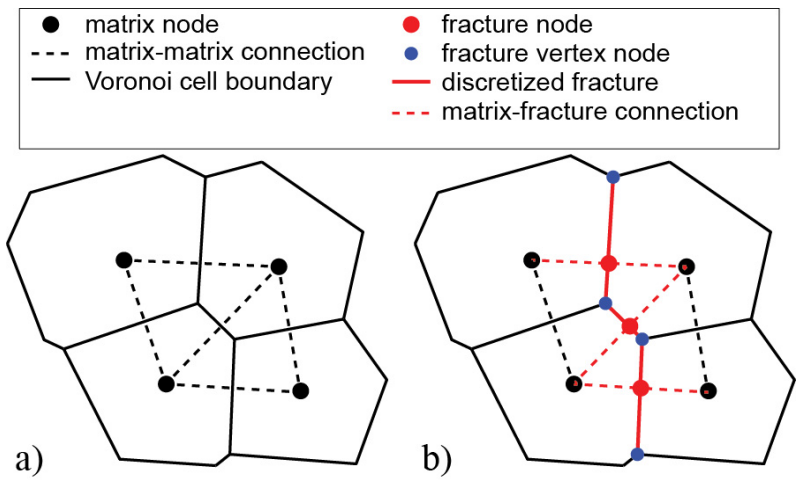

Figure 3-8. Nodal connectivity in the TOUGH2 simulator: (a) ordinary matrix nodes and connections; (b) newly established fracture nodes and connections.

The DFN is represented at selected Voronoi cell boundaries within the computational domain. To activate dynamically forming flow pathways along a discrete fracture, fracture nodes and associated connections are introduced at the Voronoi cell boundary (Figure 3-8). A fracture node is inserted at the intersection of a Voronoi cell boundary and the original matrix-matrix connection. Connections are generated between the fracture node and the adjacent matrix nodes. In addition, fracture vertex nodes are added to establish fracture-fracture connections along the Voronoi cell boundary. These additional nodes and connections in the TOUGH2 simulator enable transport through the DFN. Fracture permeability is based on grid geometry and local apertures, which can be either assigned for pre-existing fractures or computed by a mechanical-damage model.

3.3 Simulation of Desiccation Cracking of a Mining Waste

A possibility of desiccation cracking of a portion backfill, or buffer is a serious concern of nuclear waste disposal. Cracking can enhance advective transport of radionuclides, and decrease mechanical stability of the host rock. Here, the TOUGH-RBSN simulator is used to demonstrate the capability of modeling hydromechanically-induced fracturing. Desiccation can occur due to loss of moisture through an exposed surface, which induces differential straining within the material volume. Differential straining, and straining under restraint, can produce tensile stresses of sufficient magnitude to initiate cracking. Desiccation cracking of clay has been the subject of many experimental studies (Konrad and Ayad, 1997; Colina and Roux, 2000; Lakshmikantha et al., 2012). Numerical models have also been developed to study desiccation cracking (Kitsunezaki, 2011). Numerical results given in this section are compared with the test results of Rodríguez et al. (2007), obtained from desiccation of a mining waste material. For several sample thicknesses, comparisons are made for shrinkage strain, moisture content, fracture pattern, mean spacing of cracks, and time to crack initiation.

3.3.1 Experimental program of Rodríguez et al. (2007)

The basic framework of the experimental program of Rodríguez et al. (2007) is briefly described here for completeness. Desiccation processes and associated crack patterns were studied with thin disk specimens of a mining waste. The main component of the waste is hematite, which consists primarily of fine particles (mostly particles smaller than 80 μm) classified as low plasticity silt. The waste sample was placed in a circular plate with only the top surface exposed to atmospheric desiccation, and with the inside bottom of each plate grooved to prevent sliding between the plate and the waste. Rodríguez et al. (2007) performed two sets of drying experiments, in which samples were (1) exposed to ambient conditions, or (2) dried in hermetically closed containers. In this study, we focus on the latter set of experiments, due to its better control of temperature and air movement near the material surface. Table 3-1 summarizes the material properties measured on samples before the drying test. Figure 3-9 shows the dependencies of elastic modulus and tensile strength on degree of saturation, which were obtained from a series of experiments. The material was fully saturated at the start of the test. Gravimetric moisture contents (Figure 3-10) and vertical strain at the top surface were measured during exposure to the drying environment. Other measurements related to cracking behavior (i.e., time to crack initiation, mean spacing of cracks, moisture contents, and vertical strain at the moment of crack initiation) are given in Table 3-2. As Rodríguez et al. (2007) discuss in their conclusions, the experimental study showed the clear influence of sample thickness on distance between cracks. Such experimental observation has also been reported in the literature (Colina and Roux, 2000; Lakshmikantha et al., 2012).

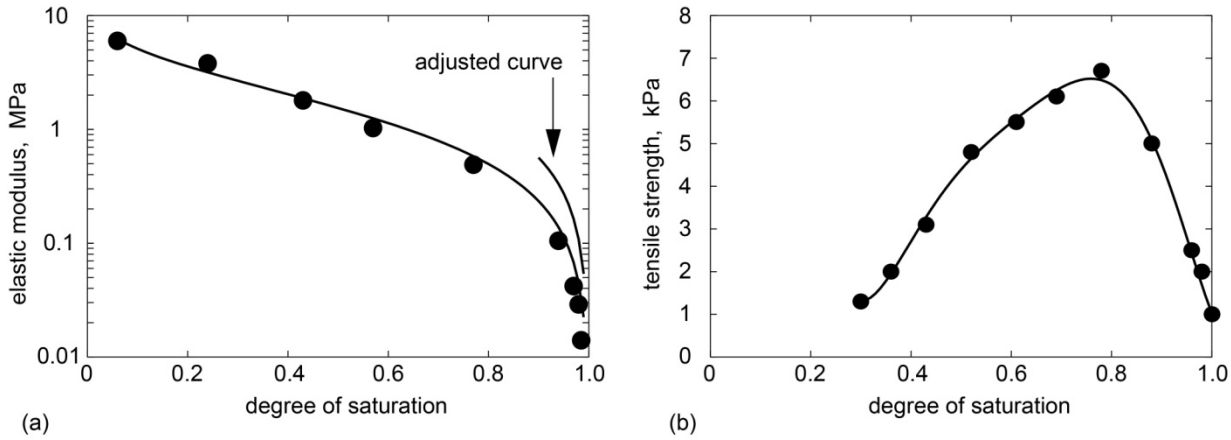

Figure 3-9. Experimental data (after Rodríguez et al., 2007) and fitted polynomial curves of: (a) Young's modulus, and (b) tensile strength with degree of saturation.

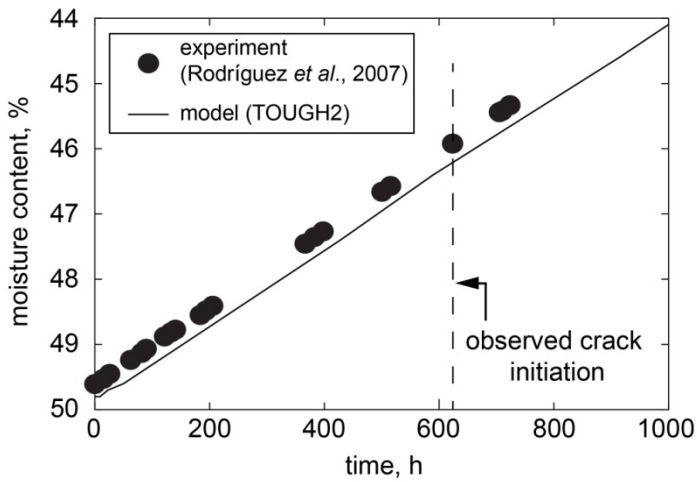

Figure 3-10. Evolution of gravimetric moisture content of sample with thickness of 16mm.

Table 3-1. Summary of material properties of the mining waste used for TOUGH-RBSN simulator. The values are obtained from Rodríguez et al. (2007).

Parameter		Value
Rock grain density (kg/m^3)		3970
Initial dry density (kg/m^3)		1330
Porosity (-)		0.665
Permeability (m^2)		1.29x10^{-15}
Diffusion coefficient (m^2/s)		2.83x10^{-5}
Temperature (°C)		22.0
Air partial pressure (Pa)		9.74x10^4
Relative humidity of environment (%)		75.7
Parameters of van Genuchten function for capillary pressure	λ	0.39
	Residual saturation	0.0
	Max. saturation	1.0
	Capillary strength (1/Pa)	9.88x10^{-6}

Note: a third power law in the water saturation is used for relative permeability.

Table 3-2. Sample geometries and results of drying test.

	Diameter (mm)	Sample thickness (mm)	# nodes	Time to crack initiation (days)	Vertical strain at crack initiation (%)	Saturation ratio at crack initiation	Averaged distance between cracks (mm)
Test results (Rodríguez et al., 2007)	225	4	-	9.00	2.7	0.90	14
	225	8	-	15.00	3.0	0.94	39
	225	16	-	26.00	2.4	0.97	55
Numerical results	225	4	56064	6.76	3.12	0.917	23.3
	225	8	41431	13.66	2.77	0.923	51.9
	225	16	16920	25.88	2.72	0.924	101.3

3.3.2 Model description

Consider the 3-D model shown in Figure 3-11, which represents the mining waste sample subjected to drying from the top surface. As indicated in Table 3-2, three different thicknesses (4 mm, 8 mm, and 16 mm) are considered as in the experimental program. A smaller nodal spacing is used for the thinner model to resolve the thickness direction. Although the crack patterns in similar desiccation tests have exhibited size effects (Colina and Acker, 2000; Bisschop, 2008), the effect of specimen lateral dimensions is less significant than that of its thickness.

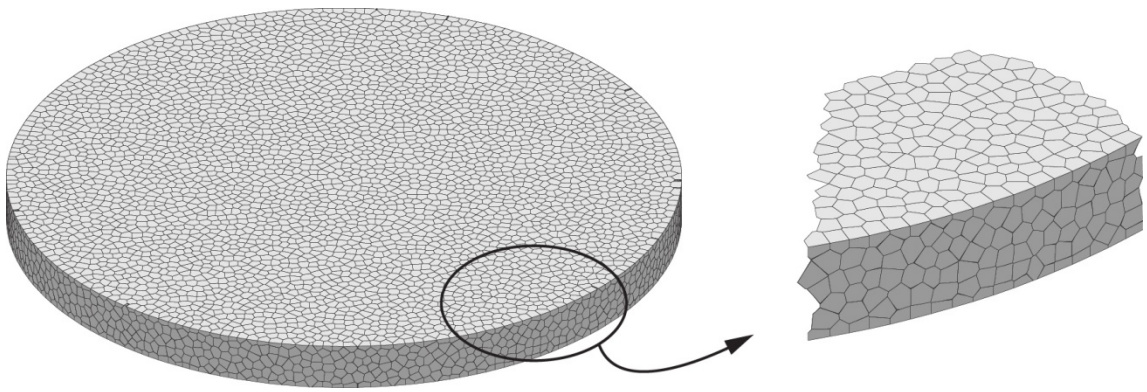

Figure 3-11. Voronoi discretization of the mining waste sample with 16 mm thickness.

The hydraulic boundary condition at the top of the specimen is implemented by prescribing the degree of saturation for a node representing a large volume above the top surface. Hydraulic connections are made to the surface nodes, but there are no connections to the mechanical model. The distance between the desiccant and the top of the sample was set using a diffusive resistance length to represent water vapor diffusion as described by Ghezzehei et al. (2004). The diffusive resistance length, δ, is related to the steady-state diffusive mass flux by

$$J_v = D_v \frac{C^0 - C^\infty}{\delta} \tag{3-13}$$

where J_v is the steady-state diffusive mass flux between constant humidity boundaries at the soil surface, C^0, and at the desiccant, C^∞, and D_v is the vapor diffusion coefficient. The vapor mass flux was computed using TOUGH2 with the EOS7R equation of state module (Oldenburg and Pruess, 1995). The model grid represented the desiccator diffusion path geometry as used in the Rodríguez et al. (2007) experiments. The value of D_v used was 2.83×10^{-5} m^2/s. The specific value of $C^0 - C^\infty$ is not important since J_v is proportional to $C^0 - C^\infty$; $C^0 - C^\infty$ is set to the same value used to calculated J_v. The steady-state diffusive flux was determined from the TOUGH2 calculation to be 7.64×10^{-7} kg/m^2-s, giving a diffusive resistance length of 0.37 m.

For mechanical boundary conditions, the bottom layer of nodes (0.1 mm above the bottom surface) is restrained, whereas others are free to move. The mechanical bond between the sides of the plate mold and the waste material is considered to be negligible. In these analyses, neither external mechanical loading nor gravitational loading is considered.

Two parameters (sample thickness and nodal density) are varied, whereas the other input parameters are kept constant. Material properties are taken directly from the experimental measurements of Rodríguez et al. (2007), as presented in Table 3-1 and Figure 3-9. In Figure 3-9, curves were fit to the experimental measurements of elastic modulus and tensile strength versus the degree of saturation. We used results from the 16 mm sample to calibrate the elastic modulus, and then performed blind forward modeling for the 4 mm and 8 mm samples to demonstrate predictability. Accurate representation of time to initial cracking of the 16 mm sample (Figure 3-10) was achieved by increasing the elastic modulus by a factor of 2.4 for degrees of saturation ranging from 0.9 to 1.0. Adjustment was made to the elastic modulus, rather than to other parameters, since few data points were provided in that region of rapid change.

The hydraulic shrinkage coefficient, α_s, is determined from the ratio of the saturation change to strain change up to the moment of crack initiation observed in the 16 mm sample. Based on the value of moisture contents in Figure 3-10, and other hydraulic variables (i.e., porosity, initial dry density), saturation at the moment of crack initiation can be calculated as 92.4%. With the average vertical strain of 2.72%, the coefficient,α_s, can be determined as 0.358 according to Equation (3-8).

Drying shrinkage produces tensile stresses in the mining waste, which leads to the formation of fractures in the RBSN model. The simulations were conducted until no significant changes occurred in the crack patterns. Other complex mechanisms associated with wetting and drying cycles, time-dependent repetitive crack growth, and crack-assisted mass transport were not included in this simulation. Furthermore, material aging and creep have not been modeled in the simulation presented here because short test durations have been considered. Such factors are being considered for extending the applicability of the simulation tools to broader classes of problems.

3.3.3 Simulation results

Sensitivity of the fracture pattern with respect to mesh size was studied using different nodal densities for sample thicknesses of 8 and 16 mm (Figure 3-12). To make quantitative comparisons between the crack patterns, the mean spacing of cracks is measured according to Colina and Roux (2000). For the comparisons presented in Figure 3-12, the mean crack spacings are: 47.2 and 51.9 mm for results (a) and (b), and 98.8 and 101.3 mm for results (c) and (d), respectively. In lieu of more rigorous studies of mesh sensitivity, these results provide assurance that crack patterns are sufficiently independent of nodal density (for the purpose of demonstrating model capabilities through the examples that follow).

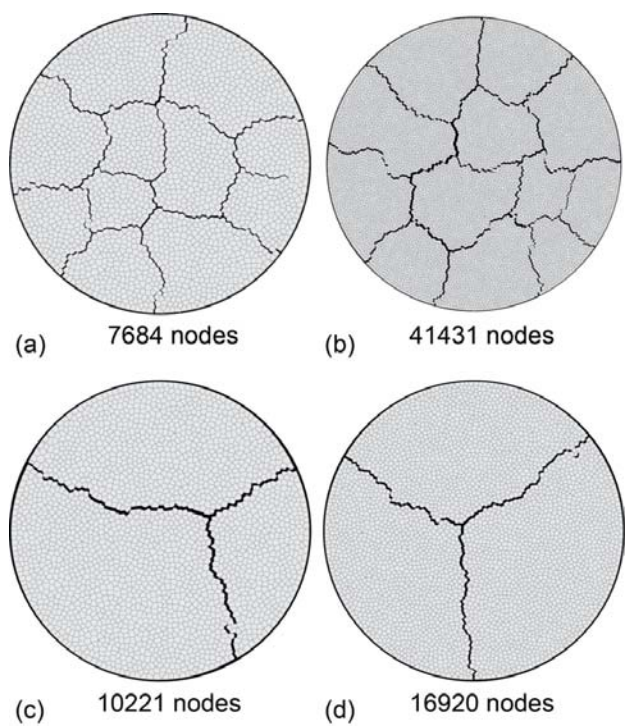

Figure 3-12. Dependence of crack patterns on nodal density for sample thicknesses of: (a), (b) 8 mm; and (c), (d) 16 mm.

Table 3-2 presents simulated results for each sample thickness. As expected, the time to crack initiation agrees with the test results for the 16 mm specimen. The results for the other specimens (i.e., those with thicknesses of 4 and 8 mm), which can be viewed as predictions, are not as accurate as the 16 mm results, but show good qualitative agreement with slight underestimation of initiative time. The saturation ratio, obtained from the gravimetric moisture contents, is the average value for all nodes. The following observations can be made (and they agree with the concluding remarks of Rodríguez et al. (2007)):

- The time of crack initiation is roughly proportional to the sample thickness.
- The vertical strain at the moment of crack initiation does not appear to be affected by the sample thickness.
- The mean spacing of cracks increases with the sample thickness.

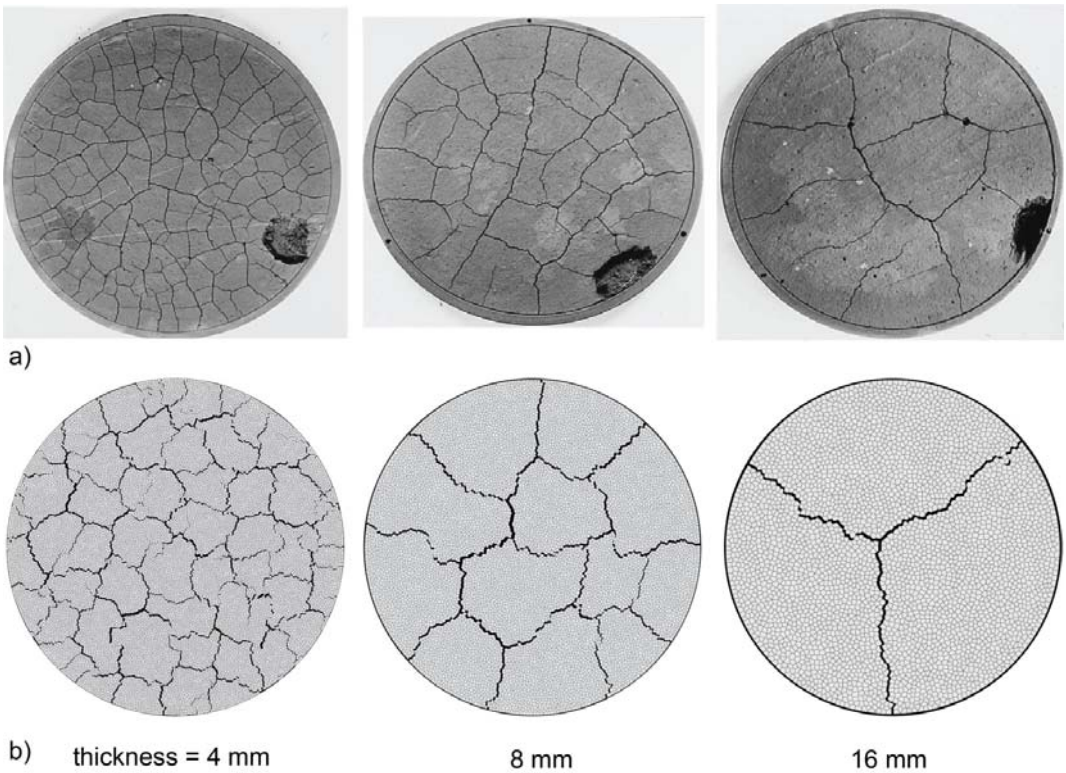

Figure 3-13. Crack patterns for different sample thicknesses: (a) experimental results of Rodríguez et al. (2007), and (b) plan view of 3-D simulation results of the TOUGH-RBSN simulator.

Figure 3-13 shows the crack patterns for the samples listed in Table 3-2. Cracks are connected and appear to bound islands of material when viewed in plan. Also, the cracks tend to meet at triple junctions in both the test results and numerical simulations. Agreement between the numerical and physical test results (with respect to time to initial cracking, trends in mean crack spacing, and qualitative representation of the crack patterns) is quite good, especially considering the strong dependence of elastic modulus and tensile strength on degree of saturation. Although the numerical results capture the general trend between mean crack spacing and sample thickness (Figure 3-14), the numerical results overestimate the crack spacings. This discrepancy is possibly due to toughening behavior of the mining waste, which was not considered

in these simulations. Lakshmikantha et al. (2012) discuss the importance of fracture toughness when studying the mechanisms of desiccation cracking. Residual stress transfer across forming cracks would promote additional cracking.

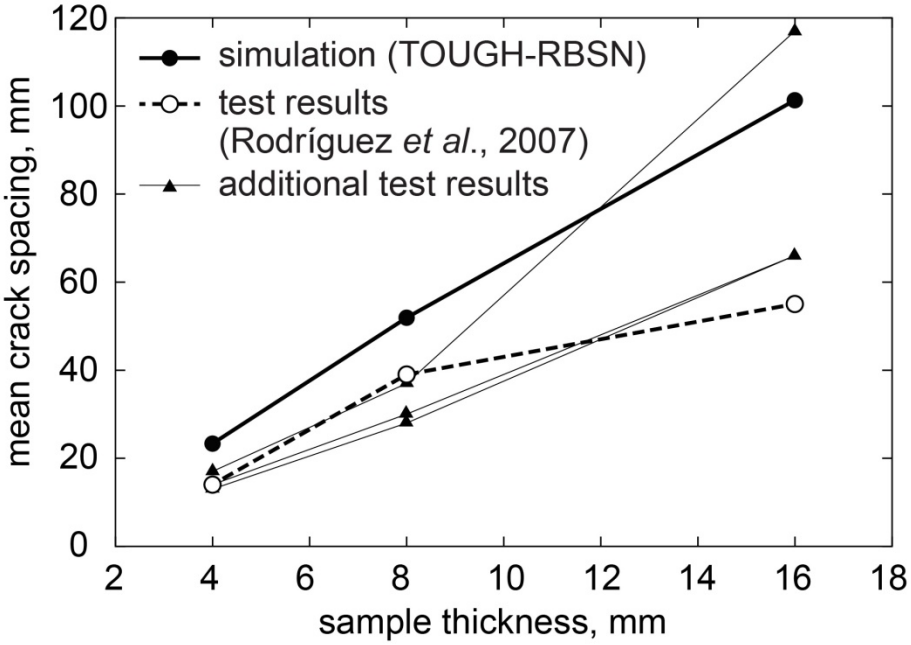

Figure 3-14. Variation of mean spacing of cracks with sample thickness. The additional test results are also taken from Rodríguez et al. (2007), but for different drying conditions.

3.4 Analysis of the HG-A Test at Mont Terri

As described in Sections 3.1 through 3.3, we are developing a coupled THM fracture damage model called TOUGH-RBSN. In particular, the development of the excavation-damaged zone (EDZ) in a clay-rich rock is a focus for this model development and application. The HG-A test is intended to provide data on the behavior of water and gas injected into a tunnel sealed by a packer. The test is specifically targeted to observe how fluids injected into the test section penetrate both into the rock and along the EDZ along the packer. The test is being conducted in the Opalinus Clay at the Mont Terri underground research laboratory (URL) near Saint-Ursanne, Switzerland. The goal of this activity is to use the Mont Terri test data to help build confidence in the TOUGH-RBSN model for predicting various facets of fracture development and evolution within the EDZ.

3.4.1 Location and description of the HG-A microtunnel test

Figure 3-15 shows the general location of the HG-A test within the Mont Terri URL. This test is being conducted in a 13-m long, 1 m diameter microtunnel located off of one of the main galleries. The tunnel was excavated in February 2005 over a period of about 3 weeks. Steel liner was installed in the first 6 m, and the mid-section where the packer is installed was coated with an epoxy resin (Meier et al., 2005). The test section is supported by a wire mesh and was backfilled with sand. A retaining wall to hold the gravel

backfill is grouted in place between the packer and the test section (Lanyon et al., 2009). Finally, the packer seals the test section from the front end of the microtunnel and Gallery 04.

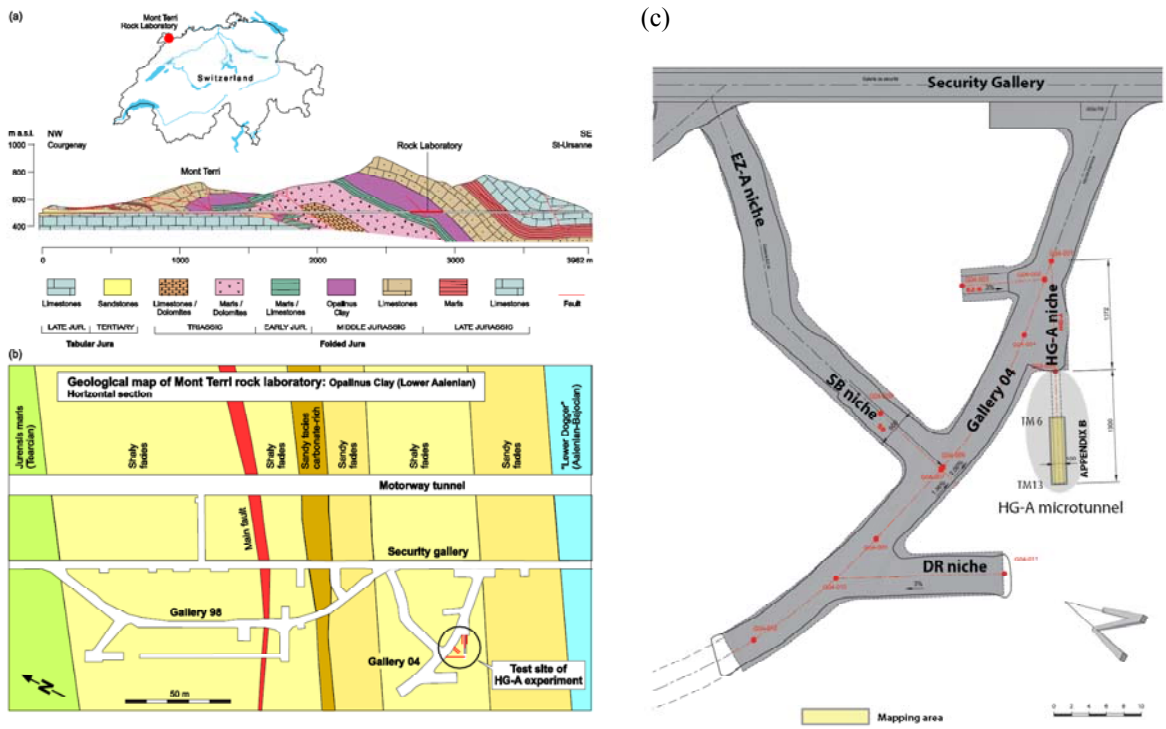

Figure 3-15. The Mont Terri underground rock laboratory: (a) geological profile of the site after Freivogel and Huggenberger (2003), (b) site map showing the underground facilities of the laboratory. The HG-A microtunnel is located in the New Gallery 04. (source: Marschall et al., 2006), (c) map view of the HG-A microtunnel and adjacent excavations; structural map of tunnel surface shown in Figure 3-17 is the area highlighted in yellow (source: Nussbaum and Bossart, 2006).

The HG-A test configuration is shown in Figure 3-16. Instrumented boreholes emanate from the nearby gallery and from the face of the HG-A niche into the rock surrounding the tunnel. The instrumentation outside the tunnel includes piezometers for monitoring water pressure, stressmeters for rock stress, and chain deflectometers for deflection of tunnel axis. The region inside and adjacent to the tunnel is instrumented with piezometers, total pressure cells along the packer for radial stress, time-domain reflectometers for water saturation, strain gauges measuring tangential movement, and extensometers for radial movement. The locations of some of these instruments are shown in Figure 3-16.

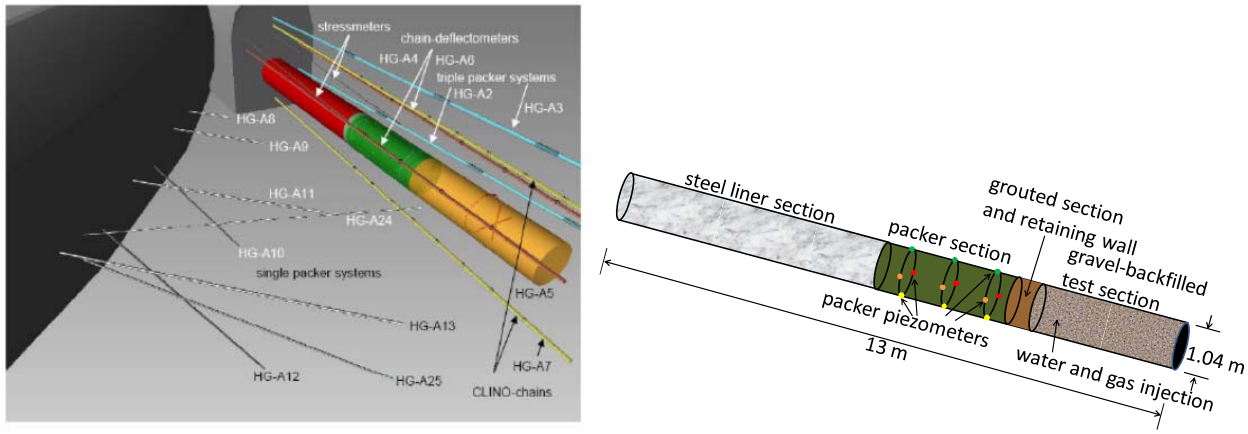

(a) (b)

Figure 3-16. HG-A test configuration: (a) schematic drawing of the microtunnel and the site instrumentation. Color coding refers to the steel liner (red), the packer seat (green) and the backfilled test section (orange) (source: Marschall et al., 2008); (b) detail of tunnel showing packer piezometers and test section for fluid injection.

3.4.2 Observations of rock features and EDZ damage

The HG-A microtunnel was mapped to identify natural structural features and any induced fracturing or damage. The tunnel map is shown in Figure 3-17. The natural features include bedding planes and tectonic-related fractures and faults. There are two main fault orientations: (1) an SSE-dipping system subparallel to the bedding planes and (2) a low-angle S to SW dipping system. The microtunnel is oriented along the bedding strike, and the bedding planes dip at 48° SSE, such that the bedding planes are tangent to the tunnel surface at about 3 to 5 o'clock and 9 to 11 o'clock (see also Figure 3-18) (Marschall et al., 2006).

Extensional and shear brittle fracturing and tunnel wall breakouts are features related to the excavation damage zone. These features are mapped in Figure 3-17 and can be seen to be quite non-uniform around the tunnel.

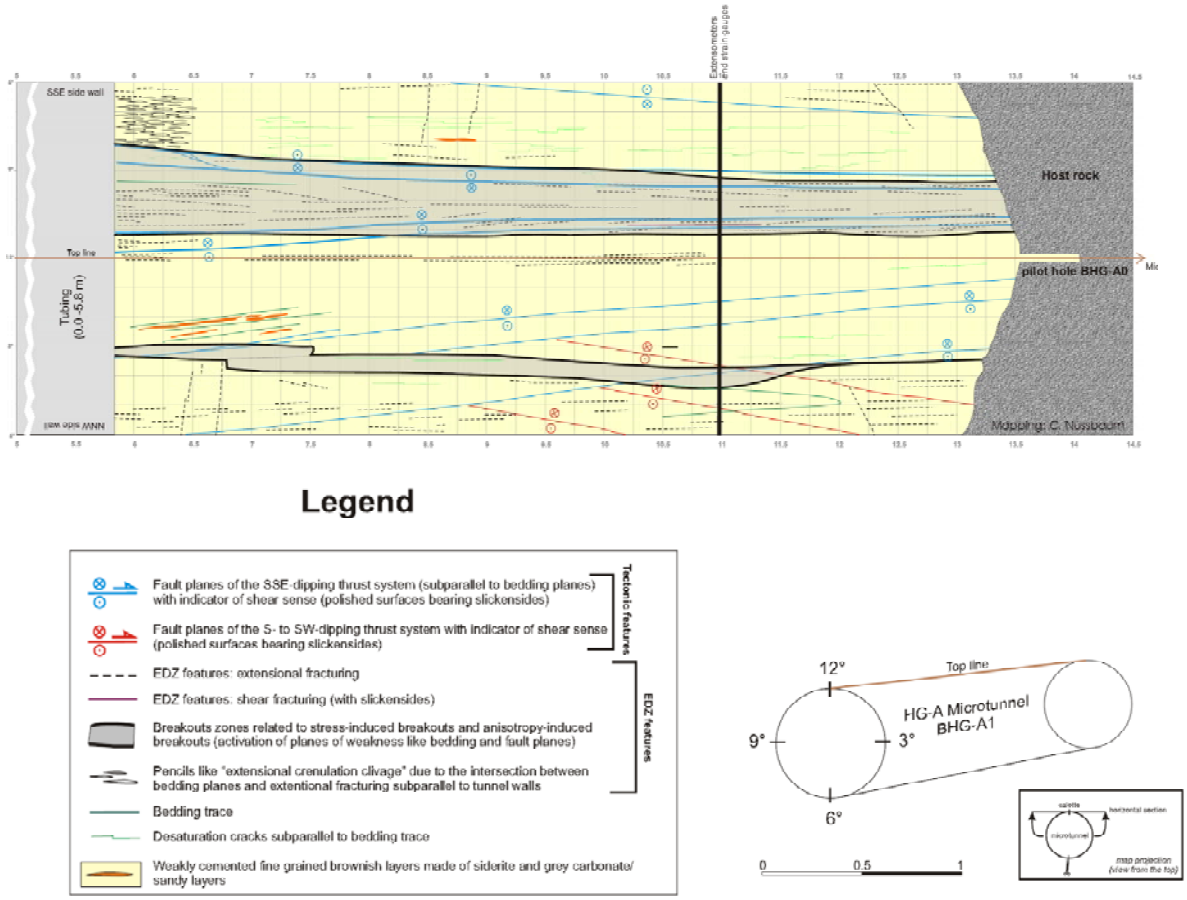

Figure 3-17. Structural Mapping of the HG-A microtunnel (source: Nussbaum and Bossart, 2006)

Excavation resulted in some visible damage along the microtunnel walls as shown in Figure 3-18(a). A conceptual model for the occurrence of damage is given in Figure 3-18(b), which attributes most of the damage to anisotropic strength characteristics of the rock and anisotropic stresses. Rock strength is found to be a function of orientation relative to the bedding (Bock, 2001). The damage is not uniform around the tunnel as shown above, a result of the relative weakness of the rock orthogonal to the bedding planes and as a result of weakness near faults intercepting the tunnel.

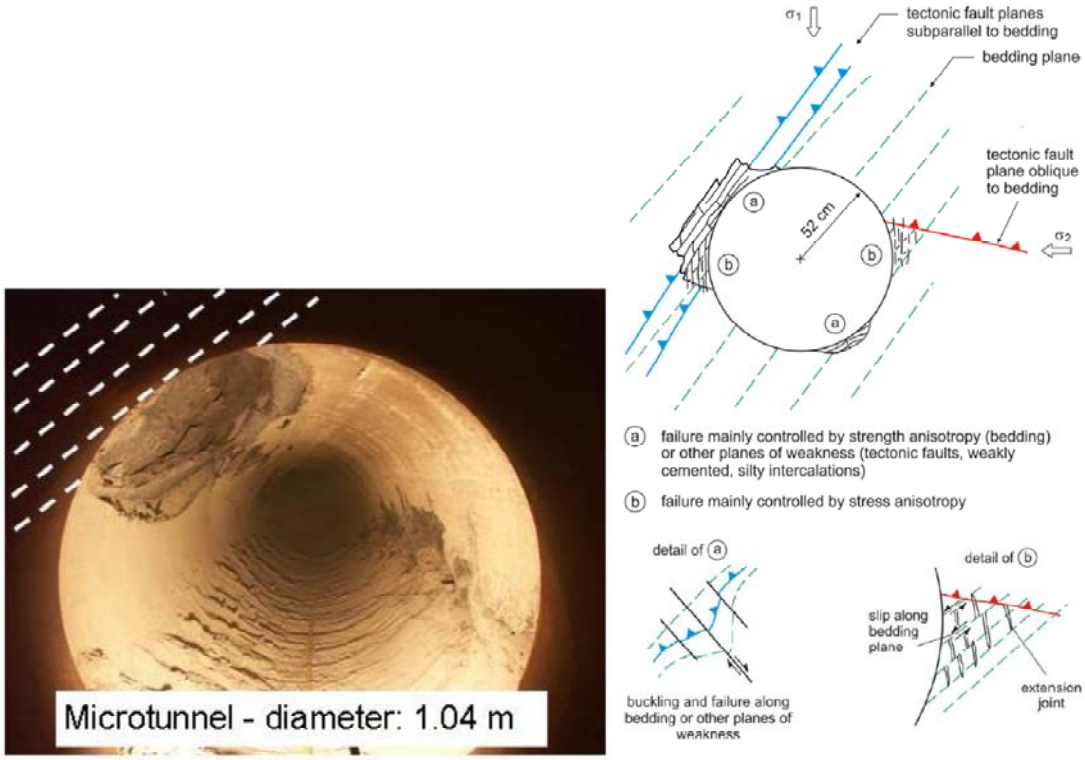

(a) (b)

Figure 3-18. Excavation damage. (a) Breakouts along microtunnel walls, with an orientation looking from the HG-A Niche towards back end of microtunnel (source: Marschall et al., 2006); (b) Conceptual diagram of the damage zone with the same orientation as in (a). (source: Lanyon et al., 2009; Marschall et al., 2006)

3.4.3 Water and gas injection testing

Water was injected into the test section at a variety of rates from 2007 to February 2010, followed by three periods of gas injection until September 2011. Pressure signals from piezometers along the packer (see Figure 3-16(b)) are shown in Figure 3-19. Figure 3-19(a) is for the piezometer ring furthest from the test section, Figure 3-19(c) is for the piezometer ring nearest to the test section, and Figure 3-19(b) is for the intermediate piezometer ring. As can be seen, pressure response is most vigorous and ubiquitous in Figure 3-19(c); moving away from the test section, pressure response dies out in several locations in Figures 3-19(b) and 3-19(a). However, the "3 o'clock position" still shows significant pressure response to the injected fluid pressure in the test section, signifying a high-permeability connection several meters from the packer. The testing has also shown indirect evidence of fracture self-sealing, where injection rate and/or pressure behavior is consistent with an increasing resistance to fluid injection into the test section. The increased resistance to injected fluids, presumably in the EDZ fractures, is identified by the sealing index, S, introduced by Lanyon et al. (2009), where $S = \frac{Q}{P-100}$ and Q is the flow rate (mL/min) and P is the pressure in (kPa), with self-sealing indicated by S decreasing with time, as shown in Figure 3-20.

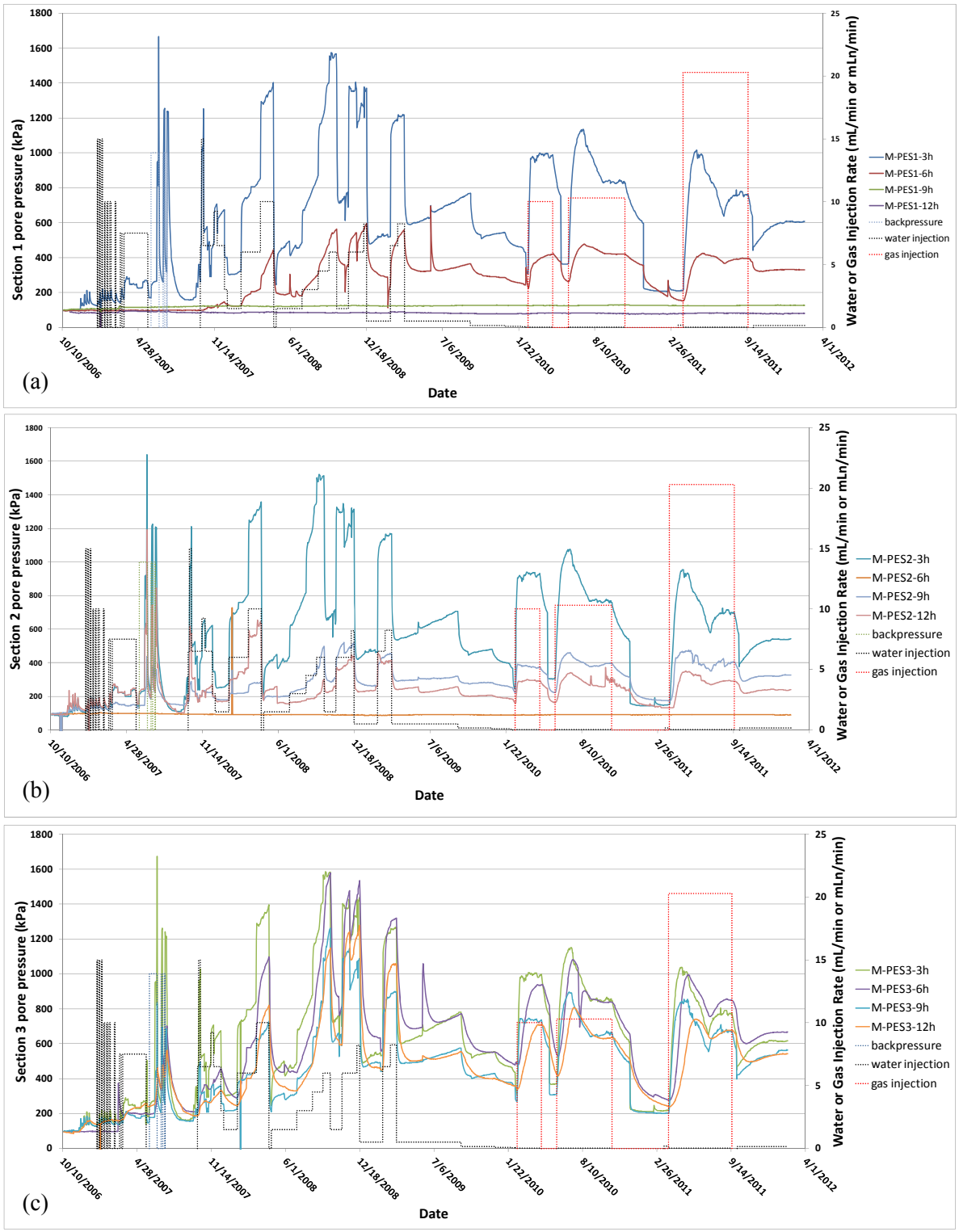

Figure 3-19. Fluid pressure response along packer section; (a) piezometer ring furthest from test section; (b) intermediate piezometer ring; (c) piezometer ring nearest to test section.

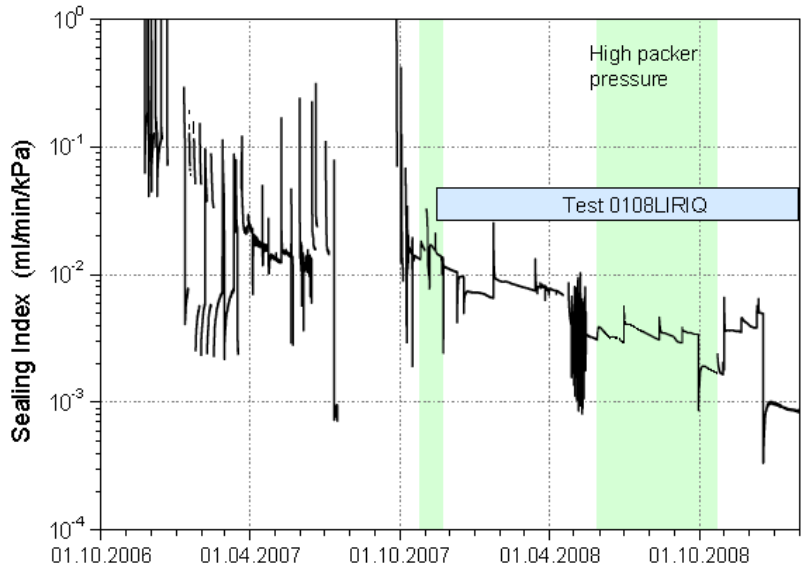

Figure 3-20. Sealing index as a function of time over a 2-year period. (source: Lanyon et al., 2009)

Packer pressure was also varied during the test over a range of 1 to 3 MPa. The effects of packer pressure on EDZ appeared to be consistent with the idea that fracture permeability decreased with increased packer pressure (Lanyon et al., 2009).

3.4.4 Scoping analysis of rock failure along the drift wall

An initial scoping analysis has been performed to investigate failure mechanisms along the tunnel wall. Failure is computed by first computing the stress around an open drift using an analytical solution for this problem derived by Kirsch (1898). The Kirsch solution is limited to a homogeneous rock mass, therefore, the effects of faults are not included. The solution also requires that the rock be treated as isotropic in terms of the elasticity parameters, Young's modulus and Poisson's ratio, but can accommodate anisotropic stress conditions at the far boundaries. The elasticity parameters for the Opalinus Clay are known to be anisotropic for measurements parallel and orthogonal to bedding (Bock, 2001). However, the assumption that these parameters are isotropic does not significantly impact the computed stress field around the tunnel if the far field can be treated as a constant stress boundary (Tonon and Amadei, 2003). It should be pointed out that displacements in response to the stress field are not accurately predicted using isotropic elastic parameters (Tonon and Amadei, 2003), but the present analysis is not evaluating displacements. Once the stress field is known, the anisotropic rock strength parameters may be used to evaluate whether tensile or shear failure is expected. Tensile failure is simply evaluated by comparing the effective normal stresses with the corresponding tensile strength. Shear failure is evaluated using a Mohr-Coulomb failure approach.

The solution for the mechanical stress, σ_{rr}^m, $\sigma_{\theta\theta}^m$, and $\sigma_{r\theta}^m$ is given by Pollard and Fletcher (2005, p. 236),

$$\sigma_{rr}^m = \left(1 - \frac{a^2}{r^2}\right)\left(\frac{\sigma_h + \sigma_H}{2}\right) - \left(1 - 4\frac{a^2}{r^2} + 3\frac{a^4}{r^4}\right)\left(\frac{\sigma_h - \sigma_H}{2}\right)\cos(2\theta) \tag{3-14}$$

$$\sigma_{\theta\theta}^m = \left(1 + \frac{a^2}{r^2}\right)\left(\frac{\sigma_h + \sigma_H}{2}\right) + \left(1 + 3\frac{a^4}{r^4}\right)\left(\frac{\sigma_h - \sigma_H}{2}\right)\cos(2\theta) \tag{3-15}$$

$$\sigma_{r\theta}^{m} = \left(1 + 2\frac{a^2}{r^2} - 3\frac{a^4}{r^4}\right)\left(\frac{\sigma_h - \sigma_H}{2}\right)\sin(2\theta) \tag{3-16}$$

where r is the radial coordinate (radially outward positive), θ is the angular coordinate (counterclockwise positive), a is the tunnel radius, p is the fluid pressure, σ_H is the minimum far-field stress (which is horizontal in this case), and σ_h is the maximum far-field stress (which is vertical in this case) (Figure 3-21). The stresses are defined here such that compression is positive.

The effective stresses accounting for fluid pore pressure are:

$$\sigma_{rr}^{e} = \sigma_{rr}^{m} - p \tag{3-17}$$

$$\sigma_{\theta\theta}^{e} = \sigma_{\theta\theta}^{m} - p \tag{3-18}$$

$$\sigma_{r\theta}^{e} = \sigma_{r\theta}^{m} \tag{3-19}$$

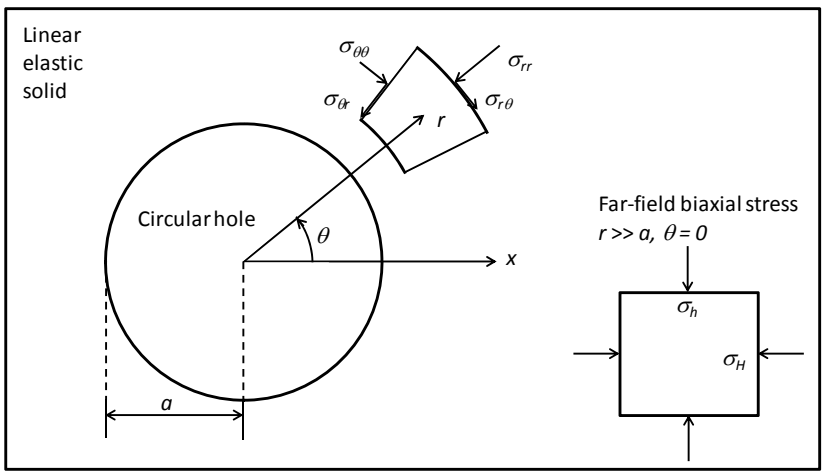

Figure 3-21. Definition diagram for plane stress around a circular hole.

First consider damage at the tunnel wall, where $r = a$. The stress Equations (3-14) through (3-16) simplify to:

$$\sigma_{rr}^{e} = -p \tag{3-20}$$

$$\sigma_{\theta\theta}^{e} = (\sigma_h + \sigma_H) + 2(\sigma_h - \sigma_H)\cos(2\theta) - p \tag{3-21}$$

$$\sigma_{r\theta}^{e} = 0 \tag{3-22}$$

Tensile failure occurs if either of the effective normal stresses fall below the negative of the tensile strength, $-T_r(\theta)$ in the radial direction, and $-T_\theta(\theta)$ in the circumferential direction, because of the anisotropic nature of the Opalinus Clay rock strength:

$$\sigma_{rr}^{e} = -p < -T_r(\theta) \tag{3-23}$$

$$\sigma_{\theta\theta}^{e} = (\sigma_h + \sigma_H) + 2(\sigma_h - \sigma_H)\cos(2\theta) - p < -T_\theta(\theta) \tag{3-24}$$

Shear failure occurs if the stress state of the system touches the Mohr-Coulomb failure curve,

$$\tau_m \geq \sigma_m \sin(\phi) + c(\theta)\cos(\phi) \tag{3-25}$$

where

$$\tau_m = \frac{|\sigma_{rr} - \sigma_{\theta\theta}|}{2} \tag{3-26}$$

$$\sigma_m = \frac{\sigma_{rr} + \sigma_{\theta\theta}}{2} \tag{3-27}$$

where the cohesive strength, $c(\theta)$, is also a function of angle because of the anisotropic nature of the Opalinus Clay rock strength, and the friction angle, ϕ.

Far-field, natural, stress conditions in the Opalinus Clay are approximated by σ_h = 6.5 MPa and σ_H =4.5 MPa, and pore pressure is approximated by, p = 1.5 MPa (Martin and Lanyon, 2003, p. 1085 and 1087). Tensile strength is characterized by values parallel and normal to bedding, T_p =2 MPa and T_n =1 MPa, respectively (Bossart, 2012, Annex 4-21). Similarly, cohesive strength is also characterized by values parallel and normal to bedding, c_p =5.5 MPa and c_n =2.2 MPa (Bossart, 2012, Annex 4-22). The friction angle ranges from 24° to 26° is adequately characterized by the value 25° (Bossart, 2012, Annex 4-22).

The radial tensile strength is represented as a function of angle through the following:

$$T_r(\theta) = T_p \cos^2(\theta - \theta_b) + T_n \sin^2(\theta - \theta_b) \tag{3-28}$$

where θ_b is the angle of the bedding, previously identified to be 48°. The circumferential tensile strength is given by

$$T_\theta(\theta) = T_p \sin^2(\theta - \theta_b) + T_n \cos^2(\theta - \theta_b) \tag{3-29}$$

The cohesive strength is given by

$$c(\theta) = c_p \cos^2(\theta - \theta_b) + c_n \sin^2(\theta - \theta_b) \tag{3-30}$$

Calculations done for effective stress and the negative of tensile strength around a tunnel are shown in Figure 3-22. When radial or circumferential stress falls below the negative of tensile strength, tensile failure occurs. As seen in Figure 3-22, tensile failure only occurs for some positions in the radial direction.

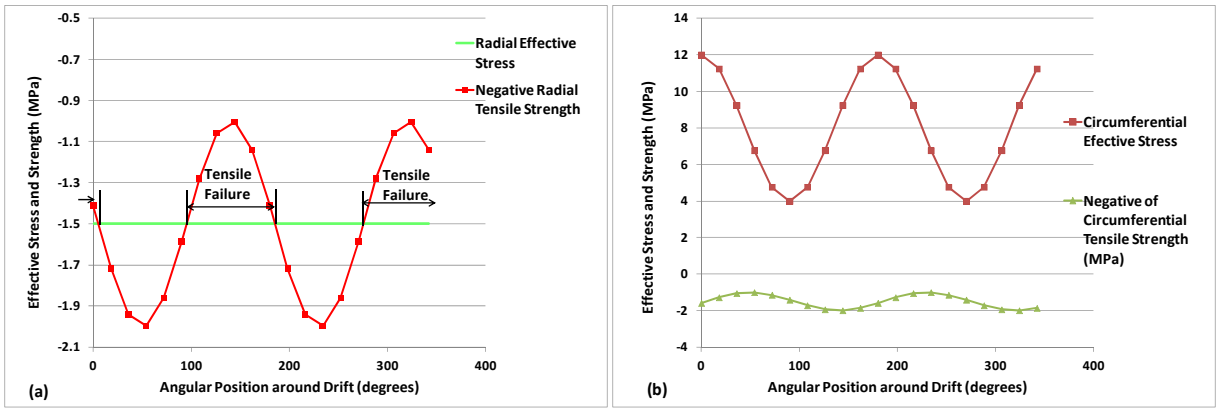

Figure 3-22. Comparison of effective stress and tensile strength to identify tensile failure: (a) radial direction; (b) circumferential direction.

Calculations for shear failure using Equation (3-25) are shown in Figure 3-23. When the ordinate in Figure 3-23 exceeds zero, shear failure occurs.

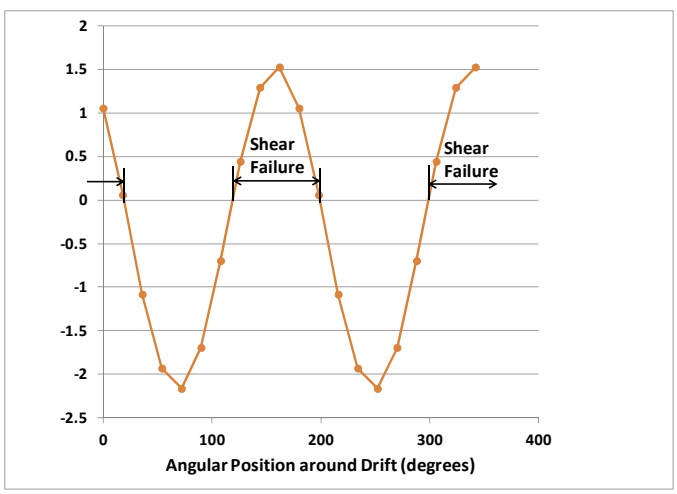

Figure 3-23. Results for shear failure.

The failure analyses results are summarized in Figure 3-24. This shows that both shear and tensile failure occur along the NNW side of the drift wall roughly between 3 and 5 o'clock, with shear failure only at 2:30 o'clock and tensile failure at 5:30 o'clock. Along the SSE side, both shear and tensile failure occur roughly between 9 and 11 o'clock, with shear failure at 8:30 o'clock and tensile failure at 11:30 o'clock. This is in qualitative agreement with the observations of failure, although the observed failure (Figure 3-17), especially on the NNW side, is restricted to a narrower region than predicted here.

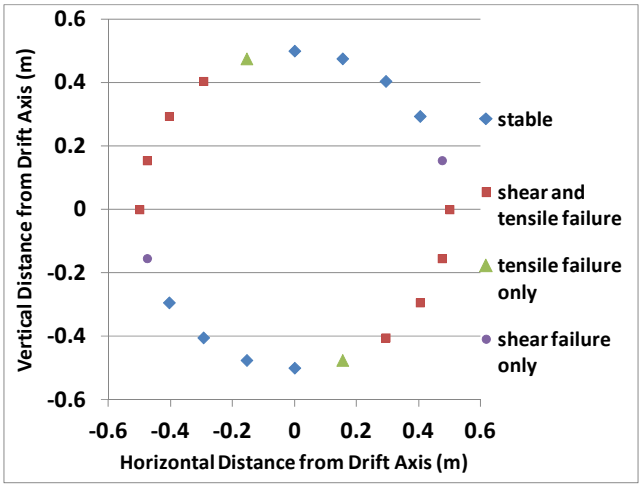

Figure 3-24. Results for failure analysis, with an orientation looking from the HG-A Niche towards back end of microtunnel.

Failure analysis at radii greater than 0.5 m (the radius of the drift) suggests that damage is confined to a narrow region around the drift. Tensile failure is found to be limited to only 3 to 4 cm into the drift wall, while shear failure is limited to about 10 cm into the drift wall. This analysis demonstrates that shear failure may be expected to play a role in the development of fractures in the EDZ.

3.5 An Analytical Model for Solute Transport through a Water-Saturated Single Fracture and Permeable Rock Matrix

The complexity of discrete fracture systems leads to a number of difficulties for mathematical models of hydrogeologic processes in such systems. There are many degrees of freedom in setting up a numerical discrete fracture model, and it is important to check the constraints on the numerical model, such that it can accurately represent the transport processes included in the model. One way to perform such a check is to compare against an analytical model that represents transport processes exactly for a limited set of idealized cases. Results from Liu et al. (2012) indicated that extremely fine matrix grids are required near the fracture to capture fracture-matrix solute exchange comparable to an analytical approach. As documented by Weatherhill et al. (2008), the necessary grid resolution to accurately capture solute transport behavior for such problems is dependent on the relative influence of different transport processes. Therefore, comparisons with analytical results are needed on a case-by-case basis to assess the accuracy of the numerical results. Given the difficulties caused by numerical discretization, analytical approaches may be needed in combination with numerical methods to provide robust solutions to solute transport in fractured rock.

The problem of solute transport through a water-saturated single fracture in a permeable rock matrix is examined here using the same analytical modeling approach as developed in Liu et al. (2012). In that report, a closed-form analytical solution was obtained that accounts for transverse and longitudinal advective transport in the fracture and matrix, and transverse diffusion in the matrix. The solution also accounted for both diffusive and advective solute exchange between the fracture and matrix, and a general

solute source position in either the fracture or matrix. The novel features of this solution are the incorporation of advective transport in the matrix and a general source position into a closed-form solution for the solute-transport problem. In this section, additional background concerning previous work and a more in-depth discussion of the problem being investigated are presented. Additional examples of the solution behavior demonstrate the effects of matrix advection in combination with advection along the fracture, transverse diffusion in the matrix, and solute release in the fracture and matrix. Furthermore, a new semi-analytical solution in the form of a superposition integral is also derived that includes these transport features, plus independent levels of longitudinal diffusion and dispersion in the matrix and fracture, respectively. Examples are presented that include advective transport in the fracture and matrix, longitudinal and transverse diffusion in the matrix, longitudinal dispersion in the fracture, as well as solute release from the fracture and matrix. An approximate criterion is proposed to evaluate the significance of longitudinal diffusion and dispersion relative to longitudinal spreading caused by fracture-matrix interaction.

While the low permeability of argillaceous rock may result in diffusive-dominated solute transport under many conditions, it is possible for advective solute transport to play a more important role if the hydraulic gradient is sufficiently perturbed beyond a static condition. The balance of advective and diffusive transport is represented by the Peclet number, which is a ratio of the diffusive transport time scale to the advective transport time scale. Given the length (L) and velocity (V) scales of a problem and the relevant diffusion or dispersion coefficient (D), the Peclet number is given by VL/D. Here we are interested in the Peclet number for the rock matrix, so the velocity and diffusion coefficient correspond to the rock matrix. Advective transport starts to become important when the Peclet number is greater than 1 (Bianchi et al., 2013). This can be expressed differently if we use Darcy's law for the magnitude of the velocity, $V = (K/\phi)(|\Delta H|/L)$, where K is the hydraulic conductivity of the rock matrix, ϕ is the porosity of the rock matrix, and $|\Delta H|$ is the change in magnitude of the hydraulic head over the length L. Using this for the velocity, the Peclet number becomes, $(K|\Delta H|)/(\phi D)$. To investigate a specific example, consider the properties of the Opalinus Clay. For transport parallel to bedding, the hydraulic conductivity is estimated to be 2×10^{-13} m/s, the porosity is about 0.1, and the diffusion coefficient (say for chloride) is about 5×10^{-11} m^2/s (Houseworth, 2012). Using these values, we find that advection may start to play a significant role in transport if $|\Delta H|$ exceeds 25 m. For a transport pathway of 100 m, this is a gradient of about 0.25 m/m, which could easily occur. In fact vertical gradients on the order of 0.2 m/m have been observed in clay formations (Mazurek et al., 2003). It is also important to keep in mind that abnormal pressure conditions may occur over the repository performance period, for example, as a result of repository heat or earthquakes.

3.5.1 Review of existing analytical models for solute transport in fracture-matrix systems

Solute transport in groundwater flow through fractured rock is a subject that has been investigated for nuclear waste disposal and other environmental groundwater contamination problems (NRC, 1996). Fractures are a common feature of consolidated rock systems and typically present much higher permeability than unfractured rock matrix, such that flow through fractures often dominates overall flow behavior. Matrix, on the other hand, typically dominates the overall pore volume of a fractured rock. These attributes often lead to much higher solute-transport velocities through fractures than in unfractured rock or unconsolidated soils (Berkowitz, 2002). This behavior often makes fracture flow and transport critical characteristics to examine for any geologic site where solute transport is a concern. However, despite their importance, fractures remain a difficult feature to represent accurately in mathematical

models for groundwater flow and transport (Matthäi et al., 2009; Wu and Pruess, 2000). Flow through fractures displays highly heterogeneous and complex flow patterns controlled by small-scale fracture features. Furthermore, transport processes at small scales that govern fracture-matrix exchange can dramatically influence larger-scale transport behavior (Grisak and Pickens, 1980).

Transport through saturated fractured rock was first investigated in an analytical model by Neretnieks (1980). Tang et al. (1981) extended this work to include the effects of longitudinal dispersion in the fracture, and Sudicky and Frind (1982) and Maloszewski and Zuber (1985) further generalized the transport problem from a single fracture to a system of parallel fractures with interceding rock matrix. Sharifi Haddad et al. (2012) developed a semi-analytical model of solute transport in a system of parallel fractures for a radially symmetric flow field associated with well injection. Maloszewski and Zuber (1990) considered the effects of linear kinetic interactions between solute and the rock for a single fracture and rock matrix. All of these models were restricted to advective transport in the fracture, transverse diffusion in the matrix, and diffusive fracture-matrix solute exchange. A review of these modeling approaches among others is provided by Bodin et al. (2003a; 2003b). Cihan and Tyner (2011) developed exact analytical solutions for advective transport through cylindrical macropores and diffusive exchange with a soil matrix, for an instantaneous release of solute into a macropore, a constant concentration of solute at the top of a macropore, and a pulse release of solute into a macropore. They also compared their analytical solutions with numerical simulations that included longitudinal and transverse matrix advection and longitudinal dispersion in the macropore. Roubinet et al. (2012) added the effects of transverse dispersion in a fracture and longitudinal diffusion in the matrix to these mechanisms, and found that transverse dispersion in fractures had little effect on solute transport, but that longitudinal diffusion in the matrix becomes important at low Peclet numbers. The solution provided by Roubinet et al. (2012) also is capable of treating spatially varying and time-dependent source conditions.

Other modeling efforts have focused on advective-dominated systems. Birkhölzer et al. (1993a, b) present an analytical model for transport through a two-dimensional fracture network and permeable rock matrix under conditions in which fracture-matrix exchange is dominated by advective processes, such that diffusion could be neglected. A diffusion-advection number was also developed to help ascertain conditions for which diffusive fracture-matrix exchange is negligible compared with advective fracture-matrix exchange. The methodology developed by Birkhölzer et al. (1993a, b) was used by Rubin et al. (1996) to investigate a tracer slug injection in a fractured rock with permeable rock matrix, and by Rubin et al. (1997) to investigate transport for cases with slow advective velocities in the fracture. Odling and Roden (1997) used a numerical model to study transport in fracture networks embedded in a permeable rock matrix, focusing on the role the permeable rock matrix plays when fracture networks have limited connectivity, including fractures that are disconnected from the network.

Cortis and Birkholzer (2008) and Geiger et al. (2010) have utilized a continuous-time random-walk numerical method to investigate the effects of diffusion and advection in fractured, permeable rock. Transport calculations for a two-dimensional fracture network having a range of fracture and matrix permeabilities were used to identify the parameter ranges over which matrix advection has a significant role or may be neglected.

Houseworth (2006) extended analytical modeling approaches for unsaturated flow, and included longitudinal and transverse flow and advective transport in the matrix, as well as advective and diffusive transport between the fracture and rock matrix. Longitudinal diffusion/dispersion was not included for the fracture or matrix, because this greatly simplifies the analytical model and is a reasonable approximation in some cases. For an unsaturated fractured rock, local differences in capillary conditions between the fracture and the rock matrix tend to dominate fracture-matrix flow exchange, such that flow exchange is

more likely to result either in fracture discharge into the matrix or convergent matrix flow into the fracture.

An analogous problem was analyzed by Zhan et al. (2009) for transport through a saturated system consisting of an aquifer confined above and below by aquitards of infinite extent. The analogy is that the aquifer corresponds to the fracture and the aquitards correspond to the rock matrix surrounding a fracture. Longitudinal advection and longitudinal and transverse dispersion were included as transport mechanisms in the aquifer. Transport in the aquitards was limited to the transverse direction but included both advection and diffusion. The general solution led to analytical results in the Laplace domain that required numerical inversion. Transverse dispersion in the aquifer and a more general treatment of transverse advection were new features introduced into the analyses. Zhan et al. (2009) compared their solution with previously derived solutions in which solute concentration was assumed to be transversely well-mixed in the aquifer. They concluded that accounting for transverse solute gradients and transverse solute-transport processes in the aquifer had a significant impact on the results. In addition, the total solute mass entering the aquitard from the aquifer was found to be sensitive to the Peclet number for advective and diffusive transport in the aquitards.

The analytical model presented here is for solute transport during steady-state saturated flow occurring in a single fracture and a porous, permeable rock matrix. This model goes beyond existing analytical models by including the combination of lateral matrix diffusion and flow through the matrix in any direction relative to the orientation of the fracture axis, as well as flow through the fracture. Thus, the flow direction in the matrix and fracture may have components both parallel to and orthogonal to the fracture axis, leading to fracture-matrix exchange through cross-flow (Birkholzer and Rouve, 1994). Diffusive fracture-matrix exchange and general diffusive transport orthogonal to the fracture axis in the rock matrix is also included. The location of solute release as an instantaneous point source is generalized for an arbitrary point within the model domain. Closed-form analytical solutions for transport are obtained for these conditions neglecting longitudinal diffusion and dispersion. Solutions are also developed including simultaneous dispersive transport along the fracture and longitudinal diffusion in the matrix. These solutions take the form of superposition integrals of the closed-form results.

3.5.2 Flow model

Transport processes are considered for a two-dimensional, saturated flow system with a single fracture embedded in a permeable rock matrix. Specification of the flow field is a necessary first step to define the transport problem. The permeability of the rock matrix is taken to be homogeneous and isotropic and the fracture is assigned a different, higher, permeability than the matrix along the fracture axis. It also has permeability equal to that of the matrix in the direction transverse to the fracture axis. This anisotropy in the fracture simplifies the flow problem. In general, the transverse permeability of the fracture is generally not too significant because of the narrow transverse dimension of the fracture, unless this permeability is much lower than the matrix and represents a flow barrier. Flow is also restricted to steady-state conditions, implying steady-state pressure boundary conditions. For simplicity, the flow process will be discussed for a situation in which flow is driven exclusively by pressure differences.

The flow system investigated is a generalization of the flow driven by a simple uniform pressure gradient aligned with the fracture axis. To understand the steady-state, two-dimensional flow field, the flow system is diagrammed in Figure 3-25 with the fracture axis oriented in the same direction as the z-axis.

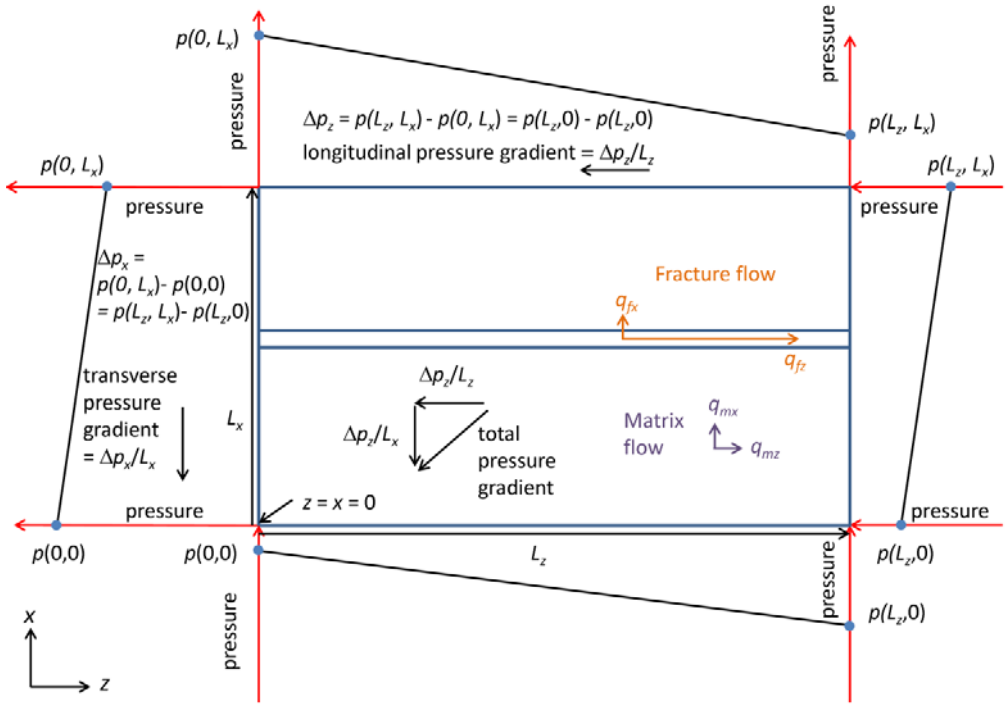

Figure 3-25. Steady-state flow field for single fracture in permeable rock matrix.

The corners of the rectangular flow domain are the origin, $z = x = 0$; $z = L_z$, $x = 0$; $z = L_z$, $x = L_x$; and $z = 0$, $x = L_x$, moving around the rectangle in counterclockwise order. The red arrows at the corners of the domain are axes displaying pressure. The pressures at the corners are set so that pressure drops across the domain in the longitudinal and transverse directions are uniform. From this configuration, it is clear that there will be a uniform transverse flow within the domain with the water flux rates $q_{fx} = q_{mx}$. Longitudinal water flux rates within the matrix (q_{mz}) and the fracture (q_{fz}) are uniform within their respective domains; however, $q_{fz} > q_{mz}$. The total pressure gradient is also shown and is uniform across the entire flow domain. Rotating the flow system in Figure 3-25 such that the rotated z-coordinate, z', aligns with the total pressure gradient results in the flow diagram given in Figure 3-26. The flow system shown in Figure 3-25 is equivalent to the system shown in Figure 3-26. Because the z' coordinate is parallel to the total pressure gradient, there is no flow along the constant x' boundaries (upper and lower boundaries in Figure 3-26) and the constant z' boundaries (left and right boundaries in Figure 3-26) coincide with contours of constant pressure. The flow field (relative to the fracture) remains the same as in Figure 3-25. Through this rotation, the flow field in Figure 3-25 is shown to be equivalent to a flow field resulting from a uniform pressure gradient that is not (necessarily) aligned with the fracture axis.

The transport problem to be solved is assumed to be sufficiently far from the pressure boundaries that any effects of these boundaries on transport are negligible. The configuration as shown in Figure 3-25 is used

to compute transport processes, with the longitudinal direction defined to be the same direction as the axis of the fracture, and the transverse direction is defined to be orthogonal to the fracture.

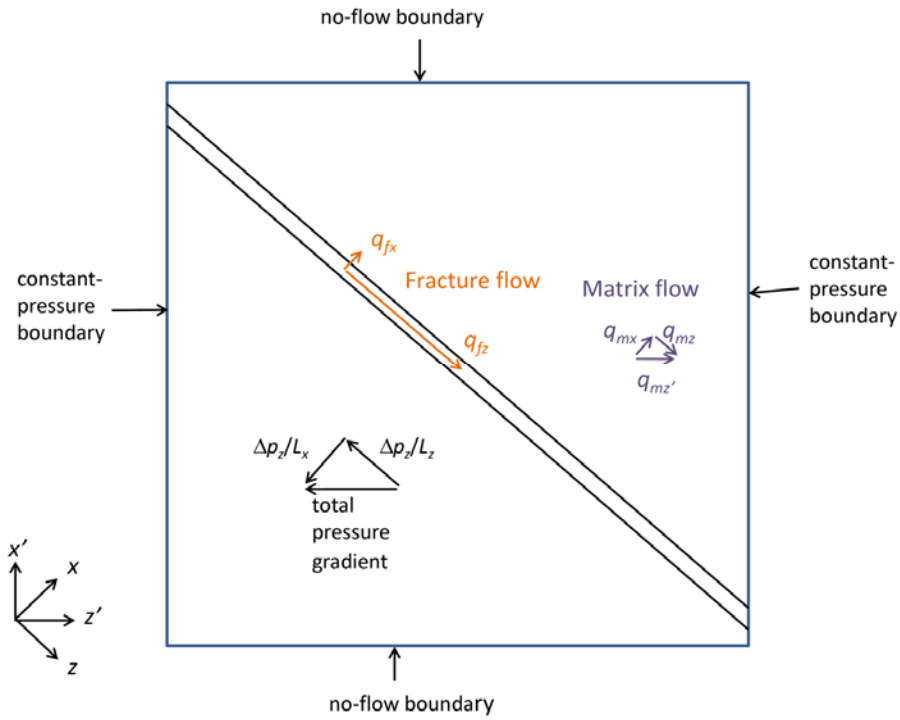

Figure 3-26. Rotated steady-state flow field for single fracture in permeable rock matrix, equivalent to that shown in Figure 3-25.

3.5.3 Transport model

A schematic diagram of the transport process to be analyzed is given in Figure 3-27. Longitudinal transport by advection occurs in both the matrix and fracture; transverse advective and diffusive transport occurs in the matrix. Solute exchange occurs through transverse advective and diffusive mechanisms. Because flow occurs in the matrix, there is formally both diffusion and hydrodynamic dispersion occurring in the matrix (Bear, 1972). For the model development, we assume that matrix diffusion dominates in comparison with hydrodynamic dispersion and will be referred to as *matrix diffusion* rather than *matrix dispersion*. Further discussion of this issue is given in Section 3.5.5. Transverse exchange between the fracture and matrix are treated through specifying source-sink terms at the fracture-matrix interface. Solute sorption and decay in both fracture and matrix are included. Solute release can be located at any point within the matrix or in the fracture. Because of a general solute release location and uni-directional transverse flow, solute concentrations are not, in general, symmetric about the fracture, and mathematical solutions for solute concentration on each side of the fracture must be developed.

Also shown in Figure 3-27 is the assumption of a well-mixed solute within the fracture in the transverse direction; therefore, there is no need to define a transverse fracture velocity or transverse diffusion in the fracture for lateral transport within the fracture. As a result, the fracture transport problem is one-dimensional in the longitudinal direction.

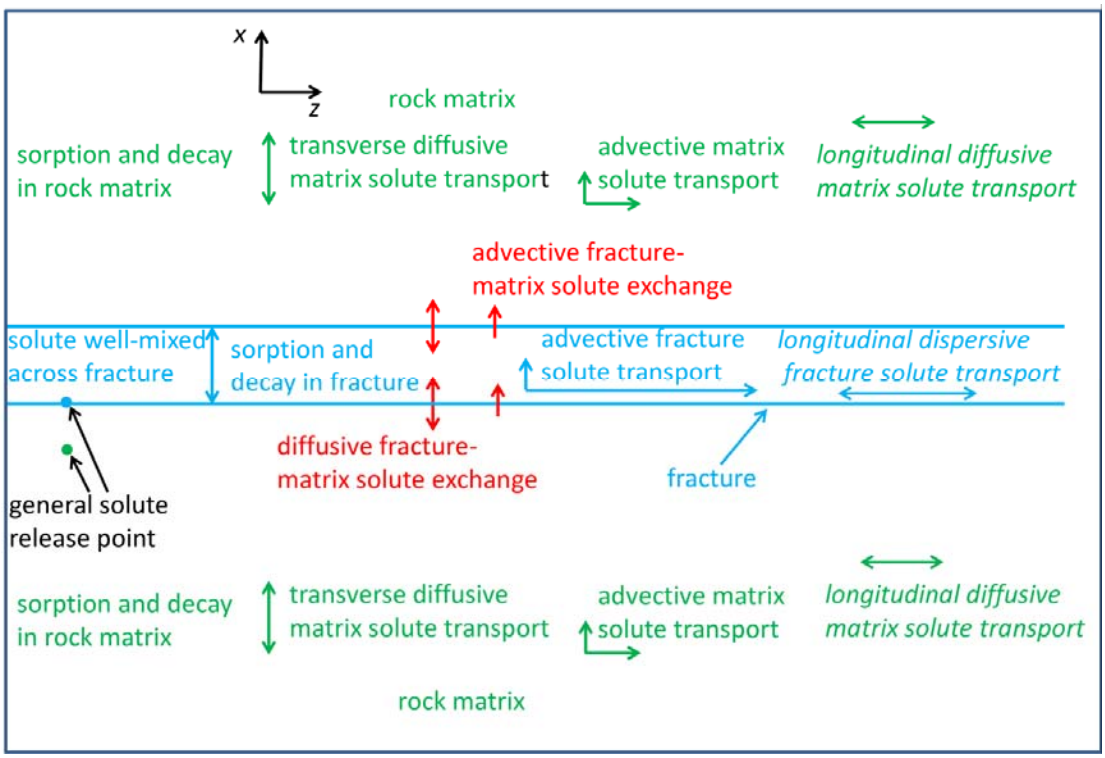

Figure 3-27. Solute transport mechanisms for single-fracture in permeable rock matrix.

Note: fracture processes in blue, matrix processes in green, and fracture-matrix exchange processes in red. Longitudinal dispersion/diffusion processes are in italic font to recognize the development of solutions in this paper both neglecting and including these processes.

Certain restrictions are required for the well-mixed assumption to be valid. Consider the time for a solute released at a point within the fracture aperture or the aquifer to become well-mixed across the fracture aperture through diffusion or dispersion. Classical diffusion theory shows that the diffusive mixing time t_d is proportional to b^2 / D_T, where b is the fracture aperture and D_T is the transverse diffusion (or dispersion) coefficient. Investigations into transport during flow through channels indicate that the mixing time required for solute concentrations to become uniform across the cross section is given by, $t_d = b^2 / 4D_T$ (Dentz and Carrera, 2007). This time should be much smaller than other times of interest, such as the fracture advective time scale, $t_f = z_e / v_f$, where z_e is the downstream solute travel distance of interest and v_f is the advective velocity in the fracture, giving the restriction $v_f b^2 / D_T z_e << 4$. For a system that includes both diffusion and transverse advection, the mixing time may be compared with the advective travel time across a fracture, $t_m = b / v_{ft}$, where v_{ft} is the advective velocity in the fracture transverse to the fracture axis, leading to a restriction on the transverse Peclet number, $v_{ft} b / D_T << 4$.

The validity of the well-mixed assumption imposes more restrictive conditions for larger fracture apertures. Natural fracture apertures generally range from a few microns up to a few millimeters (e.g.,

Nelson, 1985; Pyrak-Nolte and Morris, 2000; Hooker et al., 2013). Solute transverse dispersion coefficients inside fractures are not well known. For open fractures, solute diffusion in water may be appropriate, generally on the order of 10^{-9} m^2/s. Fractures with filling material would have reduced levels of molecular diffusion as a result of tortuosity effects, but would also experience additional mixing caused by transverse hydrodynamic dispersion associated with flow through the filled fracture. Using a value of 10^{-9} m^2/s for transverse dispersion, the diffusive mixing time for a large fracture with a 1 cm aperture is 2.5×10^4 s, or about 7 hours. A fracture with a 1 mm aperture would have a diffusive mixing time of 250 s and for an aperture of 0.1 mm, the diffusive mixing time is 2.5 s. As a rough approximation, assume that "<< 4" in the criteria above may be interpreted to mean "< 0.4". Then, over a 100 m travel distance, this leads to restrictions on the longitudinal fracture velocity to be less than about 35, 3.5×10^3, and 3.5×10^5 m/day, respectively, for the three cases (apertures of 1 cm, 1 mm, and 0.1 mm). Similarly, the transverse velocity in the fracture for these cases would be restricted to values less than about 3.5×10^{-3}, 3.5×10^{-2}, and 0.35 m/day, respectively, to be consistent with the well-mixed assumption. These restrictions are expected to be easily met in many circumstances.

Solutions will first be obtained neglecting longitudinal diffusion/dispersion in the fracture and rock matrix, indicated in Figure 3-27 by the italic font for these processes. Neglecting longitudinal diffusion/dispersion simplifies the analysis and allows for a closed-form solution of the transport problem; in many cases, this is a suitable approximation. A method to include these transport mechanisms is subsequently derived, and analytical results including these processes are presented.

The model to be analyzed does not address certain phenomena that have been identified and remain research questions concerning transport in fractured rock systems. Processes not analyzed here include scale-dependent diffusion effects, exchange between flowing and stagnant water within fractures, channeled flow in fractures due to asperities, and fracture skin effects (Liu et al., 2004, Zhou et al., 2007, Robinson et al., 1998).

3.5.3.1 Conservation equation for solute transport in the fracture

Sections 3.5.3.1, 3.5.3.2, and 3.5.3.3 repeat some of the material already presented in Liu et al. (2012), but is included here for clarity of the presentation.

For a single fracture in a porous rock matrix, the tracer mass conservation equation for the fracture is:

$$\phi_f \left(\frac{\partial c_f}{\partial t} + \lambda c_f \right) + \rho_{bf} \left(\frac{\partial c_{fa}}{\partial t} + \lambda c_{fa} \right) + q_f \frac{\partial c_f}{\partial z} =$$

$$A_{yfm} \left(\frac{1}{2} \phi_m D_m \left. \frac{\partial c_m}{\partial x} \right|_{x=0^s} + \frac{1}{2} \phi_m D_m \left. \frac{\partial c_m}{\partial x} \right|_{x=0^o} + \frac{1}{2} q_{fm} \Big|_{x=0^s} c_m \Big|_{x=0^s} + \frac{1}{2} q_{fm} \Big|_{x=0^o} c_m \Big|_{x=0^o} \right) \tag{3-31}$$

with initial and boundary conditions as follows:

$$c_f(z,0) = 0 \tag{3-32}$$

$$\lim_{z \to \infty} c_f(z,t) = 0 \tag{3-33}$$

$$c_f\left(z,t\right)=c_m\left(z,0^s,t\right)=c_m\left(z,0^o,t\right), \tag{3-34}$$

where, c_f is aqueous solute concentration in the fracture water, c_{fa} is the mass of solute sorbed per unit mass of minerals in the fracture, c_m is the aqueous solute concentration in the matrix, and q_f is the water flux in the fracture. The independent variables t, z, and x represent time, longitudinal distance, and transverse distance, respectively. The first and second terms in Equation (3-31) represent the rate of change in solute mass dissolved and sorbed to mineral surfaces, respectively, including radioactive decay represented by the decay constant λ. The intrinsic porosity of the fracture (i.e., the fracture pore volume divided by the fracture bulk volume) is ϕ_f, and ρ_{bf} is the bulk density of minerals in the fracture. If the fracture has no minerals within the fracture itself, c_{fa} would be defined as the sorbed solute per unit area of mineral surface represented by the fracture walls, in which case ρ_{bf} becomes the mineral surface area per unit fracture bulk volume. In some cases, it may be necessary to incorporate sorption on both fracture walls and minerals. The third term in Equation (3-31) represents the net longitudinal advective flux of solute at a point for a longitudinal fracture water flux rate q_f. Longitudinal diffusive/dispersive transport in the fracture is not included.

Terms on the right-hand side of Equation (3-31) represent advective and diffusive solute exchange between the fracture and matrix. The matrix diffusion coefficient is D_m, ϕ_m is the matrix porosity, and $A_{vfm}=2A_r/b$ is the fracture-matrix interface area per unit fracture bulk volume where b is the fracture aperture and A_r is the fracture-matrix area reduction factor. The x-axis is defined separately for each side of the fracture. The origin for each x-axis is zero at the fracture wall, and then increases moving away from the fracture. Fracture-matrix interface conditions are distinguished with respect to the side of the fracture where the tracer is released. The side of the fracture where tracer is released is designated with a superscript or subscript s denoting the source side of the fracture, and with a superscript or subscript o for the opposite side of the fracture from where the tracer is released. The fracture-matrix water fluxes are denoted by $q_{fm}\big|_{x=0^s}$ and $q_{fm}\big|_{x=0^o}$. Both are positive for flow away from the fracture (the positive x-direction for each side). Given the steady-state flow fields described earlier,

$$q_{fm}\big|_{x=0^s}=-q_{fm}\big|_{x=0^o}. \tag{3-35}$$

The conservation equation requires a constitutive model to link sorbed and solute concentrations. The simplest form of such a relationship, used here, is the linear, infinite capacity sorption model,

$$c_{fa}=K_{df}c_f, \tag{3-36}$$

and an analogous relationship for sorption in the matrix,

$$c_{ma}=K_{dm}c_m, \tag{3-37}$$

where K_{df} and K_{dm} are the fracture and matrix sorption coefficients, respectively, and c_{ma} is the sorbed solute mass per unit mass rock matrix. Using this sorption model and conditions in Equations (3-34) and

(3-35), Equation (3-31) may be rewritten more compactly using dimensionless retardation factors, $R_f = 1 + \rho_{bf} K_{df} / \phi_f$ and $R_m = 1 + \rho_{bm} K_{dm} / \phi_m$ for the fracture and matrix, respectively,

$$\frac{\partial c_f}{\partial t} + \lambda c_f + v_f \frac{\partial c_f}{\partial z} = A_{vfm} \frac{\phi_m R_m}{\phi_f R_f} \frac{D_m^*}{2} \left(\left. \frac{\partial c_m}{\partial x} \right|_{x=0^s} + \left. \frac{\partial c_m}{\partial x} \right|_{x=0^o} \right), \tag{3-38}$$

where ρ_{bm} is the bulk mineral density in the matrix, $v_f = q_f / \phi_f R_f$ is the fracture advective transport velocity, and $D_m^* = D_m / R_m$ is the retarded diffusion coefficient. Further simplification is achieved using the following transformations to decay-neutral concentrations:

$$c_{f\lambda} = c_f \exp(\lambda t) \tag{3-39}$$

$$c_{m\lambda} = c_m \exp(\lambda t), \tag{3-40}$$

giving

$$\frac{\partial c_{f\lambda}}{\partial t} + v_f \frac{\partial c_{f\lambda}}{\partial z} = A_{vfm} \frac{\phi_m R_m}{\phi_f R_f} \frac{D_m^*}{2} \left(\left. \frac{\partial c_{m\lambda}}{\partial x} \right|_{x=0^s} + \left. \frac{\partial c_{m\lambda}}{\partial x} \right|_{x=0^o} \right), \tag{3-41}$$

with initial and boundary conditions

$$c_{f\lambda}(z,0) = 0 \tag{3-42}$$

$$\lim_{z \to \infty} c_{f\lambda}(z,t) = 0 \tag{3-43}$$

$$c_{f\lambda}(z,t) = c_{m\lambda}(z,0^s,t) = c_{m\lambda}(z,0^o,t). \tag{3-44}$$

3.5.3.2 Conservation equation for solute transport in the matrix

The conservation equation for solute mass in the matrix is:

$$\phi_m \left(\frac{\partial c_{mk}}{\partial t} + \lambda c_{mk} \right) + \rho_{bm} \left(\frac{\partial c_{mak}}{\partial t} + \lambda c_{mak} \right) + q_{mz} \frac{\partial c_{mk}}{\partial z} + q_{mxk} \frac{\partial c_{mk}}{\partial x} = \phi_m D_m \frac{\partial^2 c_{mk}}{\partial x^2}, \tag{3-45}$$

where subscript k refers to the source (s) or the opposite (o) side of the fracture with respect to the tracer release location. The transverse flux, q_{mxk}, is defined to be positive when flowing away from the fracture for each side; therefore, $q_{mxs} = -q_{mxo}$. The solute concentration in matrix pore water is c_{mk} and the solute sorbed per unit mass of matrix minerals is c_{mak}; ρ_{bm} is the bulk density of minerals in the matrix. As for the fracture conservation equation, the first two terms represent the rate of change in dissolved and sorbed solute mass, respectively, and the third term is the net longitudinal advective flux of solute at a point for a longitudinal matrix-water flux rate q_{mz}. The fourth term is the net transverse

advective flux of solute at a point for a transverse matrix-water flux rate q_{mx}. The term on the right-hand side of Equation (3-45) is the net transverse diffusive flux of solute. As for the fracture conservation equation, diffusive/dispersive transport in the longitudinal direction is not included.

The initial and boundary conditions for the matrix conservation equation are:

$$c_{ms}\left(z,x,0\right)=\frac{bM_0}{A_f\phi_m R_m}\delta\left(x-x_0\right)\delta\left(z\right) \tag{3-46}$$

$$c_{mo}\left(z,x,0\right)=0 \tag{3-47}$$

$$c_{mk}\left(z,0,t\right)=c_f\left(z,t\right). \tag{3-48}$$

Equation (3-46) gives the initial condition on the source side of the fracture, while (3-46) gives the initial condition on the opposite side of the fracture from the source release point. Note that if $x_0=0$, the initial condition represents tracer release in the fracture because of the boundary condition (3-48). The mass of tracer released is M_0, A_f is the fracture cross-sectional area orthogonal to the fracture axis, and δ is the Dirac delta function that is dimensionally an inverse length. The effective third dimension for defining the initial solute-mass concentration is given by A_f/b. Equation (3-45) may be simplified using previously defined quantities to be

$$\frac{\partial c_{mk\lambda}}{\partial t}+v_{mz}\frac{\partial c_{mk\lambda}}{\partial z}+v_{mxk}\frac{\partial c_{mk\lambda}}{\partial x}=D_m^*\frac{\partial^2 c_{mk\lambda}}{\partial x^2}, \tag{3-49}$$

where $v_{mxk}=q_{mxk}/\left(\phi_m R_m\right)$ and $v_{mz}=q_{mz}/\left(\phi_m R_m\right)$ and the initial and boundary conditions become

$$c_{m\lambda s}\left(z,x,0\right)=\frac{bM_0}{A_f\phi_m R_m}\delta\left(x-x_0\right)\delta\left(z\right) \tag{3-50}$$

$$c_{m\lambda o}\left(z,x,0\right)=0 \tag{3-51}$$

$$c_{m\lambda k}\left(z,0,t\right)=c_f\left(z,t\right) \tag{3-52}$$

$$\lim_{x\to\infty}c_{m\lambda k}\left(z,x,t\right)=0. \tag{3-53}$$

3.5.3.3 Dimensionless form and solution

As shown in Liu et al. (2012), Equations (3-41) through (3-43) and (3-49) through (3-53) were transformed into a reference frame moving at the matrix velocity in the z direction and put into a dimensionless form to give:

$$\frac{\partial c_{fd}}{\partial \tau}+\frac{\partial c_{fd}}{\partial \xi}=\frac{1}{2}\left(\frac{1}{Pe}\frac{\partial c_{md}}{\partial \eta}\bigg|_{\eta=0^s}+\frac{1}{Pe}\frac{\partial c_{md}}{\partial \eta}\bigg|_{\eta=0^o}\right) \tag{3-54}$$

$$c_{fd}\left(\xi,0\right)=0 \tag{3-55}$$

$$\lim_{\xi\to\infty} c_{fd}\left(\xi,\tau\right)=0, \tag{3-56}$$

for Equations (3-41) through (3-43) and

$$\frac{\partial c_{mdk}}{\partial \tau}+V_k\frac{\partial c_{mdk}}{\partial \eta}=\frac{1}{Pe}\frac{\partial^2 c_{mdk}}{\partial \eta^2} \tag{3-57}$$

$$c_{mds}\left(\xi,\eta,0\right)=\delta\left(\xi\right)\delta\left(\eta-\eta_0\right) \tag{3-58}$$

$$c_{mdo}\left(\xi,\eta,0\right)=0 \tag{3-59}$$

$$c_{mdk}\left(\xi,0,\tau\right)=c_{fd}\left(\xi,\tau\right) \tag{3-60}$$

$$\lim_{\eta\to\infty} c_{mdk}\left(\xi,\eta,\tau\right)=0, \tag{3-61}$$

where the independent variables are $\tau=v_f^* t/\ell$, $\xi=\left(z-v_{mz}t\right)/\ell$, $\eta=x/\ell$ using the length scale $\ell=\left(b\,\phi_f R_f\right)/\left(2\,A_r\phi_m R_m\right)$, dimensionless concentrations $c_{fd}=\left(A_f\phi_f R_f \ell c_{f\lambda}\right)/\left(2M_0\right)$ and $c_{md}=\left(A_f\phi_f R_f \ell c_{m\lambda}\right)/\left(2M_0\right)$, and parameters $Pe=v_f^*\ell/D_m^*$ and $V_k=v_{mxk}/v_f^*$. The dimensionless delta functions at $t=0$ are given by $\delta\left(\eta-\eta_0\right)=\ell\delta\left(x-x_0\right)$ and $\delta\left(\xi\right)=\ell\delta\left(z\right)$.

The solutions for fracture and matrix dimensionless concentrations were derived in Liu et al. (2012), and are

$$c_{fd}\left(\xi,\tau\right)=H\left(\tau-\xi\right)H\left(\xi\right)\frac{\xi+Pe\eta_0}{4\sqrt{\pi}\sqrt{Pe}\left(\tau-\xi\right)^{\frac{3}{2}}}\exp\left(-\frac{PeV_s}{2}\eta_0\right)$$
$$\times\exp\left(-\frac{\left(\xi+Pe\eta_0\right)^2}{4Pe\left(\tau-\xi\right)}-\frac{PeV^2\left(\tau-\xi\right)}{4}\right). \tag{3-62}$$

Similar inversions are performed to determine the matrix concentration for the side of the fracture opposite the source, which is found to be

$$c_{mdo}\left(\xi,\eta,\tau\right)=H\left(\tau-\xi\right)H\left(\xi\right)\exp\left(\frac{PeV_o\left(\eta+\eta_0\right)}{2}\right)\frac{\xi+Pe\left(\eta+\eta_0\right)}{4\sqrt{\pi}\sqrt{Pe}\left(\tau-\xi\right)^{\frac{3}{2}}}$$
$$\times\exp\left\{-\frac{\left(\xi+Pe\left(\eta+\eta_0\right)\right)^2}{4Pe\left(\tau-\xi\right)}-\frac{PeV^2\left(\tau-\xi\right)}{4}\right\}, \tag{3-63}$$

and for the matrix on the source side of the fracture:

$$c_{mds}\left(\xi,\eta,\tau\right)=H\left(\tau-\xi\right)H\left(\xi\right)\exp\left\{\frac{PeV_s\left(\eta-\eta_0\right)}{2}\right\}\frac{\xi+Pe\left(\eta+\eta_0\right)}{4\sqrt{\pi}\sqrt{Pe}\left(\tau-\xi\right)^{\frac{3}{2}}}$$

$$\times\exp\left(-\frac{\left(\xi+Pe\left(\eta+\eta_0\right)\right)^2}{4Pe\left(\tau-\xi\right)}-\frac{PeV^2\left(\tau-\xi\right)}{4}\right)+\frac{\sqrt{Pe}\delta\left(\xi\right)}{2\sqrt{\pi\tau}}\exp\left\{\frac{PeV_s}{2}\left(\eta-\eta_0\right)-\frac{PeV^2\tau}{4}\right\}$$

$$\times\left[\exp\left\{-\frac{Pe\left(\eta-\eta_0\right)^2}{4\tau}\right\}-\exp\left\{-\frac{Pe\left(\eta+\eta_0\right)^2}{4\tau}\right\}\right]. \tag{3-64}$$

Furthermore, recognizing that $c_{fd}\left(\xi,\tau\right)=c_{mds}\left(\xi,0,\tau\right)=c_{mdo}\left(\xi,0,\tau\right)$, the solution for concentration is completely specified by (3-63) and (3-64). The matrix solute concentration on the source side of the fracture, Equation (3-64), has a term involving $\delta\left(\xi\right)$. This term represents solute in the matrix that has not interacted with the fracture and moves at the matrix advection velocity as a concentration spike at $\xi=0$. This infinite concentration occurs because the model does not include longitudinal solute diffusion in the matrix. The closed-form solutions in (3-62) through (3-64) have been verified directly by substitution into Equations (3-54) through (3-61). For some applications, it is useful to have the solution in the form of cumulative mass arrival at a downstream location as a function of time. Such a mass arrival curve from an instantaneous point source may be computed from integrals of the solutions presented in this section, with the resulting formulae given in Section 3.5.8.1. The cumulative mass results have been compared with previously published solutions (see Section 3.5.8.2) for cases without matrix advection.

3.5.4 Solution behavior without longitudinal diffusion/dispersion

The solution behavior is examined for a set of 6 cases in which the flow velocities and source positions are varied, using a fracture within a domain that is 100 m long as measured along the fracture axis. The domain orthogonal to the fracture is unbounded. Hydrogeologic properties consistent with the flow velocities used are given in Table 3-3. The intrinsic fracture permeability corresponds roughly to a parallel-plate permeability for a fracture with an aperture of 10^{-4} m. For a fracture spacing of 1 m, the bulk fracture permeability would be 1.18×10^{-13} m^2. The matrix permeability is relatively high for an argillaceous rock, but still lies within the range of observed values for mudrock reported by Yang and Aplin (2010). A high value of matrix permeability was chosen such that the effects of solute advection in the matrix would be clear in the examples.

Table 3-3. Hydrogeologic parameters and domain investigated.

Matrix permeability (m^2)	Intrinsic fracture permeability (m^2)	Regional gradient of hydraulic head	Doman length (m)
$3.06\text{x}10^{-16}$	$1.18\text{x}10^{-9}$	0.01	100

Table 3-4 provides the range of values for transport parameters and Table 3-5 presents the fixed parameters for the cases investigated. Note that sorption (K_{df} and K_{dm}) coefficients, the decay constant (λ), and all longitudinal diffusion/dispersion coefficients are zero for the examples in this section. In these examples, the pressure gradient direction is varied with respect to the fracture axis. Table 3-4 shows this angle ranges from 0° to 84.4°. As the angle between the pressure gradient and fracture axis vary, both fracture and matrix velocities are affected by the changing components of the pressure gradient. For cases 1 through 3, the source release occurs in the fracture and for cases 4 through 6, the source release occurs in the matrix 0.5 m offset from the fracture. As mentioned before, all source releases are assumed to be instantaneous at time $t = 0$.

Table 3-4. Flow and transport parameters varied.

	primary						dimensionless			
Case	v_f (m/s)	v_{mz} (m/s)	v_{mxs} (m/s)	angle (°)	x_0 (m)	t (days)	Pe	V_s	η_0	τ
1	$1.16\text{x}10^{-4}$	$3\text{x}10^{-10}$	0	0	0	200	580	0	0	$4.01\text{x}10^{6}$
2	$8.2\text{x}10^{-5}$	$2.12\text{x}10^{-10}$	$-2.12\text{x}10^{-10}$	45	0	200	410	-2.59×10^{-5}	0	$2.83\text{x}10^{6}$
3	$1.14\text{x}10^{-5}$	$2.94\text{x}10^{-11}$	-2.99×10^{-10}	84.4	0	200	56.9	-2.63×10^{-5}	0	$3.93\text{x}10^{5}$
4	$1.16\text{x}10^{-4}$	$3\text{x}10^{-10}$	0	0	-0.5	2000	580	0	10^{3}	$4.01\text{x}10^{7}$
5	$8.2\text{x}10^{-5}$	$2.12\text{x}10^{-10}$	$-2.12\text{x}10^{-10}$	45	-0.5	2000	410	-2.59×10^{-5}	10^{3}	$2.83\text{x}10^{7}$
6	$1.14\text{x}10^{-5}$	$2.94\text{x}10^{-11}$	-2.99×10^{-10}	84.4	-0.5	2000	56.9	-2.63×10^{-5}	10^{3}	$3.93\text{x}10^{6}$

Table 3-5. Parameters used for all cases.

primary											dimensionless
ϕ_f	ϕ_m	K_{df} (m^3/kg)	K_{dm} (m^3/kg)	b (m)	A_r	ℓ (m)	D_m (m^2/s) (transverse)	A_f (m^2)	M_0 (kg)	λ (s^{-1})	V_ℓ
1	0.1	0	0	10^{-4}	1	5×10^{-4}	10^{-10}	1	1	0	$2.59\text{x}10^{-6}$

An example of the analytical model transport responses using Equations (3-63) and (3-64) is given in Figure 3-28 for solute release in the fracture and flow parallel to the fracture. Figure 3-28(a) shows the contour pattern for concentration at 200 days after source release, with the elongated profile indicative of the enhanced longitudinal transport along the fracture. The symmetrical transverse spreading is a result of transverse diffusion from the fracture into the matrix. Advective longitudinal transport in the matrix cannot be resolved in this figure, because the trailing concentration front is at a longitudinal position of only 0.005 m. The cumulative-mass arrival and mass-arrival rates at 100 m from the origin are given in Figure 3-28(b) and 3-28(c), respectively. Cumulative-mass-arrival curves are computed using Equations (3-92), (3-95), and (3-96) as given in Section 3.5.8.1, and the mass-arrival rates are computed from the time derivatives of these equations. Mass arrivals and arrival rates are given for the fracture and for each

side of the matrix. The "matrix source" and "matrix opposite" terms in Figures 3-18(b) and 3-28(c) refer to cumulative mass and mass-arrival rates in the matrix on the negative and positive sides of the fracture, respectively, in terms of the transverse coordinate. For this case, the matrix-mass arrivals and arrival rates are the same on both sides of the fracture, because of the symmetry of this problem about the fracture axis. The trailing edge of the mass arrival rate in Figure 3-28(c) shows a sharp decrease near 10,000 years. This is close to the time required for a solute to arrive 100 m downstream moving at the matrix advection velocity (10,563 years). Because there is no longitudinal diffusion or dispersion, any solute that has had minimal interaction with the fracture will arrive at the 100 m boundary close to this time.

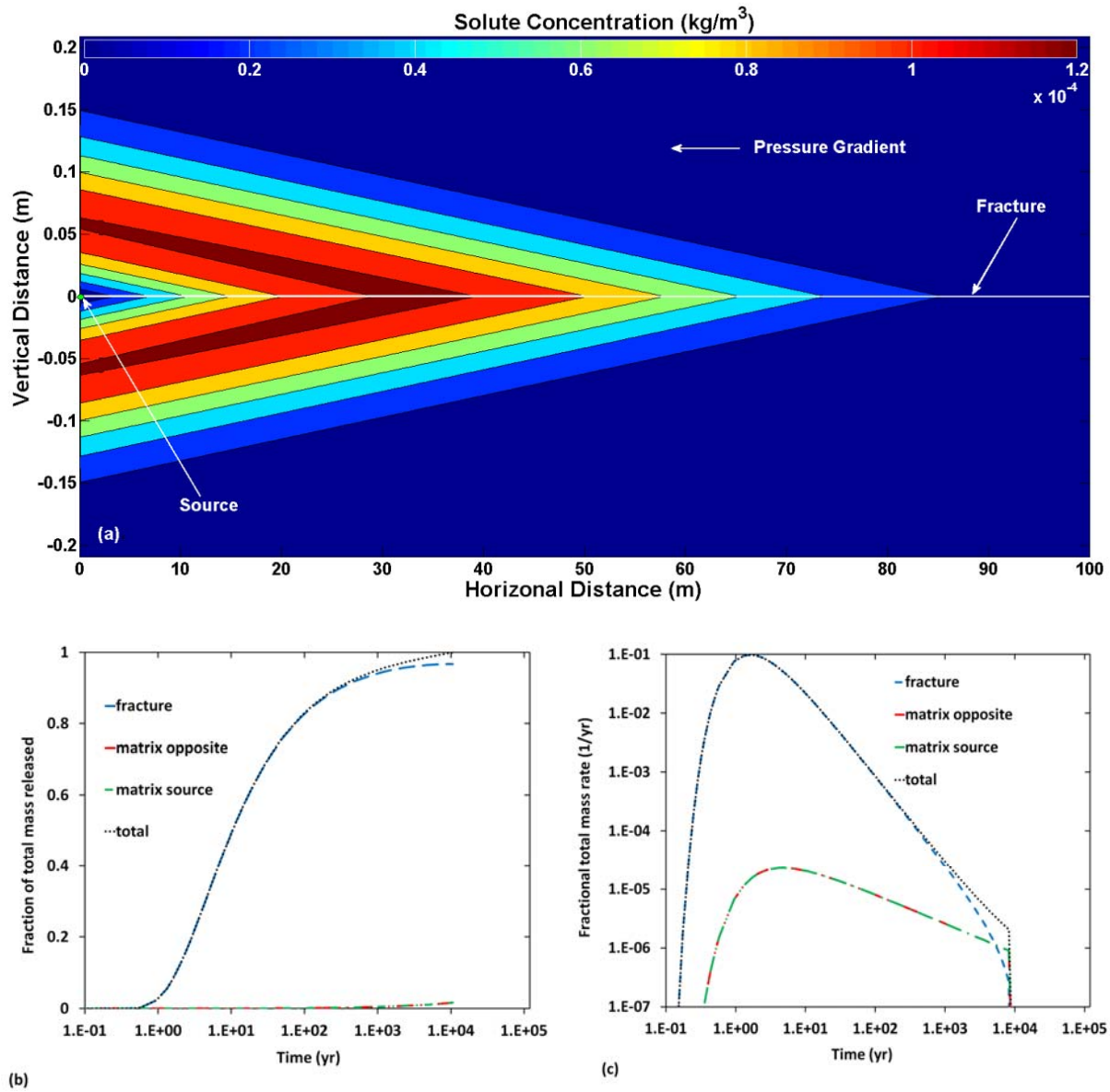

Figure 3-28. Case 1: transport results for matrix flow parallel to the fracture and solute release in the fracture. (a) concentration contours at 200 days; (b) cumulative mass arrivals at 100 m; (c) mass arrival rates at 100 m.

An example with an oblique cross-flow is shown in Figure 3-29. The only difference between this case and Case 1 in Figure 3-28 is that the hydraulic gradient is at a 45° angle to the fracture axis. The asymmetry of the contour plot relative to the fracture in Figure 3-29(a) is a result of the matrix cross-flow component orthogonal to the fracture. As a result of cross flow, the highest-concentration portion of the profile is displaced laterally, which results in retardation of the main solute mass as shown in Figures 3-29(b) and 3-29(c) and reduces solute interaction with the fracture, limiting dispersion through fracture-matrix interaction and resulting in higher peak concentrations. A more substantial mass of solute arrives in the matrix at the downstream boundary as shown in Figure 3-29(b), arriving through the matrix on the downstream side (positive x -coordinate side) of the fracture relative to matrix cross-flow.

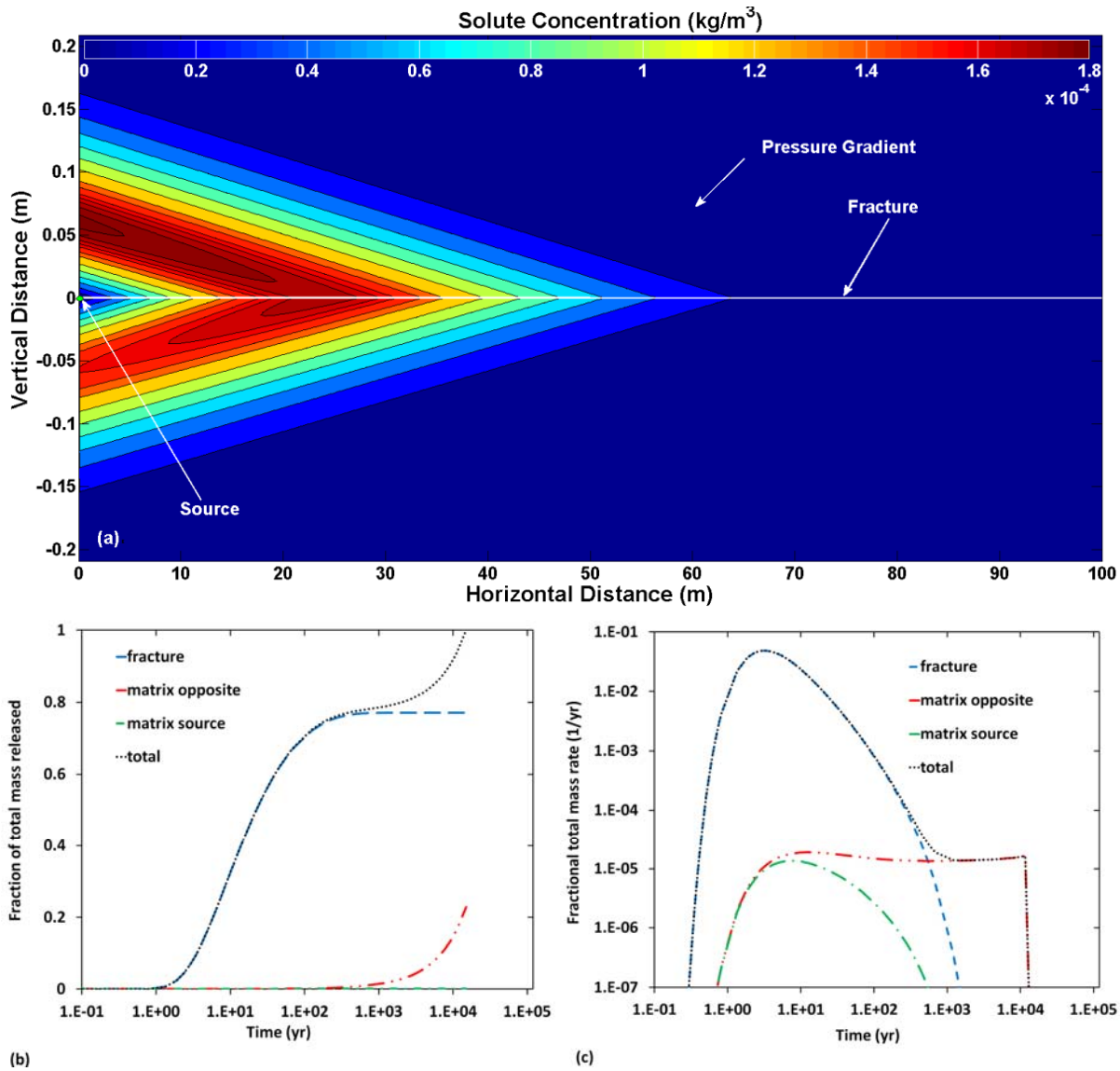

Figure 3-29. Case 2: Same as case 1 but with the hydraulic gradient at a 45°angle to the fracture. (a) concentration contours at 200 days; (b) cumulative mass arrivals at 100 m; (c) mass arrival rates at 100 m.

An example with stronger cross-flow is shown in Figure 3-30, in which the hydraulic gradient is at an 84.4° angle to the fracture axis. Contours are shown in Figure 3-30(a) at 200 days and in Figure 3-30(b) at 6000 days. The relatively slower velocity in the fracture and greater advective losses of solute to the matrix reduce the rate of solute advance as compared with Figures 3-28 and 3-29. Peak solute concentrations are correspondingly higher than in Figures 3-28 and 3-29. By comparison with Figure 3-28, where diffusion is the only mechanism for fracture-matrix exchange, this example clearly shows that matrix cross-flow can have a significant influence on fracture-matrix exchange. The effects of cross-flow create significant lateral movement of solute relative to the fracture, limiting the interaction of solute with the fracture. Such effects would be moderated in a fracture-network setting as a result of interactions with other fractures in the network. This is also seen clearly in the mass-arrival and arrival-rate curves in Figures 3-30(c) and 3-30(d). A large fraction of solute travels to the downstream location mainly through the matrix, as indicated in Figure 3-30(c) by the large increase in cumulative mass arrivals close to the matrix travel time, 100 m divided by the matrix longitudinal velocity, or 1.08×10^5 years.

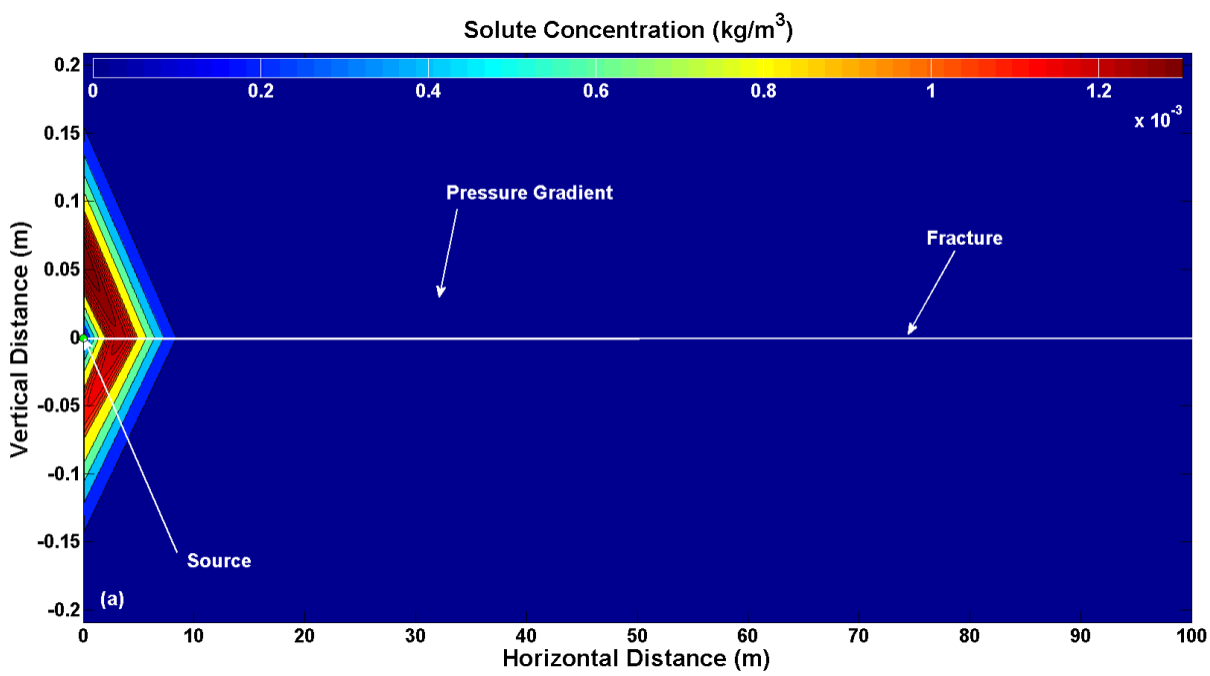

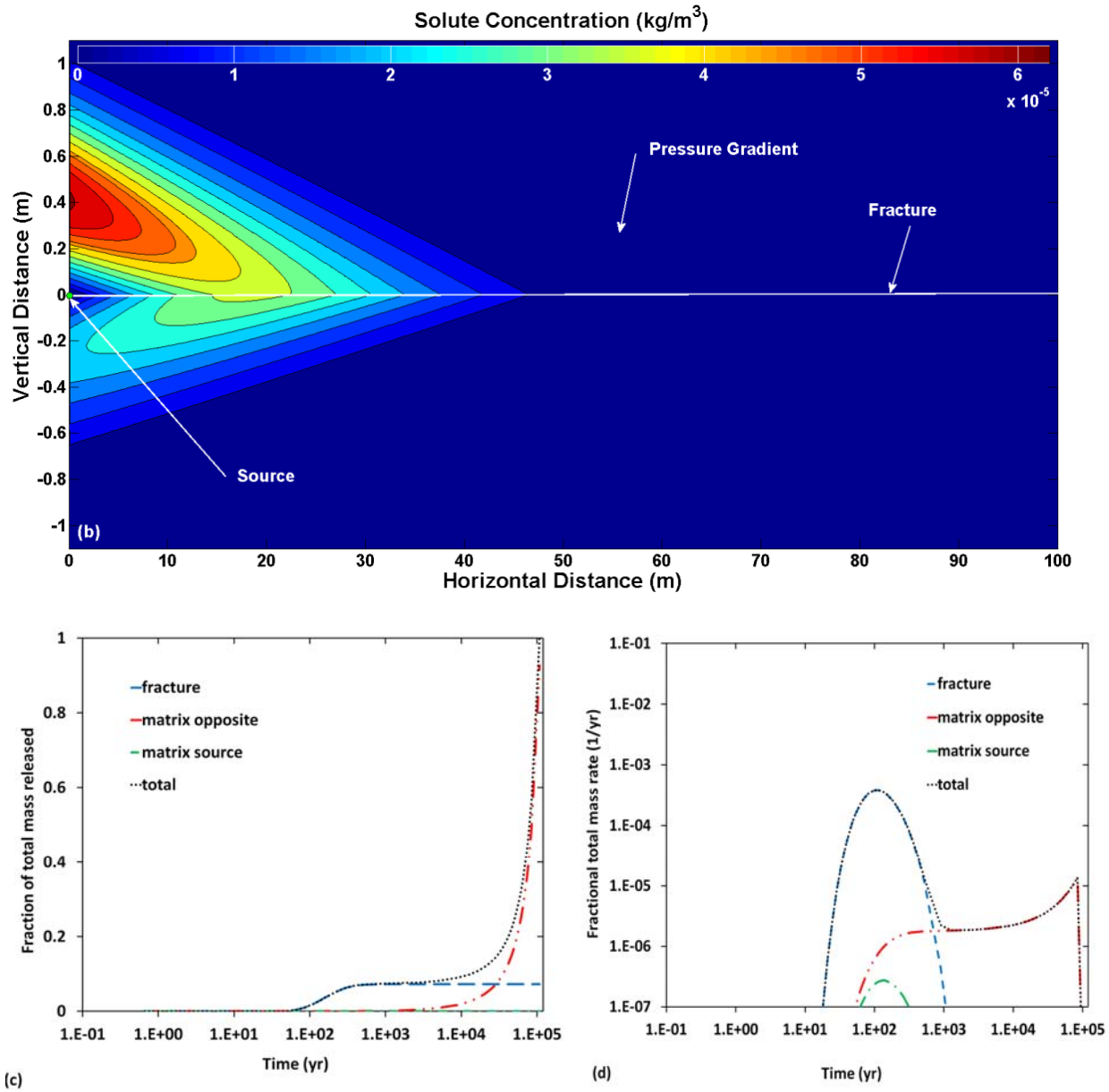

Figure 3-30. Case 3: Same as case 1 but with the hydraulic gradient at an 84.4° angle to the fracture. (a) concentration contours at 200 days; (b) concentration at 6,000 days – note expanded y-axis scale; (c) cumulative mass arrivals at 100 m; (d) mass arrival rates at 100 m. Note that the transverse scale is expanded for this high cross-flow velocity case.

The profile in Figure 3-31 is a result of modifying case 1 (Figure 3-28, pressure gradient parallel to the fracture) by moving the source into the matrix by 0.5 m. Solute transport through the fracture is delayed because of the source location, and the contours in Figure 3-31(a) are at 2000 days instead of 200 days as in Figure 3-28(a). The resulting profile shows the reduced degree of interaction between the solute and the fracture caused by the source offset position. Concentrations in the figure are limited to solute mass

that has diffused from the source to interact with the fracture and thereby disperse longitudinally. The trailing concentration spike in the matrix represents solute that has not interacted with the fracture and has an infinite concentration, as a result of no longitudinal diffusion in the matrix. The early parts of the cumulative mass-arrival and mass-arrival-rate curves in Figures 3-31(b) and 3-31(c) are delayed relative to those in Figure 3-28(b) and 3-28(c) and the peak mass-arrival rate is significantly higher for Case 1.

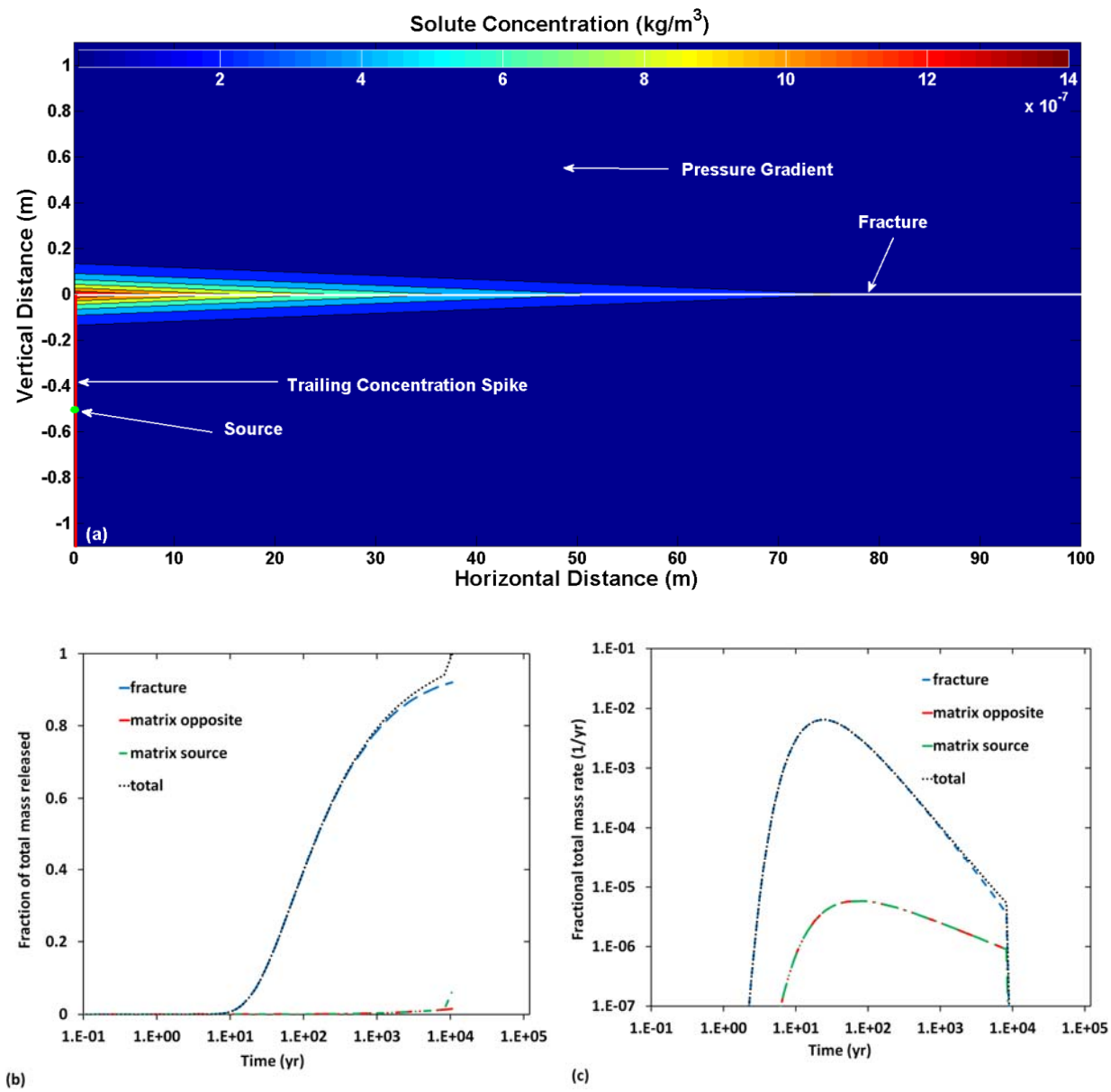

Figure 3-31. Case 4: Same as Case 1 but with source located in matrix 0.5 m from fracture. (a) concentration contours at 2000 days; (b) cumulative mass arrivals at 100 m; (c) mass arrival rates at 100 m.

Figure 3-32 shows a case that is comparable with Case 2 (Figure 3-29, pressure gradient at a 45° angle to the fracture), except that the source is located in the matrix 0.5 m from the fracture. The trailing concentration spike is present in the matrix as a result of solute in the matrix that has not yet interacted with the fracture. Concentration contours in Figure 3-32(a) are slightly displaced to the side of the fracture opposite the source as compared with Figure 3-31(a), because of the transverse flow in the matrix in that direction. Note that for Figure 3-32(a), the simulation time is 2000 days compared with 200 days for Figure 3-29(a). The reduced fracture velocity and increased matrix cross-flow cause the latter part of the cumulative arrival curve and mass arrival rates in Figure 3-32(b) and 3-32(c) to be delayed in comparison with Case 2.

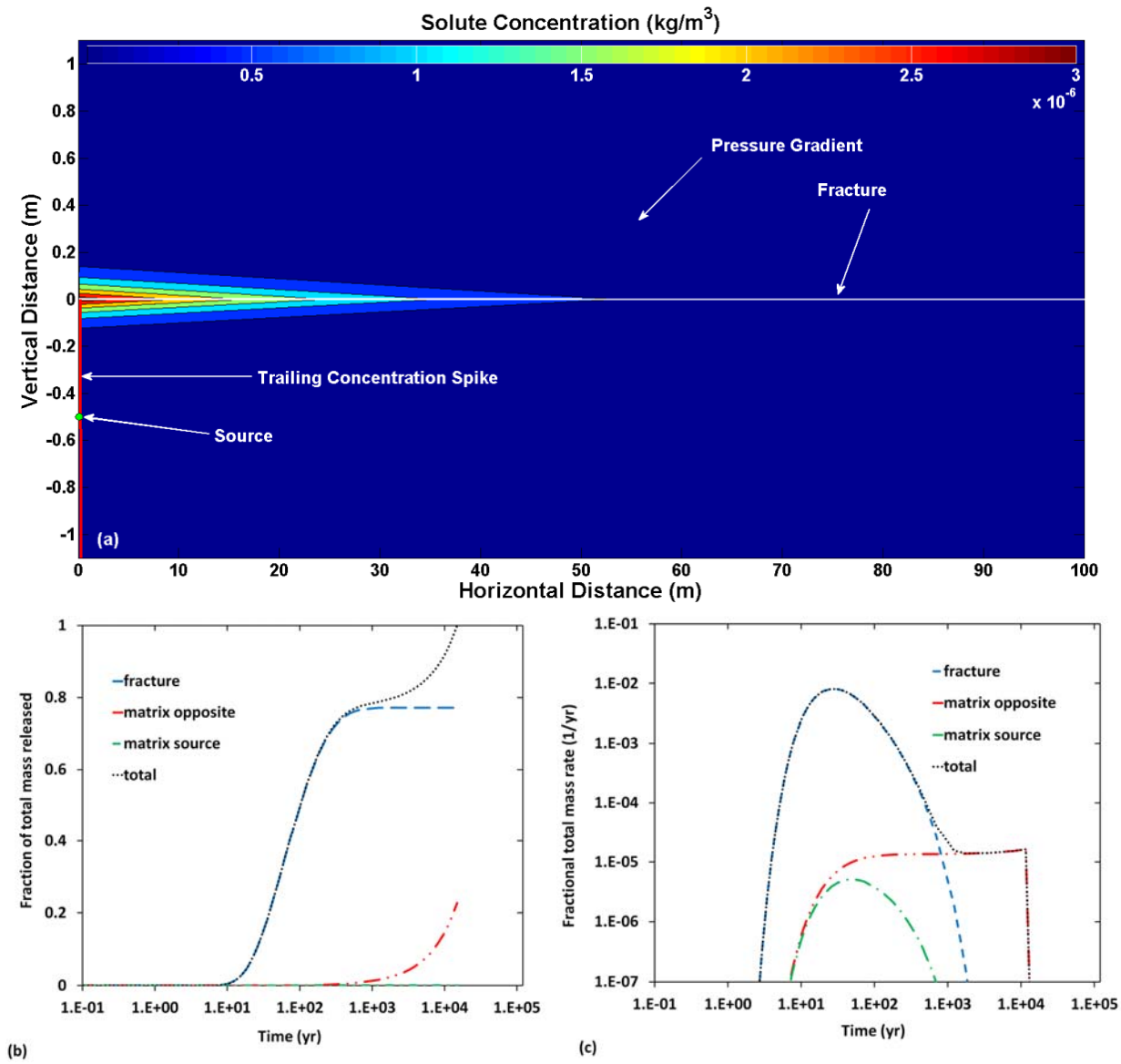

Figure 3-32. Case 5: Same as Case 2 but with source located in matrix 0.5 m from fracture. (a) concentration contours at 2000 days; (b) cumulative mass arrivals at 100 m; (c) mass arrival rates at 100 m.

Figure 3-33 shows Case 6, comparable with Case 3 (Figure 3-30, pressure gradient at a 84.4° angle to the fracture), except that the source is located in the matrix 0.5 m from the fracture. Contours are shown in Figure 3-33(a) at 2000 days and in Figure 3-33(b) at 40,000 days. The relatively slower velocity in the fracture reduces the rate of advance of the solute as compared with Figures 3-31 and 3-32. The concentration contours in Figure 3-33(b) are significantly displaced to the side of the fracture opposite the source, because of the transverse flow within the matrix in that direction. The reduced fracture velocity and increased matrix cross-flow cause the latter part of the cumulative-arrival and arrival-rate curves in Figure 3-33(c) and 3-33(d) to be delayed, similar to Case 3. If the cross-flow direction is reversed for cases 5 and 6, even more solute travels entirely (or almost entirely) within the matrix to the downstream observation point.

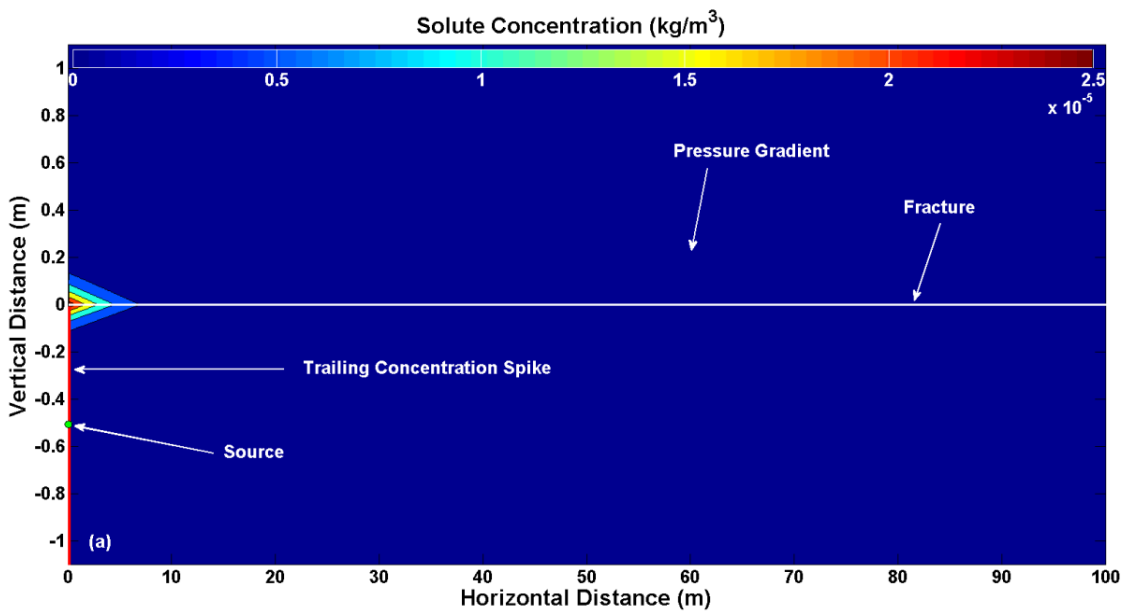

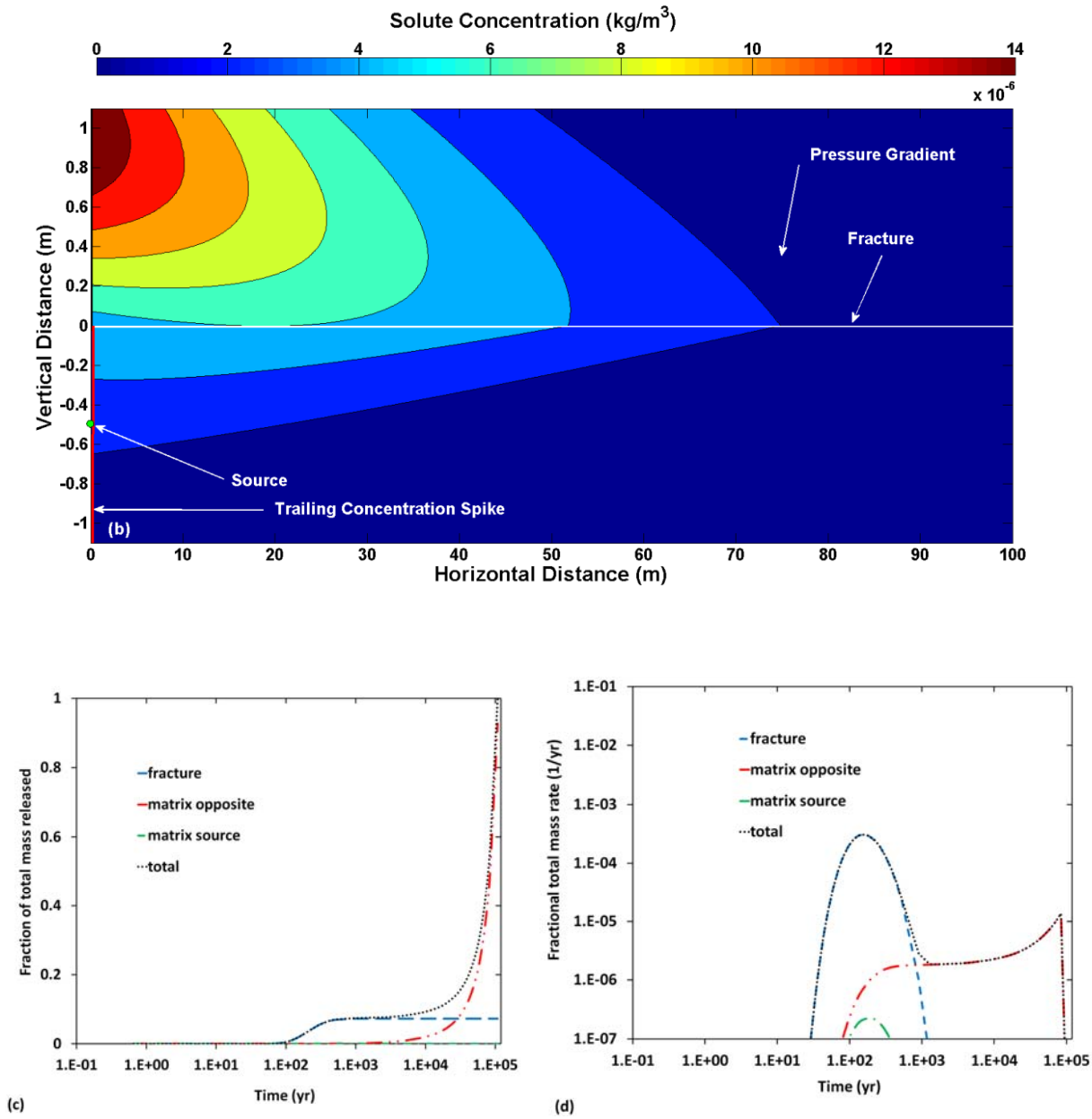

Figure 3-33. Case 6: Same as Case 3 but with source located in matrix 0.5 m from fracture. (a) concentration contours at 2000 days; (b) concentration contours at 40,000 days; (c) cumulative mass arrivals at 100 m; (d) mass arrival rates at 100 m.

3.5.5 Longitudinal diffusion and dispersion

Analytical models of advective-dispersive transport in a fracture with diffusive exchange with a porous matrix have been given by Tang et al. (1981), Sudicky and Frind (1982), and Maloszewski and Zuber (1985, 1990). However, these models did not include advective transport in the matrix or longitudinal diffusion in the matrix. For the purposes of the following analysis, diffusion in the matrix will be assumed

to dominate dispersive effects, so that diffusive transport is approximately isotropic. This condition is expected when advective velocities in the matrix are sufficiently small (Bear, 1972). Under certain conditions, these restrictions may be relaxed; this will be discussed following the results for the restricted case below.

Consider a simple case in which fracture and matrix longitudinal and transverse velocities are the same, v_z and v_x, respectively, and isotropic diffusion with an apparent diffusion coefficient of D^*. The release of an instantaneous point source of solute, mass M_0, would result in a solute distribution, $\mathbb{C}(z,x,t)$, that can be written down immediately as the product of independent one-dimensional solutions for the x and z directions with constant drifts (Carslaw and Jaeger, 1959, Sections 10.7 and 1.15):

$$\mathrm{C}\left(z,x,t\right)=\frac{M_0}{4\pi D^* t}\exp\left\{-\frac{\left(z-v_z t\right)^2+\left(x-v_x t\right)^2}{4D^* t}\right\}. \tag{3-65}$$

This solution can also be obtained by starting with the solution excluding longitudinal diffusion:

$$c\left(z,x,t\right)=\frac{M_0\delta\left(z-v_z t\right)}{\sqrt{4\pi D^* t}}\exp\left\{-\frac{\left(x-v_x t\right)^2}{4D^* t}\right\}. \tag{3-66}$$

The fundamental solution for longitudinal diffusion from an instantaneous point source is

$$\tilde{c}\left(z,t\right)=\frac{M\left(z,x,t\right)}{\sqrt{4\pi D^* t}}\exp\left(-\frac{z^2}{4D^* t}\right). \tag{3-67}$$

Equation (3-66) may be used as a source term (which is now spatially distributed in the x-direction) for a longitudinal diffusion process given by (3-66). This amounts to freezing advection and lateral diffusion over the time period t to assess solute diffusion in the longitudinal direction. This can be done because diffusion in the longitudinal direction is independent of diffusion in the transverse direction, and independent of advection in both directions. The resulting concentration including longitudinal diffusion takes the form of a superposition integral, involving mass releases at all longitudinal positions according to the spatial distribution of mass at time t, $M\left(z,x,t\right)$:

$$\mathrm{C}\left(z,x,t\right)=\int_{-\infty}^{\infty}\tilde{c}\left(z-z',t\right)dM\left(z',x,t\right). \tag{3-68}$$

Letting $dM\left(z',x,t\right)=c\left(z',x,t\right)dz'$ gives

$$\mathrm{C}\left(z,x,t\right)=\int_{-\infty}^{\infty}c\left(z',x,t\right)\tilde{c}\left(z-z',t\right)dz'=\frac{M_0}{4\pi D^* t}\exp\left\{-\frac{\left(z-v_z t\right)^2+\left(x-v_x t\right)^2}{4D^* t}\right\}, \tag{3-69}$$

which is the same result as in Equation (3-65). The same superposition concept was recognized by Thacker (1976) for incorporating longitudinal dispersion occurring within shear layers into a global transport solution for shear dispersion.

This same procedure for incorporating longitudinal diffusion may be used even if the advective velocity in the z-direction is a function of the transverse position x. It is perhaps simpler to visualize this method by focusing on individual solute molecular paths. For the case with no longitudinal diffusion, a solute molecule drifts in the longitudinal direction according to the local longitudinal velocity and also drifts in the transverse direction by the constant transverse velocity. Transverse movement is also caused by a transverse random walk associated with diffusion. The addition of longitudinal diffusion results in a longitudinal random walk superimposed on the original particle movement, but does not impact the transverse movement of the solute or the distribution of longitudinal flow velocities experienced by the solute. The only effect of longitudinal diffusion is to randomize the longitudinal position of the solute according to the longitudinal diffusive process.

A solution analogous to Equation (3-66) excluding longitudinal diffusion cannot be solved for a case in which the advective velocity in the z-direction is a general function of the transverse position, x. However, the result for c_{mdk} from Section 3.5.3 represents this type of solution for the particular case of a single fracture and matrix involving two longitudinal velocities. Consider again the case in which longitudinal diffusion is the same in the fracture and matrix, and matrix diffusion is isotropic. Since all solute diffuses at the same rate, the solution of the transport problem including longitudinal diffusion is given by

$$\mathrm{C}_{mdk}\left(z,x,t\right)=\int_{v_{mz}t}^{v_f t}\frac{c_{mdk}\left(\frac{z'-v_{mz}t}{\ell},\frac{x}{\ell},\frac{v_f^* t}{\ell}\right)}{\sqrt{4\pi D_m^* t}}\exp\left\{-\frac{\left(z-z'\right)^2}{4D_m^* t}\right\}dz' \quad . \tag{3-70}$$

The limits of integration extend exclusively over the range of longitudinal positions that have non-zero values of solute concentration from the source function. Putting Equation (3-70) into dimensionless form yields

$$\mathrm{C}_{mdk}\left(\xi,\eta,\tau\right)=\int_0^{\tau}c_{mdk}\left(\xi',\eta,\tau\right)\frac{\sqrt{Pe}}{\sqrt{4\pi\tau}}\exp\left\{-\frac{Pe\left(\xi-\xi'\right)^2}{4\tau}\right\}d\xi' \quad . \tag{3-71}$$

This method may be extended to address different rates of diffusion/dispersion in the fracture and matrix. With only two longitudinal velocities, the longitudinal position of the solute defines the amount of time spent in the fracture and matrix, because in the absence of longitudinal dispersion/diffusion, this location is given by

$$v_f t_f + v_{mz}\left(t-t_f\right)=z' \quad , \tag{3-72}$$

where t_f is the time spent in the fracture.

Consider the dispersion/diffusion coefficient for any particular solute particle path starting at $z=0$ and $t=0$ and ending at $z=z'$ in the absence of longitudinal dispersion/diffusion. The dispersion/diffusion coefficient is a function of time that varies in response to solute movement between the fracture and matrix as a result of transverse advection and diffusion Therefore, the longitudinal diffusion/dispersion process is described by

$$\frac{\partial \tilde{c}}{\partial t} = D^*\left(t;z'\right)\frac{\partial^2 \tilde{c}}{\partial z^2} \quad . \tag{3-73}$$

This equation has the following fundamental solution:

$$\tilde{c}\left(z,t;z'\right) = \frac{1}{\sqrt{4\pi \overline{D^*}\left(t,z'\right)t}}\exp\left\{-\frac{z^2}{4\overline{D^*}\left(t,z'\right)t}\right\} \quad , \tag{3-74}$$

where the time-averaged longitudinal diffusion/dispersion coefficient is

$$\overline{D^*}\left(t;z'\right) = \frac{1}{t}\left\{D_f^* t_f + D_m^*\left(t - t_f\right)\right\} \quad . \tag{3-75}$$

and D_f^* is the longitudinal dispersion coefficient for the fracture divided the fracture retardation factor. Using Equation (3-72) to solve fort_f, the time-averaged longitudinal diffusion/dispersion coefficient in (3-74) can be put in dimensionless form:

$$\overline{D_r^*}\left(\tau;\xi'\right) = 1 + \left(D_{fm}^* - 1\right)\frac{\xi'}{\tau} \quad , \tag{3-76}$$

where $\overline{D_r^*} = \overline{D^*} / D_m^*$ and $D_{fm}^* = D_f^* / D_m^*$. The fact that solute concentrations for ξ' near τ tend to zero as $\tau \to \infty$ in Equations (3-63) and (3-64) means that the effects of longitudinal dispersion in the fracture tend to diminish at longer times. This is a reflection of the fact that solute spreading into the matrix leads to a decreasing level of solute interaction with the fracture over time. The solute concentration including variable diffusion and dispersion between matrix and fracture is

$$\mathrm{C}_{mdk}\left(z,x,t\right) = \int_{v_{mz}t}^{v_f t} \frac{c_{mdk}\left(\frac{z' - v_{mz}t}{\ell}, \frac{x}{\ell}, \frac{v_f^* t}{\ell}\right)}{\sqrt{4\pi \overline{D^*}\left(t;z'\right)t}}\exp\left\{-\frac{\left(z - z'\right)^2}{4\overline{D^*}\left(t;z'\right)t}\right\}dz' \quad , \tag{3-77}$$

or, in dimensionless form,

$$\mathrm{C}_{mdk}\left(\xi,\eta,\tau\right) = \int_0^{\tau} c_{mdk}\left(\xi',\eta,\tau\right)\frac{\sqrt{Pe}}{\sqrt{4\pi \overline{D_r^*}\left(\tau;\xi'\right)\tau}}\exp\left\{-\frac{Pe\left(\xi - \xi'\right)^2}{4\overline{D_r^*}\left(\tau;\xi'\right)\tau}\right\}d\xi' \quad . \tag{3-78}$$

This result has been derived for isotropic diffusion in the matrix. If the material is inherently anisotropic or if flow rates are sufficiently large to result in matrix dispersion, the diffusion or dispersion process will be anisotropic. If a principal axis of the material anisotropy or the overall matrix flow direction is parallel (or orthogonal) to the fracture, then the principal axes for the dispersion or diffusion processes are also in these directions. For these situations, longitudinal and transverse dispersion are independent processes and can be incorporated into the transport solution in the same way. The system analyzed by Roubinet et al. (2012) also had one of the principal axes of the diffusion process line up in the longitudinal (fracture) direction, with the other principal axis lining up in the orthogonal (transverse) direction. The case of a

general orientation of the principal axes relative to the fracture results in transverse and longitudinal matrix diffusion/dispersion processes that are not independent; therefore, the superposition method presented here for incorporating longitudinal diffusion and dispersion is not applicable.

Equation (3-78) was used to solve a problem that could be compared with an existing solution by Tang et al. (1981) that includes longitudinal dispersion in the fracture. The problem includes advection and dispersion in the fracture and lateral diffusion in the rock matrix, but does not include advection or longitudinal diffusion in the matrix. The assumption that solute is well-mixed in the fracture cross section is also used. The Tang et al. (1981) solution was derived by directly solving the differential equations including longitudinal dispersion in the fracture. The problem solved by Tang et al. (1981) has a fixed concentration in the fracture at $z = 0$ for $t > 0$ and an initial concentration of zero in the fracture and matrix for $z > 0$. An equivalent initial value problem was constructed using a finite series of instantaneous point sources evenly spaced in the fracture along the negative z -axis. The concentration evolution from each point source is given by Equation (3-78). These concentrations are then linearly superimposed (summed) to generate the overall solution. The parameters of the problem are given in Figure 3-34. For these parameters, 150 instantaneous point sources, spaced 0.5 m starting at $z = -0.5$ m, were found to provide sufficient accuracy. The mass released at each source was determined by adjusting the 150 source masses such that the concentrations at $z = 0$ remained close to a constant value, c_0, for 2000 evenly spaced times over a 5-day period. This resulted in a root-mean square difference of 0.0035 between the 2000 computed relative concentrations, c / c_0, at $z = 0$ and the target value of 1. Figure 3-34 shows the comparison of fracture concentrations computed using solutions based on Tang et al. (1981), both including longitudinal dispersion in the fracture and without longitudinal dispersion ($D_f = 0$), and the superposition of solutions including longitudinal dispersion based on Equation (3-78). The solution without longitudinal dispersion is included in the figure to show the effects of longitudinal dispersion on the solution. These comparisons show that the effects of longitudinal dispersion in this case are significant, and that the proposed method for introducing longitudinal dispersion into the solution matches the Tang et al. (1981) solution.

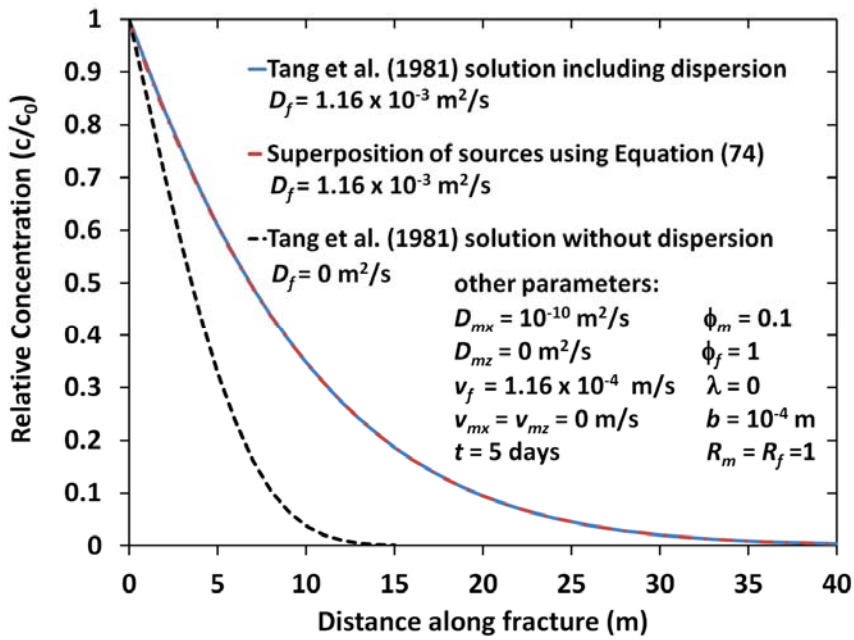

Figure 3-34. Exact solution including longitudinal dispersion for fracture concentration from Tang et al. (1981) compared with the superposition of instantaneous point-source solutions using Equation (3-78); Tang et al. (1981) solution without dispersion is also shown.

The formulation for cumulative-mass arrivals including longitudinal dispersion/diffusion is given in Section 3.5.8.3.

3.5.6 Solution behavior including longitudinal diffusion/dispersion

An estimate of longitudinal dispersion within a fracture for the configuration in this model may be derived from the method for analyzing shear dispersion developed by Taylor (1953, 1954) and Aris (1956). The result for the asymptotic shear dispersion coefficient for solute transport between parallel plates is (Wooding, 1960)

$$D_f^* = D_{f0}^* + \frac{1}{210}\frac{v_f^2 b^2}{D_{f0}^*}, \tag{3-79}$$

where D_{f0}^* is the molecular diffusion coefficient in the fracture divided by the fracture retardation factor. Assuming $D_{f0}^* = D_m^*$, and using values for the parameters from Case 1 discussed in Section 3.5.4, gives $D_f^* = 6.5\times10^{-9}$ m^2/s, which is less than two orders of magnitude larger than the molecular diffusion coefficient, $D_m^* =$ 10^{-10} m^2/s. Zhou et al. (2007) evaluated dispersion data from field-test results for both fracture networks and single fractures. Results on solute transport and dispersion for six single-fracture tests were documented. Their findings indicated that dispersion in a real (single) fracture is typically more

than two orders of magnitude larger than for flow between parallel plates. This is believed to be a result of fracture surface roughness and spatial heterogeneity of the fracture aperture. The tests for single fractures were found to have dispersivities ranging from 0.18 m to 2.4 m and dispersion coefficients ranging from 2 × 10^{-5} m^2/s to 8 × 10^{-4} m^2/s. We span this range by computing low, moderate and high dispersion cases as shown in Table 3-6. The two highest dispersion coefficients were selected such that fracture dispersivities (the ratio of the fracture dispersion coefficient to the fracture velocity) have values of 1 and 10 m, respectively. As will be seen, the higher levels of the dispersion coefficient are needed to show the effects of fracture dispersion in the results. Other parameters used for these calculations are given in Tables 3-4 and 3-5. Note that sorption $(K_{df}$ and $K_{dm})$ coefficients and the decay constant (λ) are zero.

Table 3-6. Fracture longitudinal dispersion coefficients

Case	7 and 10	8 and 11	9 and 12
Fracture longitudinal dispersion coefficient (m^2/s)	7×10^{-8}	1.16×10^{-4}	1.16×10^{-3}

Note: A longitudinal matrix diffusion coefficient of 10^{-10} m^2/s is used for cases 7 through 12. All other parameters for cases 7 through 9 are the same as for case 1 and cases 10 through 12 have the same parameters as case 4. See Tables 3-4 and 3-5.

Solutions including longitudinal dispersion in the fracture and longitudinal diffusion in the matrix are shown in Figures 3-35 and 3-36. Cases 7, 8, and 9 are shown in Figure 3-35 and are equivalent to Case 1, but now include varying levels of longitudinal dispersion in the fracture and a fixed level of longitudinal diffusion in the matrix (10^{-10} m^2/s). Some additional longitudinal spreading can be seen in the profile in Figure 3-35(a), also at 200 days, as compared with Figure 3-28(a). At higher levels of longitudinal dispersion in the fracture in Figures 3-35(b) and 3-35(c), the effects of dispersion on the concentration contours becomes more noticeable, and increased levels of solute movement upstream of the release point are also observed. While solute diffusion upstream of the release point can occur as a result of molecular diffusion, its enhancement as a result of higher levels of longitudinal dispersion is not physical. This occurs because longitudinal dispersion in the fracture is represented as a Fickian process, which is an approximation that becomes valid at long times. The fracture concentration profiles in Figure 3-35(d) show the similarity of the concentrations for no dispersion (Case 1) and low dispersion (Case 7), but deviates perceptibly for the moderate dispersion case (Case 8) and significantly for the high-dispersion (Case 9).

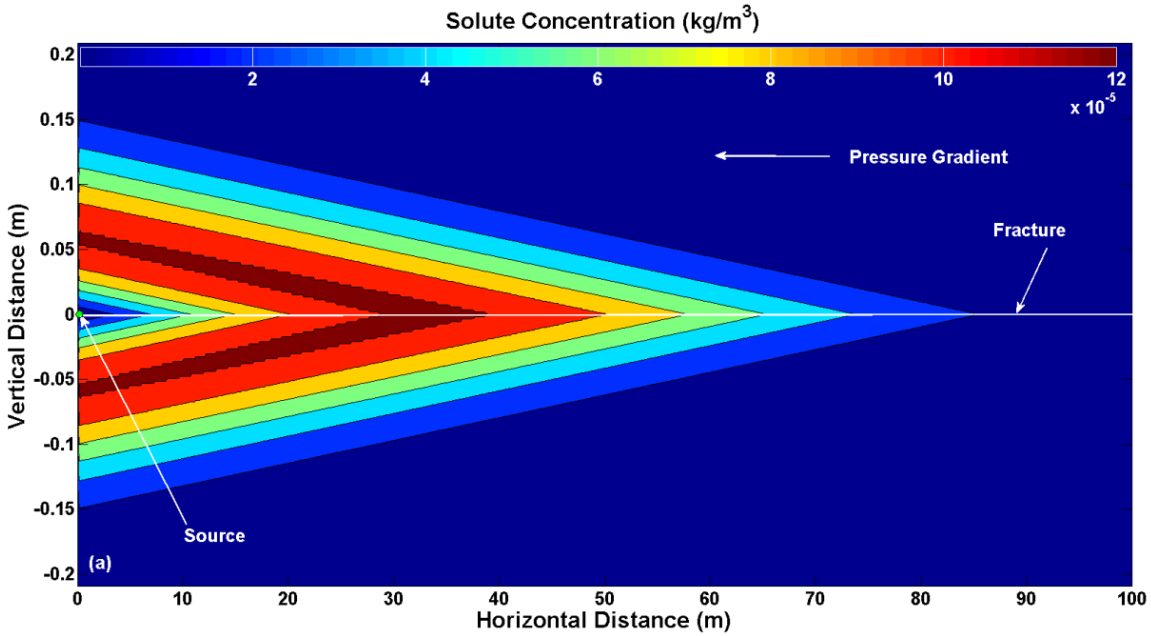
Solute Concentration (kg/m3)
2
4
6
8
10
12
x 10-5
Pressure Gradient
Fracture
Source
(a)
Vertical Distance (m)
Horizontal Distance (m)
0.2
0.15
0.1
0.05
0
-0.05
-0.1
-0.15
-0.2
0
10
20
30
40
50
60
70
80
90
100

(a)

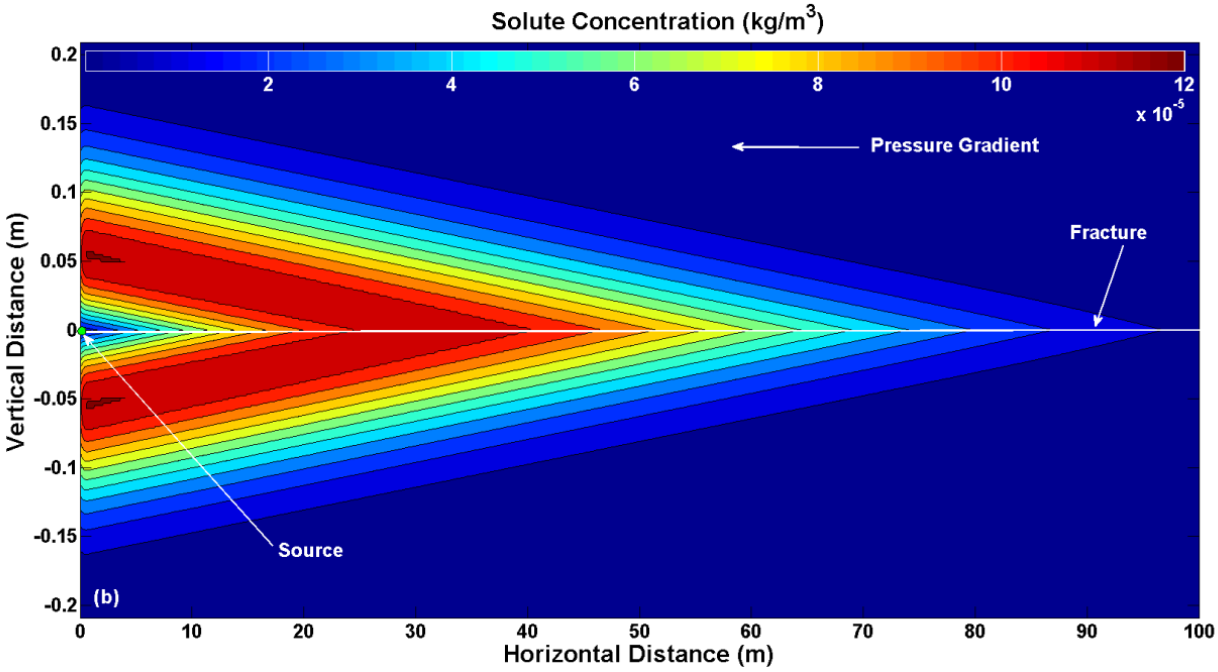
Solute Concentration (kg/m3)
2
4
6
8
10
12
x 10-5
Pressure Gradient
Fracture
Source
(b)
Vertical Distance (m)
Horizontal Distance (m)
0.2
0.15
0.1
0.05
0
-0.05
-0.1
-0.15
-0.2
0
10
20
30
40
50
60
70
80
90
100

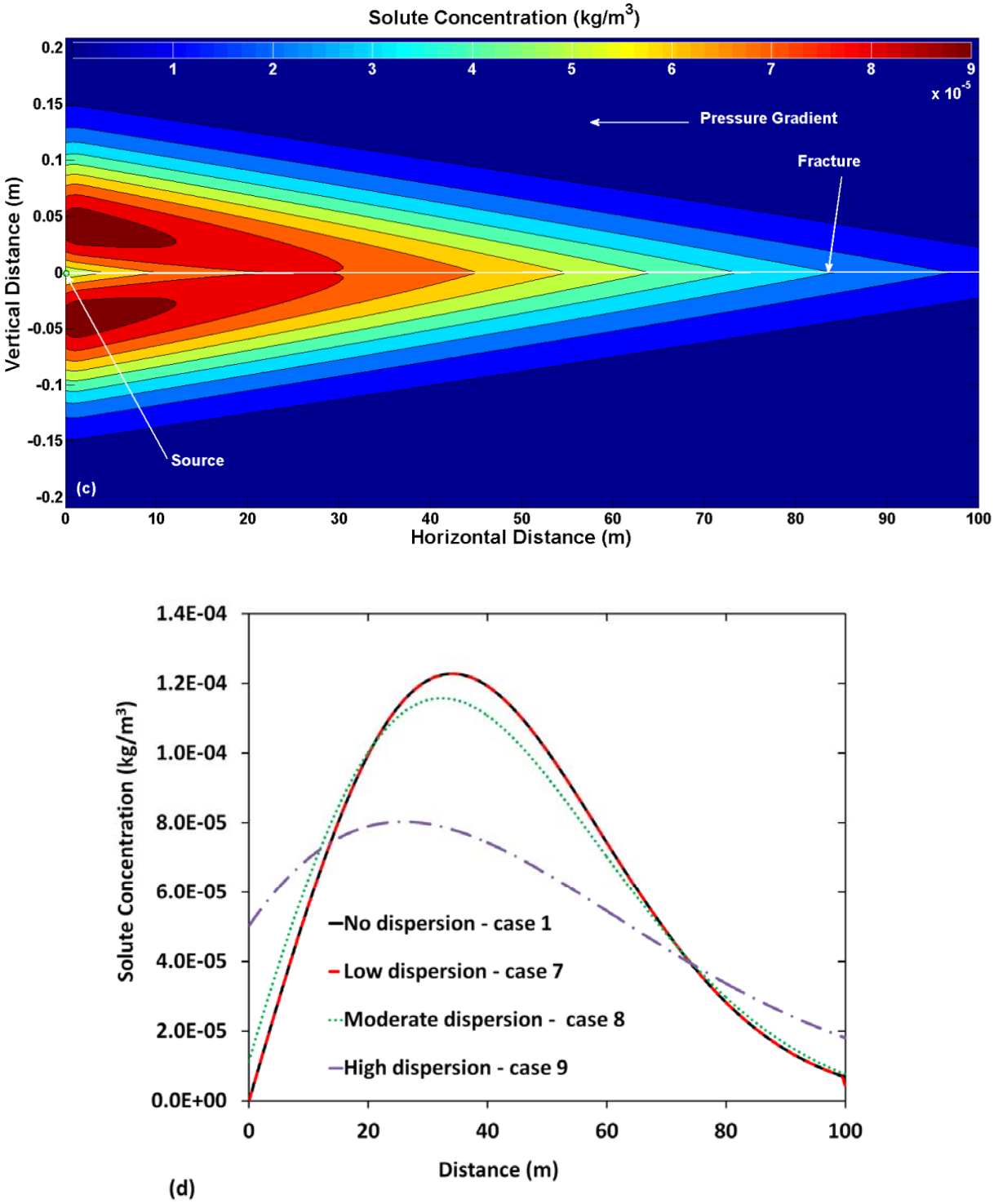

Figure 3-35. Cases 7, 8, and 9: Concentration contours at 200 days using Case 1 parameters but with a matrix longitudinal diffusion coefficient of 10^{-10} m^2/s and fracture longitudinal dispersion coefficient of (a) 7×10^{-8} m^2/s ; (b)1.16×10^{-4} m^2/s; (c) 1.16×10^{-3} m^2/s; (d) centerline concentration profiles for cases 1, 7, 8, and 9.

Cases 10, 11 and 12 shown in Figure 3-36 are for a matrix-release initial conditions and are the same as that shown in Case 4, except here, varying levels of longitudinal dispersion in the fracture and a fixed level of longitudinal diffusion in the matrix are included (10^{-10} m^2/s). Longitudinal diffusion in the matrix helps to reveal the behavior of solute that is in the matrix prior to interaction with the fracture. Most of the solute released has not interacted with the fracture, so the concentration profile in the matrix follows a fairly simple advection-diffusion pattern. The differences in concentration contours caused by changes in fracture dispersion coefficient are difficult to distinguish; therefore, only the contours for the low-dispersion case are shown in Figure 3-36(a) and an expanded view in Figure 3-36(b) near the source for 2000 days. As in Figure 3-35(d), the centerline profile in Figure 3-36(c) shows virtually no difference between the no-dispersion (Case 4) and low dispersion (Case 10), and only a modest difference for the moderate dispersion case (Case 11), but a noticeable change for the high-dispersion (Case 12).

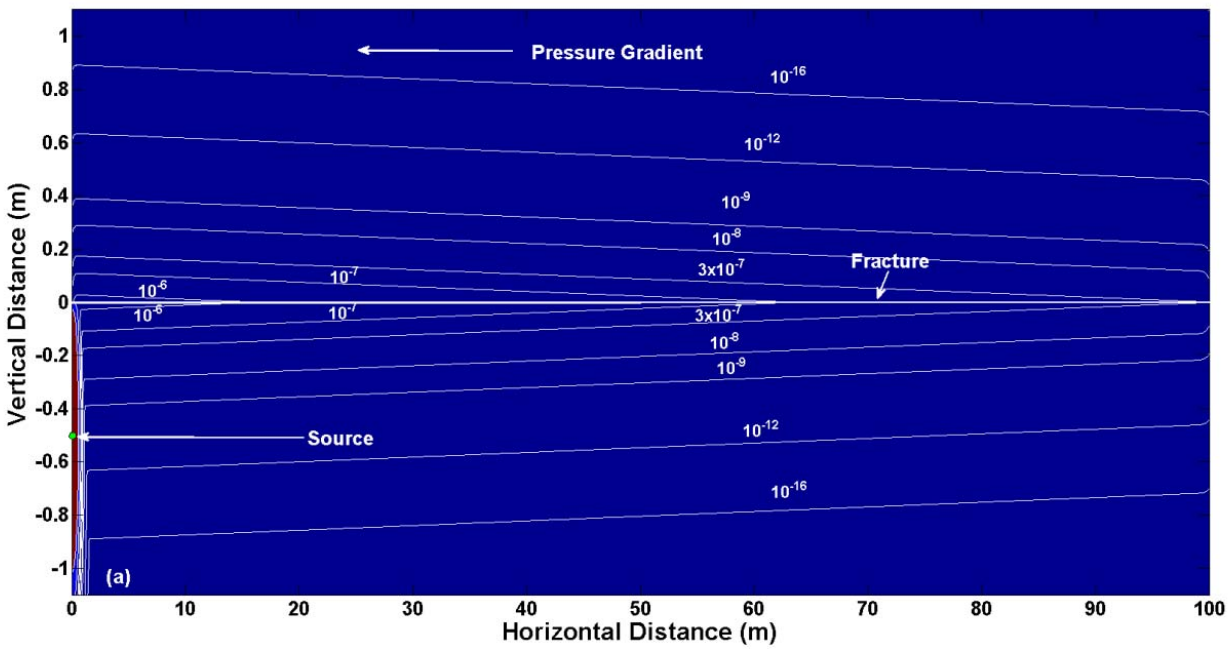

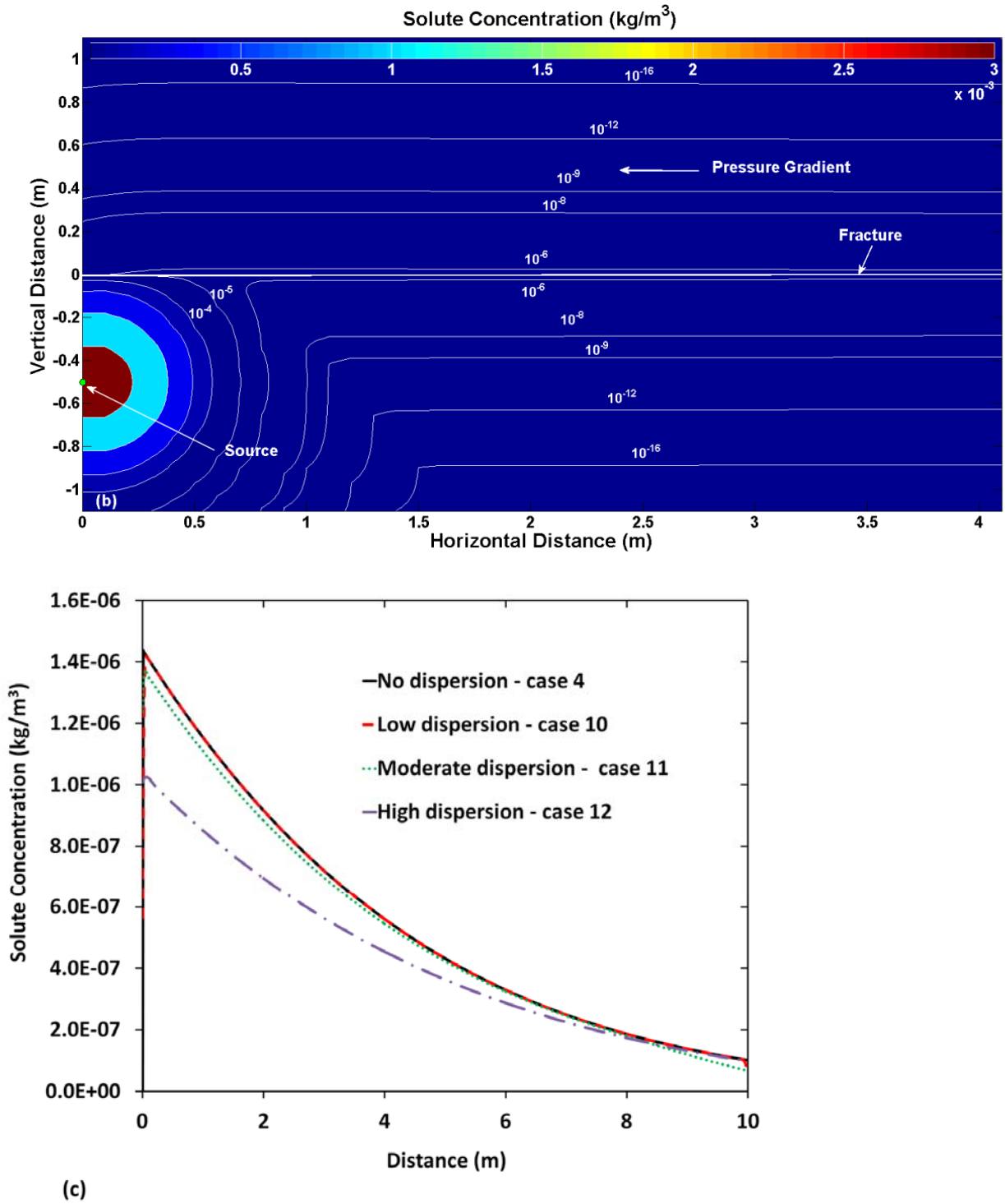

Figure 3-36. Case 10: Concentration contours at 2000 days using Case 4 parameters but with a matrix longitudinal diffusion coefficient of 10^{-10} m^2/s and fracture longitudinal dispersion coefficient of 7×10^{-8} m^2/s, (a) full-scale version; contour lines are marked with concentrations in kg/m^3; (b) detail of contours near the source; (c) centerline concentration profiles for cases 4, 10, 11, and 12.

For solute release in the matrix, solute that has not interacted with the fracture remains at $\xi = 0$ (the solute release location in a coordinate system moving at the matrix longitudinal velocity) unless longitudinal diffusion is included. Roubinet et al. (2012) have shown that at low Peclet numbers, longitudinal diffusion in the matrix can have a significant effect on solute transport through the fracture. For solute that has interacted with the fracture, differential advection caused by fracture-matrix interaction can overshadow other dispersion/diffusion processes, as shown here for the low fracture-dispersion case based on parallel-plate fracture geometry. Higher levels of longitudinal dispersion associated with natural fractures can lead to a more significant impact on the overall dispersion.

3.5.7 Evaluation of longitudinal diffusion and dispersion

To determine an approximate criterion for when longitudinal dispersion in the fracture becomes important for the overall transport process, we first compute the integral of the concentrations in Equations (3-63) and (3-63) over the transverse coordinate, which gives, respectively,

$$\int_0^\infty c_{mdo}(\xi,\eta,\tau)\,d\eta = \bar{c}_{mdo}(\xi,\tau) =$$

$$\frac{H(\tau-\xi)H(\xi)}{2\sqrt{\pi}\sqrt{Pe}\sqrt{\tau-\xi}}\exp\left(-\frac{PeV_o\eta_0}{2}\right)\exp\left[-\frac{(\xi+Pe\eta_0)^2+Pe^2V^2(\tau-\xi)^2}{4Pe(\tau-\xi)}\right]$$

$$-H(\tau-\xi)H(\xi)\frac{V_o}{4}\exp\left(\frac{V_o\xi}{2}\right)\operatorname{erfc}\left[\frac{\xi+Pe\eta_0+PeV_o(\tau-\xi)}{2\sqrt{Pe}\sqrt{\tau-\xi}}\right] \tag{3-80}$$

$$\int_0^\infty c_{mds}(\xi,\eta,\tau)\,d\eta = \bar{c}_{mds}(\xi,\tau) =$$

$$\frac{H(\tau-\xi)H(\xi)}{2\sqrt{\pi}\sqrt{Pe}\sqrt{\tau-\xi}}\exp\left(\frac{PeV_s\eta_0}{2}\right)\exp\left(-\frac{(\xi+Pe\eta_0)^2+Pe^2V^2(\tau-\xi)^2}{4Pe(\tau-\xi)}\right)$$

$$-H(\tau-\xi)H(\xi)\frac{V_s}{4}\exp\left(\frac{V_s\xi}{2}\right)\exp(PeV_s\eta_0)\operatorname{erfc}\left[\frac{\xi+Pe\eta_0+PeV_s(\tau-\xi)}{2\sqrt{Pe}\sqrt{\tau-\xi}}\right], \tag{3-81}$$

where the trailing spike on the source side is not included because this solute has not interacted with the fracture and is not dispersed longitudinally.

Equations (3-80) and (3-81) are still complex, mainly as a result of the effects of cross-flow and source offset from the fracture. These factors affect the amount of spreading caused by fracture-matrix interaction, and they also have a similar affect on the amount of spreading caused by longitudinal dispersion in the fracture, because both are impacted mainly by the same delay in solute interaction with the fracture imposed by these conditions. Therefore, longitudinal spreading is evaluated for the simpler case with $\eta_0 = V_s = V_o = 0$. Then,

$$\overline{c}_{mdo}(\xi,\tau)=\overline{c}_{mds}(\xi,\tau)=\frac{H(\tau-\xi)H(\xi)}{2\sqrt{\pi}\sqrt{Pe}\sqrt{\tau-\xi}}\exp\left(-\frac{\xi^2}{4Pe(\tau-\xi)}\right). \tag{3-82}$$

As τ increases, most of the solute mass lies at longitudinal positions where $\xi \ll \tau$, suggesting that $(\tau-\xi)\approx\tau$ giving

$$\overline{c}_{mdo}(\xi,\tau)=\overline{c}_{mds}(\xi,\tau)=\frac{H(\tau-\xi)H(\xi)}{2\sqrt{\pi}\sqrt{Pe}\sqrt{\tau}}\exp\left(-\frac{\xi^2}{4Pe\tau}\right). \tag{3-83}$$

This shows that the form of the integrated solution is like diffusion from an instantaneous point source that originated at $\xi=0$, but the solution is truncated at $\xi=0$ and $\xi=\tau$. The standard deviation of the distribution as a dimensional quantity, not accounting for the truncation, is $\sqrt{2Pe\tau\ell^2}$. The truncation essentially represents a half-space over which the spreading occurs, because the boundary at $\xi=\tau$ is relatively far removed from the main solute mass. As a result, one-half of the standard deviation may be considered a length scale for the degree of longitudinal spreading induced by fracture-matrix interaction, which is, as a dimensional quantity,

$$S_{fm}\sim\frac{1}{2}\sqrt{2Pe\tau\ell^2}. \tag{3-84}$$

The spreading caused by longitudinal diffusion/dispersion is given by $\sqrt{2\overline{\overline{D^*}}t}$, where $\overline{\overline{D^*}}$ is the solute-mass weighted average of $\overline{D^*}$:

$$\overline{\overline{D^*}}(\tau)=\int_0^\tau\frac{\overline{D^*}(\tau,\xi)}{2\sqrt{\pi}\sqrt{Pe}\sqrt{\tau}}\exp\left(-\frac{\xi^2}{4Pe\tau}\right)d\xi. \tag{3-85}$$

The solute-mass concentration distribution used for the average in (3-84) is the approximate distribution given by (3-84). Integrating (3-84) using Equation (3-75) for $\overline{D^*}(\tau,\xi)$ gives

$$\overline{\overline{D^*}}(\tau)=\frac{D_m^*}{2}\operatorname{erf}\left(\sqrt{\frac{\tau}{4Pe}}\right)+\frac{D_f^*-D_m^*}{\sqrt{\pi}}\sqrt{\frac{Pe}{\tau}}\left\{1-\exp\left(-\frac{\tau}{4Pe}\right)\right\}. \tag{3-86}$$

The comparable longitudinal spreading caused by dispersion and diffusion is

$$S_{disp-dif}\sim\sqrt{2\overline{\overline{D^*}}(\tau)t} \tag{3-87}$$

Therefore, an approximate criterion for when longitudinal diffusion and dispersion in the fracture and matrix are small relative to spreading caused by fracture-matrix differential advection is when S_{fm} in (80) is large compared with $S_{disp-dif}$ in (3-86). Using Equations (3-84), (3-86), and (3-87), and stipulating that $S_{disp-dif}<S_{fm}$, gives:

$$\beta\sqrt{D_m^*\mathrm{erf}\left(\sqrt{\frac{\tau}{4Pe}}\right)t+\frac{2\left(D_f^*-D_m^*\right)t}{\sqrt{\pi}}\sqrt{\frac{Pe}{\tau}}\left\{1-\exp\left(-\frac{\tau}{4Pe}\right)\right\}}<\frac{1}{2}\sqrt{2Pe\tau\ell^2}\,, \tag{3-88}$$

where β is a factor to be determined.

Putting Equation (3-88) entirely in terms of non-dimensional variables gives

$$\Omega=\frac{2\beta^2}{Pe^2}\left[\mathrm{erf}\left(\sqrt{\frac{\tau}{4Pe}}\right)+\frac{D_{fm}^*-1}{\sqrt{\pi}}\sqrt{\frac{4Pe}{\tau}}\left\{1-\exp\left(-\frac{\tau}{4Pe}\right)\right\}\right]<1\,. \tag{3-89}$$

Equation (3-89) indicates that fracture-matrix interaction dominates longitudinal spreading if $\Omega<1$. The value of Ω is strongly influenced by the Peclet number and the ratio of the fracture longitudinal dispersion coefficient to the matrix diffusion coefficient, with somewhat weaker dependence on time. The value of β represents the ratio of longitudinal spreading length scales associated with fracture-matrix interaction and matrix diffusion/fracture dispersion, such that fracture-matrix interaction dominates longitudinal spreading. Conceptually, this is expected to be greater than 1 but probably less than 10; therefore, β is assigned a value of 3. With this choice, the values of Ω are 0.0014, 0.86, and 48.4 for the low, moderate and high longitudinal dispersion cases in Figure 3-35(d), respectively. For the low, moderate, and high longitudinal dispersion cases in Figure 3-36(c), Ω is 0.0045, 0.27, and 2.7, respectively. The values of Ω are smaller for corresponding low, moderate, and high dispersion cases in Figure 3-36(c) as compared with 3-35(d), because the value of τ is an order of magnitude larger for Figure 3-36(c) as compared with Figure 3-35(d). These values of Ω indicate that longitudinal dispersion and diffusion should have negligible effects on longitudinal spreading for cases 7 and 10, which use the low longitudinal dispersion coefficient, a minor effect for Case 8, and an even smaller effect for Case 11, both of which use the moderate longitudinal dispersion coefficient; and significant effects for cases 9 and 12, where the high longitudinal dispersion coefficient is used.

Roubinet et al. (2012) investigated the effects of longitudinal diffusion in the matrix on transport for an instantaneous point source and computed three cases for different Peclet numbers. They found that longitudinal matrix diffusion effects are less significant as the Peclet number increases (Roubinet et al., 2012). Application of Equation (3-89) to these cases gives values of Ω of 0.2, 0.8, and 20 for high-, middle-, and low-Peclet-number cases, respectively. These values of Ω are consistent with the responses found by Roubinet et al. (2012, Figure 5), which show almost no effect of longitudinal-matrix diffusion for the high-Peclet-number case, a small but distinct effect for the middle-Peclet-number case, and a significant effect for the low-Peclet-number case.

3.5.8 Results for cumulative arrivals at a downstream location from an instantaneous point source

3.5.8.1 Cumulative arrivals neglecting longitudinal diffusion/dispersion

The results for concentrations obtained in Section 3.5.3 can be integrated at a position downstream along the fracture for cumulative mass arrivals in the fracture, M_f, and on both sides of the matrix, M_k. The procedure for the cumulative mass integration is the same as reported in Houseworth (2006).

The cumulative mass arrival in the fracture at a location z_ℓ along the fracture axis is given by

$$M_f(T) = \int_0^T A_f \phi_f R_f v_f c_f(z_e, t)\, dt \tag{3-90}$$

Putting this into dimensionless form gives

$$\frac{M_f(\psi)}{M_0} = 2\int_0^{\psi} c_{fd}\left(\zeta_e - V_\ell \sigma, (1-V_\ell)\sigma\right) \exp\left(-\lambda_d \sigma\right) d\sigma \tag{3-91}$$

For the cumulative mass solutions, the following additional dimensionless variables are defined: $V_\ell = v_{mz} / v_f$, $\zeta_e = z_e / \ell$, $\lambda_d = \lambda \ell / v_f$, $\psi = v_f T / \ell$, where z_e is the downstream location at which cumulative mass arrivals are computed and T is the time of observation at z_e. The result for cumulative mass arrival in the fracture is:

$$\begin{aligned}
\frac{M_f(\psi)}{M_0} &= \frac{\sqrt{V_\ell^2 + Pe^2 V^2 + 4Pe\lambda_d} + V_\ell}{2\sqrt{V_\ell^2 + Pe^2 V^2 + 4Pe\lambda_d}} \\
&\times \exp\left(\frac{\left\{\zeta_e(1-V_\ell) + Pe\eta_0\right\}\left\{\sqrt{V_\ell^2 + Pe^2 V^2 + 4Pe\lambda_d} + V_\ell\right\} - 2Pe\lambda_d \zeta_e}{2Pe} - \frac{PeV_s\eta_0}{2} \right) \\
&\times \operatorname{erfc}\left(\frac{\left\{\zeta_e(1-V_\ell) + Pe\eta_0\right\}}{2\sqrt{Pe}\sqrt{\psi - \zeta_e}} + \frac{\sqrt{V_\ell^2 + Pe^2 V^2 + 4Pe\lambda_d}\sqrt{\psi - \zeta_e}}{2\sqrt{Pe}} \right) \\
&+ \frac{\sqrt{V_\ell^2 + Pe^2 V^2 + 4Pe\lambda_d} - V_\ell}{2\sqrt{V_\ell^2 + Pe^2 V^2 + 4Pe\lambda_d}} \\
&\times \exp\left(-\frac{\left\{\zeta_e(1-V_\ell) + Pe\eta_0\right\}\left\{\sqrt{V_\ell^2 + Pe^2 V^2 + 4Pe\lambda_d} - V_\ell\right\} + 2Pe\lambda_d \zeta_e}{2Pe} - \frac{PeV_s\eta_0}{2} \right) \\
&\times \operatorname{erfc}\left(\frac{\left\{\zeta_e(1-V_\ell) + Pe\eta_0\right\}}{2\sqrt{Pe}\sqrt{\psi - \zeta_e}} - \frac{\sqrt{V_\ell^2 + Pe^2 V^2 + 4Pe\lambda_d}\sqrt{\psi - \zeta_e}}{2\sqrt{Pe}} \right)
\end{aligned} \tag{3-92}$$

The cumulative mass arrival in the downstream matrix at a boundary passing through z_e on the fracture axis is given by

$$M_{mk}(T)=\int_0^T\int_0^\infty \frac{A_f A_r}{b}\phi_m R_m v_{mz} c_{mk}(z_e,x,t)\,dx\,dt \tag{3-93}$$

Putting this into dimensionless form gives

$$\frac{M_{mk}(\psi)}{M_0}=V_\ell\int_0^\psi\int_0^\infty c_{mdk}\left(\zeta_e-V_\ell\sigma,\eta,(1-V_\ell)\sigma\right)\exp(-\lambda_d\sigma)\,d\eta\,d\sigma \tag{3-94}$$

The result for cumulative mass arrival in matrix on opposite side of fracture from the source release location is:

$$\begin{aligned}
\frac{M_{mo}(\psi)}{M_0}=&\frac{V_\ell V_s}{2(V_sV_\ell+2\lambda_d)}\exp\left(-\frac{(V_sV_\ell+2\lambda_d)(\psi-\zeta_e)-V_s(1-V_\ell)\zeta_e+2\lambda_d\zeta_e}{2}\right)\\
&\times\operatorname{erfc}\left\{\frac{\{\zeta_e(1-V_\ell)+Pe\eta_0\}+(PeV_s-V_\ell)(\psi-\zeta_e)}{2\sqrt{Pe}\sqrt{\psi-\zeta_e}}\right\}\\
&-\left\{\frac{V_\ell V_s(PeV_s-V_\ell)+V_\ell V_s\sqrt{Pe^2V^2+V_\ell^2+4Pe\lambda_d}}{4(V_sV_\ell+2\lambda_d)\sqrt{Pe^2V^2+V_\ell^2+4Pe\lambda_d}}+\frac{V_\ell}{2\sqrt{Pe^2V^2+V_\ell^2+4Pe\lambda_d}}\right\}\\
&\times\exp\left(\frac{\{\zeta_e(1-V_\ell)+Pe\eta_0\}\left\{\sqrt{Pe^2V^2+V_\ell^2+4Pe\lambda_d}+V_\ell\right\}-2Pe\lambda_d\zeta_e}{2Pe}-PeV_s\eta_0\right)\\
&\times\operatorname{erfc}\left(\frac{\{\zeta_e(1-V_\ell)+Pe\eta_0\}+(\psi-\zeta_e)\sqrt{Pe^2V^2+V_\ell^2+4Pe\lambda_d}}{2\sqrt{Pe}\sqrt{\psi-\zeta_e}}\right)\\
&+\left\{\frac{V_\ell V_s(PeV_s-V_\ell)-V_\ell V_s\sqrt{Pe^2V^2+V_\ell^2+4Pe\lambda_d}}{4(V_oV_\ell+2\lambda_d)\sqrt{Pe^2V^2+V_\ell^2+4Pe\lambda_d}}+\frac{V_\ell}{2\sqrt{Pe^2V^2+V_\ell^2+4Pe\lambda_d}}\right\}\\
&\times\exp\left(-\frac{\{\zeta_e(1-V_\ell)+Pe\eta_0\}\left\{\sqrt{Pe^2V^2+V_\ell^2+4Pe\lambda_d}-V_\ell\right\}+2Pe\lambda_d\zeta_e}{2Pe}-PeV_s\eta_0\right)\\
&\times\operatorname{erfc}\left(\frac{\{\zeta_e(1-V_\ell)+Pe\eta_0\}-(\psi-\zeta_e)\sqrt{Pe^2V^2+V_\ell^2+4Pe\lambda_d}}{2\sqrt{Pe}\sqrt{\psi-\zeta_e}}\right)
\end{aligned} \tag{3-95}$$

The cumulative mass arrival in matrix on same side of fracture as the source release location is:

$$
\begin{aligned}
\frac{M_{ms}(\psi)}{M_0} = {} & \frac{V_\ell V_s}{2\left(V_s V_\ell - 2\lambda_d\right)} \exp\left(\frac{\left(V_s V_\ell - 2\lambda_d\right)\left(\psi - \zeta_e\right) - V_s\left(1 - V_\ell\right)\zeta_e - 2PeV_s\eta_0 - 2\lambda_d\zeta_e}{2} \right) \\
& \times \operatorname{erfc}\left\{ \frac{\left\{\zeta_e\left(1 - V_\ell\right) + Pe\eta_0\right\} - \left(PeV + V_\ell\right)\left(\psi - \zeta_e\right)}{2\sqrt{Pe}\sqrt{\psi - \zeta_e}} \right\} \\
& + \left\{ \frac{V_\ell V_s\left(PeV_s + V_\ell\right) - V_\ell V_s\sqrt{Pe^2V^2 + V_\ell^2 + 4Pe\lambda_d}}{4\left(V_s V_\ell - 2\lambda_d\right)\sqrt{Pe^2V^2 + V_\ell^2 + 4Pe\lambda_d}} - \frac{V_\ell}{2\sqrt{Pe^2V^2 + V_\ell^2 + 4Pe\lambda_d}} \right\} \\
& \times \exp\left(\frac{\left\{\zeta_e\left(1 - V_\ell\right) + Pe\eta_0\right\}\left\{\sqrt{Pe^2V^2 + V_\ell^2 + 4Pe\lambda_d} + V_\ell\right\} - 2Pe\lambda_d\zeta_e}{2Pe} - \frac{PeV_s\eta_0}{2} \right) \\
& \times \operatorname{erfc}\left(\frac{\left\{\zeta_e\left(1 - V_\ell\right) + Pe\eta_0\right\} + \left(\psi - \zeta_e\right)\sqrt{Pe^2V^2 + V_\ell^2 + 4Pe\lambda_d}}{2\sqrt{Pe}\sqrt{\psi - \zeta_e}} \right) \\
& - \left\{ \frac{V_\ell V_s\left(PeV_s + V_\ell\right) + V_\ell V_s\sqrt{Pe^2V^2 + V_\ell^2 + 4Pe\lambda_d}}{4\left(V_s V_\ell - 2\lambda_d\right)\sqrt{Pe^2V^2 + V_\ell^2 + 4Pe\lambda_d}} - \frac{V_\ell}{2\sqrt{Pe^2V^2 + V_\ell^2 + 4Pe\lambda_d}} \right\} \\
& \times \exp\left(-\frac{\left\{\zeta_e\left(1 - V_\ell\right) + Pe\eta_0\right\}\left\{\sqrt{Pe^2V^2 + V_\ell^2 + 4Pe\lambda_d} - V_\ell\right\} + 2Pe\lambda_d\zeta_e}{2Pe} - \frac{PeV_s\eta_0}{2} \right) \\
& \times \operatorname{erfc}\left(\frac{\left\{\zeta_e\left(1 - V_\ell\right) + Pe\eta_0\right\} - \left(\psi - \zeta_e\right)\sqrt{Pe^2V^2 + V_\ell^2 + 4Pe\lambda_d}}{2\sqrt{Pe}\sqrt{\psi - \zeta_e}} \right) \\
& + \frac{1}{2} H\left(V_\ell\psi - \zeta_e\right)\left[1 + \operatorname{erf}\left\{ \frac{\sqrt{Pe}\left(\eta_0 + V_s\left(1 - V_\ell\right)\psi\right)}{2\sqrt{\left(1 - V_\ell\right)\psi}} \right\} \right] \\
& - \frac{1}{2} H\left(V_\ell\psi - \zeta_e\right)\exp\left(-PeV_s\eta_0\right)\operatorname{erfc}\left\{ \frac{\sqrt{Pe}\left(\eta_0 - V_s\left(1 - V_\ell\right)\psi\right)}{2\sqrt{\left(1 - V_\ell\right)\psi}} \right\}
\end{aligned}
\tag{3-96}
$$

where the term involving the step function represents the arrival of solute mass in the matrix that did not interact with the fracture.

3.5.8.2 Relationship between the solution for concentration from a constant-rate continuous source and the cumulative mass solution for an instantaneous point source for cases with no longitudinal diffusion or dispersion

The cumulative mass solutions in Section 3.5.8.1 are related to the concentration from a constant-rate continuous source. This is demonstrated here for a source release in the fracture. Starting with Equation (3-90), we assign a Green's function, $g_f\left(z_e,t\right)$, for the fracture cumulative mass equation through the relationship $c_f\left(z_e,t\right)=M_0 g_f\left(z_e,t\right)$, giving

$$\frac{M_f\left(T\right)}{M_0}=A_f\phi_f R_f v_f\int_0^T g_f\left(z_e,t\right)dt \tag{3-97}$$

The concentration from a continuous source solution for a boundary concentration of c_0 can be written as a superposition integral for a constant-rate mass release $\dot{M}$ at the origin,

$$c_f=\dot{M}\int_0^T g_f\left(z_e,T-\sigma\right)d\sigma=\dot{M}\int_0^T g_f\left(z_e,t\right)dt \tag{3-98}$$

The mass release rate equals the advective mass flux at a concentration of c_0:

$$\dot{M}=A_f\phi_f R_f v_f c_0 \tag{3-99}$$

Therefore,

$$\frac{c_f}{c_0}=\frac{M_f\left(T\right)}{M_0}=A_f\phi_f R_f v_f\int_0^T g_f\left(z_e,\tau\right)d\tau \tag{3-100}$$

Based on Equation (3-100), when $V_\ell=V=\eta_0=0$, Equation (3-92) reduces to Tang et al. (1981, Equation (42)) for concentration in the fracture from a continuous source.

For the matrix, we assign a Green's function $c_{mk}\left(z_e,x,t\right)=M_0 g_m\left(z_e,x,t\right)$ and use it in Equation (3-93) to yield,

$$\frac{M_{mk}\left(T\right)}{M_0}=\int_0^T\int_0^\infty\frac{A_f}{b}\phi_m R_m v_{mz} g\left(z_e,x,t\right)dxdt \tag{3-101}$$

Simplifying Equation (3-101) gives

$$\frac{2\ell M_{mk}\left(T\right)}{M_0 V_\ell}=A_f\phi_f R_f v_f\int_0^T\int_0^\infty g\left(z_e,x,t\right)dxdt \tag{3-102}$$

As for the fracture, the continuous source solution at a concentration of c_0 can be written as a superposition integral for a constant-rate mass release $\dot{M}$ at the origin:

$$\int_0^\infty c_m dx = \dot{M}\int_0^T\int_0^\infty g_m\left(z_e, x, T-\sigma\right) dx d\sigma = \dot{M}\int_0^T\int_0^\infty g_m\left(z_e, x, t\right) dx dt \tag{3-103}$$

Using (3-98) for $\dot{M}$ gives

$$\int_0^\infty \frac{c_m}{c_0} dx = \frac{2\ell M_{mk}\left(T\right)}{M_0 V_\ell} = A_f \phi_f R_f v_f \int_0^T\int_0^\infty g_m\left(z_e, x, t\right) dx dt \tag{3-104}$$

Based on Equation (3-104), when $V_\ell = V_s = \eta_0 = 0$, the expression for $2\ell M_{mk}\left(T\right)/\left(M_0 V_\ell\right)$ using Equations (3-95) or (3-96) gives the same result as found when the solution given by Tang et al. (1981, Equation (44)) is integrated over the lateral direction (x) from b to ∞. Note that for Tang et al. (1981), the integral of c_m / c_0 goes from b to ∞ (in the notation of Tang et al. (1981)) rather than from 0 to ∞, because the origin for the transverse coordinate is at the center of the fracture. Also, b in Tang et al. (1981) notation is the fracture half-aperture; in this paper, b is the fracture aperture.

3.5.8.3 Cumulative arrivals including longitudinal diffusion/dispersion

Cumulative arrivals at a downstream location including dispersion/diffusion result from advective and diffusive/dispersive transport. Therefore, Equations (3-90) and (3-93) must be modified as follows:

$$M_f\left(T\right) = \int_0^T A_f \phi_f R_f v_f \mathrm{C}_{mk}\left(z_e, 0, t\right) dt + \int_0^T A_f \phi_f R_f D_f^* \left.\frac{\partial \mathrm{C}_{mk}\left(z, 0, t\right)}{\partial z}\right|_{z_e} dt \tag{3-105}$$

$$M_{mk}\left(T\right) = \int_0^T\int_0^\infty \frac{A_f A_r}{b} \phi_m R_m v_{mz} \mathrm{C}_{mk}\left(z_e, x, t\right) dx dt + \int_0^T\int_0^\infty \frac{A_f A_r}{b} \phi_m R_m D_m^* \left.\frac{\partial \mathrm{C}_{mk}\left(z, x, t\right)}{\partial z}\right|_{z_e} dx dt. \tag{3-106}$$

where $\mathrm{C}_{mk}\left(z, x, t\right)$ is the dimensional form of concentration corresponding to Equation (3-77), accounting for longitudinal dispersion in the fracture and longitudinal diffusion in the matrix.

The first terms in Equations (3-105) and (3-106) account for longitudinal advective transport; the second terms are for longitudinal dispersive and diffusive transport. These may be put into dimensionless form:

$$\frac{M_f\left(\psi\right)}{M_0} = \sqrt{\frac{Pe}{\pi}} \int_0^\psi \exp\left(-\lambda_d \sigma\right) \int_{V_\ell \sigma}^{\sigma} \left\{ \frac{D_{fm}^*\left(\zeta' - V_\ell \sigma\right) + \left(\sigma - \zeta'\right) + D_{fm}^*\left(\frac{1-V_\ell}{2}\right)\left(\zeta_e - \zeta'\right)}{\left\{D_{fm}^*\left(\zeta' - V_\ell \sigma\right) + \left(\sigma - \zeta'\right)\right\}^{3/2}} \right\}$$

$$\times \exp\left\{-\frac{Pe\left(\zeta_e-\zeta'\right)^2}{4D_{fm}^*\left(\zeta'-V_\ell\sigma\right)+4\left(\sigma-\zeta'\right)}\right\}c_{mdk}\left(\zeta'-V_\ell\sigma,0,\left(1-V_\ell\right)\sigma\right)d\zeta' d\sigma \tag{3-107}$$

$$\frac{M_{mk}\left(\psi\right)}{M_0}=\frac{V_\ell}{2}\sqrt{\frac{Pe}{\pi}}\int_0^\psi \exp\left(-\lambda_d\sigma\right)\int_{V_\ell\sigma}^{\sigma}\frac{D_{fm}^*\left(\zeta'-V_\ell\sigma\right)+\left(\sigma-\zeta'\right)+\left(\frac{1-V_\ell}{2V_\ell}\right)\left(\zeta_e-\zeta'\right)}{\left\{D_{fm}^*\left(\zeta'-V_\ell\sigma\right)+\left(\sigma-\zeta'\right)\right\}^{3/2}}$$

$$\times \exp\left\{-\frac{Pe\left(\zeta_e-\zeta'\right)^2}{4D_{fm}^*\left(\zeta'-V_\ell\sigma\right)+4\left(\sigma-\zeta'\right)}\right\}\left\{\int_0^\infty c_{mdk}\left(\zeta'-V_\ell\sigma,\eta,\left(1-V_\ell\right)\sigma\right)d\eta\right\}d\zeta' d\sigma \tag{3-108}$$

The integral over η in the matrix cumulative-mass-arrival formula can be reduced analytically, but is left here in the integral form.

3.6 A Potential Approach to Compute Fracture-Matrix Interaction for Solute Transport in a Discrete Fracture Models

An important computational issue for transport in discrete fracture models with a porous, permeable rock matrix is the representation of fracture-matrix interaction. As mentioned in the previous section, extremely fine gridding in the matrix next to the fracture is needed for any transient solute transport problem to appropriately account for fracture-matrix solute exchange. A similar problem is encountered for the calculation of transient flow in a fracture-matrix system in terms of fracture-matrix exchange of water (Zimmerman et al., 1993). The fine gridding is needed to resolve steep gradients in solute concentration in the matrix orthogonal to the fracture as solute initially penetrates along fractures and moves into the matrix by diffusion and perhaps advection. Fine gridding represents two impediments to computational efficiency for TOUGH-RBSN. First, the number of grid cells becomes large for systems having large numbers of fractures. Second, the TOUGH-RBSN model is based on a Voronoi gridding scheme that would, in principal, require extensive regridding during a calculation to incorporate fine matrix grids near fractures formed during the computation.

Analytical modeling tools have been investigated to help facilitate fracture-matrix interaction in numerical discrete fracture models (e.g., Painter et al., 2008). However, such methods have not addressed full communication of fracture-matrix interaction accounting for a general fracture network. These previous studies have focused on situations in which fracture spacing is effectively infinite or in which some type of geometrical symmetry is assumed between interacting fractures, such as equal solute concentrations advancing in parallel fractures. However, transport pathways that include solute movement through matrix between fractures for arbitrary fracture network geometry may be important for poorly connected fracture networks.

3.6.1 Concept for fracture-matrix interaction

Divide the matrix block adjacent to a fracture into two storage compartments. These are a globally-interacting compartment (GIC) that communicates with other grid cells except for the fracture, and a locally-interacting compartment (LIC) that takes care of fracture-matrix exchange. The LIC exchanges solute with the fracture and the GIC. The LIC is a one-dimensional system accounting for fracture-matrix exchange by diffusion (and perhaps also advection) and works between two concentration reservoirs: the local fracture and the GIC. The transport in the LIC is solved analytically for each time step, assuming

fixed concentrations over the time step in the fracture and the GIC. There is also a spatial distribution of concentration within each LIC that is solved analytically and independent of the global numerical solution. This provides an initial condition to run the analytical solution as the fracture and GIC reservoir concentrations change. At each time step, fluxes between the fracture and the LIC as well as between the LIC and the GIC are computed. In addition, the LIC spatial distribution of concentration is updated. Then the numerical model updates the fracture and GIC concentrations accounting for global solute exchange. The LIC is then ready to compute a new time step using the updated boundary concentrations and solute concentration profile within the LIC.

3.6.2 Partial demonstration of the approach

As a partial demonstration of the approach, assume fracture-matrix interaction is exclusively a result of diffusive transport (no advective transport).

$$\frac{\partial c}{\partial t} = D_m \frac{\partial^2 c}{\partial x^2} \tag{3-109}$$

where c is solute concentration, D_m is the matrix diffusion coefficient, x is the distance from the fracture-matrix interface, and t is time.

The initial and boundary conditions are:

$$c(x,0) = f(x) \tag{3-110}$$

$$c(0,t) = c_f \tag{3-111}$$

$$c(\ell,t) = c_m \tag{3-112}$$

where $f(x)$ is the initial concentration, c_f is the fracture concentration, and c_m is the matrix concentration representing the GIC. The concentration boundaries are assumed to be constant over time because the solution is only going to be applied over a numerical computational time step in which concentrations are modeled as constants. The solution is then obtained for a given time step, t_s.

This problem has been solved (Carslaw and Jaeger, 1959) in terms of an expression suitable for computing results at long times:

$$c(x,t_s) = c_f + (c_m - c_f)\frac{x}{\ell} + \frac{2}{\pi}\sum_{n=1}^{\infty}\frac{(-1)^n c_m - c_f}{n}\sin\left(\frac{n\pi x}{\ell}\right)\exp\left(-\frac{D_m n^2 \pi^2 t_s}{\ell^2}\right)$$
$$+\frac{2}{\ell}\sum_{n=1}^{\infty}\sin\left(\frac{n\pi x}{\ell}\right)\exp\left(-\frac{D_m n^2 \pi^2 t_s}{\ell^2}\right)\int_0^{\ell} f(x')\sin\left(\frac{n\pi x'}{\ell}\right)dx' \tag{3-113}$$

where "long times" means $\frac{D_m t_s}{\ell^2}$ is large. Although the infinite series could be a computational obstacle, excellent accuracy is possible with only the first term in each series if $\frac{D_m t_s}{\ell^2} > 1$ and only two terms are needed if $1 > \frac{D_m t_s}{\ell^2} > 0.165$.

For smaller values of this parameter, $\frac{D_m t_s}{\ell^2} < 0.165$, the following solution is to be used,

$$
\begin{aligned}
c(x,t_s) = & \int_0^\ell \frac{f(x')}{2\sqrt{\pi D_m t_s}} \sum_{n=0}^{\infty} \exp\left\{ -\frac{\left\{2n\ell + |x-x'|\right\}^2}{4D_m t_s} \right\} dx' \\
& + \int_0^\ell \frac{f(x')}{2\sqrt{\pi D_m t_s}} \sum_{n=0}^{\infty} \exp\left\{ -\frac{\left\{2(n+1)\ell - |x-x'|\right\}^2}{4D_m t_s} \right\} dx' \\
& - \int_0^\ell \frac{f(x')}{2\sqrt{\pi D_m t_s}} \sum_{n=0}^{\infty} \exp\left\{ -\frac{\left\{2n\ell + (x'+x)\right\}^2}{4D_m t_s} \right\} dx' \\
& - \int_0^\ell \frac{f(x')}{2\sqrt{\pi D_m t_s}} \sum_{n=0}^{\infty} \exp\left\{ -\frac{\left\{2(n+1)\ell - (x'+x)\right\}^2}{4D_m t_s} \right\} dx' \\
& + c_f \sum_{n=0}^{\infty} \operatorname{erfc}\left(\frac{x+2n\ell}{\sqrt{4D_m t_s}} \right) - c_f \sum_{n=0}^{\infty} \operatorname{erfc}\left(\frac{2(n+1)\ell - x}{\sqrt{4D_m t_s}} \right) \\
& + c_m \sum_{n=0}^{\infty} \operatorname{erfc}\left(\frac{(2n+1)\ell - x}{\sqrt{4D_m t_s}} \right) - c_m \sum_{n=0}^{\infty} \operatorname{erfc}\left(\frac{(2n+1)\ell + x}{\sqrt{4D_m t_s}} \right)
\end{aligned}
\tag{3-114}
$$

In this case, two terms are needed in each series for $0.05 < \frac{D_m t_s}{\ell^2} < 0.165$; for $\frac{D_m t_s}{\ell^2} < 0.05$, only one term is needed in each series.

The time-averaged solute mass flow rate over the time step at the LIC and GIC interfaces, $x = 0$ and $x = \ell$, respectively, can be computed from the time-integrated derivative of the concentration times the interface area and diffusion coefficient and divided by the time step, or

$$
\dot{M}_{avg} = -AD_m \left\{ \frac{1}{t_s} \int_0^{t_s} \left. \frac{\partial c(x,t)}{dx} \right|_{x=0 \text{ or } \ell} dt \right\}
\tag{3-115}
$$

The integrals can be evaluated analytically. The time averaged mass fluxes are linear functions of the fracture and GIC concentrations, c_f and c_m, respectively along with the weighted integral of the

concentration profile representing the initial condition within the LIC. Note that this initial condition is not dependent on the unknown values of c_f and c_m at the end of the time step (which are to be computed as part of the global solution for concentration at this time step) but is exclusively a function of earlier known values of concentration at the fracture and the GIC. The traditional diffusive flux relationship between cells used to compute the average solute mass flow rate is:

$$\dot{M}_{avg} = -AD_m \frac{c_m - c_f}{\ell} \tag{3-116}$$

The differences between Equations (3-115) and (3-116) for average mass flux are that for Equation (3-115), the history of concentration changes is retained through the initial condition of the LIC and the (constant) coefficients of c_f and c_m.

Another question from a computational standpoint is, how many points are needed to define the initial condition in the integrals of Equations (3-113) and (3-114)? Results cited by Zimmerman et al. (1993) suggest that something on the order of 10 integration points may be needed, although these are most likely not to be evenly divided. Results cited by Weatherhill et al. (2008) suggest that the initial point should lie about one fracture aperture from the interface and that increasing spacing by a factor of 2 retains reasonable accuracy. Therefore, for a fracture aperture of 0.1 mm and a grid spacing multiplier of 2, 10 integration points corresponds to a global fracture-matrix cell spacing on the order of centimeters; about 15 to 20 integration points are needed to cover a global fracture-matrix cell spacing on the order of meters to tens of meters.

The integration points serve a similar function as the additional grids needed for a direct fine-grid simulation; they resolve the local concentration distribution near the fracture-matrix interface, so that the solution can account for local concentration gradients. However, it is expected to be a much simpler operation to utilize the analytical treatment of fracture-matrix exchange than to regrid the matrix. Furthermore, the calculation using the analytical method proposed here may be computationally faster than a fine-grid simulation. This is because the concentrations representing the initial condition in the analytical method do not represent additional unknowns in the matrix solution for global cell concentrations, but are computed independently for each fracture-matrix interface at each time step. Therefore, the number of unknowns in the global matrix solution for cell concentration does not increase, even though the solution captures fine-scale fracture matrix interaction.

Figure 3-37 shows a comparison, for $\frac{D_m t_s}{\ell^2} = 0.05$, of the two solutions, Equations (3-113) and (3-114). This is for a step function increase in fracture concentration to a relative concentration of 1, with a concentration of 0 at the GIC. Only two terms are used in each of the series in Equation (3-114), but ten terms are used for each of the series in Equation (3-113). The solutions are shown to be identical.

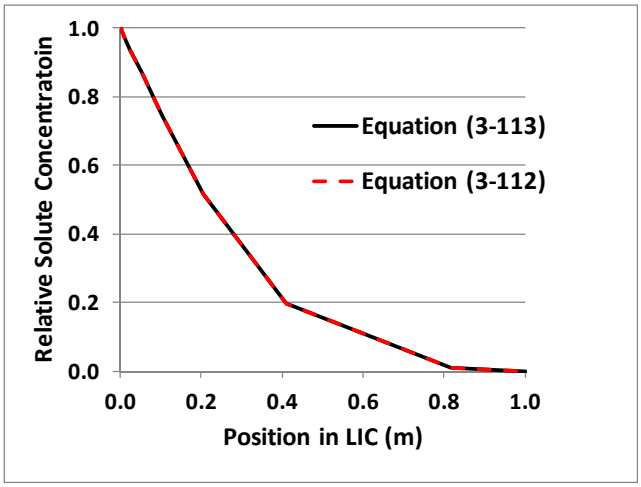

Figure 3-37. Comparison of Equation (3-114), preferred for $D_m t_s / \ell^2$ small, with Equation (3-113), preferred for $D_m t_s / \ell^2$ large.

Figure 3-38 shows a comparison of computing concentration profiles at three times. This is also for a step function increase in fracture concentration to a relative concentration of 1, with a concentration of 0 at the GIC. In the case of the dashed lines for time steps $2t_s$ and $3t_s$, the profiles are each computed for a single time step, t_s, but initialized from the concentration profile computed at the end of the previous time step. The profile uses 15 points with a grid-spacing multiplier of 2. The solid lines are each computed from an initial profile concentration of 0 throughout the LIC as a single time step to values of t_s, $2t_s$ and $3t_s$. The two computational approaches are shown to give nearly identical results.

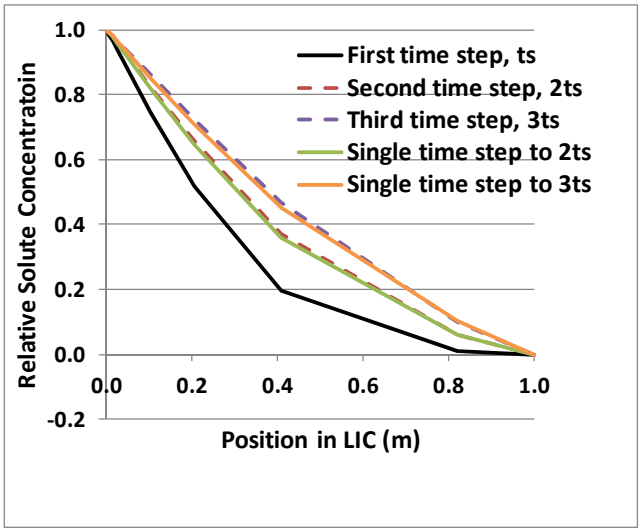

Figure 3-38. Comparison of computational approaches (1) re-initializing solution from previous time step (dashed lines) with (2) computing solution for entire time starting from initial concentration of 0 in the LIC.

3.7 Conclusions

The RBSN method was previously limited in its ability to compute elastic geomechanical behavior because it could not accurately represent the Poisson effect. Representing the Poisson effect is in fact a general problem for discrete models such as RBSN. A new approach documented here addresses this problem. A demonstration of this new RBSN method is provided, in which both global and local representations of Poisson affect are captured. This is an important development for the RBSN method for computing classical elastic geomechanical behavior.

We have established an effective linking of two numerical methods: the finite volume method (via the TOUGH2 package) to simulate heat and mass transport within porous rock formations; and the RBSN method, which provides a discrete representation of material elasticity and fracture development in three dimensions. One main advantage of linking TOUGH2 and RBSN is that both codes utilize the same set of nodal points, along with the natural neighbor and volume rendering definitions according to the corresponding Voronoi tessellation.

The capabilities of the linked TOUGH-RBSN simulator are validated, through simulating desiccation cracking of a mining waste. Agreement between the numerical and physical test results (with respect to time to initial cracking, trends in mean crack spacing, and qualitative representation of the crack patterns) is quite good, especially when considering the strong dependence of elastic modulus and tensile strength on degree of saturation. Discrepancies in calculated observed crack spacing suggest a need for further work, including study of the effects of material toughness on desiccation cracking.

Initial work on modeling the HG-A test (Mont Terri URL) is reported. The goal of this activity is to use the test data to help build confidence in the TOUGH-RBSN model for predicting various facets of fracture development and evolution within the EDZ. An initial analysis of rock failure at the HG-A test at the Mont Terri URL shows that both shear and tensile failure occur along the NNW and SSE sides of the drift wall These results are in qualitative agreement with the observations of failure, although the observed failure (Figure 3-17), especially on the NNW side, is restricted to a narrower region than

predicted here. Failure analysis at radii greater than 0.5 m (the radius of the drift) suggests that damage is confined to a narrow region around the drift. Tensile failure is found to be limited to only 3 to 4 cm into the drift wall, while shear failure is limited to about 10 cm into the drift wall.

We have developed a mathematical model for two-dimensional flow and transport through a water-saturated single fracture and permeable rock matrix for which analytical solutions have been obtained. This model incorporates several factors not included in existing analytical solutions for this kind of transport problem. The new model capabilities are (1) two-dimensional flow in the matrix with an arbitrary flow direction relative to the fracture orientation, (2) a general solute source-release point that can be either in the fracture or matrix, and (3) independent longitudinal dispersion and diffusion in the fracture and matrix, respectively. A closed-form analytical solution was obtained for two-dimensional solute concentration if longitudinal dispersion and diffusion could be neglected. Some example calculations show that significant delay in radionuclide transport can occur as a result of an offset of the source location from the fracture or as a result of matrix cross flow. We then developed a method for incorporating the effects of longitudinal dispersion in the fracture and longitudinal diffusion in the matrix. The resulting solution including these mechanisms takes the form of a superposition integral. A closed-form analytical solution is used to develop an approximate criterion to evaluate conditions in which longitudinal dispersion in the fracture and longitudinal diffusion in the matrix are expected to be significant, relative to longitudinal spreading caused by fracture-matrix interaction. The significance of longitudinal dispersion in the fracture and longitudinal diffusion in the matrix has been shown to be a strong function of Peclet number, with the influence of these processes decreasing as Peclet number increases. The effects of fracture longitudinal dispersion also diminish with the ratio of fracture longitudinal dispersion coefficient to matrix diffusion coefficient. The new transport solutions presented here are valuable for checking the influence of the various advective and diffusive processes on transport through a rock fracture and matrix when matrix advective transport is not negligible, and can be used to verify the ability of numerical simulations to capture these transport processes.

Solute transport cases analyzed with the analytical model show that matrix cross-flow has an increasing effect on solute transport, as the orientation of the fracture relative to the hydraulic gradient goes from parallel to orthogonal. This is a result of increasing cross-flow and decreasing flow along the fracture. The effects of cross-flow result in reduced solute interaction with the fracture, such that a greater degree of longitudinal advance of solute occurs in the matrix. As the effects of cross-flow become stronger, more of the solute transport occurs in the matrix, and transport times approach the time for advection through the matrix. Significant delays in transport can also occur for cases in which solute is released into the matrix, with the main impact found on the early breakthrough behavior and the secondary impact on the trailing portion of the breakthrough.

Previous work has shown that extremely fine gridding in the matrix next to the fracture is needed for a traditional numerical treatment of transient solute transport in a fractured, porous, and permeable rock to appropriately account for fracture-matrix solute exchange. The fine gridding is needed to resolve steep gradients in solute concentration in the matrix orthogonal to the fracture as solute initially penetrates along fractures and moves into the matrix by diffusion and perhaps advection. The need for fine gridding presents serious computational impediments using TOUGH-RBSN for solute transport problems. A potential approach utilizing an analytical treatment of fine-scale fracture-matrix interaction has been described. While many aspects of this approach still need to be investigated in terms of implementation, computational burden, and accuracy, the advantages are that it: (1) accounts for highly transient interactions near the fracture-matrix interface; (2) does not restrict solute-transport interactions between fractures; and (3) allows for a globally connected matrix.

4. THM Modeling of the FE Experiment at the Mont Terri Site

4.1 FE Experiment at the Mont Terri Site

The Full-Scale Emplacement Experiment (FE) at the Mont Terri URL, Switzerland will be one of the largest and longest-duration heater tests worldwide (Figures 4-1 through 4-3). This heater experiment is undertaken by NAGRA and other international partners as an ultimate test for the performance of geologic disposal in Opalinus Clay, with focus on both the EBS components and the host-rock behavior. The experiment will provide data useful for the validation of THM coupling effects regarding the processes in the host rock while correctly accounting for (and examining) the conditions in the emplacement tunnel (temperature, saturation, and swelling pressure). Due to the 1:1 scale of the experiment, it will be possible to achieve realistic temperature, saturation, and stress gradients. It will also be possible to test backfilling technology with granular bentonite, as well as lining technology with shotcrete, anchors, and steel rips. Processes examined in the test cover many aspects of repository evolution, such as EDZ creation and desaturation of the EDZ during tunnel excavation and operation (including ventilation for about one year), as well as reconsolidation of the EDZ, resaturation, thermal stresses, and thermal pore-pressure increase after backfilling and heating (heating and monitoring period > 10 years).

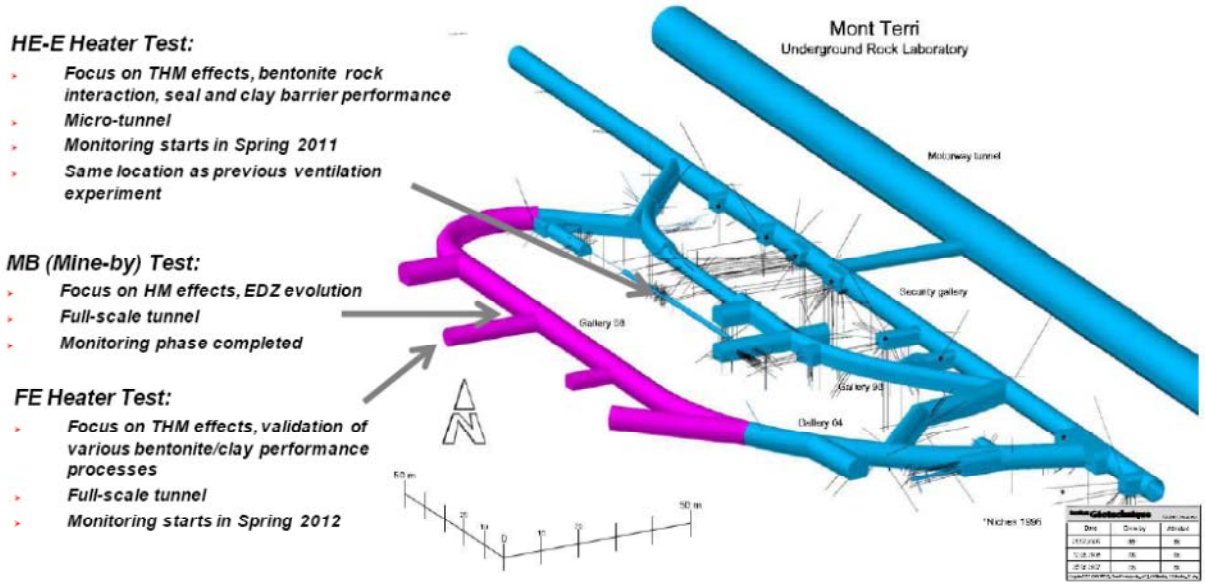

Figure 4-1. Summary schematic of the Mont Terri URL with side galleries and drifts for testing. Three specific experiments of relevance to UFDC are highlighted (based on Garitte and Gens, 2012).

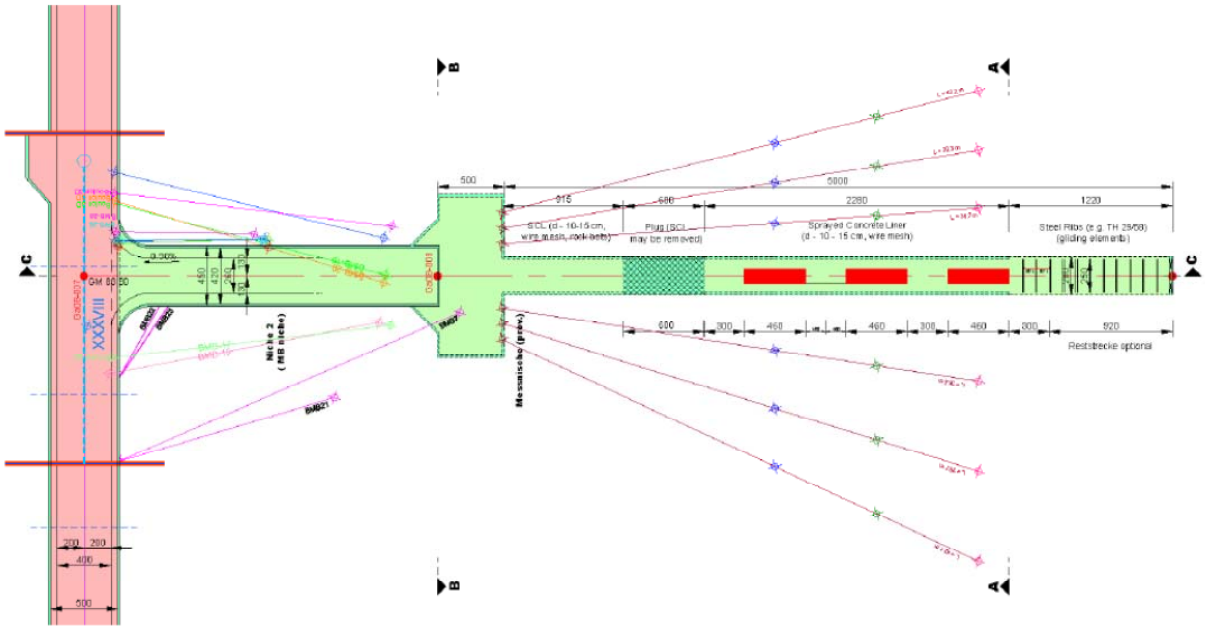

Figure 4-2. Plan view of experiment setup and borehole layout (from Garitte and Gens, 2012).

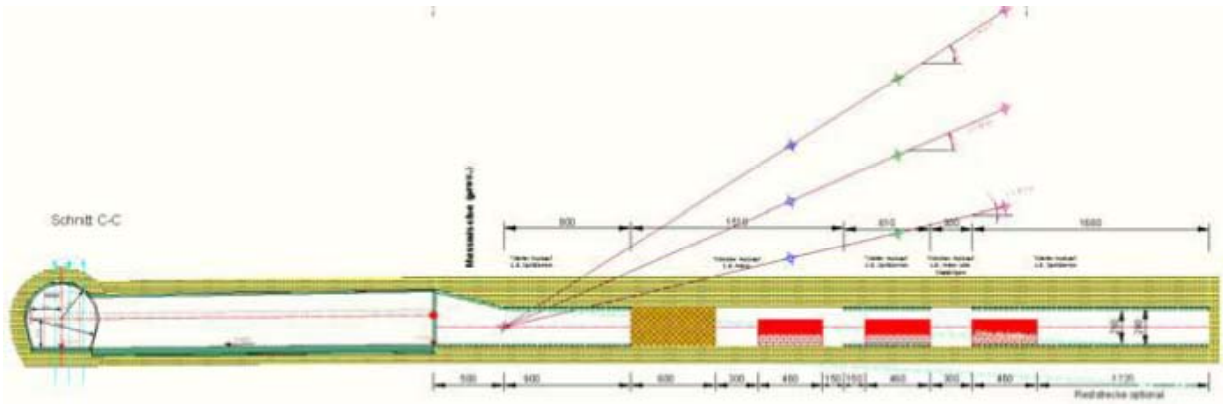

Figure 4-3. Side view of experiment setup and borehole layout (from Garitte and Gens, 2012).

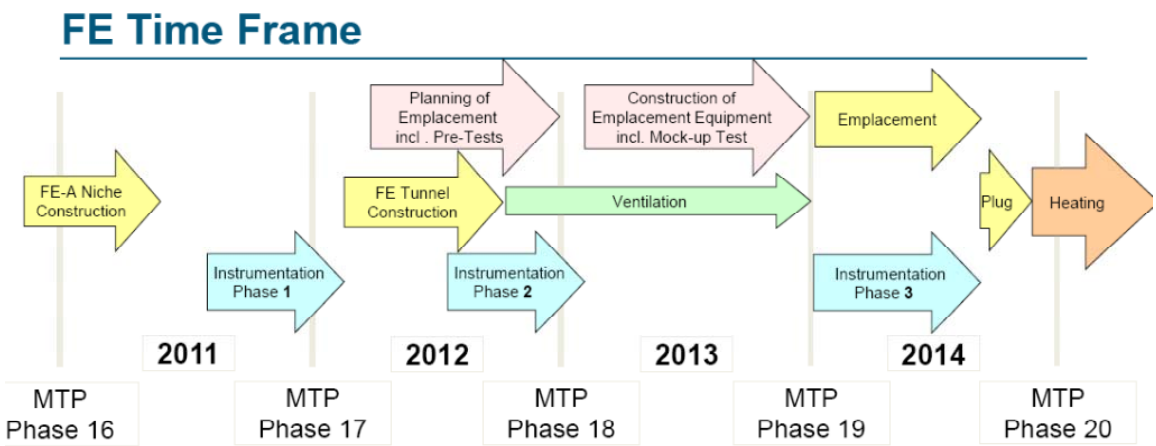

Figure 4-4. FE experiment time frame. Phases 16 to 20 refer to Mont Terri project phases (Vietor, 2012).

As shown in Figures 4-1 through 4-3, the FE experiment will be conducted in a side tunnel at Mont Terri, excavated along the claystone bedding planes for this purpose, extending 50 m in length and about 2.8 m in diameter. Heating from emplaced waste will be simulated by three heat-producing canisters of 1500 W maximum power. A sophisticated monitoring program is planned, including dense pre-instrumentation of the site for *in situ* characterization, dense instrumentation of the bentonite buffer and host rock, and extensive geophysical monitoring (seismic and electric tomography). A THM modeling program will be conducted in parallel with the testing and monitoring activities.

Figure 4-4 shows the FE experiment time frame (Vietor, 2012). A niche in front of the FE tunnel was constructed in 2011, followed by a first phase of instrumentation of the rock mass surrounding the tunnel using boreholes from the niche. The FE tunnel was then excavated by road-header in 2012, and this was followed by another phase of instrumentation. The tunnel is currently open for a 1-year ventilation period.

This will be followed by the emplacement of the heaters, bentonite buffer, and a concrete plug, after which the heating is expected to start at the end of 2014. The heating is then expected to go on for at least 15 years, with continuous monitoring of THM processes in both the bentonite buffer and surrounding rock.

DOE is one of the experimental partners for the FE heater experiment, and LBNL is one of the modeling teams. The plans for the THM modeling program were determined in meetings with the FE modeling teams during 2012. Model simulation tasks for each of the international modeling teams (currently 6 modeling teams participate) include three types of computations:

1) Scoping computations
2) Bench Marking
3) Predictive computations

The scoping computations included brainstorming on potential ongoing processes, evaluating their significance and parameter range, comparing simulation results and input parameters derived by each team, and lessons learnt (parameter range, importance, expected response). The benchmarking uses well-defined geometry problems with exact parameter values given to the teams, focusing on process modeling with precise comparison of codes. In the predictive calculations, likely parameters values and the as-built information of the experiment will be frozen. The modeling will be used to predict the behavior of the system, and this should be reported prior to heating start (in 2014). Currently, each modeling team develops their conceptual models and material properties using available literature (papers and reports) on lab experiments and previous Mont Terri *in situ* tests etc. Moreover, this is complemented with a restricted benchmark test for code comparison, in which properties and model geometry are set by NAGRA. In the FY2012 NS report, we presented our first initial 2D modeling of the FE experiment, including a parameter study, to evaluate the importance of the different coupled processes and different components of the FE experiment. The following main conclusions were drawn from the FY2012 2D modeling of the FE experiment:

- The canister surface reaches the maximum temperature of 94.5°C after 4.8 years (for 2D model).
- Resaturation of the bentonite buffer is slow and is still unsaturated after 30 years.
- Temperature, water saturation, and pore pressure in the bentonite buffer are largely affected by the bentonite capillary pressure.
- Minor rock failure occurring during excavation did not expand much further during the 20-year heating, meaning that the rock mass remained in an elastic mechanical state.

While the 2D analysis is very useful for performing such parameter studies, we also acknowledge that the 2D simplification does not provide an accurate quantitative prediction of the temperature evolution and the peak temperature. Consequently, in FY2013, we have developed a new full 3D model of the FE experiment. Using the 3D model, we conducted simulations, first for a prediction of the thermal-hydrologic evolution and then to predict the peak temperature. We have also conducted full-scale 3D THM simulation using the Barcelona Basic Model for the bentonite buffer. These new 3D model simulations are presented in this section of the natural systems report.

4.2 Modeling Approach

LBNL's model simulations of the FE experiment are carried out using the TOUGH-FLAC software (Rutqvist et al., 2002; 2011), which is based on linking the TOUGH2 multiphase flow and heat transport simulator (Pruess et al., 2011) with the FLAC3D geomechanical simulator (Itasca, 2009). The TOUGH-

FLAC simulator has in recent years been extended and applied to issues related to nuclear waste disposal in clay host rock within bentonite backfilled tunnels (Rutqvist et al., 2011; 2013). This includes implementation of the Barcelona Basic model (BBM), for the mechanical behavior of unsaturated soils and applied for modeling of bentonite back-fill behavior (Alonso et al., 1990). Recently, as part of the UFD EBS program, the BBM has been extended to a double structure model, corresponding to the Barcelona Expansive Model (BExM), a model that we also plan to use for advanced modeling of the FE experiment. For the modeling of the FE experiment, we have developed an initial conceptual model and modeling approach based on experiences from recent design scoping calculations conducted by teams contracted by NAGRA, to help with the experimental design:

1) Pöyry (Engineering and Consulting): Modeling for excavation design using FLAC3D with ubiquitous joint model (anisotropic plasticity with different shear strength along bedding planes). This modeling approach was used to analyze the ground support design (Nater, 2012).

2) CINEMAT and UPC of Spain conducted scoping calculations for thermal and monitoring design using the CODE-Bright FEM code, and they used the BBM for modeling bentonite mechanical behavior (Garitte and Gens, 2012).

3) The Interra Swiss Branch performed 3D TOUGH2 model simulations with anisotropic properties and inclined mesh. Their modeling was limited to thermal-hydrological processes (no mechanics) and done for thermal and monitoring design (Ewing and Senger, 2011).

Our modeling approach contains important components from these three models. The host rock is modeled using TOUGH-FLAC with anisotropic properties considering bedding planes of the Opalinus Clay. The bedding planes across the FE tunnel can be seen in Figure 4-5. These bedding planes are oriented with its strike along the tunnel axis, and dipping about 45°. To accurately model anisotropic thermal and hydrological behavior, we created an inclined TOUGH2 mesh, the same way as done by the INTERA team. Anisotropic mechanical material behavior is simulated using the FLAC3D ubiquitous joint model, with initial properties of those derived from the excavation design analysis by the Pöyry team (Nater, 2012). For the bentonite, we started with the BBM model as applied by the CINEMAT and UPC (Garitte and Gens, 2012), and derived specific input material parameters for the MX-80 bentonite pellets that will be used as emplacing bentonite buffer around the heaters. With this modeling approach, we are able to simulate THM processes in both the bentonite and host rock, as well as their interactions.

Figure 4-5. View of FE tunnel face from the FE niche showing beddings dipping 45° (Vietor, 2012).

4.3 FE Model Setup

Figure 4-6 presents the new 3D numerical grid that has been developed as an extension of the previous 2D grid. This model grid includes all vital material components for the modeling of the FE experiment, including layered Opalinus Clay host rock, excavation disturbed zone, tunnel, 3 heaters, bentonite buffer, concrete liner, and concrete plug. The initial conditions for the model simulation are 2 MPa in pore fluid pressure and 15°C in temperature for the host rock. The 2 MPa of pore pressure is not under hydrostatic conditions, and the process is affected by the existing tunnel system at the site. In our simulations, we first run a simulation with an open tunnel at the atmospheric pressure for 1 year, creating a pressure drop and hydraulic gradient around the tunnel. Potential desaturation caused by ventilation effects will be considered in future simulations. Thereafter, we assume instantaneous emplacement of the heater and buffer, and start our heating simulation.

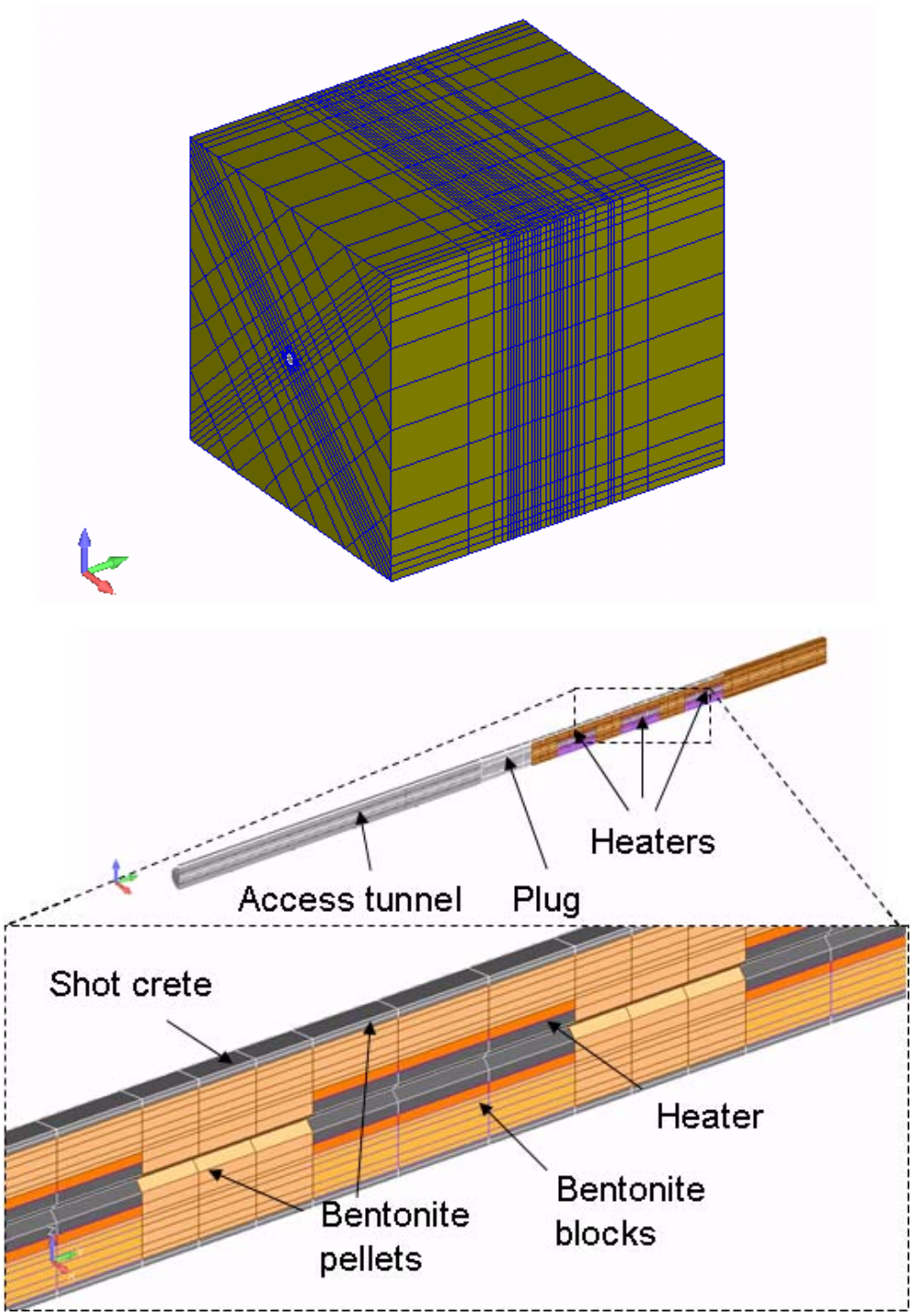

Figure 4-6. TOUGH-FLAC 3D numerical grid of the FE experiment.

The output from each of the heaters will be approximately 1500 W, according to the specifications set by NAGRA, and this is the heat power assumed in the current model. However, the heater power may be regulated to achieve a desired temperature evolution. For example, the targeted maximum temperature at the heater/bentonite interface is 125 to 135°C. On the other hand, a preliminary model simulation by the UPC team indicates that the temperature might not exceed 110°C, if the initial bentonite saturation is about 20 to 25%. A much higher peak temperature was calculated by the INTERA when assuming an initial saturation of 1%. Since buffer thermal conductivity depends on water saturation, the 1% initial saturation leads to a lower thermal conductivity in the buffer, which in turn results in a relatively high temperature at the heater/bentonite interface. A 1% saturation is reasonable for the pellets being deposited into the tunnel during buffer emplacement. However, experience from the ongoing HE-E heater test at Mont Terri shows that the bentonite pellets quickly draw moisture from the air and equilibrate with air relative humidity. Therefore, the initial buffer saturation of 18% is a reasonable value for the modeling.

Table 4-1. Parameters for the Opalinus and Bentonite clay

Properties	Parameters	Symbol	Opalinus Clay	Bentonite	Unit
Physical	Grain density	ρ_g	2.7×10^{3}	2.7×10^{3}	kg/m^3
	Porosity	$\varnothing$	0.15	0.389	-
	Pore compressibility	β	1.0×10^{-9}	5.0×10^{-8}	Pa^{-1}
Hydraulic	Intrinsic permeability	k	5.0×10^{-20}	2.0×10^{-21}	m^2
	Liquid relative permeability	n	-	3	-
	Capillary curve	P_0	1.47×10^{7}	2.00×10^{7}	Pa
	Capillary curve	λ	0.595	0.51	-
	Capillary curve	S_{ls}	1.0	1.0	-
	Capillary curve	S_{lr}	0.01	0.00	-
Thermal	Thermal conductivity (wet)	λ_{sat}	2.0	1.3	W/m/K
	Thermal conductivity (dry)	λ_{dry}	2.0	0.3	W/m/K
	Grain specific heat	C	900	800	J/kg/K
Mechanical	Bulk modulus	K	4170	-	MPa
	Shear modulus	G	1920	-	MPa
	Cohesion	C	5	-	MPa
	Friction angle	ϕ	25	-	°
	Thermal exp. coeff.	α_T	1.0×10^{-5}	$1.5\cdot10^{-4}$	1/°C
	Dilation angle	d	10	-	°
	Tensile strength	T	1.0	-	MPa
	Joint cohesion	C_J	2.2	-	MPa
	Joint friction	ϕ_J	23	-	°
	Joint tensile strength	T_J	0.5	-	MPa
	Joint dilation angle	d_J	10	-	°

The basic thermal and hydraulic material parameters are presented in Table 4-1. These are equivalent to the material parameters used in our previous 2D model analysis of the FE experiment. We started with bentonite properties, including the thermal and hydraulic properties, derived from laboratory experiments and *in situ* tests related to the FEBEX experiment at Grimsel, Switzerland (Rutqvist et al., 2011). We then modified some of the properties to represent a bentonite buffer composed of MX-80 pellets. In our initial modeling we also consider the water-retention curves for the bentonite and Opalinus Clay as important

parameters for the behavior. The capillary curves used in the model are shown in Figure 4-7. We use the van Genuchten formulation to describe the water-retention characteristic curves (van Genuchten, 1980):

$$P_c = -P_0 \left[\left(\frac{S_l - S_{lr}}{S_{ls} - S_{lr}} \right)^{-1/\lambda} - 1 \right]^{1-\lambda} \tag{4-1}$$

where P_0 is the air entry pressure, S_l is water saturation, the subscripts ls and lr refer to the fully saturated and residual conditions, respectively, and λ is a curve fitting parameter. These values are presented in Table 4-1. Those for the Opalinus Cay are taken from the previous simulation and fit against a series of laboratory and *in situ* measurements (Garitte et al., 2012), and those for Bentonite clay are adjusted to match an *in situ* measurement of the initial state at the Mont Terri site (approximately 100 MPa at water saturation of 20%).

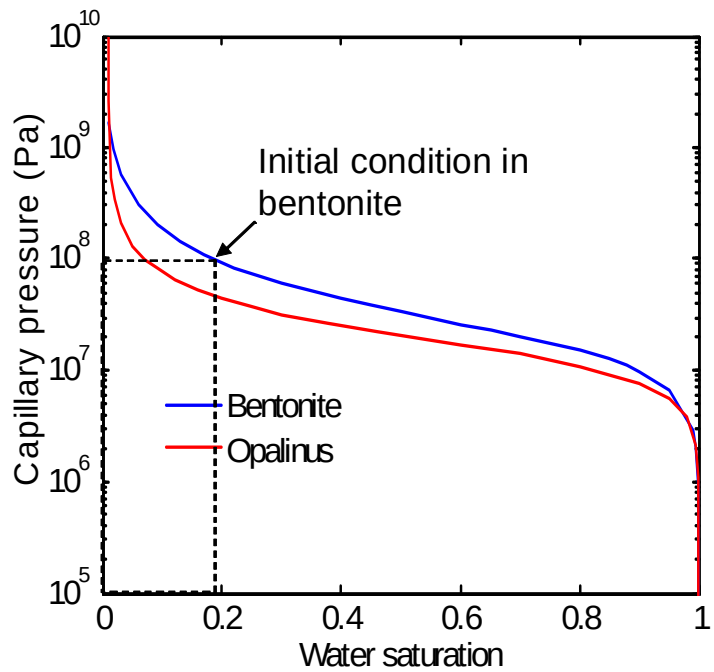

Figure 4-7. Capillary curves for Bentonite and Opalinus clays

4.4 3D TH Simulation with Comparison to 2D Results

Figure 4-8 shows the TH results from the new 3D analysis, and in Figure 4-9 we compare the results of the new 3D and the previous 2D analyses. In the new 3D simulation, the peak temperature in the bentonite near the heater surface (0.55 m) is higher than in the 2D analysis; it is about 120°C (Figure 4-8(a)). Similarly to the 2D analysis, the buffer is not fully saturated after 30 years (Figure 4-8(b)). At the buffer and concrete interface (1.18 m), the temperature peaks at about 67°C after 20 years, i.e., slightly lower than in the 2D analysis. Similarly to the previous 2D analysis, as soon as the bentonite buffer is installed, liquid water is pulled from the host rock due to the strong capillary pressure at an initial saturation of 18%. Water saturation near the bentonite buffer and concrete liner interface (1.18 m in Figure 4-8 (b)) increases immediately after the installation; correspondingly, a slight desaturation is

observed in the host rock. The resaturation process is quite slow due to the low permeability of the host rock and bentonite buffer. The water saturation near the canister is approximately 68% after 30 years.

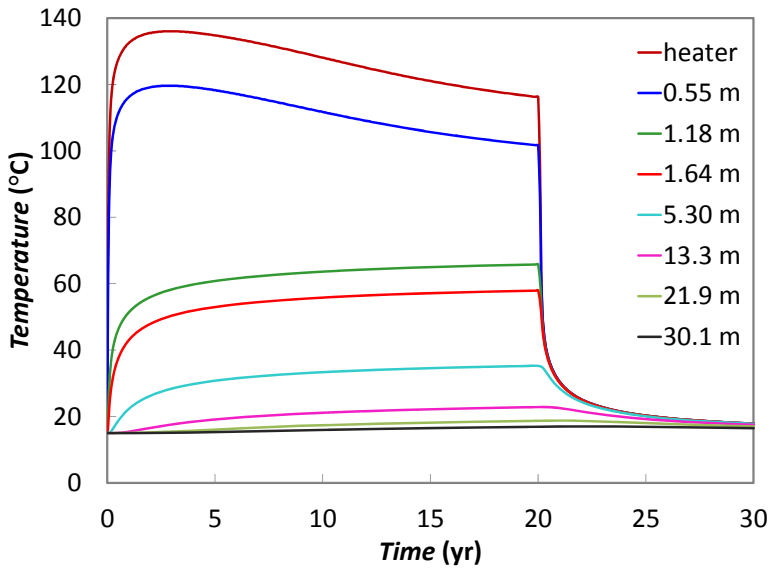

(a)

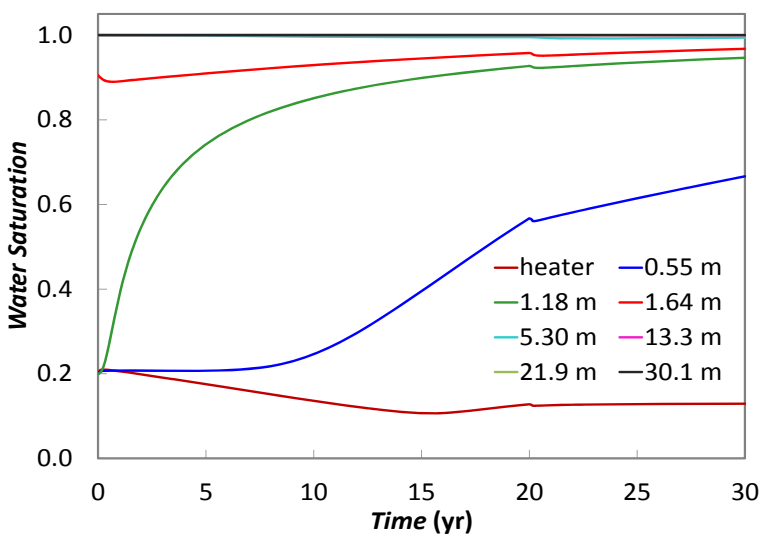

(b)

Figure 4-8. New 3D simulation results related to the evolution of TH processes in the buffer and host rock: (a) temperature, (b) liquid saturation.

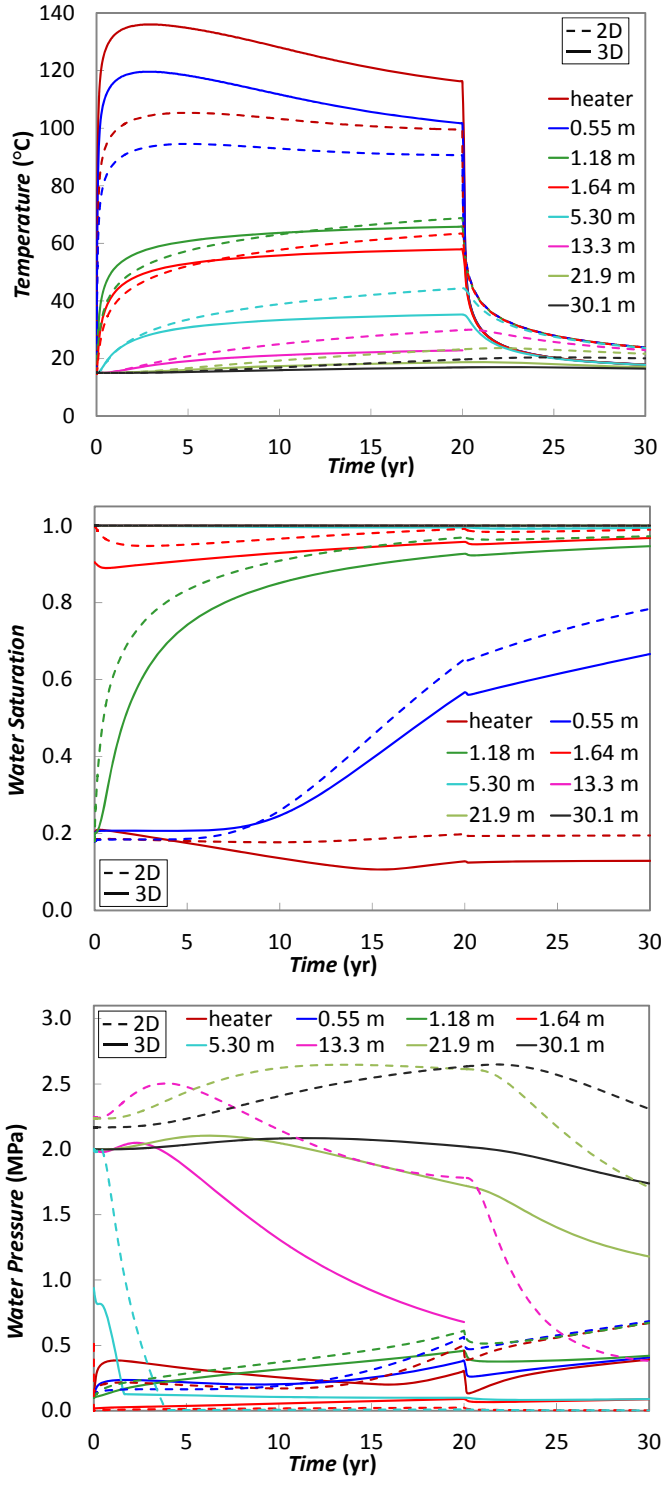

Figure 4-9. Comparison of previous 2D and new 3D simulation results: (a) temperature, (b) liquid saturation, (c) fluid pressure.

The pore-pressure evolution is rather complex in the buffer and rock system around the FE experiment, but these are all responses that can be explained by the coupled TH processes. The pressure increases gradually in the bentonite buffer along with the resaturation of the buffer. The host rock near the concrete/Opalinus interface experiences a sudden depressurization after the installation of the bentonite buffer. Because the rock is unsaturated, the pore pressure remains low during the 20 years of heating. However, the deep host rock (>13.3 m away from canister) is pressurized owing to the increase in temperature in the first few years, whereupon the pressure decline again as a result of suction from the bentonite-filled tunnel.

In the comparison of the new 3D versus the previous 2D analysis, we can observe that the most significant difference occurred in the temperature evolution close to the heater and in the pressure evolution in the Opalinus clay at some distance away from the tunnel (Figure 4-9). The 3D analysis predicts a higher peak temperature at the heater; this is expected, because in the 2D analysis the heat load was based on an average line thermal load of 197 W/m, taking into account the spacing between individual heaters. The 3D analysis is more accurate for calculating the peak temperature at mid-heater surface; this was about 120°C compared to 94°C for the 2D analysis. The fluid pressure in the host rock away from the tunnel is different in terms of magnitude of thermal pressurization, which is significantly higher in the case of the 2D model analysis. In the 2D analysis, an incremental pressure increase of about 5 MPa can be observed (e.g., black dashed line in Figure 4-9(c)), whereas the maximum pressure increase is about 1 MPa in the 3D analysis (e.g., black solid line in Figure 4-9(c)). The thermal pressurization is lower in the case of the 3D analysis, because the pressure can escape in the third dimension, whereas in the 2D analysis, the pressure is confined within the 2D model.

4.5 3D Peak Temperature Considering Thermal Diffusion in the Buffer

In the previous simulation, we had neglected the diffusion of the water vapor, which is an important process for capturing early time drying of the bentonite buffer near the heater. Figure 4-10 presents the evolution of temperature and saturation in the case where the thermal diffusion causes drying and a decrease in saturation near the heater. This reduction in liquid saturation results in a lower buffer thermal conductivity and (consequently) a higher peak temperature of 130°C. We note that the evolution of the liquid saturation in the buffer is important for the peak temperature, and that the 130°C is right within the targeted 125 to 135°C temperature range. However, further analysis should be made once the accurate thermal properties have been determined for the MX-80 granular bentonite to be used in the actual experiment.

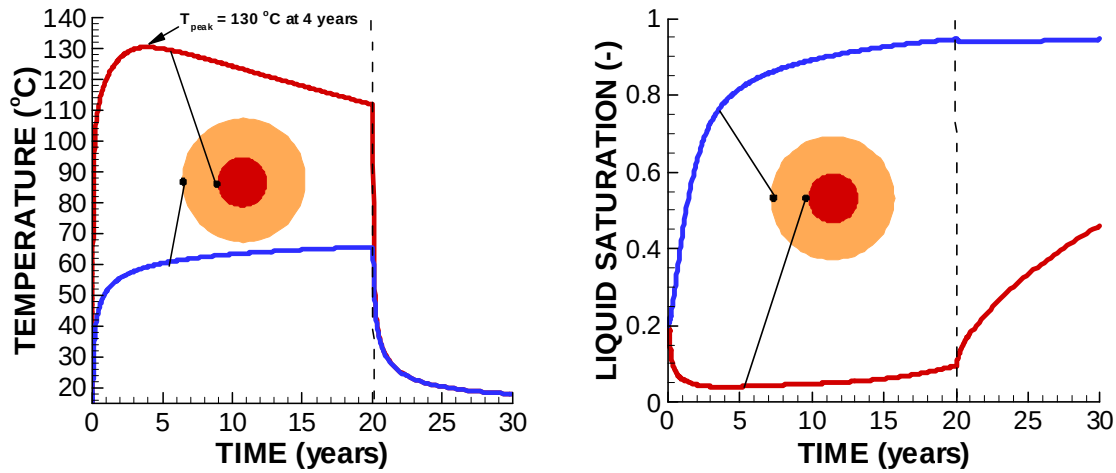

(a) **(b)**

Figure 4-10. Simulation results considering drying induced by diffusion of water vapor within the buffer: (a) temperature, (b) liquid saturation.

4.6 3D THM Simulation Results using the BBM

We have conducted new modeling simulations using (for the first time) the BBM in a full 3D setting. The BBM (Alonso et al., 1990) has been implemented into TOUGH-FLAC as part of the UFD EBS program. In this model simulation, we are using the same TH properties, which are given in Table 4-1. In addition, we now add the material parameters for the BBM, which are given in Table 4-2. The parameters for the BBM used in this initial 3D THM model simulation are those derived for FEBEX bentonite by Gens et al. (2009), and also applied in Rutqvist et al. (2013) for the modeling of THM processes around a generic nuclear waste repository. A large number of material parameters are required to describe the THM material behavior, and those given in Table 4-2 have been determined from laboratory experiments. As mentioned, for the rock-mass behavior, we used a ubiquitous joint model (anisotropic plasticity with different shear strength along bedding planes) consistent with the previous ground-support design analysis (Nater, 2012). The rock mechanical properties for the Opalinus Clay were taken from Corkum and Martin (2007).

Table 4-2. BBM material parameter values for the bentonite buffer (Gens et al., 2009)

Parameter	Value
Compressibility parameter for stress-induced elastic strain, κ_{PS0} [-]	0.05
Compressibility parameter for suction-induced elastic strain, κ_{SP0} [-]	0.25
Shear modulus, G [MPa]	NA
Poisson's ratio, ν [-]	0.4
Parameter for suction induced elastic strain, α_{SS} [-]	0
Parameter for stress-induced strain α_{PS} [MPa^{-1}]	-0.003
Parameter for stress-induced strain, α_{SP} [-]	-0.161
Reference stress state for relating elastic compressibility to suction, P_{ref} [MPa]	0.5
Parameters that relate elastic volumetric strain and temperature changes, α_0 [°C^{-1}]	1.5e-4
Compressibility parameter in virgin soil states at zero suction, λ_{PS0} [-]	0.15
Parameter defining soil stiffness associated with loading collapse yield, r_λ [-]	0.925
Parameter for the increase of soil stiffness with suction, β_λ [MPa^{-1}]	0.1
Parameter that relates cohesion to temperature, ρ_s [°C^{-1}]	0
Parameter describing the increase of cohesion with suction, k_s [-]	0.1
Tensile strength at saturated conditions, P_{S0} [MPa]	0
A reference stress state for compressibility relation in virgin states, P^C [MPa]	0.5
Slope of the critical state line, M [-]	1
Nonassociativity parameter in the plasticity flow rule, α_a [-]	0.53
Specific volume at reference stress states P^C in virgin states, v^c [-]	1.937
Net mean yield stress for saturated conditions at reference temperature, P^*_{0T} [MPa]	12.0

A significant number of measurements using different procedures (borehole slotter, undercoring, and hydraulic fracturing) of the in situ stress have been made at Mont Terri. A synthesis of these is given in Garitte et al. (2012):

- Major principal stress is subvertical and corresponds approximately with overburden weight (about 7 MPa)
- The magnitude of the intermediate principal stress obtained from the undercoring technique is consistent with the results from hydraulic fracture tests (about 5 MPa)
- The value of the minor principal stress is quite low and probably controlled by the presence of a deep valley to the SW of the laboratory. A low value of the minor principal stress is consistent with the small number of breakouts observed in vertical boreholes (about 2 MPa).

In our modeling we then set the vertical stress to 7 MPa, whereas the maximum horizontal stress perpendicular to the tunnel is set to 5 MPa.

Figure 4-11 shows the stress evolution in the buffer; Figure 4-12 shows the evolution of the mean effective stress and bulk modulus in the buffer. The compressive stress increases along with the resaturation of the buffer, which first takes place at the tunnel wall. The maximum stress at the end of heating (20 years) is about -2.5 MPa (compressive stress), with highest maximum occurring at the tunnel wall, i.e., at the buffer and concrete lining interface. After 20 years, there is a sudden drop in compressive stress as a result of the temperature drop once the heater is turned off. This drop in buffer stress, caused by the cooling shrinkage, results in a quite substantial stress drop because the buffer is relatively stiff at that time (Figure 4-12). The radial compressive stress in the buffer is quite uniform (similar to the magnitude at the heater and concrete lining) and is about -1.7 MPa at the end of this simulation. This compressive stress is applied on the concrete lining and supports the rock wall.

The rock stress evolution is shown in Figure 4-13. The initial stress is quite anisotropic at the tunnel wall, with a relatively high tangential stress, while the radial stress is small as a result of the free rock surface. However, the concrete lining provides some support, so the radial stress is not zero, but rather a few MPa. During the heating of the rock, and as a result of the buffer swelling, the stress changes with time (as expected). At 20 years, the stress at the tunnel wall is about -3.3 MPa, which is higher than initial, as the swelling pressure from the buffer provides some support to the rock wall. Note that in our FY2012 report, we presented 2D results for stress evolution using a simple swell model for the buffer and achieving a higher swelling stress in the buffer. The magnitude of this swelling stress depends on the parameter input governing the swelling in both the simple swell model and the BBM. However, the higher swelling pressure in our previous model simulation resulted in more substantial effects on the rock stress near the tunnel wall, making the stress more isotropic than was achieved in the current 3D model simulation. A detailed back analysis of swelling stress parameters will be made for the MX-80 granular bentonite material to be used in the FE experiment.

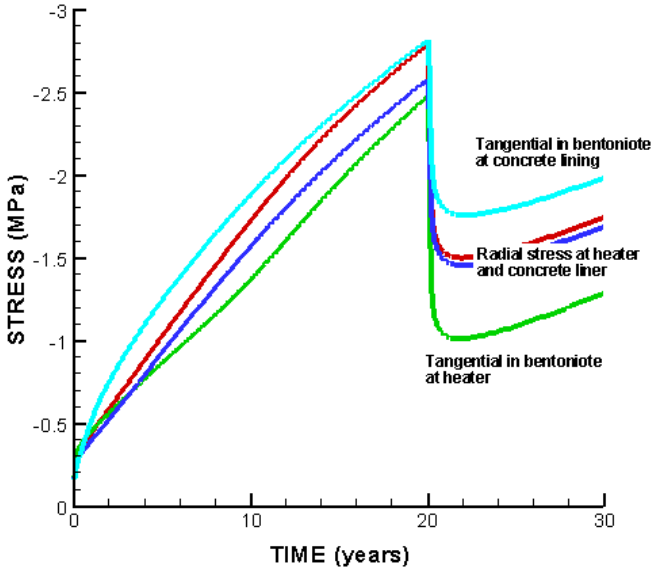

Figure 4-11. Simulated stress evolution within the bentonite buffer.

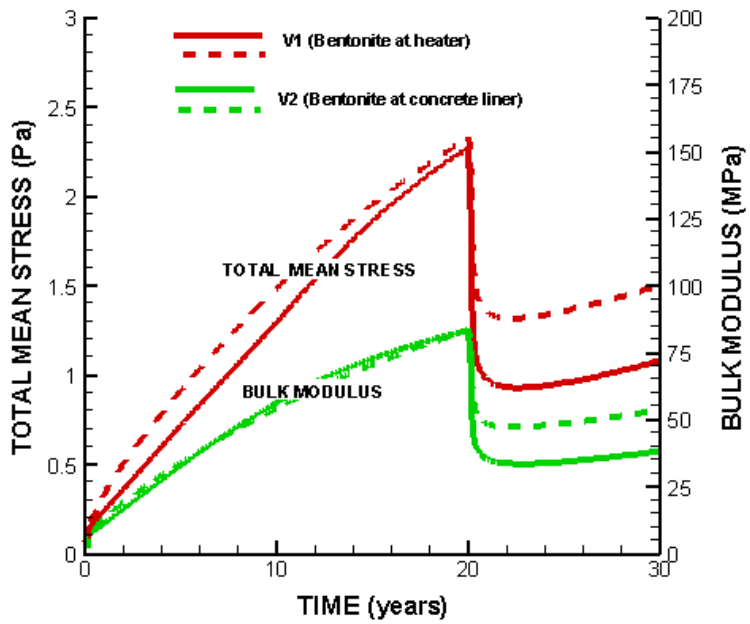

Figure 4-12. Simulated evolution of mean stress and bulk modulus within the buffer.

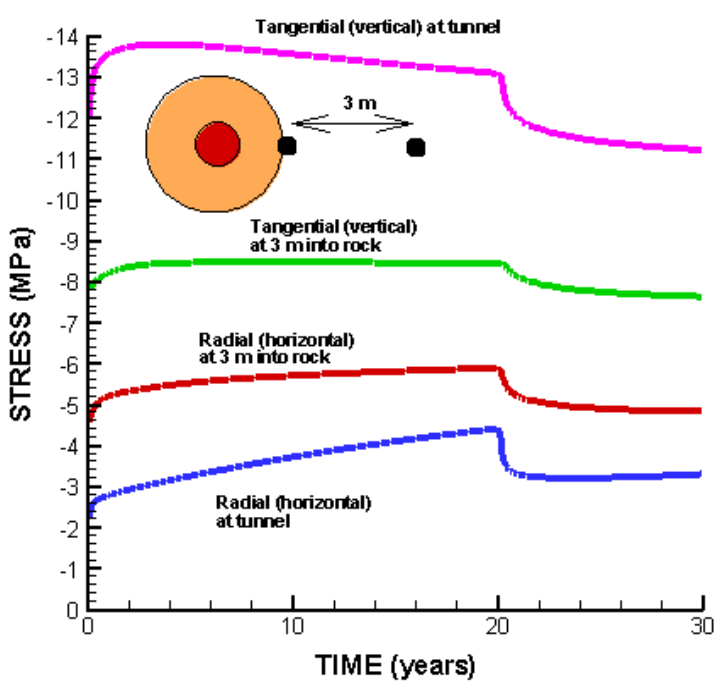

Figure 4-13. Simulated stress evolution within the Opalinus Clay.

4.7 Conclusions

We conducted new 3D TH and THM model simulations of the FE test at Mont Terri. We conducted (for the first time) a THM analysis involving the BBM in a full 3D field setting for modeling the geomechanical behavior of the buffer. Our TH modeling shows that the canister surface reaches the maximum temperature of 130°C after about 2 to 3 years. After the installation of bentonite buffer, water is pulled from the host rock, and the resaturation of the bentonite buffer is slow because of the low permeability of host rock. The buffer is still unsaturated after 30 years. Compared to our previous 2D model analysis, this 3D analysis provides a much more accurate estimate of the temperature evolution near the heater and thereby should provide a better prediction of the peak temperature.

Overall, our initial model analyses showed that our adopted modeling approach is adequate for modeling the coupled THM processes at the FE heater, including all components of bentonite, concrete lining, and Opalinus Clay. We managed to discretize the 3D model using the inclined mesh in both TOUGH2 and FLAC3D, and the modeling results are reasonable. Our next steps will be (1) modeling of laboratory-scale experiments on MX-80 bentonite pellets, (2) perform benchmarking for code-to-code verification with other FE modeling teams, (3) provide a final prediction of FE heater experiment (should be completed and reported before start of heating).

5. Investigation of the Impacts of High Temperature Limits

5.1 Background

Maximum allowable temperature is one of the most important design variables for a geological repository, because it determines waste package spacing, distance between disposal galleries, and therefore the overall size (and cost) of repository for a given amount of waste (Horseman and McEwen, 1996). This is especially important for a clay repository, because argillaceous rocks have relatively small values for heat conductivity. Table 5-1 shows the thermal constraints on engineered barrier system (EBS) or natural system (NS) imposed in disposal concepts throughout the world, as well as the considerations based on which thermal constraints are used. A 100 ^{o}C thermal limit is imposed unanimously in all these concepts despite their differences in design concepts. The major concerns are steam generation, corrosion of container, chemical alteration, and mechanical deformation. Without any question, these are legitimate concerns. Steam generation apparently will be enhanced at higher temperature. Higher temperature is certainly one of the factors that could increase the corrosion rate. A high temperature could also result in chemical alteration of buffer and backfill materials (bentonite) within the EBS through illitization and cementation, which compromise the function of these EBS components by reducing their plasticity and capability to swell when wetting (Pusch and Karnland, 1996; Pusch et al., 2010; Wersin, 2007). The swelling capability of clay is important for sealing gaps between bentonite blocks, among related EBS components, and between EBS and surrounding host rock. Chemical alteration may also occur in the near-field host rock, which could reduce the clay capability for self-sealing within the excavation damaged zone (EDZ). As a result of the low permeability of a clay rock, a high temperature may induce significant pore pressure build-up (through pore water expansion and vaporization) in the near field, which could generate adverse mechanical deformation (such as fracturing), damaging the integrity of the host rock (Horseman and McEwen, 1996).

Table 5-1. Thermal constraints on EBS in different disposal concepts (based on Hicks et al., 2009)

Country	Concept	Thermal constraint (^oC)	Concerns
Belgium	Carbon steel container ; Concrete EBS; Clay NS	100	Steam generation (boiling)
Canada	Titanium container; Mixture of bentonite and sand for EBS; Granite NS	100	Crevice corrosion of titanium container and illitization in bentonite
Finland	Copper container ; Bentonite EBS; Crystalline rock NS	100	Chemical alteration (illitization and cementation by silica) and the subsequent mechanical effect, water boiling, corrosion of copper container, etc.
France	Carbon steel container; Bentonite EBS (or not); Clay NS	100 for NS	Not specified
Korea	Carbon steel+copper container; Ca-Bentonite EBS; Granite NS	100	Chemical alteration of bentonite and corrosion of canister surface
Japan	Carbon steel container; Bentonite EBS; NS (not specified)	100	Chemical alteration (illitization)
Spain	Carbon steel container; Bentonite EBS; Granite NS	100	Chemical alteration (precipitation of calcite, illitization)
Sweden	Copper container ; Bentonite EBS; Crystalline rock NS	100	Water boiling, excessive dry bentonite, corrosion of copper canister.

However, these concerns have not been addressed by rigorous scientific studies. For example, although steam generation will be enhanced at higher temperature, the boiling of water near the EBS-canister interface is quite unlikely to occur because after the EBS becomes hydraulically connected with the NS, it undergoes an increase in pore pressure that is largely dependent on the depth of the tunnel and is therefore much higher than atmosphere pressure. For a tunnel located at 500 m depth, and assuming hydrostatic conditions, the pore pressure is around 50 bars. At this condition the boiling point is 264 ^oC rather than 100 ^oC. Wersin et al. (2007), after reviewing a number of data sets, concluded that this criterion of 100^oC for the maximum temperature within the bentonite buffer is too conservative, based on their findings that no significant changes in bentonite properties occur at temperatures of at least 120^oC under wet conditions and bentonite is stable to even much higher temperature under dry conditions. Pusch (2000) and Pusch et al. (2003) also found that the swelling pressure of compacted bentonite was not significantly affected by heating up to 125 ^oC.

While there is some speculation on the impact of high temperature on a clay repository (e.g., Horseman and McEwen, 1996), a systematic and careful study of temperature-induced processes (including chemical alteration and mechanical deformation) and how they might affect repository performance is lacking in the literature. Up to now, the maximum allowable temperature, and what the impact of high temperature on repository performance might be, are largely open questions for a clay repository. In this report, we attempt to systematically study the temperature-induced processes in a clay disposal repository using the following tools:

- Detailed mechanistic THMC modeling that evaluates the chemical alteration and subsequent mechanical changes in bentonite and the clay formation under various scenarios (Section 5.2).
- Performance assessment level modeling that studies the impact of high-temperature THMC changes on radionuclide transport and other PA drivers (Section 5.3).
- A laboratory study that strengthens our understanding of physical and chemical alterations in buffer and backfill materials (bentonite) and clay host rock, as a result of heating (Section 5.4).

5.2 Detailed Mechanistic Modeling of THMC Alterations

As mentioned above, in this report we specifically address one type of repository, composed of a clay formation NS and a bentonite EBS. Bentonite is an impure clay consisting of swelling clay minerals such as smectite (or montmorillonite), non-swelling clay minerals such as illite and kaolinite, and other non-clay minerals such as quartz and feldspar. The mineralogical composition of a clay formation is similar to that of bentonite, except that it typically contains less smectite, more non-swelling clay and other non-clay minerals. Swelling is a key property of both the EBS bentonite and the clay formation because it plays an important role in lowering the permeability of the EBS, facilitating the EBS in providing mechanical support to surrounding tunnels, as well as EDZ self sealing. The swelling capacity of EBS bentonite is directly related to the abundance of smectite in the bentonite. Illitization, which refers to the transformation of smectite to illite, is of great importance, because it results in a loss of smectite and subsequently a loss in the swelling capacity of the EBS bentonite. Fairly extensive studies have been conducted to evaluate the occurrence of illitization in bentonite and clay formation; some of these studies are listed in Table 5-2 and a brief summary of each study is given below.

Table 5-2. List of studies on illitization in clay formation and bentonite

Reference	Illitization or not	Medium	Temperature	Research type
Pusch and Madsen (1995)	Yes	Kinnekulle bentonite, Sweden	130-400	Natural analogue
Kamei et al. (2005)	Yes	argillaceous rock formation	Up to 260	Natural analogue
Pusch et al. (2010)	No	MX-80 saturated with weakly brackish water	90-130	Lab test
Pusch et al. (2010)	No	Smectite clay grouts	130-200	Lab test
Mosser-Ruck and Cathelineau (2004)	No	Na- and Ca-smectite	150	Lab test
Caporuscio et al. (2012)	No	Bentonite from Colony, Wyoming	125-300	Lab test
Pacovsky et al. (2005), Stríček et al. (2009)	No	Fe-rich montmorillonite buffer	45-90	Mock up test
Pusch et al. (2010)	No	MX-80 bentonite	< 85	Field scale test
Montes-H et al. (2005a; 2005b; 2005c)	No	Treated MX-80 bentonite	100	Model
Marty et al. (2010)	Yes	MX-80 bentonite	100	Model

Illitization is clearly evidenced in geological system (Wersin et al., 2007), as exemplified by several natural analogue studies (Pusch and Madsen, 1995; Kamei et al., 2004; Cuadros, 2006; Casciello et al., 2011). Illite/smectite mixed-layer clay is commonly observed in the clayey sediments, and typically the deep formation contains more illite than shallow formation (Cuadros, 2006), which lead to a conclusion that smectite is gradually transformed to illite during diagenesis. Pusch and Madsen (1995) investigated the illitization of kinnekulle bentonite, a 5 m thick illite/smectite interlayers with upper and lower part having 50-70% illite and the central part 30-50% illite. This indicates that illitization proceeds from the surrounding environment and moves toward the center. The supply of diffusive potassium cation K^+ could not explain all the illitization, and the dissolution of accessory mineral might be one of the sources for K^+. In another analogue study concerning the Hamra clay on the island of Gotland, offshore Sweden (Pusch and Karnland, 1988), the evidence suggests that potassium availability for the smectite to illite reaction was limited by diffusive transport of potassium available in thicker marine sediments adjacent to the bentonite. Illitization is typically described in the clay science community with a kinetic model that relates the time derivative of illite (or smectite) mass fraction in the illite/smectite mixed layer to temperature, activation energy, and concentration of K^+, etc. But the details of the kinetic equations vary a great deal, as detailed in Cuadros (2006). The overall illitization rates encompass great uncertainties as well, because the assumptions regarding starting point and temperature history of the formation vary significantly from one case to another. For example, the illitization rate calibrated in Kamei et al. (2004) is two orders of magnitude higher than that in Cuadros (2006). However, even though they observe quite high illitization rate, Kamei et al. (2004) conclude that there would be little illitization if the temperature of the nuclear waste disposal repository is kept under 100 ^oC. In general, the natural analogue studies agree that temperature and the availability of K^+ (Casciello et al., 2011) are the primary factors that affect illitization. But as to the importance of availability of K^+ in illitization, Cuadros (2006) realized that this is a more complicated issue and therefore proposed to use 'effective K^+ concentration" in the illitization kinetic model to accommodate the effect of other actions like Ca^{+2}, Mg^{+2}, and Na^+.

Laboratory experiments that typically involve hydrating bentonite samples with various type of solutions and exposing the sample to different temperature conditions for a given time period, have been conducted to evaluate the degree of illitization in bentonite. Pusch et al. (2010) summarized two of these kinds of studies. In one study, samples of MX-80 clay saturated with weakly brackish water were heated from one end through radiation and contacted at the other end with a solution that contained about 300 ppm Na^+ and 10 ppm K^+. The temperature was about 130 ^oC at the radiation end, and 90 ^oC at the other end. Comparison of untreated and hydrothermally treated clay showed that there were almost no differences geochemically, but the treated sample became stiffer. In another study (Pusch et al., 1991), the clay was placed in large vessels with initially distilled water, a solution (10,000 ppm) of $CaCl_2$, and 50% artificial ocean water. Then the sample was heated to 200 °C. The most noticeable chemical change is the dissolution of calcite. K- and Na-feldspar dissolves slightly at 130 ^oC but completely dissolves at 200 °C. Increase in shear strength was also observed. In another study, Mosser-Ruck and Cathelineau (2004) heated Na- and Ca-smectite at 150 ^oC for two months in batch experiments. Three types of experimental solutions were used: 0.01 m NaOH, 1 M K_2CO_3 and mixtures of 1 or 3 M KCl with 10^{-4} or 10^{-2} m KOH. No chemical alteration was observed in the experiment with Na solution, whereas transformation of low-charge smectite to high-charge smectite was observed for K solutions, with byproducts of quartz, feldspars, zeolites and calcium silicate hydrates (CSH). Caporuscio et al. (2012) and Cheshire et al., (2013) conducted experiments with the bentonite from Colony, Wyoming, consisting of smectite with minor mineral impurities (feldspar, silicas, zeolites, pyrite). In the batch experiments described in Caporuscio et al. (2012), the sample was saturated with Na-Ca-K-Cl-based brine and cooked at ~160 bar and 125º to 300º C for one month. No significant mineralogical alteration of smectite was observed, and illite was not formed during these reactions. Cheshire et al. (2013) specifically focused their study on the stability and alteration of zeolites. The sample was immersed in a K-rich solution with 9:1 water:rock ratio. Experiments were performed at ~150 bars and T ≤ 300° C for four to six weeks. Clinoptilolite was altering to analcime through a possible recrystallization reaction. Cristobalite or opal-C was formed over the course of clinoptilolite transformation to analcime.

Pacovsky et al. (2005, cited in Pusch et al. 2010) performed a mockup test on the Czech buffer candidate "RMN" under repository-like conditions for two years. This buffer consisted of highly compacted blocks of clay with 75% Ca-Fe-montmorillonite, 10% finely ground quartz, and 5% graphite powder. The sample was emplaced in a cylinder, heated from inside with a constant temperature of 95 ^oC and saturated from the outer rings with solution that primarily contained Na and Cl. Chemical and mechanical changes exhibited spatial heterogeneity, with the most significant change occurring near the heater. Significant dissolution of the Fe-montmorillonite was observed, leading to the precipitation of iron minerals, causing cementation within the entire buffer. However, the dissolution of montmorillonite did not lead to the formation of illite. On the contrary, intergrowth of illite and kaolinite that was obvious in untreated clay dissolved near the heater after being exposed to heating and hydration. Also observed were a drop in swelling pressure and increase in hydraulic conductivity in the hot part of the buffer. The material from the Pacovsky et al. (2005) mockup test of was also analyzed in Stríček et al. (2009). Their results showed that no recrystallization occurred and the cation exchange capacity did not show any systematic changes.

While these laboratory and mockup tests have greatly improved our understanding of geochemical and mechanical alterations in EBS bentonite at high temperature, findings from these studies must be taken cautiously, because the experimental conditions deviated somewhat from the real repository conditions. Eventually, we have to rely on the field scale experiment to study the alterations at conditions of a real disposal repository. There are several field scale experiments ongoing or having been accomplished such as the FEBEX project (ENRESA, 2000). A large-scale 5-year field experiment at SKB's underground laboratory at Äspö (Pusch et al., 2010) was one of these tests: it carefully evaluated the alteration of clay minerals in bentonite by comparing the hydrothermal treated and untreated samples. The test was

conducted with a very dense MX-80 clay buffer surrounding a full-size copper-lined KBS-3 canister in an 8-meter-deep, 1.75 m diameter deposition hole in granite. Surface temperature of the canister was maintained at 85°C for a couple of years and at successively lower temperatures later in the experiment. The properties of a sample taken from the vicinity of the heater were analyzed. Chemical alteration of the montmorillonites was quite complicated—depending on the type of montmorillonite, different changes occurred. Montmorillonite in MX-80 clay can generally be grouped into two types: (1) montmorillonite with a normal charge as the end member of an illite/smectite mixed layers series, and (2) low-charge montmorillonite as the end member of dioctahedral vermiculite–smectite mixed layer phases. The frequency of type 1 montmorillonite within the illite/smectite mixed layers in the hydrothermally treated clay was actually higher than that of untreated clay, whereas the fraction of type 2 montmorillonite dropped in heated clay in comparison with untreated clay. But the overall interlayer charge of both montmorillonite decreased, due to the replacement of original Mg in the octahedral layer by Al, which should increase the swelling pressure according to the double-layer theory. In comparison with the untreated bentonite, this sample has much higher hydraulic conductivity but almost the same swelling pressure. Pusch et al. (2010) mentioned that the increase in hydraulic conductivity was probably caused by an alteration in micro-structural particle morphology.

Numerical modeling has also been used to study the chemical alteration in EBS and NS for time frame ranging from 1000 to 100,000 years. The geochemical changes in 1 m thick, fully saturated MX-80 bentonite, sandwiched between a canister and a unit full of geological fluid, were simulated in Montes-H et al. (2005a) under a constant temperature of 100 ^{o}C. MX-80 bentonite was pre-treated with Ca and Na chloride solution (the bentonite was composed of 85% Na/Ca-montmorillonite and 15% accessory minerals). Their simulations showed that Na/Ca-montmorillonite was converted to Ca-montmorillonite by cation exchange, and there was minimal neo-formation of saponites, vermiculites and chlorites. The swelling capacity of EBS bentonite was just slightly affected over 1000 years, based on an evaluation using a simplified method in which swell capacity is merely a function of the volume of swelling clay. In fact, Montes-H et al. (2005b), using the same method, predicted that the loss of swelling capability is only about 11% to 14%, even if Na/Ca-montmorillonite is completely converted to Ca-montmorillonite. The model in Montes-H et al. (2005a) was repeated in Montes-H et al. (2005c), but run for a longer time, up to 10000 years. This model predicted more drastic swelling capability loss at the EBS-NS interface, but in the rest of EBS, change of swelling capability was about 5 to 11%. Marty et al. (2010) used a similar model setup as in Montes-H et al. (2005a), except that the host rock was Callovo-Oxfordian argillite, and the corrosion of the steel canister was specifically considered. Their model results showed that significant illitization occurred near the EBS-NS interface after 10,000 years, and several Fe^{+2} minerals, such as chlorite and Fe-saponite, were formed near the canister.

There are also some laboratory tests that focus exclusively on the temperature effect of mechanical and hydrological changes. Villar and Lloret (2004) and Lloret and Villar (2007) reported that the swelling capacity of clay decreased at high temperatures (30-80 ^{o}C), although the influence of temperature was less evident when the applied stress was high. Furthermore, a decrease in swelling pressure as a function of temperature was observed. On the other hand, the measured increase in permeability with temperature was lower than expected on the basis of thermal changes in water kinematic viscosity. The transfer induced by temperature between intra-aggregate adsorbed water and inter-aggregate free water may explain most of the features observed, taking into account that the physical characteristics (density, viscosity) of water in each one of these two states are different. But Towhata et al. (1998) (cited in Hicks et al., 2009) seemed to reach the opposite conclusion, i.e., that no heating effects were observed on the liquid and plastic limits or on the amount of free swelling of this bentonite. The reason for that could be that their experiments used dried bentonite powder that had been cooled after heating at 60°C, 100°C, and

200°C for 5 days, and after which the bentonite powder was mixed with distilled water to measure the mechanical parameters. When they did that, the loss of physically bound water was reversible because the loss of chemically bound water was thought to occur at much higher temperatures (over 500°C for dehydroxylation or loss of OH groups from the clay crystal structure). If the temperature were above the water boiling point, how steam affects the mechanical properties of bentonite would also be debatable. Martin and Barcala (2005) reported an overheating even at the mockup for FEBEX bentonite. During the temperature transient, the total pressure increased due to the effects of thermally induced stresses and drying of the bentonite. However, after the transient, the total pressure reduced to levels lower than prior to the transient, indicating irreversible structural changes and reduced swelling capacity. This finding was consistent with a study by Couture (1985), who showed that the reaction of bentonite to steam at 150−250 °C resulted in rapid irreversible loss of swelling capacity, which could lead to increases in permeability. However, Pusch (2000) and Pusch et al. (2003) found that the swelling pressure of compacted bentonite was not significantly affected by heating up to 125 ^{o}C.

Current literature review thus shows that chemical alteration in the EBS bentonite and the NS clay formation is rather complicated, and that subsequent mechanical and hydrological changes, either caused directly by temperature increases or by geochemical reactions, are still a matter of debate. However, several general observations from these studies are : (1) although illitization is widely observed in geological systems (e.g., Pusch and Madsen, 1995), it has not been confirmed for EBS bentonite in either small scale laboratory experiments, or large scale mockup and field tests; (2) not forming illite does not mean smectite stays intact — rather, smectite undergoes various changes, including transformation of low-charge smectite to high-charge smectite (Mosser-Ruck and Cathelineau, 2004), conversion of Na/Ca-montmorillonite to Ca-montmorillonite (Montes-H et al., 2005a), dissolution of the Fe-montmorillonite (Pacovsky et al., 2005), and an increase in interlayer charge of montmorillonite as observed in the only field scale test (Pusch et al., 2010); (3) the role of K^+ in illitization and/or smectite alteration is well recognized in natural analogue studies (Cuadros, 2006) and supported by some laboratory studies (Mosser-Ruck and Cathelineau, 2004), but could be debatable; (4) the role of temperature in chemical alteration is not evident—studies with temperature as high as 300 ^{o}C (Caporuscio et al., 2012; Cheshire et al., 2013) did not lead to clear alteration of smectite; (5) as a result of heating, increase in permeability is observed in most studies, but the change in swelling capacity is inconclusive; (6) there is a lack of long-term, high temperature experimentation.

Illitization or alteration of smectite, as part of the entire chemical reaction network, cannot be evaluated in an isolated manner. Moreover, chemical reactions as a whole are one chain of the coupled processes that occur in the EBS bentonite and the NS clay formation. All these warrant a model that could take into account all relevant processes and consider their interactions. In this section, we report on our coupled THMC simulations to evaluate the chemical alterations and subsequent mechanical changes taking place while EBS bentonite and NS clay formation undergo simultaneously hydrological and thermal changes.

5.2.1 Technical approach

5.2.1.1 Simulator

The numerical simulations are conducted with TOUGHREACT Version 2 (Xu et al., 2011), a non-isothermal reactive transport simulator, and TOUGHREACT-FLAC3D, which integrates TOUGH-FLAC (Rutqvist, 2011) and TOUGHREACT Version 2 (Xu et al., 2011). TOUGH-FLAC3D sequentially couples the finite-difference geomechanical code FLAC3D with the finite-volume, multiphase fluid flow code, TOUGH2 (Pruess et al., 1999).

TOUGHREACT was written in Fortran 77 and developed by introducing reactive chemistry into the multiphase fluid and heat flow simulator TOUGH2 (Pruess et al., 1999). The code can be applied to one-, two-, or three-dimensional porous and fractured media with physical and chemical heterogeneity, and can accommodate any number of chemical species present in liquid, gas, and solid phases. A variety of subsurface thermal, physical, chemical, and biological processes are considered in TOUGHREACT code under a wide range of conditions of pressure, temperature, water saturation, ionic strength, and pH and Eh. TOUGHREACT Version 2 (Xu et al., 2011) is the latest version of TOUGHREACT. The major chemical reactions that can be considered in TOUGHREACT include aqueous complexation, acid-base, redox, gas dissolution/ exsolution, cation exchange mineral dissolution/precipitation, and surface complexation.

TOUGHREACT-FLAC3D was developed in Zheng et al. (2011) to provide the necessary numerical framework for modeling fully coupled THMC processes. It was equipped with a linear elastic swelling model (Zheng et al., 2012; Rutqvist et al., 2013) to account for swelling as a result of changes in saturation and pore-water composition. In this study, this linear elastic swelling model is further extended by incorporating the effect of changes in the abundance of swelling clay on stress.

5.2.1.2 Mechanical model

While development of a more comprehensive and rigorous chemical-mechanical model is underway (Davis et al., 2013), in this report we use a linear elastic swelling model that is extended by incorporating the changes in the abundance of swelling clay to evaluate the consequence of illitization on stress in EBS bentonite. The mechanical model for the clay formation is the same as in Rutqvist et al. (2013).

Rutqvist (2011) included a linear elastic swelling model using a swelling stress, σ_s, that is linearly proportional to the saturation:

$$d\sigma_s = 3K\beta_{sw} ds_l \tag{5-1}$$

where K is the bulk modulus and β_{sw} is a moisture swelling coefficient. In this report, β_{sw} is 0.238 (Rutqvist, 2011).

To consider the swelling due to both moisture and chemical concentration changes, we include the stress due to a change of chemical concentration and abundance of swelling clay:

$$d\sigma_s = 3K\beta_{sw} ds_l + A_n dC + A_{sc} dm_s \tag{5-2}$$

where A_n is a constant that linearly relates chemical concentration (C) variation and the corresponding stress change, and Laredj et al. (2010) proposed the following expression for A_n:

$$A_n = \frac{(5.312 \ln C - 23.596)}{\sqrt{C}} - \frac{7.252 \times 10^{-4}}{C^2} \tag{5-3}$$

A_{sc} is a constant that relates the changes in mass fraction of swelling clay, m_s, to the stress. An empirical value is derived from published data in this report.

If a linear regression curve can be found for swelling pressure versus the mass fraction of smectite, A_{sc} would be the slope of the linear regression curve. Karnland et al. (2006) is one of the few studies in which both the swelling pressure data and smectite mass fraction are available for various bentonites. Table 5-3 is one example of measured swelling pressure reported in Karnland et al. (2006). It shows that swelling pressure is a function of the dry density and the ion concentration of the solution used to saturate the bentonite samples. To make use of these data to derive A_{sc}, we narrow down to the swelling pressure measured with deionized water ("H_2O" in Table 5-3). Because in this report, the EBS is Kunigel VI bentonite that has a dry density of 1600 kg/m^3, we focus on those data for dry density of 1600 kg/m^3. If there were no data available for a dry density of exactly 1600 kg/m^3, as in the case for Czech reference material in Table 5-3, we first derive a relationship between swelling pressure and dry density for a particular bentonite, and based on that derivation, we calculate the swelling pressure for dry density of 1600 kg/m^3. The same process is repeated for other bentonites. Finally, the swelling pressure versus mass fraction of smectite of various bentonites is plotted in Figure 5-1. A linear regression is conducted to these data, which leads to a slope of 9.3×10^6. But a R^2 of 0.4 indicates that the scatter of these data cannot be fitted with one linear relationship. Slopes ranging from 9.3×10^6 to 1.4×10^7 could also be possible. To be conservative, we use A_{sc} of 1.4×10^7 to evaluate the effect of changes in the abundance of smectite on the stress in this report.

Table 5-3. Swelling pressures in the Czech reference materials. The first column shows clay dry density (D_d) in kg/m^3 and the following columns show the $CaCl_2$ concentrations (moles/L) in the test solutions successively in contact with the samples. Pressure values in kPa (Karnland et al., 2006).

Material	D_d, kg/m^3	H_2O	0.1 M	0.3 M	1.0 M	3.0 M	0.1 M
DnR1	849	10					
	1,386	360	340	320	270	210	330
	1,342	280	270	270	250	200	260
RoR1	816	50					
	1,156	523					
	1,474	7,150					
SkR1	936	43	36	36	36	28	36
	1,274	563	524	511	480	350	540
	1,565	6,300	6,270	6,260	6,100	5,400	6,300
StR1	949	83	75	75	75	74	75
	1,236	200	170	160	145	110	170
	1,618	5,500	5,300	5,200	4,700	3,600	4,900

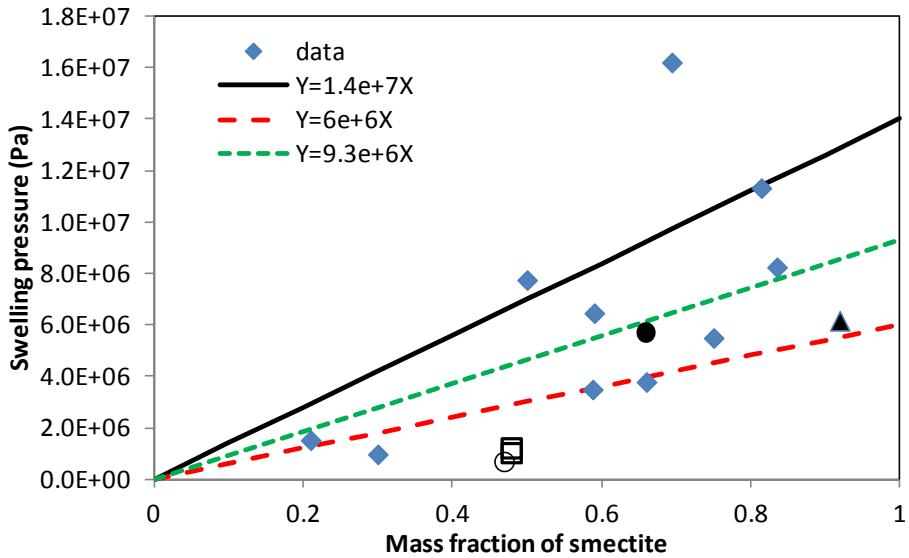

Figure 5-1. Swelling pressure versus mass fraction of smectite for various bentonites. ▲, FEBEX bentonite (ENRESA, 2000); ●, Montigel bentonite (Bucher and Muller-Vonmoos, 1989); □, Kunigel VI bentonite (JNC, 1999); ○, Kunigel bentonite (Konime and Ogata, 1996), ♦ are data for reference material from Czech, Danish, Friedland, Milos Deponit CA-N, Kutch (Indian) and Wyoming MX-80 (Karnland et al., 2006).

5.2.1.3 Chemical model

In this generic case, it is assumed that the EBS is composed of Kunigel-V1 bentonite (Ochs et al., 2004) and the mineral composition of the bentonite is listed in Table 5-4. It is also assumed that the host rock is Opalinus Clay with the mineral composition listed in Table 5-4 as well. The measured mineralogical composition of Opalinus Clay varies remarkably probably because of the spatial heterogeneity in mineralogical composition and the analytical method used. For example, Bossart (2011) summarized measured mineralogical composition from Waber et al. (1998), De Canniere (1997), Thury and Bossart (1999), and NAGRA (2003), and reported that the illite/smectite mixed layer ranges from 5% to 11%. However, Lauber et al., (2000) reported that the illite/smectite mixed layer ranges from 14% to 22%. In this report, the mineralogical compositions (Table 5-4) are the average of the Bossart (2011) and Lauber et al., (2000).

Table 5-4. Mineral volume fraction (dimensionless, ratio of the volume for a mineral to the total volume of medium) of the bentonite (Ochs et al., 2004) and the clay formation (Bossart, 2011; Lauber et al., 2000) used in the model.

Mineral	**Clay formation : Opalinus Clay**	**EBS Bentonite: Kunigel-V1**
Calcite	0.093	0.016
Dolomite	0.050	0.018
Illite	0.273	0.000
Kaolinite	0.186	0.000
Smectite	0.035	0.314
Chlorite	0.076	0.000
Quartz	0.111	0.228
K-Feldspar	0.015	0.029
Siderite	0.020	0.000
Ankerite	0.045	0.000

The pore-water composition of the bentonite (Ochs et al., 2004) and the clay formation (Fernandez et al., 2007) are listed in Table 5-5. The initial water for EBS bentonite was taken from Sonnenthal et al. (2008) and used in the benchmark for the DECOVALEX-THMC project (Sonnenthal et al., 2008).

Table 5-5. Pore-water composition of EBS bentonite and host clay rock.

	EBS Bentonite: Kunigel-V1	**Clay formation : Opalinus Clay**
pH	8.40	7.40
Eh	0.268	0.268
Cl	1.50E-05	3.32E-01
SO_4^{-2}	1.10E-04	1.86E-02
HCO_3^-	3.49E-03	5.18E-03
Ca^{+2}	1.37E-04	2.26E-02
Mg^{+2}	1.77E-05	2.09E-02
Na^+	3.60E-03	2.76E-01
K^+	6.14E-05	2.16E-03
Fe^{+2}	2.06E-08	3.46E-06
$SiO_2(aq)$	3.38E-04	1.10E-04
AlO_2^-	1.91E-09	3.89E-08

Mineral dissolution/precipitation is kinetically controlled. The kinetic law for mineral dissolution/precipitation is given in Xu et al. (2011). The kinetic rate for the mineral considered in current model is given in Table 5-6. Note that the surface areas listed in Table 5-6 are calculated for tuff (Sonnenthal et al., 2005). Their applicability to a clay formation is thought to be questionable. Further refinement of the surface-area calculation is needed in the future, when the model is applied to a realistic scenario.

Table 5-6. Kinetic properties for minerals considered in the model (Xu et al., 2006).

Mineral	**A (cm^2/g)**	**Parameters for Kinetic Rate Law**							
		Neutral Mechanism		**Acid Mechanism**			**Base Mechanism**		
		k_{25} ($mol/m^2/s$)	**E_a (KJ /mol)**	**k_{25}**	**E_a**	**$n(H^+)$**	**k_{25}**	**E_a**	**$n(H^+)$**
Primary:									
Quartz	9.8	1.023×10^{-14}	87.7						
K-feldspar	9.8	3.89×10^{-13}	38	8.71×10^{-11}	51.7	0.5	6.31×10^{-12}	94.1	-0.823
Kaolinite	151.6	6.91×10^{-14}	22.2	4.89×10^{-12}	65.9	0.777	8.91×10^{-18}	17.9	-0.472
Illite	*1.18×10^{4}	1.66×10^{-13}	&105						
Chlorite	9.8	3.02×10^{-13}	88	7.76×10^{-12}	88	0.5			
Calcite	3.5	1.6×10^{-7}	23.5						
Dolomite	12.9	2.52×10^{-12}	62.76	2.34×10^{-7}	43.54	1			
Ankerite	9.8	1.26×10^{-9}	62.76	6.46×10^{-4}	36.1	0.5			
Smectite	*1.18×10^{4}	1.66×10^{-13}	&105						

*were calibrated based on the field illitization data (see section 5.5.2.2)

& from Pusch and Madsen (1995)

Table 5-7 lists the thermal and hydrodynamic parameters used in the model. The majority of these parameter are taken from Sonnenthal (2008) for the EBS bentonite and Thury (2002) for the NS clay formation. Permeability for the clay formation is from Soler (2001) and that for the bentonite is from JNC (2000).

Table 5-7. Thermal and hydrodynamic parameters.

Parameter	Clay formation : Opalinus Clay	EBS Bentonite: Kunigel-V1
Grain density [kg/m^3]	2450	2700
Porosity ϕ	0.162	0.33
Saturated permeability [m^2]	2.0×10^{-20}	2.0×10^{-21}
Relative permeability, k_{rl}	$m = 0.6$, $S_{rl} = 0.01$	$K_{rl} = S^3$
Van Genuchten α [1/Pa]	6.8×10^{-7}	3.3×10^{-8}
Van Genuchten m	0.6	0.3
Compressibility, β [1/Pa]	3.2×10^{-9}	5.0×10-8
Thermal expansion coeff., [1/^{o}C]	0.0	1.0×10^{-4}
Dry specific heat, [J/kg ^{o}C]	860	800
Thermal conductivity [W/m ^{o}C] dry/wet	1.48/1.7$^\$$	1.1/1.5
Tortuosity for vapor phase	$\phi^{1/3} S_g^{10/3}$	$\phi^{1/3} S_g^{10/3}$

$^\$$from http://www.mont-terri.ch/internet/mont-terri/en/home/geology/key_characteristics.html

5.2.2 Technical results

5.2.2.1 Model setup and TH evolution in the EBS and NS

The THMC model simulates a hypothetical bentonite-back-filled nuclear waste repository in clay rock, a repository example that involves a horizontal nuclear waste emplacement tunnel at 500 m depth (Figure 5-2) (Rutqvist et al., 2009) and has been used in the DECOVALEX IV project (Rutqvist et al., 2009) and UFD program (e.g., Zheng et al., 2012). The numerical model was constructed with a geometry containing one circular tunnel and consisting of 368 grid blocks. The configuration of the model is shown in Figure 5-3. The Z-axis is set as vertical in the model, while the horizontal Y- and X-axes are aligned parallel and perpendicular to the emplacement tunnel, respectively. Note here that the canister is modeled only as a heat source—the THC changes in canister and its interaction with EBS bentonite are not considered here for simplicity's sake.

An initial stress field is subjected to the self-weight of the rock mass. Zero normal displacements are prescribed on the lateral boundaries of the model. Vertical displacements are prevented at the bottom. The model simulation was conducted in a nonisothermal mode with a time-dependent heat power input (Rutqvist et al., 2009), adopted from the heat load developed for the Generic Disposal System Environment (GDSE) within the UFD for Pressurized Water Reactor (PWR) used nuclear fuel.

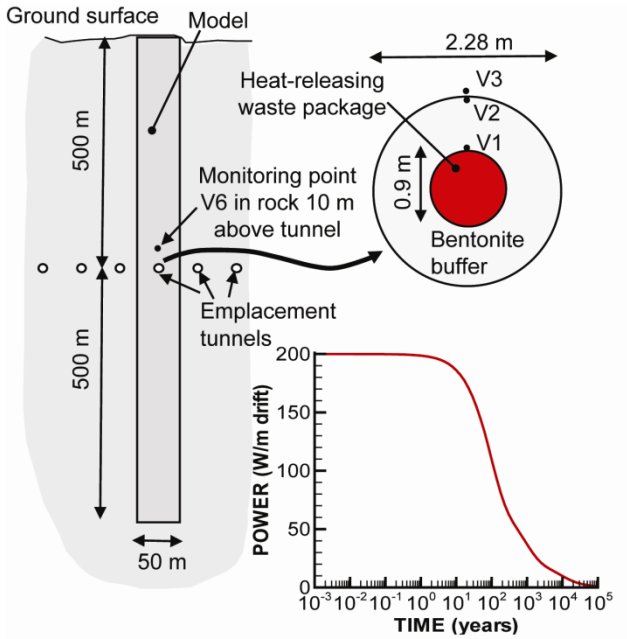

Figure 5-2. Domain for the test example of a bentonite back-filled horizontal emplacement drift at 500 m (Rutqvist et al., 2009).

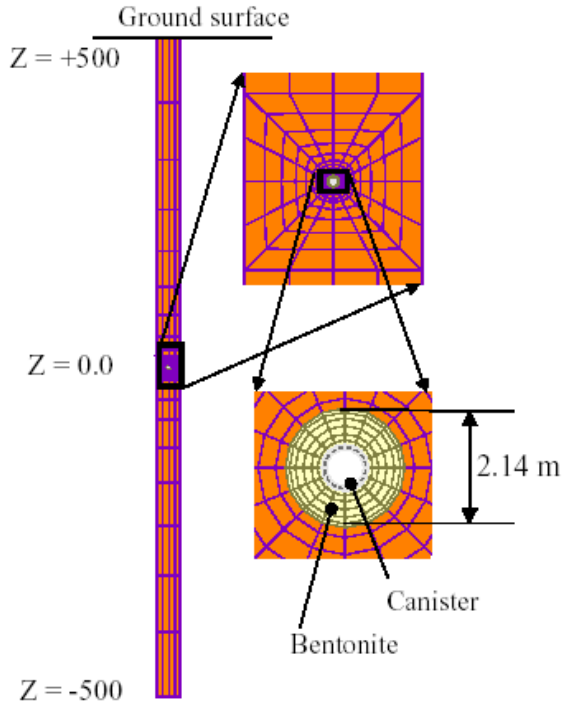

Figure 5-3. Mesh for modeling of horizontal emplacement drift at 500 m depth.

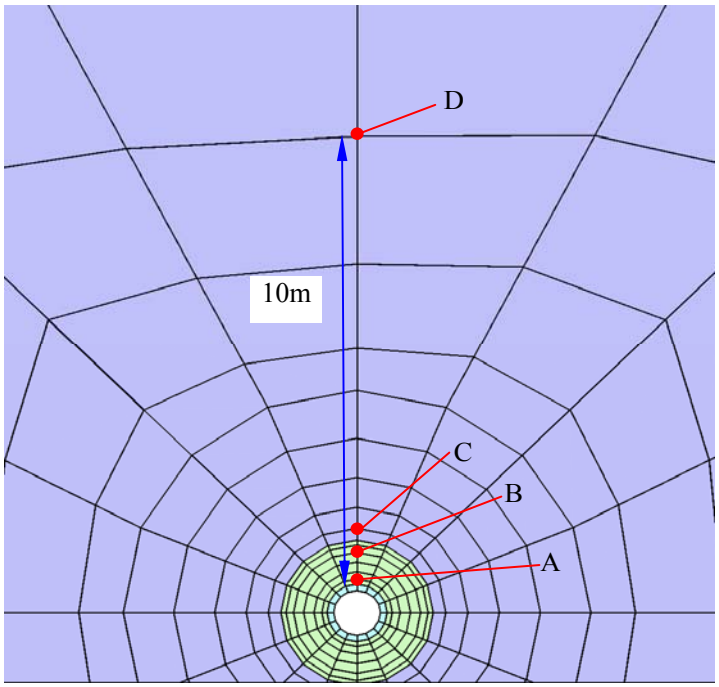

Figure 5-4. Location of key points for monitoring parameter variations in numerical simulations.

The time function for heat release is shown in Figure 5-2. Heat release rates are adjusted to make two cases for comparison: a "high T" case, in which the temperature near the canister can reach about 200 °C; and a "low T" case, in which the temperature near the canister peaks at about 100 °C. The temporal evolution of temperature at four monitoring points A, B, C, and D (see Figure 5-4 for their position) is shown in Figure 5-5. In 1000 years, the EBS bentonite undergoes >120 °C heating for the "high T" case, whereas it stays around 60-70 °C in the "low T" case. Figure 5-6 shows the water saturation degree at these four points. It takes about 20 years for the low T case to fully saturate EBS bentonite, and about 25 years for the "high T" case.

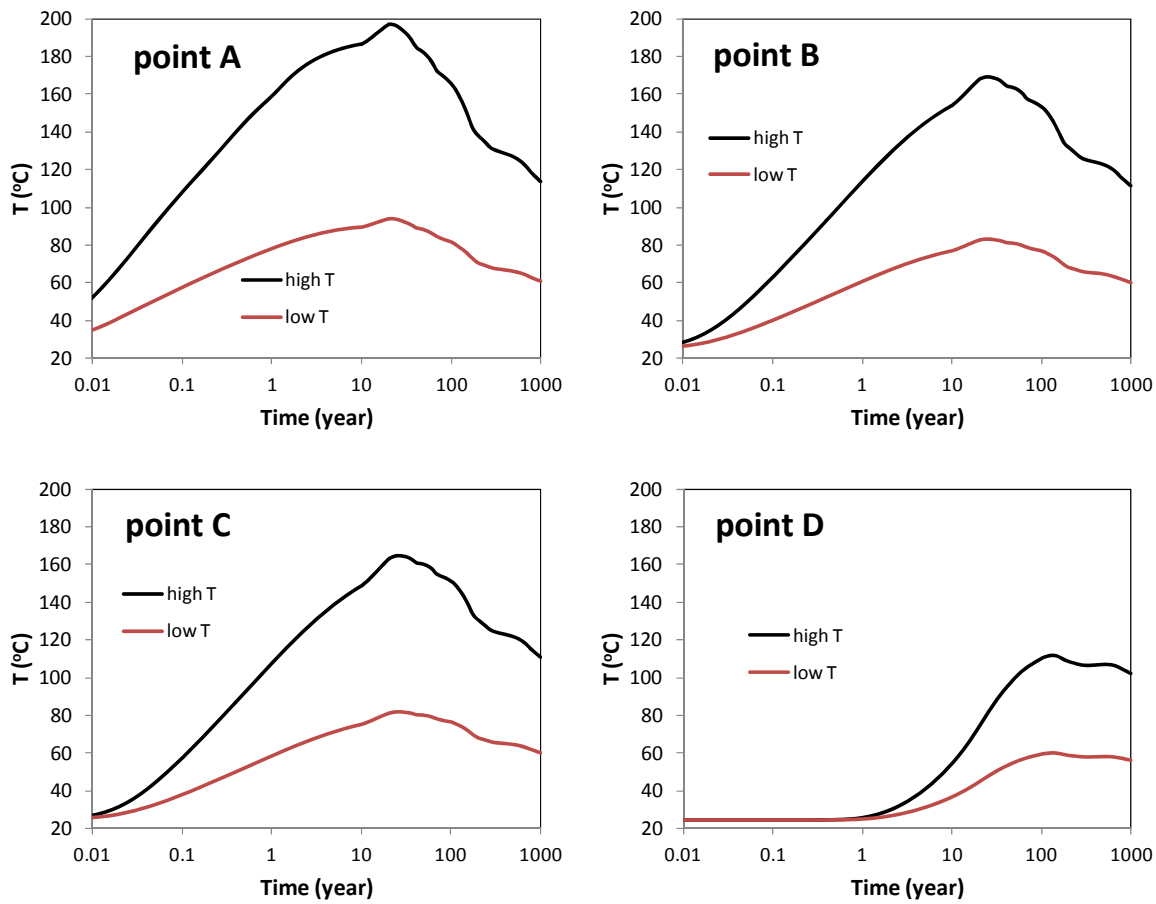

Figure 5-5. The temporal evolution of temperature at point A (near the canister), point B (inside the bentonite and near the EBS-NS interface), point C (inside the clay formation and near the EBS-NS interface), and point D (in the far field with a distance from canister of 10 m).

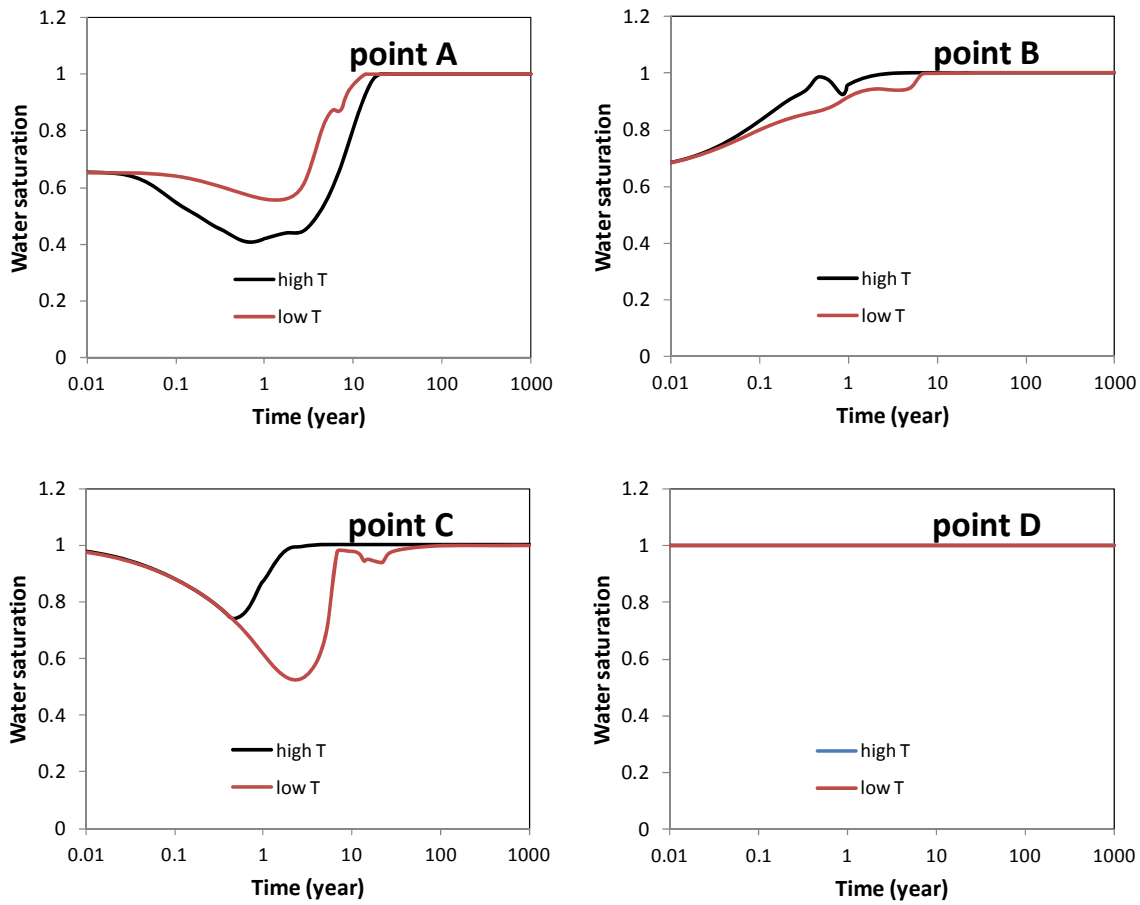

Figure 5-6. The temporal evolution of water saturation at point A (near the canister), point B (inside the bentonite and near the EBS-NS interface), point C (inside the clay formation and near the EBS-NS interface), and point D (in the far field with a distance from canister of 10 m).

5.2.2.2 Calibration of the illitization rate against field data

The dissolution/precipitation rate of illite and smectite is obviously critical in determining the degree of illitization. Typically the reaction rate is determined by a rate constant and the specific surface area of the mineral of interest, as shown in the following Equation (Xu et al., 2006), which has been used in TOUGHREACT-FLAC:

$$r = kA\left|1 - \left(\frac{K}{Q}\right)^{\theta}\right|^{\eta} \tag{5-4}$$

where r is the kinetic rate, k is the rate constant (mol/m^2/s) which is temperature dependent, A is the reactive surface area per kg water, K is the equilibrium constant for the mineral–water reaction written for the destruction of one mole of mineral, and Q is the reaction quotient. Here, for simplicity, the exponents θ and η are assumed equal to 1. The reactive surface area, A, is a function of the mineral specific surface area (e.g., cm^2/g$_{mineral}$) and the volume fraction of the mineral in the sediment. Because many rate constants are reported at 25°C, it is convenient to approximate rate constant dependency as a function of temperature, thus

$$k = k_{25} \exp\left[\frac{-E_a}{R}\left(\frac{1}{T} - \frac{1}{298.15}\right)\right] \tag{5-5}$$

where E_a is the activation energy (kJ/mol), k_{25} is the rate constant at 25°C, R is gas constant, and T is absolute temperature.

The dissolution/precipitation rate could vary significantly. For example, Zhu et al. (2005) reported that the discrepancy between laboratory-scale and field-scale measurements of effective reaction rates for silicate minerals is up to 5-6 orders of magnitude. The variation in reaction rates could have many different causes: Reactive surface area is the primary source of uncertainty, with the rate constant less uncertain but still causing remarkable variation. While researchers are attempting to reduce the discrepancy between reaction rates measured at laboratory scale and field scale, it is always recommended to calibrate the reaction rate based on field data if the model is designed for evaluating large-scale and long-term changes. In this report, we therefore firstly calibrate the illitization rate (the rate of illite precipitation and smectite dissolution) based on the measured illite percentage in an illite/smectite (I/S) mixed layer from Kinnekulle bentonite, Sweden (Pusch and Madsen, 1995).

The bentonite layer is located in the Kinnekulle hill area, ~95 meters below the diabase cap (Figure 5-7). It is about 2 meters thick. Mineralogical characterization carried out by Swedish Geological Survey found that illite percentages (I%) in I/S mixed layer measured for samples taken from depths of 5.9 to 7.1 m (See Table 5-8) show a lesser degree of illitization towards the center of the bentonite layer. These data will be used to calibrate the illitization rate.

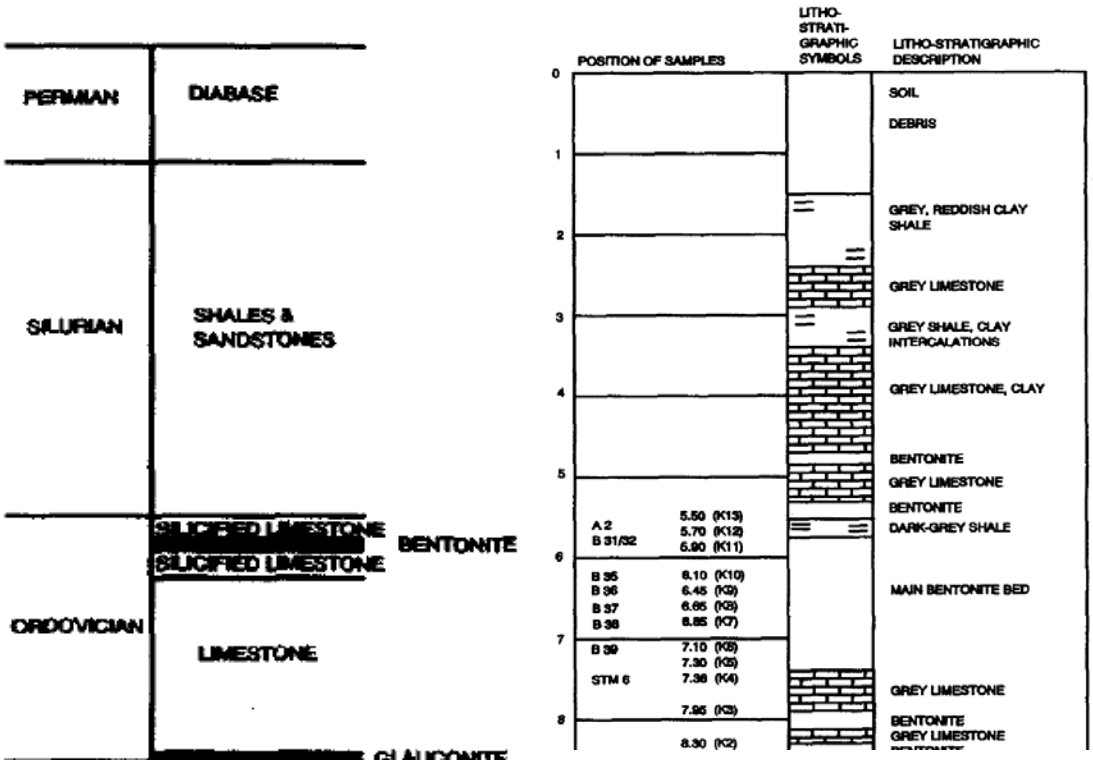

Figure 5-7. The Kinnekulle strata (left) and detailed stratigraphy of the about 2 m thick bentonite bed and adjacent strata (right). Scale denotes stratigraphic distance in meters from top of exposure (from Pusch and Madsen, 1995).

Table 5-8. Mineral content in the < 1/~m fraction (evaluated from Brusevitz, 1986, cited in Pusch and Madsen, 1995).

Sample no. [Fig. 2]	Distance [m] below level zero	Minerals in <1 μm fraction		
		I% in I/S	Q and K [wt%]	
K13	5.50			
K12	5.70			
K11, B31	5.90	52–65	5	2
K10, B35	6.10	41–54	8	4
K9, B36	6.45	37–54	5	5
K8, B37	6.65	38–51	5	2
K7, B38	6.85	36–49	3	3
K6, B39	7.10	32–46	2	2
K5	7.30			
K4	7.36			
K3	7.95			
K2	8.30			
K1	9.20			
K71	10.10	59–70		

The illitization processes at this site had been studied extensively because of its relevance to the repository of highly radioactive waste. Inoue et al (1990) concluded that the dominant process of conversion for a smectite precursor in the Kinnekulle clay was cationic substitution, described as a solid-state transformation mechanism. However, Pusch and Madsen (1995) proved that it was actually the neoformation of a separate illite phase that was dominant. Based on the concept proposed by Pusch and Madsen (1995), we established a reactive transport model to simulate the illitization process. The major assumptions in the models are (1) magma intrusion forming the diabase results in a heating period of 1000 years, with temperature ranging between 100°C and 160°C; (2) initially, the bentonite layer is composed exclusively of smectite, and illitization occurs exclusively during the heating period; and (3) a constant K^+ concentration of 0.05 mol/L in the formation above the bentonite layer supplies K^+ by diffusion. Figure 5-8 compares measured and computed illite percentages (I%), and best fit is acheived with a reaction rate ranging from 4.5×10^{-14} to 2.4×10^{-13} mol/g/s. In order to fit the average of measured I%, we need to increase the surface area from 115 cm^2/g (Sonnenthal et al., 2005) to 1.18×10^4 cm^2/g, but keep the reaction constant at 1.66×10^{-13} $mol/m^2/s$, leading to an illitization rate of 1.9×10^{13} mol/g/s.

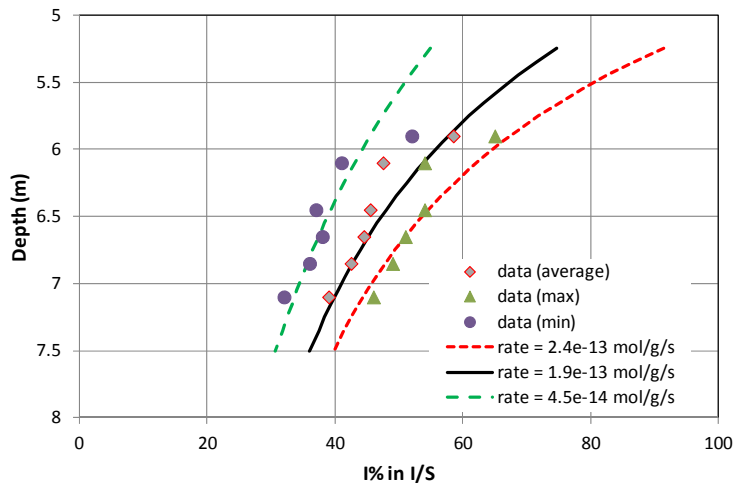

Figure 5-8. Measured illite percentage (I%) in the Kinnekulle bentonite layer (Pusch and Madsen, 1995) and model results with difference illitization rate.

5.2.2.3 Chemical alteration of the EBS and the NS clay formation

Clay minerals are the major component in bentonite and clay rock. In this section, we focus largely on the change to clay minerals, especially smectite and illite. Clay minerals are compositionally complex hydrous aluminum silicates and have a continuous sheet structure. The layers are typically described as octahedral (O) and tetrahedral (T). The octahedral layer is called dioctahedral if it contains two Al^{+3} coordinated with O^{-2} or OH^{-}. Tetrahedral layers are composed of cations fourfold coordinated with six O^{-2} or OH^{-}. The dominant cation is Si^{+4}, but may also be Al^{+3}. Both smectite and illite have a repeated T:O:T structure. The substitution of Al^{+3} in the octahedral layer with bivalence cations, or the replacement of Si^{+4} in the tetrahedral layer with Al^{+3} or Fe^{+3}, results in a negative charge in the clay crystal, which is usually compensated by interlayer cations. Smectite differs from illite in the interlayer charge and the interlayer cations. Illite has more Al^{+3} substitution for Si^{+4} in the tetrahedral layer and therefore higher interlayer charge, and the interlayer cations are predominantly K^{+}, held electrostatically and fairly strongly between adjacent tetrahedral layers—it therefore does not swell. Smectite has less isomorphous substitution and less interlayer charge; interlayer cations are typically Ca^{+2}, Mg^{+2}, Na^{+} and smectite swells. Illitization refers to the transformation of smectite to illite. Consensus has not yet been reached with regard to the details of the reaction process (Wersin et al., 2007). But in general, two mechanisms could be at play (Wersin et al., 2007): (1) solid state transformation by substitution of intracrystal cations (e.g., Cuadros and Linares, 1996) or (2) a dissolution–precipitation process (e.g., Mosser-Ruck et al., 1999). Either transformation process could occur, depending on the physico-chemical conditions (Cuadros and Linares, 1996). In our current model, we consider only the second illitization mechanism, i.e., the dissolution of smectite and precipitation of illite.

Although illitization is the focus while discussing chemical alteration of EBS bentonite and NS clay formation, changes of other minerals are briefly discussed as well because they are either the byproducts of, or interfere with, the illitization process.

The base case

As mentioned in the previous section, illitization is modeled as the dissolution of smectite and precipitation of illite. The overall reaction can be written as:

$$\text{Smectite} + 0.52H^{+} + 0.63AlO_2^{-} + 0.6K = \text{illite} + 0.26H_2O + 0.08Mg^{+2} + 0.33Na^{+} + 0.5SiO_2(aq)$$

Note that in the current model, Na-smectite, a smectite with Na dominating the interlayer cations, is used. If Ca-smectite is used, Ca is involved in the reaction as well. Many factors can trigger the chemical reaction, such as initial water-mineral disequilibrium in bentonite (since the water used for making bentonite blocks is not necessarily in equilibrium with the mineral phase in bentonite, and it takes time to reach that equilibrium), as well as thermal and hydrological disturbances. In the base model, results confirm that the clay formation undergoes illitization that is widely observed in the geological system (e.g. Wersin et al., 2007; Pusch and Masden, 1995), as illustrated by the smectite dissolution at point C and D in Figure 5-9 and illite precipitation at point C and D in Figure 5-10. Smectite dissolution and illite precipitation at point D for the "low T" case represent, for the most part, the illitization occurring at an undisturbed condition, except that the temperature is a little higher than the ambient condition in the clay

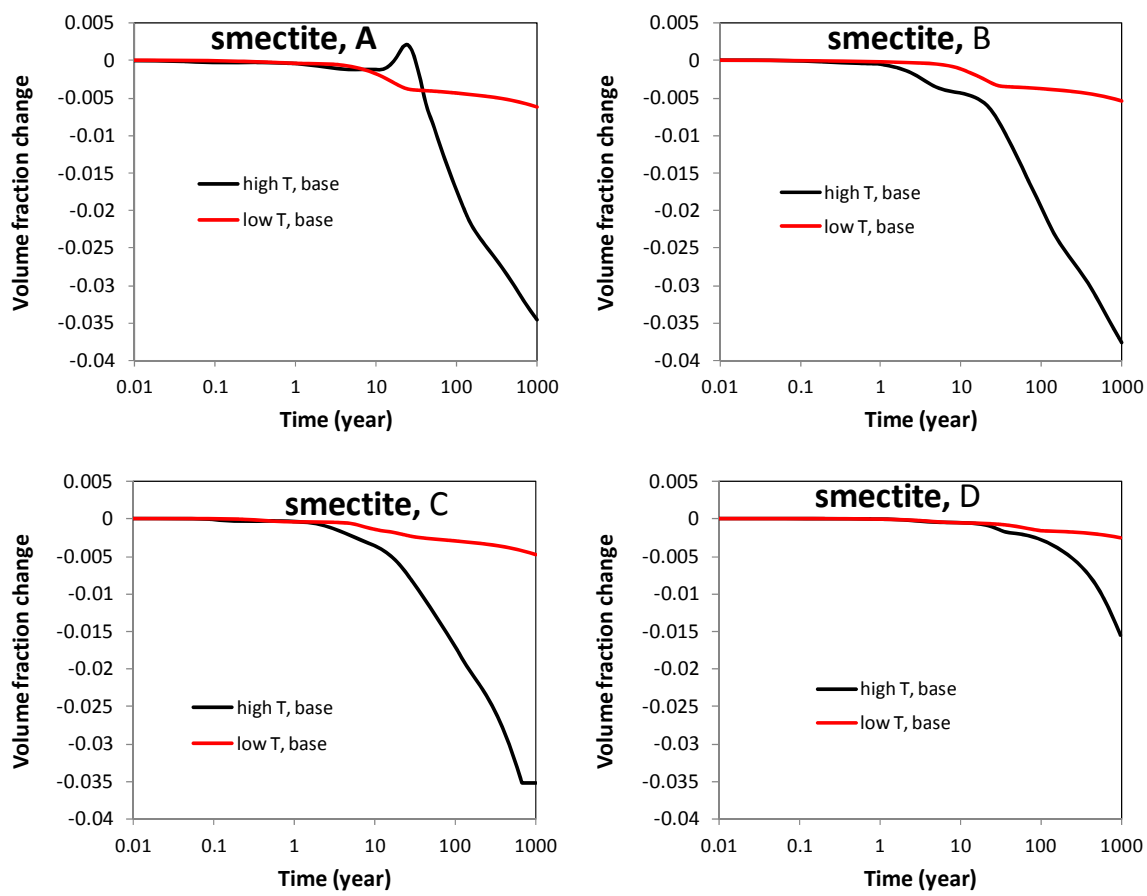

Figure 5-9. The temporal evolution of smectite volume fraction at point A (near the canister), point B (inside the bentonite and near the EBS-NS interface), point C (inside the clay formation and near the EBS-NS interface), and point D (in the far field with a distance of canister of 10 m).

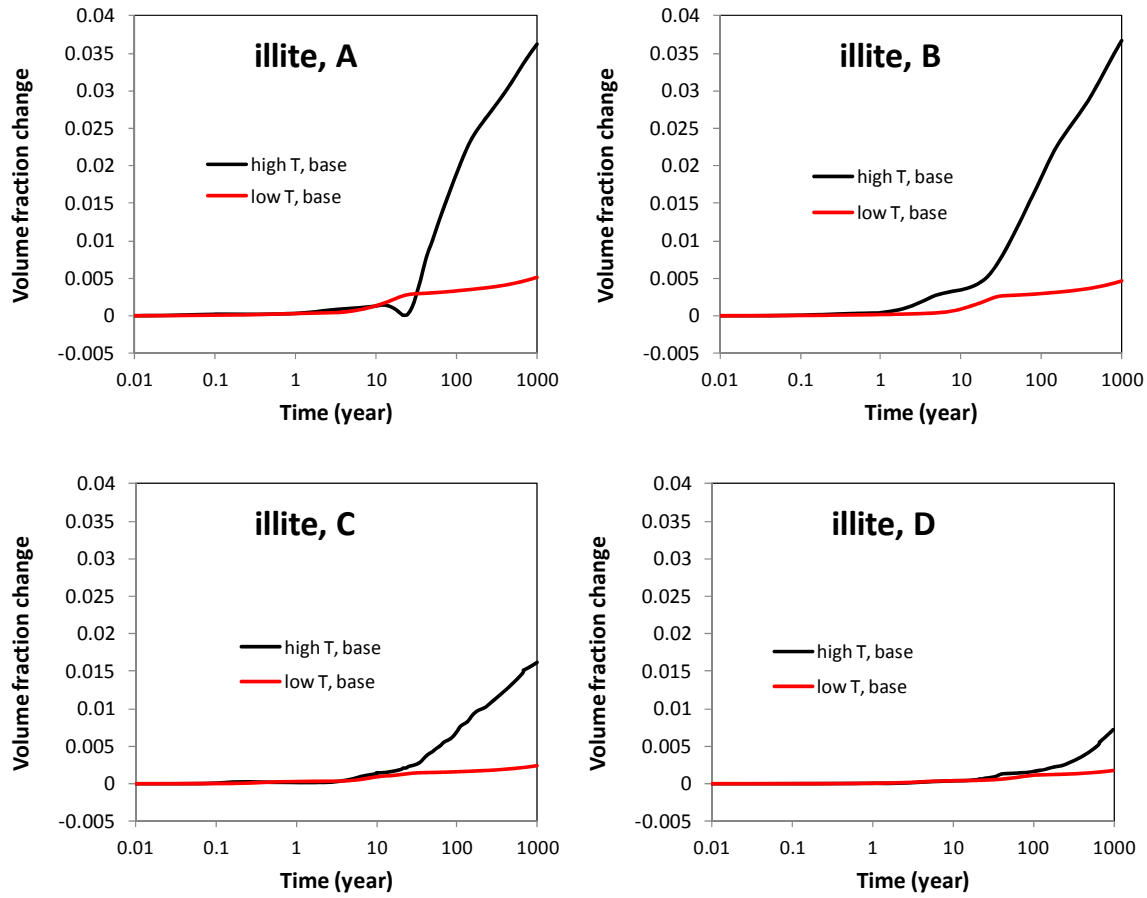

Figure 5-10. The temporal evolution of illite volume fraction at point A (near the canister), point B (inside the bentonite and near the EBS-NS interface), point C (inside the clay formation and near the EBS-NS interface), and point D (in the far field with a distance of canister of 10 m).

formation. It is a relatively slow process, and the volume fraction of smectite decreases only about 0.002 in 1000 years. If the temperature is higher, as shown with the smectite dissolution and illite precipitation at point D for the "high T" case, illitization is clearly accelerated, as shown by a decrease of 0.015 in the smectite volume fraction. At point C, located near the EBS-NS interface, more hydrological and chemical interactions between bentonite and the clay formation take place. Subsequently, more smectite dissolves and illite precipitates. For the "high T" case, the smectite volume fraction decreases by 0.035. This means about an 11% loss of smectite in comparison to the initial volume fraction of smectite of 0.314.

Illitization also occurs in bentonite, as shown by the smectite and illite volume fraction changes at point A and B in Figures 5-9 and 5-10. This is caused, first, by the initial disequilibrium between the pore-water solution and the mineral phase. Table 5-9 shows the initial saturation indexes of mineral phases. Initially, the pore water in bentonite is oversaturated with respect to illite and undersaturated with respect to smectite. Second, pore water in the clay formation contains a much higher concentration of K and Al, and provides a source of Al and K for the bentonite through diffusion and advection, which is manifested by

the increase in Al and K concentrations at point A (Figure 5-11). Note that the increase in Al and K concentrations in bentonite is caused not only by diffusion and advection, but also by the dissolution of other minerals, such as K-feldspar and quartz. Third, the increase in temperature is also in favor of illitization. Note that pore water in the clay formation also has a higher concentration of Mg and Na, which results in an increase in their concentration due to diffusion and advection (Figure 5-12), which inhibits the illitization. But it seems that the factors in favor of illitization outpace those against illitization. At the end of 1000 years, smectite volume fraction decreases by 0.035 and illite volume fraction increases by 0.035. Clearly the "high T" case demonstrates stronger illitization than the "low T" case.

Table 5-9. Saturation indexes of initial pore water in bentonite with respect to the minerals considered in the model.

Mineral	Saturation index (log(Q/K))
Calcite	-0.11
Illite	1.36
Chlorite	-0.02
Kaolinite	-1.15
Na-smectite	-1.93
Quartz	0.27
k-feldspar	-0.50
Siderite	-2.71
Dolomite	0.10
Ankerite	-1.56

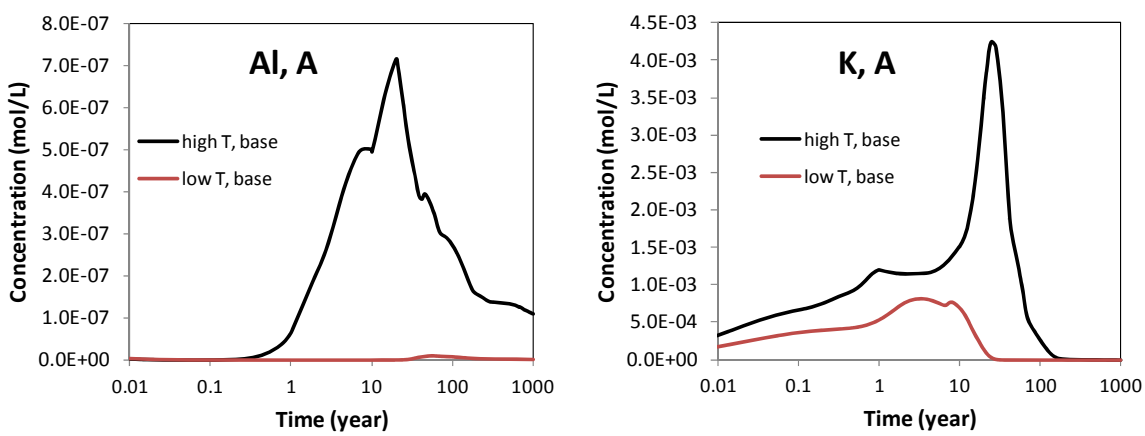

Figure 5-11. The temporal evolution of Al and K concentration at point A (near the canister).

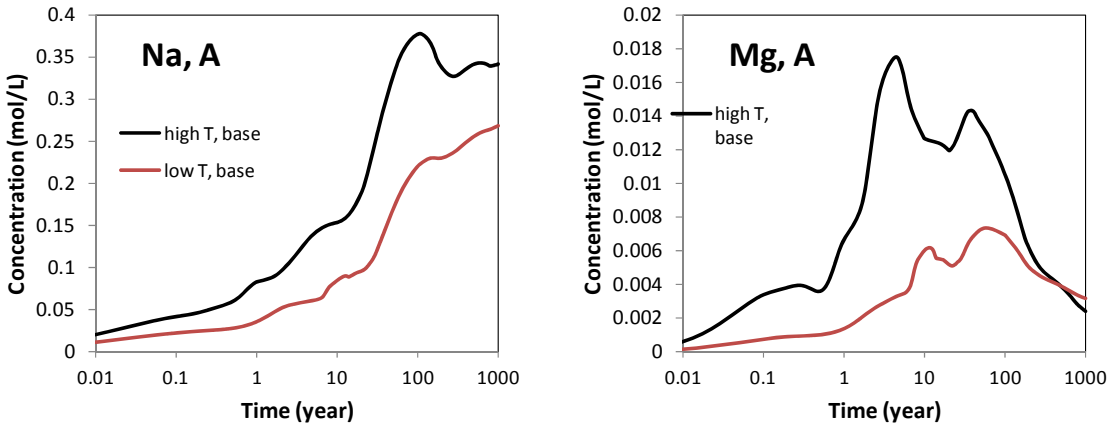

Figure 5-12. The temporal evolution of Na and Mg concentration at point A (near the canister).

Dissolution of K-feldspar and precipitation of quartz is also observed in the model results; their effect on illitization will be discussed in the following section. Calcite dissolution observed in the laboratory test (Pusch et al., 1991) is also shown in our current simulation (Figure 5-13). But calcite dissolution in EBS bentonite only occurs during the hydration period. Calcite dissolution plays a less significant role in illitization but is important in controlling the acid-base conditions in the EBS and NS.

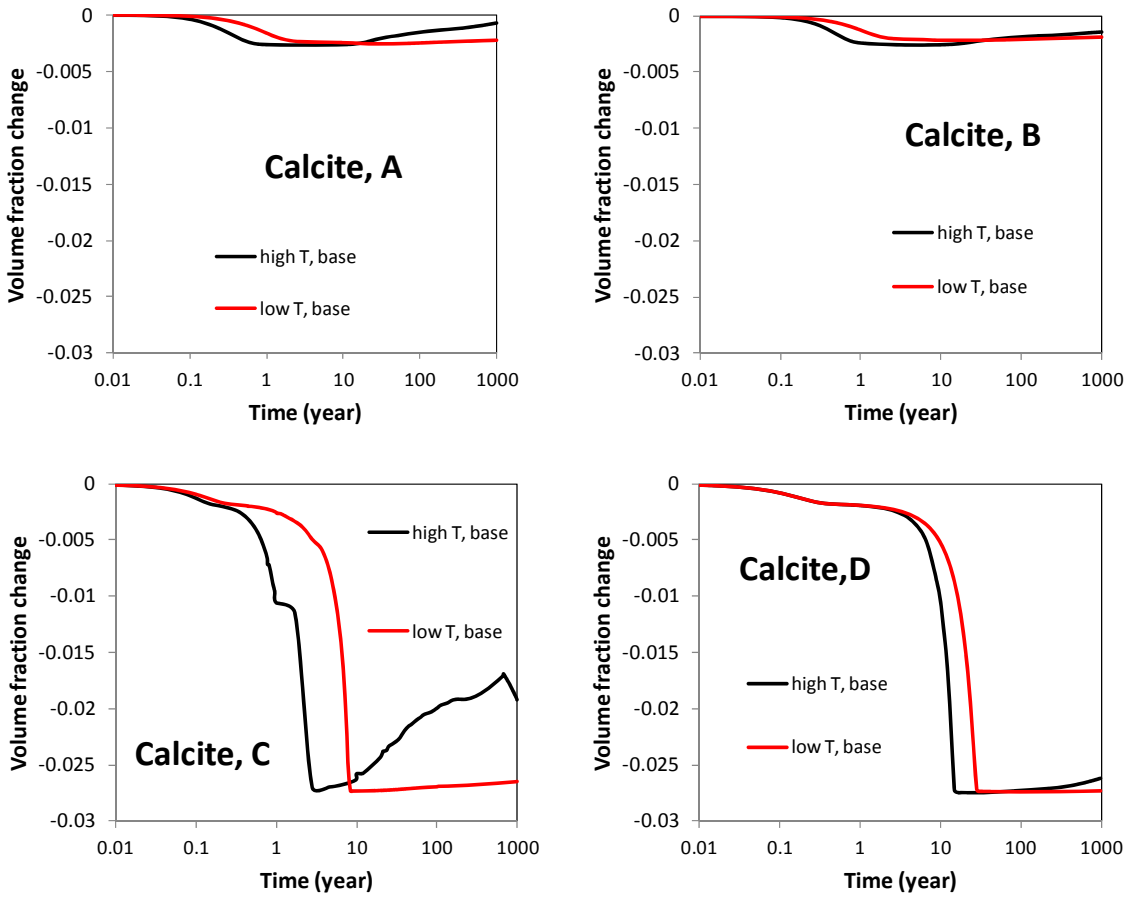

Figure 5-13. The temporal evolution of calcite volume fraction at point A (near the canister), point B (inside the bentonite and near the EBS-NS interface), point C (inside the clay formation and near the EBS-NS interface), and point D (in the far field with a distance of canister of 10 m).

The effect of aqueous composition

If illitization takes place via the dissolution of smectite and neo-formation of illite, as assumed in current simulations, it must be initiated by changes in concentrations of relevant chemical species in aqueous phase. Among these chemical species, K plays a key role: its importance for illitization has been well recognized (e.g., Pusch and Karnland, 1996; Wersin et al., 2007). In a sensitivity study presented in this section, the initial concentration of K in clay formation is increased to 0.01 mol/L, which is about 4 fold that of the base case. The 0.01 mol/L value is close to the concentration of K in sea water. Such high K concentration in the clay formation is only possible when there is sea water intrusion, or the clay formation has marine origin and diagenesis process has not consumed too much K.

An increase in the initial K concentration in the clay formation boosts the illitization in the formation, as illustrated by the illite precipitation at point C and D in Figure 5-14, and smectite dissolution at point C and D in Figure 5-15. It confirms the importance of K over the course of illitization. As shown by the evolution of K concentration at point D in Figure 5-16, illitization that incorporates most of the K into the

mineral phases eventually drags the K concentration to a low level. The evolution of K concentration at point C in Figure 5-14 shows that the K concentration undergoes a much faster decrease, partially because of illitization that occurs locally and partially because of the transport of K to bentonite, indicating that the clay formation would not be sustainable as a K source for bentonite in the long run. Increasing the K concentration in the clay formation seems to have a rather moderate effect on illitization in bentonite (see results at points A and B in Figure 5-14 and 5-15)— it certainly affects the bentonite nearer the NS-EBS interface, and less near the canister, because the farther from the clay formation, the less K is transported. Although such observation confirms that an external source of K is relevant for illitization in bentonite, that external source does not seem to be the only source of K, and is probably not even the major one.

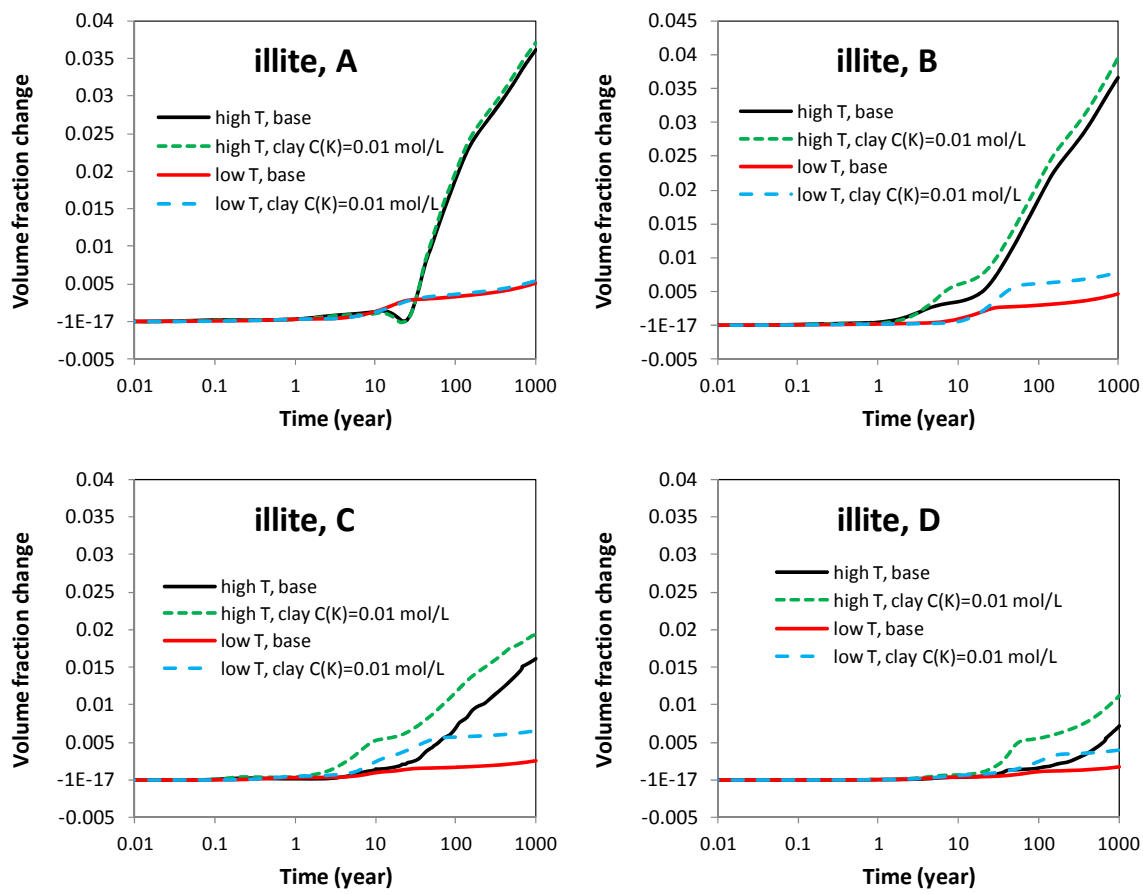

Figure 5-14. The temporal evolution of illite volume fraction at s A, B, C, and D for base and sensitivity case with K concentration in the NS clay formation equal to 0.01 mol/L.

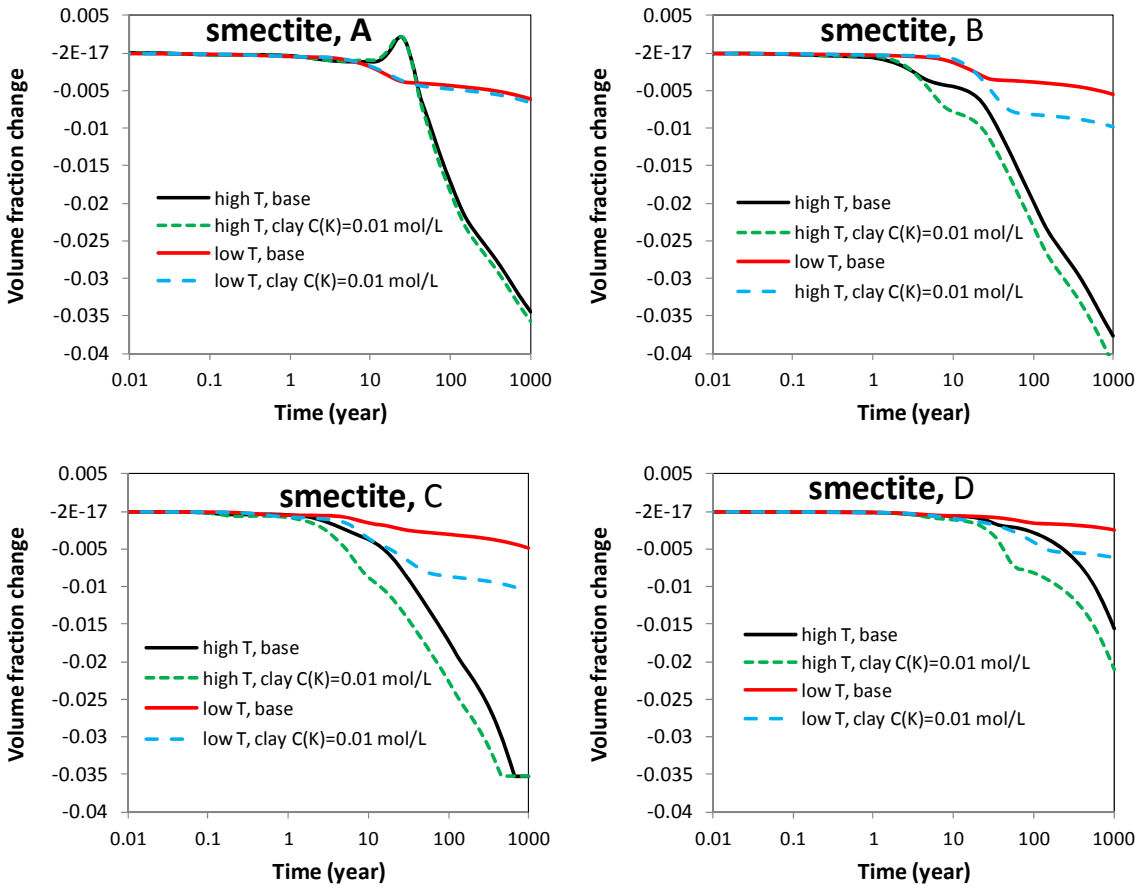

Figure 5-15. The temporal evolution of smectite volume fraction at points A, B, C, and D for base and sensitivity case with K concentration in the NS clay formation equal to 0.01 mol/L.

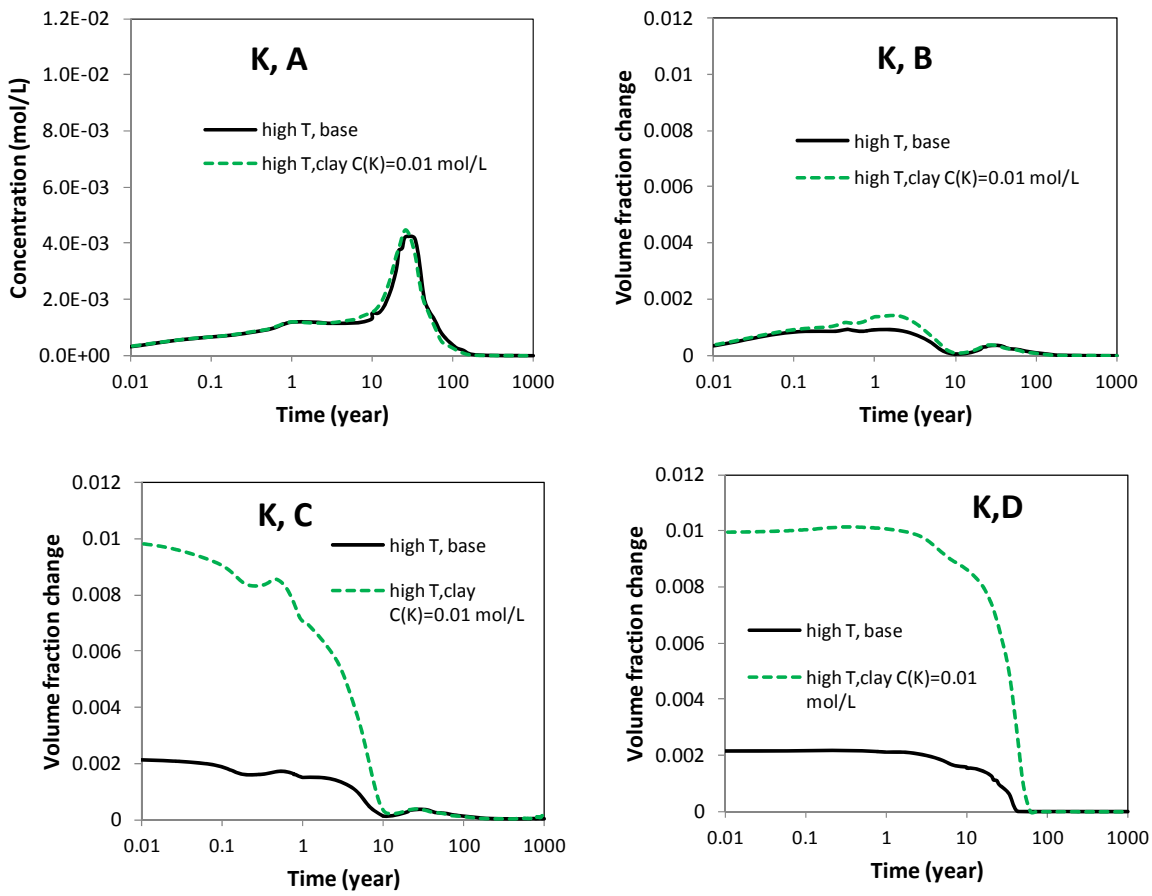

Figure 5-16. The temporal evolution of K concentration at points A, B, C, and D for base and sensitivity case with initial K concentration in the NS clay formation equal to 0.01 mol/L.

As mentioned above, an increase in the K concentration within the clay formation has a fairly limited effect on the illitization in bentonite; largely due to the migration of K from the clay formation to the bentonite is retarded by the illitization occurring along the pathway. This raises the question, how is illitization in bentonite affected if the pore water in bentonite initially contains more K? To answer this question, we conducted a sensitivity run in which the concentration of K in the pore water of bentonite is one order of magnitude higher: model results are plotted in Figure 5-17 and 5-18. Significant enhancement of illitization in bentonite is observed, as illustrated by the smectite dissolution and illite precipitation at points A and B in Figures 5-17 and 5-18. The results suggest that if the bentonite powder initially contains more K, or the water that is used to fabricate the bentonite blocks has a high K concentration, illitization might be a concern. The clay formation in the far field (see results at point D in Figures 5-17 and 5-18) is (not surprisingly) unaffected by the changes in the K concentration in bentonite. However, illitization near the NS-EBS interface in the clay formation does speed up slightly, because the high K concentration in the bentonite slows down the migration of K from the clay formation to bentonite, and therefore leaves more K for the illitization in the clay formation, which illustrates the interaction between EBS bentonite and the clay formation.

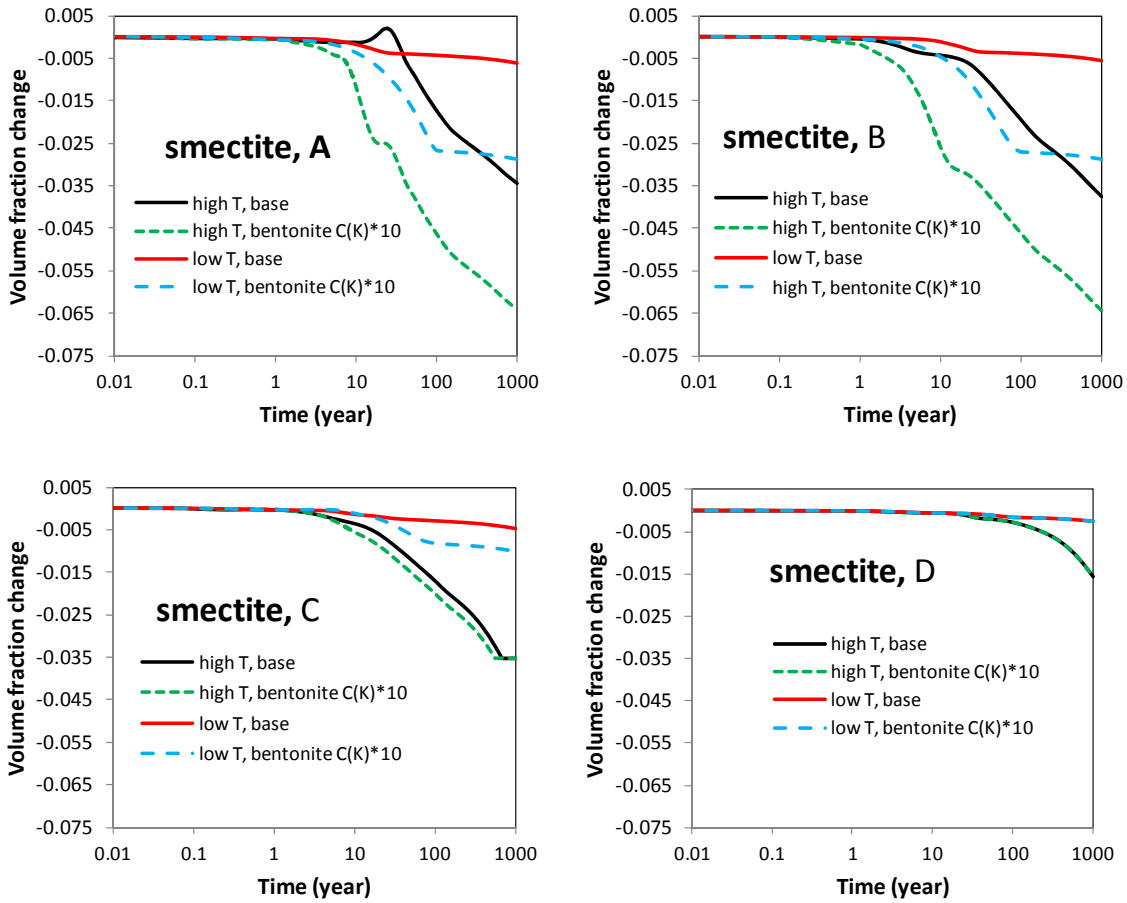

Figure 5-17. The temporal evolution of smectite volume fraction at points A, B, C, and D for base and sensitivity case with K concentration in bentonite increased by one order of magnitude.

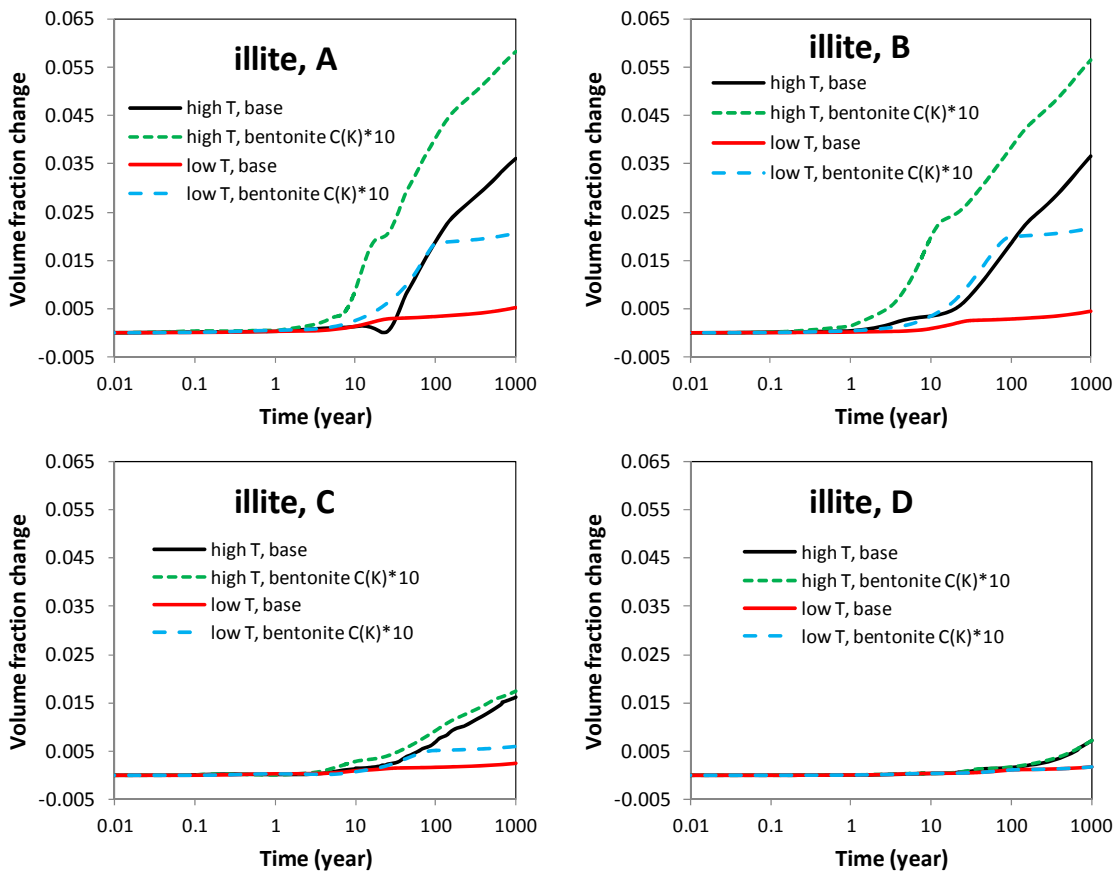

Figure 5-18. The temporal evolution of illite volume fraction at points A, B, C, and D for base and sensitivity case with K concentration in bentonite increased by one order of magnitude.

One of the byproducts of illitization is the precipitation of quartz. As the illitization is enhanced when the K concentration of K in bentonite increases, the production of quartz increases as well (Figure 5-19). The cementation by quartz (or amorphous SiO_2 minerals) might lower the swelling of bentonite and increase the brittleness of the bentonite. This gives us another reason for not using solution with high K content to fabricate bentonite blocks that are used to construct the EBS.

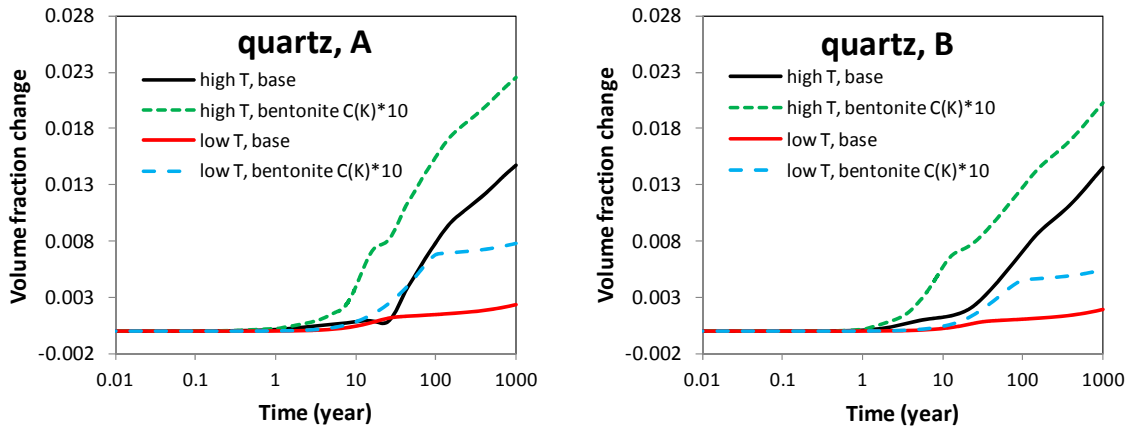

Figure 5-19. The temporal evolution of quartz volume fraction at points A and B, for base and sensitivity case with K concentration in bentonite increased by one order of magnitude.

According to the illitization reaction, illitization might be suppressed if the concentration of Na in bentonite were higher. In a sensitivity run, we increased the concentration of Na in the bentonite and smectite dissolution, and the subsequent illite precipitation at points A and B is plotted in Figures 5-20 and 5-21. Model results show that for the "high T' scenario, the volume fraction of smectite decreases about 0.025 in the sensitivity run, compared to a decrease of 0.035 in the base run near the canister—whereas for the "low T" case, smectite dissolution is very limited in the sensitivity run. Near the NS-EBS interface, we observe similar behavior. All these finding suggest that illitization is inhibited by the higher concentration of Na in the bentonite. This might be the reason why no chemical alteration was observed in the experiment with Na solution (Mosser-Ruck and Cathelineau, 2004). If illitization constrains the EBS and NS from surviving higher temperature, making bentonite with a solution of higher Na concentration could be one way to ease the constraint.

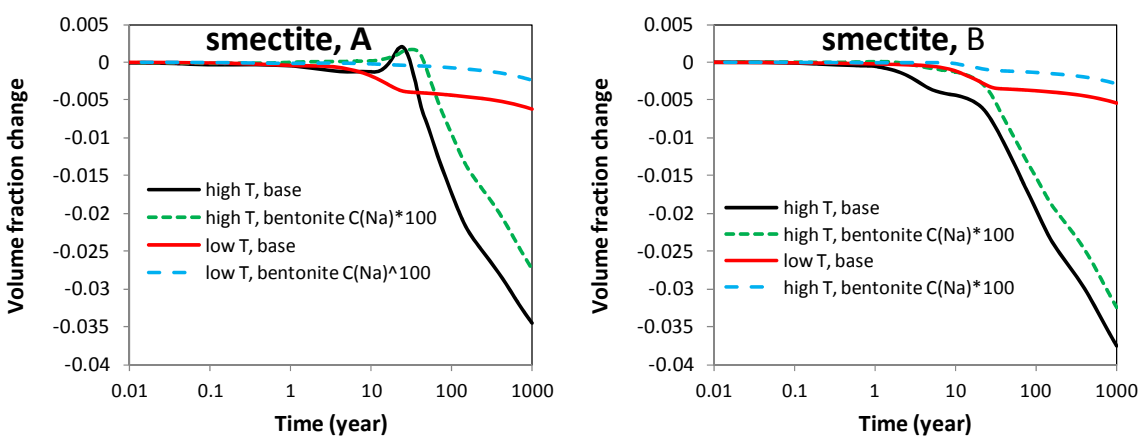

Figure 5-20. The temporal evolution of smectite volume fraction at points A and B, for base and sensitivity case with K concentration in bentonite increased by one order of magnitude.

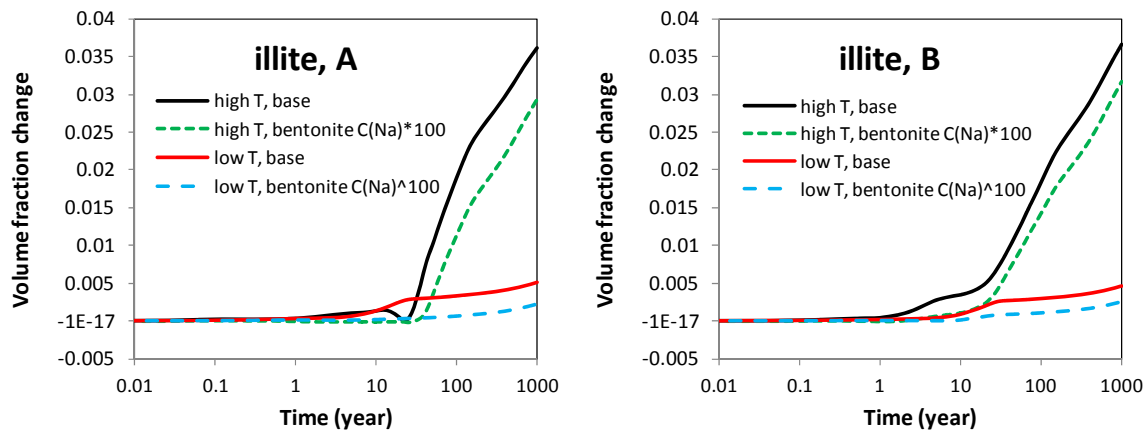

Figure 5-21. The temporal evolution of smectite volume fraction at points A and B, for base and sensitivity case with K concentration in bentonite increased by one order of magnitude.

The effect of accessory minerals

Although the role of K in illitization and/or smectite alteration is well recognized in natural analogue studies (e.g., Cuadros, 2006) and supported by some laboratory studies (Mosser-Ruck and Cathelineau, 2004), the source of K could be debatable. Pusch and Madsen (1995) realized that the concentration of K in the external source for illitization in the bentonite layer used in their concept was probably unrealistically high. As shown in the previous section, adjusting the K concentration in the clay formation has some effect on the illitization in bentonite, and to a degree less than what it should be if K in bentonite were to come exclusively from the clay formation. This suggests that the K from the clay formation could not be the only source of K that would be necessary to form illite. What would be the other sources of K for illitization? Sensitivity analyses presented in this section show that K-feldspar is actually the most important source.

Figures 5-22 and 5-23 shows the smectite dissolution and illite precipitation in a sensitivity run in which K-feldspar is not part of the mineral assemblage in both the bentonite and the clay formation, i.e., there is no K-feldspar dissolution. Near the canister (see smectite dissolution and illite precipitation at point A in Figures 5-22 and 5-23), the illitization in the bentonite for the "no feldspar" scenario is dramatically inhibited in comparison with that in the base case. In the "no feldspar" case, smectite volume fraction only decreases about ~0.001–0.003 which is about one order of magnitude lower than that in the base case. The following reaction clearly shows the importance of feldspar dissolution for illitization: it provides not only K but also Al.

$$\text{K-feldspar} = AlO_2^- + K^+ + 3SiO_2(aq)$$

Near the NS-EBS interface, the illitization in the bentonite is also significantly suppressed (see smectite dissolution and illite precipitation at point B in Figures 5-22 and 5-23), but to a lesser degree than that near the canister, because bentonite still receives K from the clay formation, whereas bentonite near the canister is almost entirely dependent on the dissolution of feldspar for the supply of K.

Smectite dissolution and illite precipitation at points C and D in Figures 5-22 and 5-23 show the impact of not considering K-feldspar on illitization within the clay formation. In contrast, not considering the

impact of K-feldspar dissolution on illitization in the bentonite affects illitization in the clay formation less, as there is an initially high concentration of K that could sustain some degree of illitization.

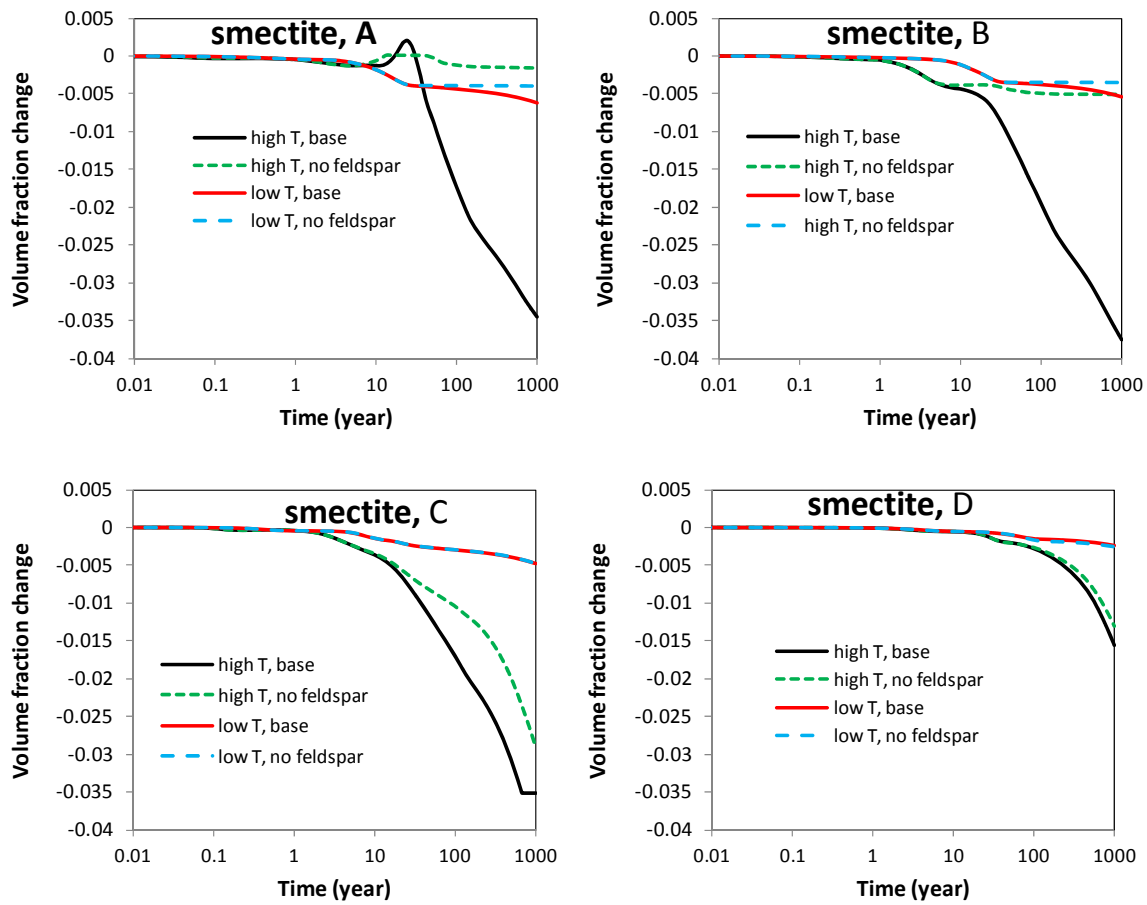

Figure 5-22. The temporal evolution of smectite volume fraction at points A, B, C, and D for base and sensitivity case that there is no K-feldspar dissolution.

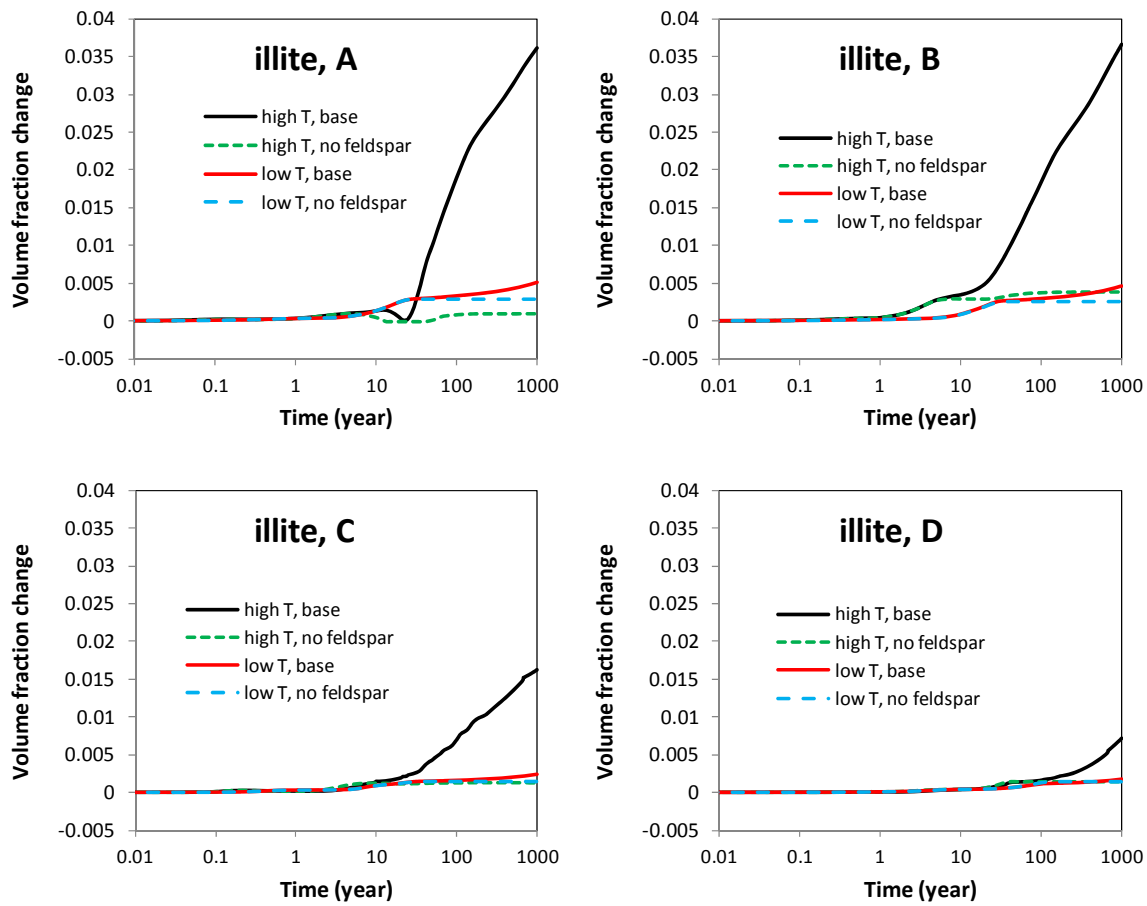

Figure 5-23. The temporal evolution of illite volume fraction at points A, B, C, and D for base and sensitivity case that there is no K-feldspar dissolution.

As already mentioned in the report, the dissolution rate of silicate minerals (e.g., Chen et al., 2005) could vary by orders of magnitude. The K-feldspar dissolution could be much higher than the value used in the base case. In another sensitivity run, we increased the K-feldspar dissolution rate by two orders of magnitude to check if illitization is enhanced, and by how much. As expected, illitization in the bentonite is enhanced, and smectite volume fraction decreases by 0.085 near the NS-EBS interface and 0.055 near the canister (see results at points A and B in Figures 5-24 and 5-25). In comparison with the initial smectite volume fraction in bentonite (0.314), about 18–27% of smectite dissolves. In the clay formation, illitization is also accelerated, and eventually all smectite is transferred to illite, as shown by the plateau of the volume fraction change of smectite and illite at points C and D in Figures 5-24 and 5-25.

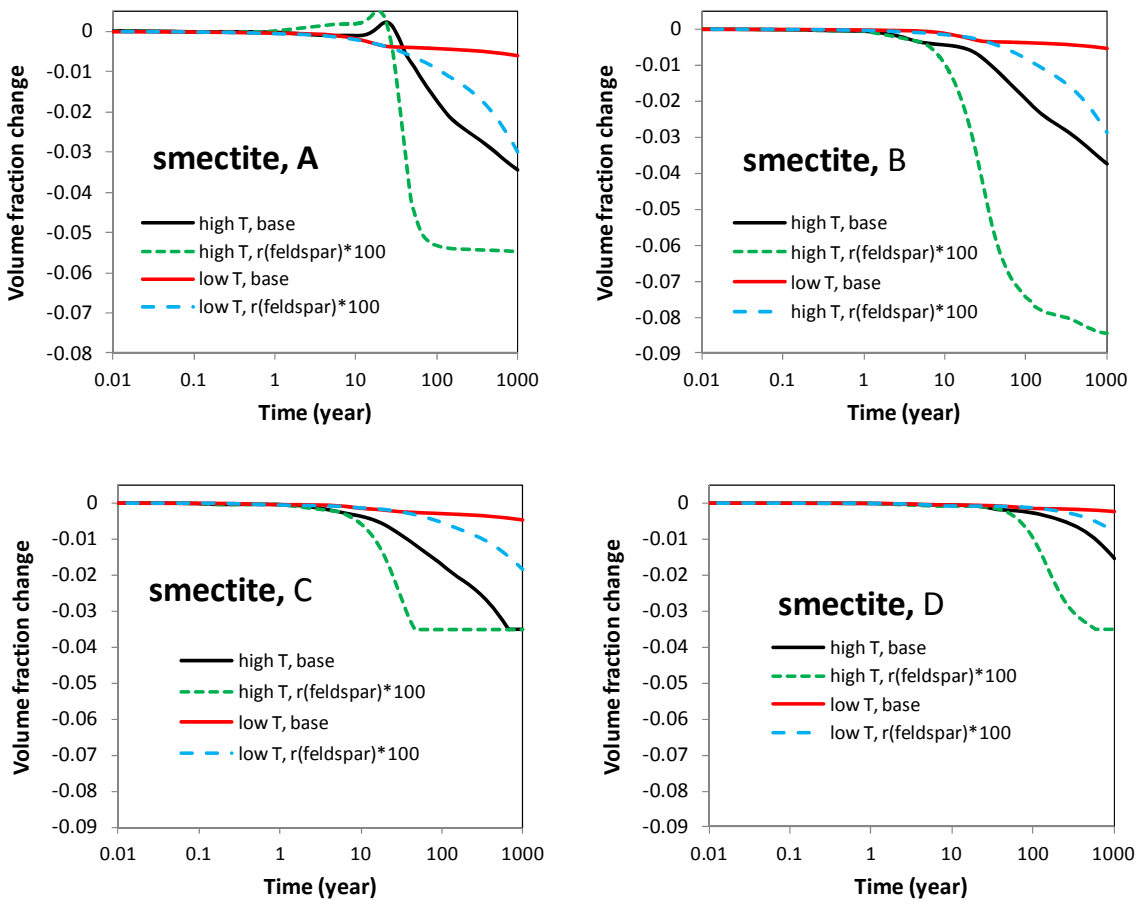

Figure 5-24. The temporal evolution of smectite volume fraction at points A, B, C, and D for base and sensitivity case that k-feldspar dissolution rate is two orders of magnitude higher.

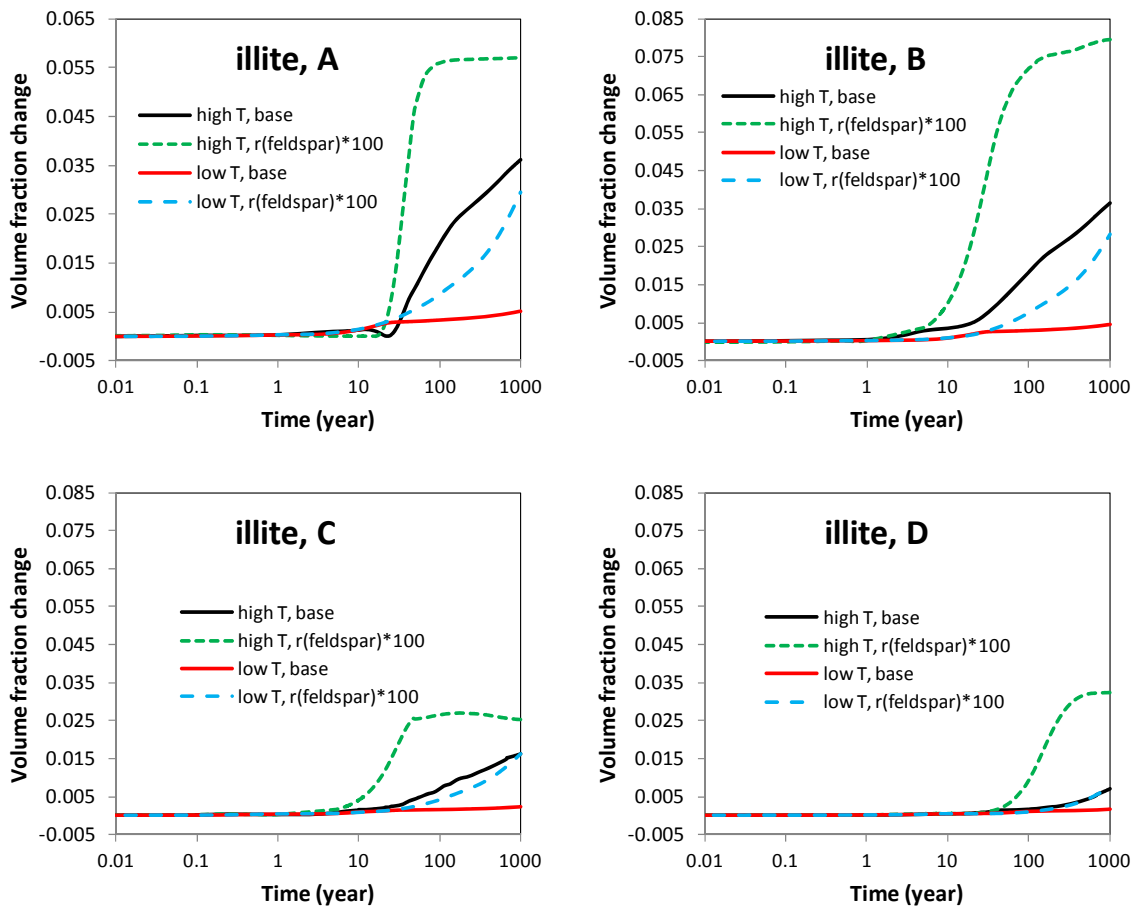

Figure 5-25. The temporal evolution of illite volume fraction at points A, B, C, and D for base and sensitivity case that k-feldspar dissolution rate is two orders of magnitude higher.

Because quartz precipitation is a product of illitization, it is conceivable that the illitization process might be faster if the quartz precipitation rate were to increase. To test this notion we increased the quartz precipitation rate by two orders of magnitude in a sensitivity run. Apparently, more quartz precipitates out in the bentonite and the clay formation as the reaction rate increases, as shown by the quartz volume fraction change in Figure 5-26. But the clay formation is more affected by the faster quartz precipitation rate than the bentonite. In addition to the reaction rate, the saturation index is another limit to mineral precipitation (or dissolution). Because water is closer to equilibrium with quartz in bentonite than in the clay formation, increasing the quartz precipitation rate has less impact.

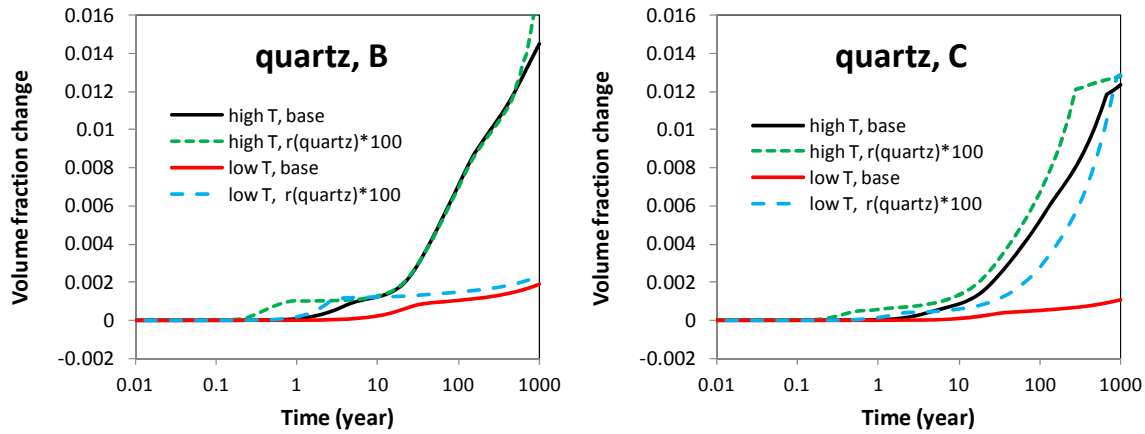

Figure 5-26. The temporal evolution of quartz volume fraction at points B and C, for base and sensitivity case that quartz dissolution rate is two orders of magnitude higher.

The increase in quartz precipitation appears to markedly increase illitization in the clay formation, as shown by the smectite and illite volume fraction changes at points C and D in Figures 5-27 and 5-28. For the "high T" scenario, eventually, in ~300 years, all smectite at point C dissolves; in ~ 500 years, all smectite at point D dissolves. This illustrates that illitization is not an independent process—it is interrupted by other reactions. Quartz precipitation is just one example. Also observed in the current simulation is the formation of chlorite and kaolinite: they form in very small amounts and therefore have limited effect on illitization. However, based on what we learned from the sensitivity to quartz precipitation rate, they could have larger impact if their reaction rates were higher. Since the quartz itself in the bentonite is not significantly affected by the changes in precipitation rate (see Figure 5-26), illitization therein is not affected significantly either (see smectite and illite volume fraction changes at points A and B in Figures 5-27 and 5-28).

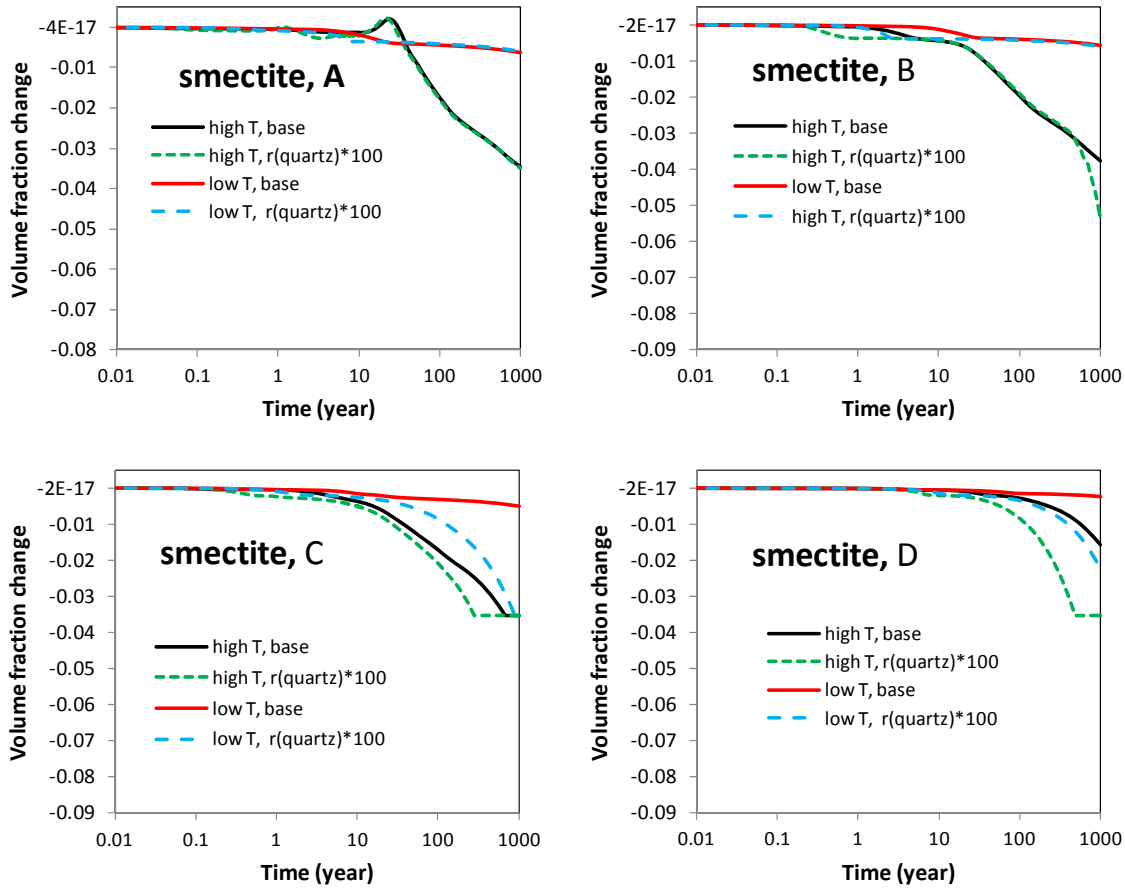

Figure 5-27. The temporal evolution of smectite volume fraction at points A, B, C, and D for base and sensitivity case that quartz dissolution rate is two orders of magnitude higher.

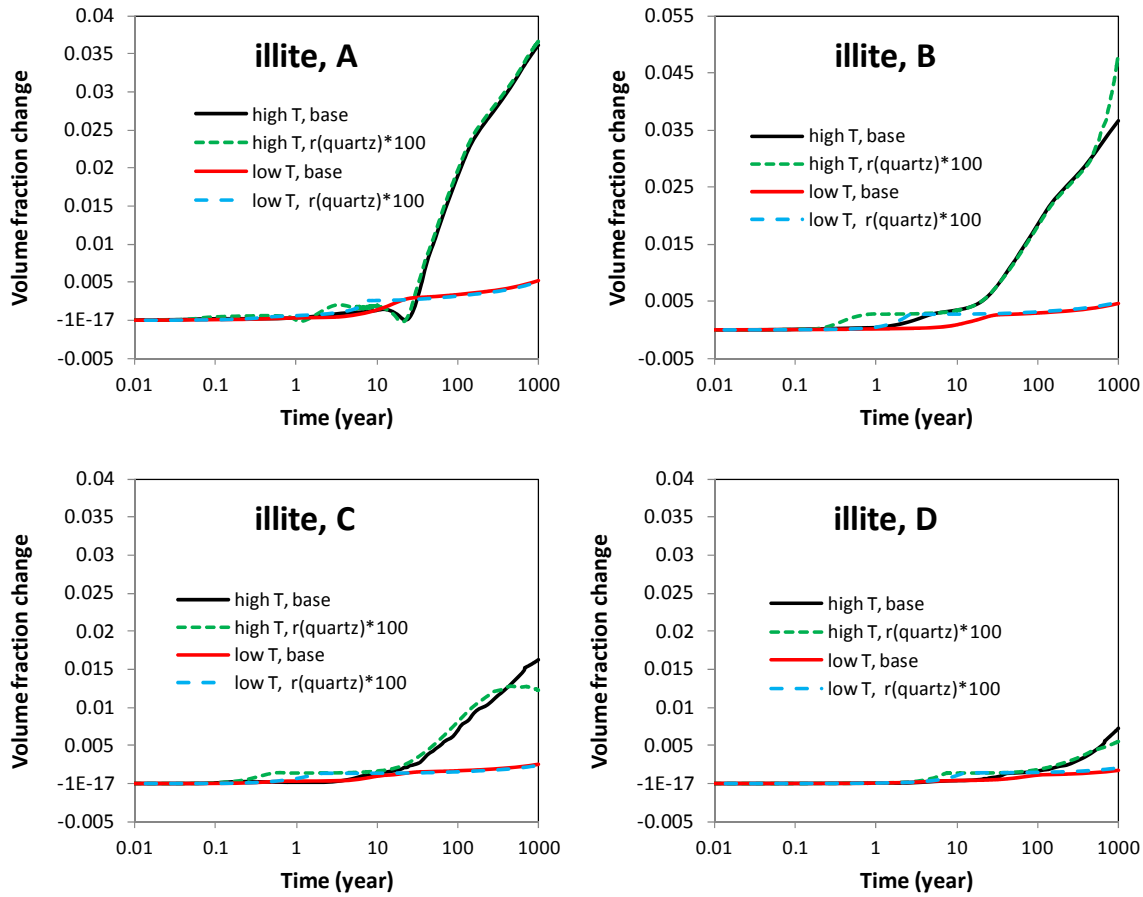

Figure 5-28. The temporal evolution of illite volume fraction at points A, B, C, and D for base and sensitivity case that quartz dissolution rate is two orders of magnitude higher.

5.2.2.4 The mechanical consequence as a result of chemical changes

The base case

The constitutive relationship described by Equation (5-2) gives us an opportunity to evaluate the effect of chemical changes on stress. The mechanical results presented in this section are based on the chemical results in Section 5.5.2.3. In order to isolate the contribution of ion concentration changes and smectite changes to stress, we present three sets of calculated stress. In the first set, denoted in the Figures as "S=f(Sl,C,Sc)", stress is the function of liquid saturation (Sl), ion concentration (C) changes, and smectite (Sc) changes (Equation 5-2); in the second set, denoted as "S=f(Sl,C)", stress is the function of moisture change and ion concentration changes, as in the following Equation:

$$d\sigma_s = 3K\beta_{sw}ds_l + A_n dC \tag{5-6}$$

In the third set, denoted as "S=f(Sl)", stress is the function of moisture change only, as in the following Equation:

$$d\sigma_s = 3K\beta_{sw} ds_l \tag{5-7}$$

Figure 5-29 shows the stress in the bentonite near the canister (point A) for the "low T" scenario, in which the peak temperature near the canister is about 100°C. The increase in pore pressure due to hydration and the thermal pressurization drive the stress in bentonite up to around 8 MPa after 1000 years. At early time (< 10 years), the fact that results for "S=f(Sl,C,Sc)" and "S=f(Sl,C)" cases are indistinguishable indicates that smectite changes have not yet contributed to the stress change, because the volume fraction of smectite only shows significant changes after about 20 years (see Figure 5-9 in Section 5.5.2.3). At the end of 1000 years' simulation, the ion-concentration increase leads to a drop in stress of about 0.2 MPa, and the dissolution of smectite makes the stress decrease further by about 0.06 MPa. In general, the chemical changes in bentonite have a fairly moderate effect on stress. The stress changes near the NS-EBS (point B) interface behave similarly to those near the canister, except the stress starts to increase earlier; the stress after 1000 years is similar as well.

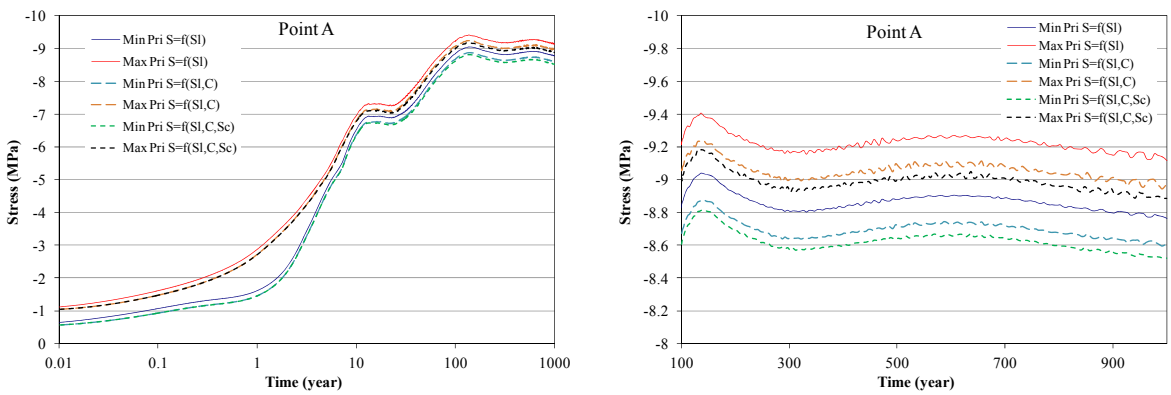

Figure 5-29. Simulation results of maximum and minimum principal compressive effective stresses ($\sigma_1^{'}$ and $\sigma_3^{'}$) at point A for the "low T" scenario. The right figure shows the same data as the left figure, but focuses on a shorter time window to illustrate the difference between different cases.

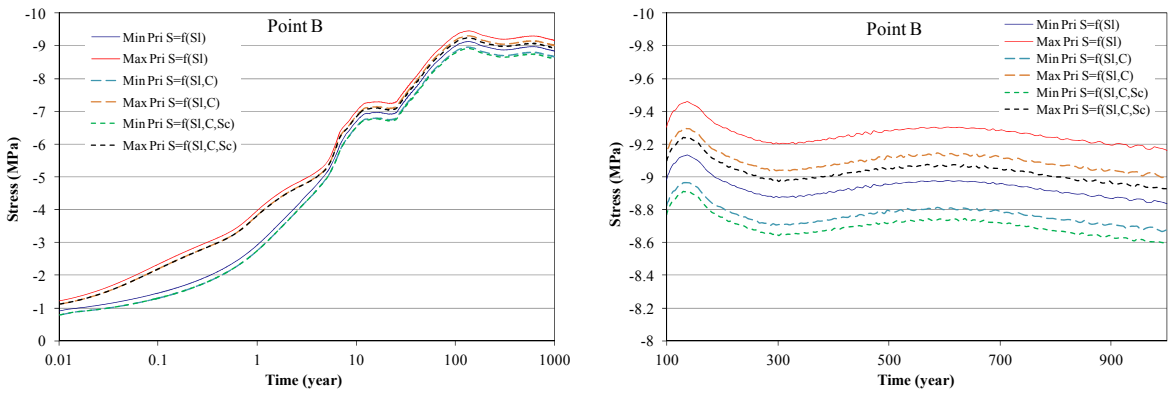

Figure 5-30. Simulation results of maximum and minimum principal compressive effective stresses ($\sigma_1^{'}$ and $\sigma_3^{'}$) at point B for the "low T" scenario. The right figure shows the same data as the left figure, but focuses on a shorter time window to illustrate the difference between different cases.

Figure 5-31 and 5-32 show the stress in the bentonite near the canister and NS-EBS interface for the "high-T" scenario, in which the temperature near the canister can reach about 200°C. In comparison with the "low T" case, clearly the stronger thermal pressurization leads to much higher stress in the bentonite. In terms of the effect of chemical changes on stress, ion concentration changes start to affect stress at early times (< 20 years) and maintain such effect afterwards. After 1000 years, ion concentration changes cause about a 0.2 MPa decrease in stress. The loss of smectite due to dissolution starts to take effect after about 20 years, and at the end of the 1000-year simulation, it results in about a 0.5 MPa reduction of stress. The reason that more stress reduction is observed for the "high T" scenario is simply because smectite dissolves more, as shown in Section 5.5.2.3. But this is only about a 3% difference. However, if we compare Figure 5-29 with Figure 5-31, the increase in temperature itself causes a significant rise in stress.

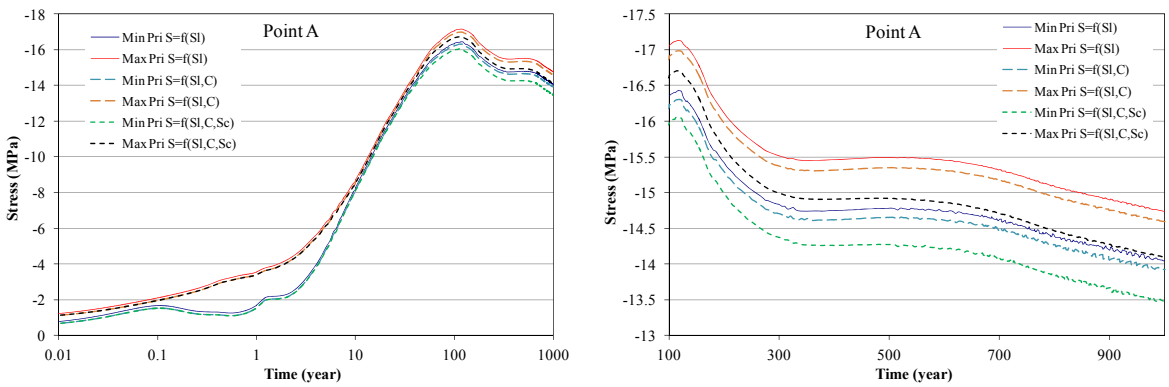

Figure 5-31. Simulation results of maximum and minimum principal compressive effective stresses ($\sigma_1^{'}$ and $\sigma_3^{'}$) at point A for the "high T" scenario. The right figure shows the same data as the left figure, but focuses on a shorter time window to illustrate the difference between different cases.

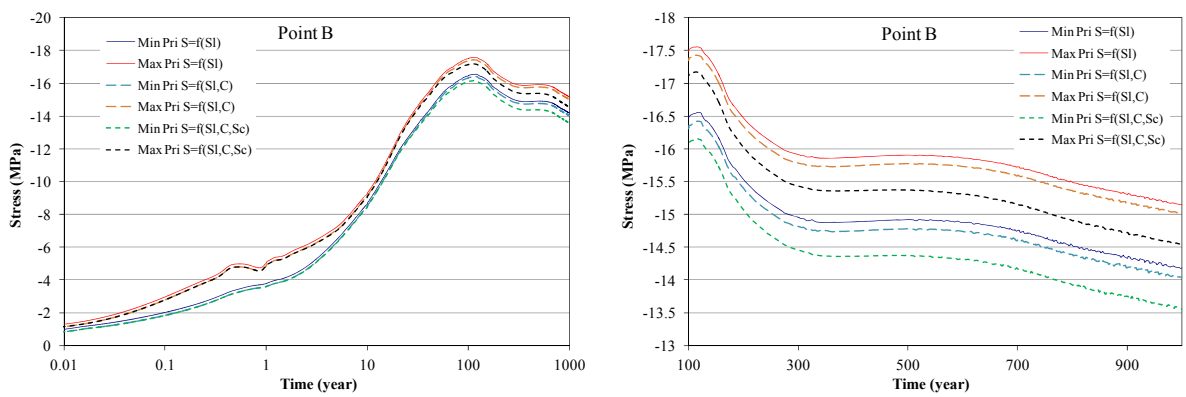

Figure 5-32. Simulation results of maximum and minimum principal compressive effective stresses ($\sigma_1^{'}$ and $\sigma_3^{'}$) at point B for "high T" scenario. The right figure shows the same data as the left figure, but focuses on a shorter time window to illustrate the difference between different cases.

The calculation of porosity changes caused by mineral precipitation/dissolution is rather straight forward. The porosity of the medium is given by (Xu et al., 2011):

$$\phi = 1 - \sum_{m=1}^{nm} fr_m - fr_u \tag{5-8}$$

where nm is the number of minerals, fr_m is the volume fraction of mineral m in the rock ($V_{mineral}/V_{medium}$, including porosity), and fr_u is the volume fraction of nonreactive rock.

However, the porosity change in bentonite over the course of hydration is a very complicated issue because of the pore structure of bentonite (e.g. Sanchez et al., 2005). Mechanical model such as Barcelona Basic Model (Alonso et al., 1990) or Barcelona Expansive Model (BExM) (Sanchez et al., 2005) may provide a more reliable analysis of the porosity changes caused by mechanical changes. In this report, we calculate the stress-induced porosity changes from volumetric strain as follows:

$$d\varepsilon_v = \frac{de}{1+e_0} \tag{5-9}$$

where $d\varepsilon_v$ is the volumetric volume changes, e is void ratio and e_0 is the initial void ratio.

Mineral precipitation/dissolution leads to very small porosity changes—after 1000 years, near the canister (where the most significant change occurs), the decrease in porosity is only about 0.1% (Figure 5-33), because the volume loss due to the dissolution of some minerals (including smectite, K-feldspar, and calcite) is compensated for by the volume gain caused by the precipitation of minerals such as illite and quartz.

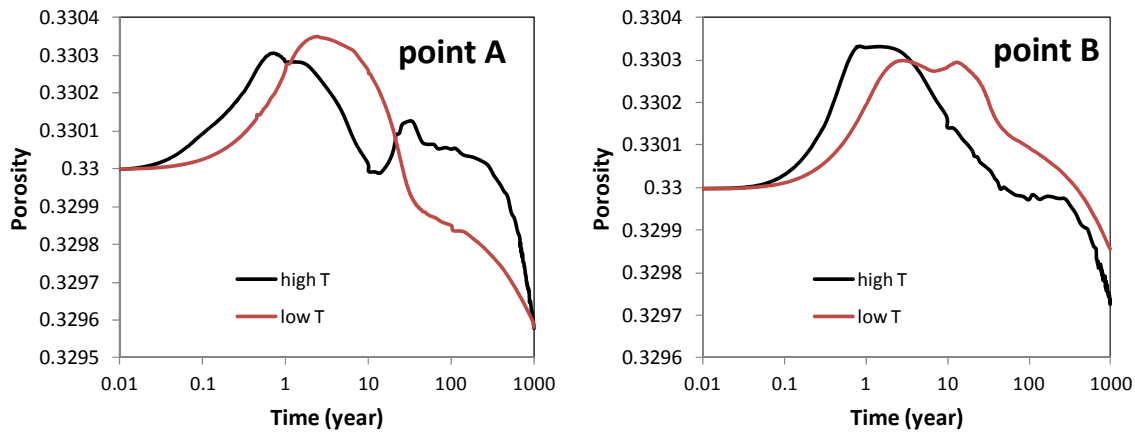

Figure 5-33. Porosity changes due to mineral precipitation/dissolution at point A (near the canister), point B (inside the bentonite and near the EBS-NS interface) for "high T" and "low T" scenarios.

The stress-induced porosity changes are plotted in Figures 5-34 and 5-35. The porosity near the canister (Figure 5-34) first decreases as result of drying and suction, but after the bentonite becomes fully saturated, the porosity increases. The porosity drop during early time is more manifest for the "high T" case as the bentonite undergoes more drying under higher temperature. The porosity near the NS-EBS interface (Figure 5-35) increases from the very beginning, due to the moisture-induced swelling, but gradually decreases due to compression. Also shown in Figures 5-34 and 5-35 are porosities for "S=f(Sl,C,Sc)","S=f(Sl,C)" and "S=f(Sl)" scenarios under "high T" and "low T" cases. A comparison between these three scenarios allows us to delineate the effect of loss of smectite on porosity exerted via its effect on stress. Because the loss of smectite causes only a 3% drop (maximum) in stress at later times (Figure 5-32), it has a fairly insignificant effect on porosity.

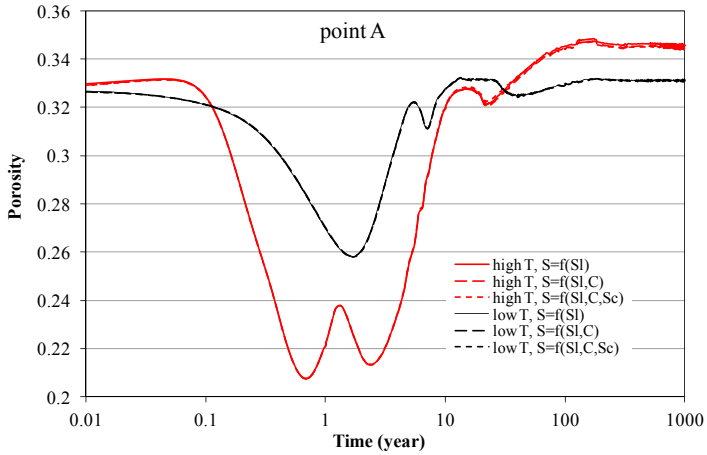

Figure 5-34. Porosity changes due to stress changes at point A (near the canister) for "high T" and "low T" scenarios.

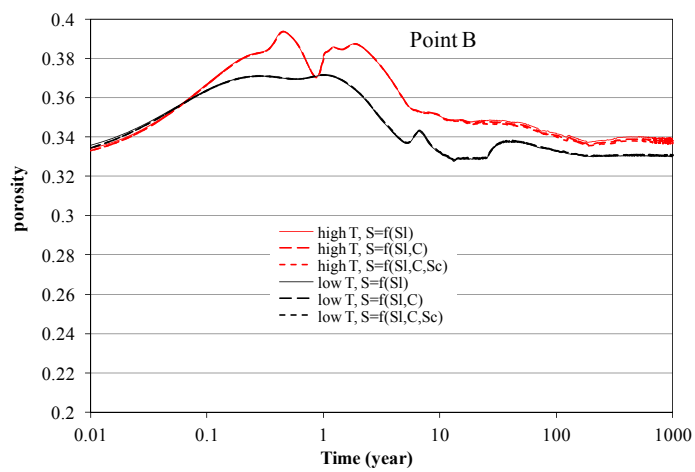

Figure 5-35. Porosity changes due to stress changes at point B (near the canister) for "high T" and "low T" scenarios.

Our mechanical model for the clay formation is inherited from Rutqvist et al. (2013), and therefore the stress response in the clay formation is the same. This mechanical model is not tied to chemical variables, which prevents further analysis of the effects of chemical changes on the mechanical behavior in the clay formation. The stress change at points C and D (Figures 5-36 and 5-37) are mainly caused by the thermal pressurization. Near the NS-EBS interface, higher temperature leads to much higher stress (Figure 5-36), but in the far field at point D, the higher temperature causes higher stress only in the short term (< 20 years).

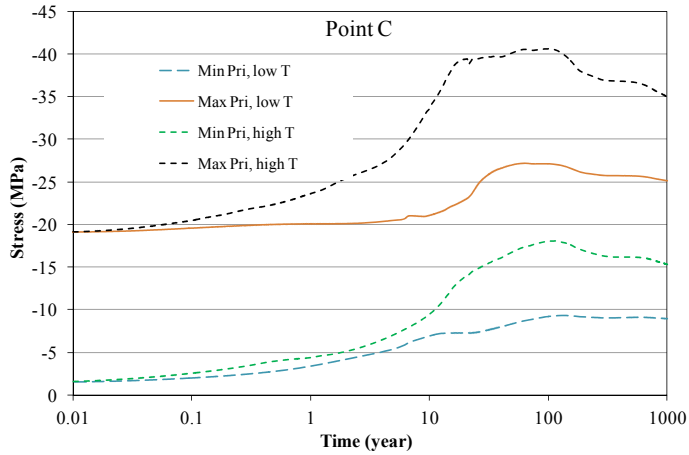

Figure 5-36. Simulation results of maximum and minimum principal compressive effective stresses ($\sigma_1^{'}$ and $\sigma_3^{'}$) at point C for "low T' and "high T' scenarios.

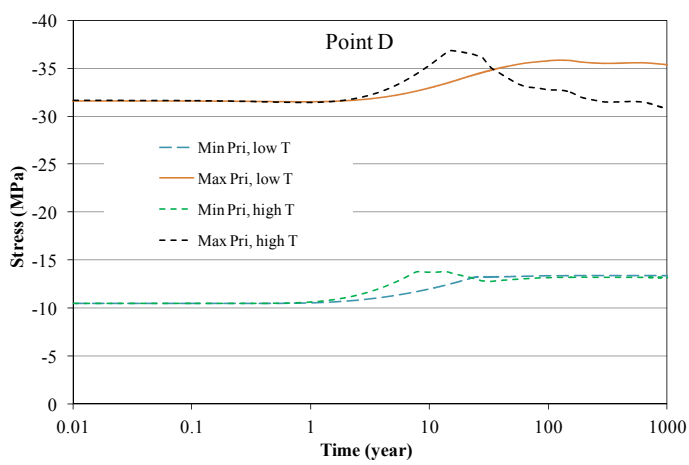

Figure 5-37. Simulation results of maximum and minimum principal compressive effective stresses ($\sigma_1^{'}$ and $\sigma_3^{'}$) at point D for "low T' and "high T' scenarios.

In the future, a constitutive relation that incorporates the chemical component within the mechanical model for a clay formation will be implemented. Based on this development, we will be able to analyze the effects of chemical changes on mechanical behavior in a clay formation.

A sensitivity run with the maximum dissolution of smectite

The model results for the base case suggest that the loss of smectite (via illitization) has minimal effect on stress and subsequently on porosity, largely because the loss of smectite is only 11% for the "high T" case

and much less for the "low T" case. In Section 5.5.2.3, we evaluate several chemical scenarios and find that if the dissolution rate of K-feldspar is higher, more dissolution of smectite occurs, with a maximum as high as 27% (see Section 5.5.2.3) for the "high T" case. The calculated stress for this "r(feldspar)*100" case is shown in Figures 5-36 and 5-37. In comparison with the "high T" base case, the stress at points A and B in the sensitivity case is about 0.4 MPa lower. Such a difference is mainly caused by the more significant dissolution of smectite in the sensitivity case, and therefore reflects the contribution of smectite dissolution on stress. It accounts for only about 3% of the total stress. Unsurprisingly, such a small change in stress leads to only minimal differences in porosity, as shown in Figure 5-38 and 5-39.

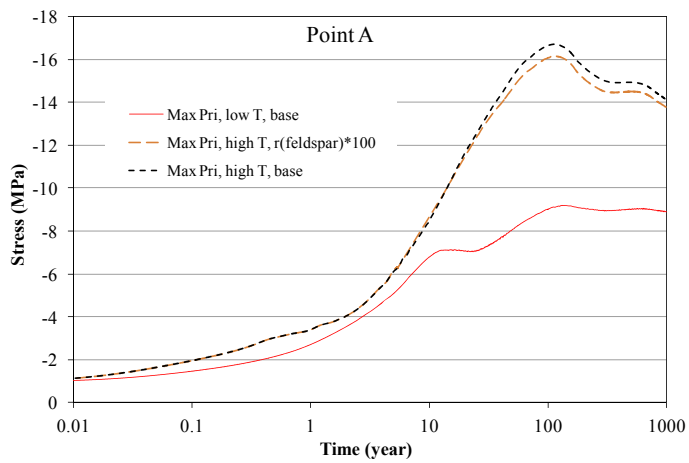

Figure 5-38. Simulation results of maximum principal compressive effective stresses ($\sigma_3^{'}$) at point A for "S=f(Sl,C,Sc)" scenario.

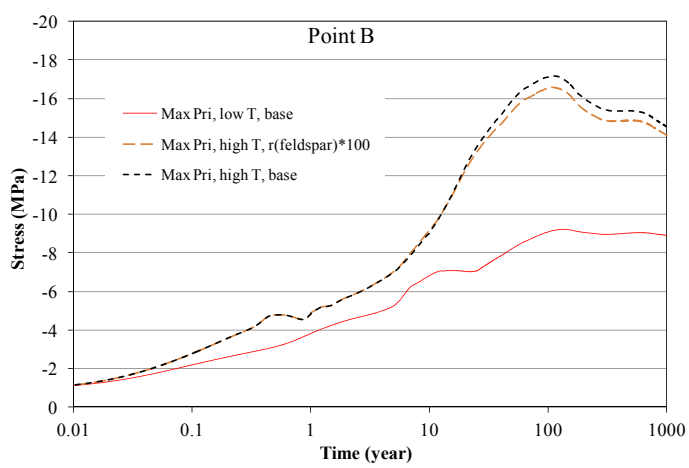

Figure 5-39. Simulation results of maximum principal compressive effective stresses ($\sigma_3^{'}$) at point B for "S=f(Sl,C,Sc)" scenario.

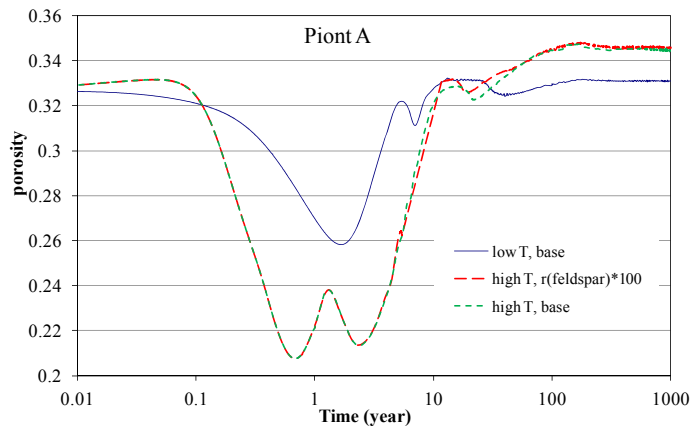

Figure 5-40. Porosity changes due to stress changes at point A for "high T" and "low T" base case and a "high T" case with K-feldspar dissolution rate two orders of magnitude higher.

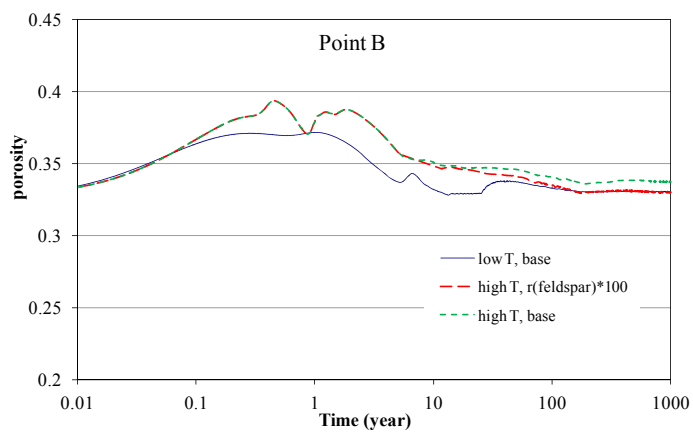

Figure 5-41. Porosity changes due to stress changes at point B for "high T" and "low T" base case and a "high T" case with K-feldspar dissolution rate two orders of magnitude higher.

5.2.3 Summary

In this section, we developed coupled THMC simulations to evaluate the chemical alteration and subsequent mechanical changes in the EBS bentonite and the NS clay formation. Two scenarios were developed for comparison: a "high T" case in which the temperature near the canister can reach about 200 ^{o}C and a "low T" scenario in which the temperature near the canister peaks at about 100 ^{o}C. In these generic cases, it is assumed that the EBS is composed of Kunigel-V1 bentonite (Ochs et al., 2004) and the NS is Opalinus Clay. Illitization is simulated as a dissolution-precipitation process, i.e. the dissolution of smectite and neo-formation of illite, and the illitization rate is calibrated against field data (Pusch and Madsen, 1995).

The models confirm the occurrence of illitization in the NS clay formation, as revealed by several natural analogue studies, and also show that illitization occurs in the EBS bentonite. Other chemical alterations include the dissolution of K-feldspar and calcite, and precipitation of quartz, chlorite, and kaolinite. In general, illitization in the bentonite and clay formation is enhanced at higher temperature. However, the quantity of illitization, expressed as the smectite volume fraction change, is affected by many chemical factors and subsequently varies a great deal. The most important chemical factors are the concentration of K and dissolution rate of K-feldspar; less important are the concentration of Na and quartz precipitation rate. The decrease in smectite volume fraction in bentonite ranges from 0.004 to a maximum of 0.085, about 27% of the initial volume fraction of smectite. Smectite volume fraction in the clay formation decreases moderately in some cases, but in other cases it decreases as much as 0.035.

The effect of illitization (smectite dissolution) on stress in the bentonite is calculated by an extended linear elastic model. That model shows that higher temperature leads to much higher stress, due to thermal pressurization. However, smectite dissolution causes only minimal changes in the stress. Even for the case with the maximum dissolution rate for smectite, smectite dissolution only results in about a 3% drop in stress and therefore contributes very little to stress-induced porosity changes. The current mechanical model for the NS clay formation is not tied with chemical variables, i.e., mechanical-chemical coupling is not considered for the NS clay formation in current simulations, which prevent further analysis of the effects of chemical changes on mechanical behavior in the NS clay formation.

In the remaining months of FY13, we will:

- Conduct additional sensitivity analyses to hydrological parameters, to understand the hydrological impact on chemical alteration and mechanical changes at higher temperature.
- Refine the current chemical model. In our current model, the canister serves only as a heat source; chemical changes within the canister are neglected for simplification. The model should consider chemical changes in canister, specifically the release of Fe^{+2}, which might enhance the dissolution of smectite by forming chlorite.

5.3 Impact of High-Temperature THMC Changes on Radionuclide Transport and Other PA Drivers

5.3.1 Introduction

5.3.1.1 Motivation

As outlined in Section 5.1, there is considerable practical and economic motivation to examine high-temperature scenarios for a high-level nuclear waste repository in argillaceous formations. Higher temperatures may be reached as a result of a higher heat load assigned to a given repository section. The heat load depends on the overall disposal concept, which affects the inventory, waste canister design, and surface storage times. Moreover, even for a given heat load, the temperature at various control points within the multi-barrier repository system may increase depending on the chosen emplacement mode, schedule and ventilation times, the repository layout, and particularly the geometric design and materials used as buffers, backfills, and plugs.

The key question is whether higher repository temperatures can trigger mechanisms that alter these material properties and potentially compromise the various barrier functions assigned to the engineered components (specifically the bentonite buffer) and host rock. Such mechanisms tend to impact repository performance in a complex manner that is difficult to assess and predict.

Most repository programs impose an upper temperature limit of typically 100°C (see Table 5-1 and Hicks et al., 2009). There are multiple reasons for imposing such a thermal limit. Some are related to the increase in the canister corrosion rate, which may be further accelerated by the enrichment of salts due to boiling. Another set of concerns is related to the bentonite buffer, whose barrier-relevant properties may degrade at higher temperatures. A third argument against higher temperatures (specifically when they exceed the boiling point under in situ conditions) is based on our lack of understanding and inability to reliably predict the complex coupled THMC processes and feedback mechanisms across the various repository components. This subtask is mainly concerned with the latter two issues, i.e., that of potential bentonite alteration and the impact of higher temperatures on overall repository performance.

Sections 5.2 and 5.4 discuss modeling and experimental approaches to examine some of the coupled thermo-hydraulic-chemical-mechanical (THMC) processes, and how they may affect bentonite properties (specifically swelling behavior and thus porosity and permeability, as well as sorption coefficients) that are critical for the buffer's hydraulic and chemical barrier function.

5.3.1.2 Objectives and scope

The general objective of this subtask is to develop a modeling methodology that supports performance assessment studies for a high-temperature repository. More specifically, such a modeling methodology is intended to include the ability to examine various high-temperature scenarios and the related effects on buffer, backfill and host rock properties, system states, and eventually safety-relevant performance measures. This complex cascade of causes and effects must be implemented in an abstracted, parameterized manner to be accessible for a system-level analysis and sampling-based uncertainty quantification.

The scope of the work presented in this subsection is limited to a preliminary demonstration of how THMC processes associated with high-temperature scenarios and the resulting changes in parameter values could be integrated into a simplified model to assess their effects on repository performance. The results of process-level modeling and experimental studies described in Sections 5.2 and 5.4—once finalized—will be suitably abstracted for inclusion into a performance assessment model. Currently, the abstraction is only schematic to demonstrate the analysis approach.

5.3.1.3 General approach

The general approach of this subtask is to first review temperature-related factors that could impact repository performance. As briefly outlined above, increased temperatures can be the result of a number of potential scenarios. We do not intend to go through a formal scenario analysis, but instead focus on demonstrating how a given scenario with complex THMC processes can be abstracted and evaluated within a performance assessment context. To do this, a highly simplified model of a repository system is developed for a given scenario, where features and processes are represented by parameterized functions. A limited number of performance measures are defined, and their sensitivity with respect to the model input parameters is evaluated. Uncertainties in these parameters can also be propagated through the model to obtain a better understanding of the potential relevance of a given factor and the need to reduce its uncertainty through experimentation or refined mechanistic modeling.

5.3.2 Background

5.3.2.1 Barrier role of bentonite

The high-temperature scenarios to be considered are mainly concerned with the potential degradation of the barrier functions of the bentonite buffer, as the buffer is the location where the highest temperatures within the near field will occur. We therefore first recall what these barrier functions are. Bentonite is chosen for its specific properties that address a diversity of functional requirements within the repository system. Bentonite is expected to play several roles, which can be characterized as hydraulic, chemical, mechanical, and thermal. Bentonite is primarily chosen for its hydraulic role, which is to ensure that water flow around the waste package is very small, so that transport of radionuclides from the waste form to the host rock is limited to diffusion. Second, bentonite plays a chemical containment role, with favorable sorptive and solubility retention properties for many radionuclides. Bentonite also acts as a chemical buffer, as it shows limited geochemical evolution without significant mineralogical transformations when in contact with the host rock. Third, bentonite mechanically supports and protects the waste package and contributes to the long-term mechanical stability of the deposition holes and near field. In addition to these primary roles, bentonite is also intended to conduct heat away from the waste packages to avoid excessive temperatures, which can be referred to as its thermal role.

It should be noted that bentonite may not be the optimum material for each of these functional requirements individually, but its properties are such that bentonite has become the material of choice for many repository components. Moreover, there are multiple types of bentonite and mixtures of bentonite with other materials, designed to improve one specific function or the overall barrier performance. Homogenized Na-type montmorillonite (either compacted, as bricks, or in the form of pellets or powder installed with various dry densities and moisture contents) is typically used as the main component of buffers, backfills, and plugs in nuclear waste repositories.

The specific properties that make bentonite suitable as a barrier material include its low hydraulic conductivity, plasticity and self-sealing, swelling capacity, cation exchange and sorption capacity, colloid filtration capacity, and inhibition of microbial growth. Depending on the specifics of the repository safety cases, the analysis of THMC processes thus has to either (1) demonstrate that these desirable properties are not significantly altered as a result of various high-temperature scenarios, or (2) provide information on the impact of high temperature on barrier components and the degree to which their performance might be compromised.

5.3.2.2 Temperature dependence of properties

It is generally expected that high temperatures change the mineralogy of the bentonite and thus some of the properties that are relevant for its intended barrier function. Specifically, as discussed in detail in Section 5.2, illitization of smectite is a function of temperature (and the availability of exchangeable cations, specifically potassium). Illitization is a crucial process as the smectite volume fraction (or illite-water ratio) in the bentonite affects the swelling pressure during resaturation (along with dry density, water content, salinity, and alkalinity). This potential reduction in swelling capacity then affects safety-relevant functions, specifically the permeability of the buffer after resaturation, the ability to close gaps, as well as the uniformity and plasticity of the buffer. Furthermore, there are various feedback mechanisms that come into play. For example, the degree of swelling affects the thermal conductivity, which in turn determines the temperature distribution and thus illitization in the bentonite. Moreover, the uniformity of the resaturation process (and thus swelling itself) depends on the swelling properties of the bentonite. Significantly stronger THMC coupling and feedback mechanisms may occur if temperatures exceed the

boiling point. The presence of steam may significantly, rapidly and irreducibly lower the swelling capacity of bentonite (Couture, 1985); it also leads to viscous driving forces (with associated convective transport processes), drastic changes in effective hydraulic and thermal conductivities, and the potential for dry-out and associated desiccation cracking.

The chemical barrier role of bentonite may be compromised by a reduction in sorptive capacity. Changes in porosity caused by different swelling behavior affect both diffusive and advective transport.

It should also be noted that temperature affects the density, viscosity, and surface tension (and thus capillarity) of water. Thermal expansivity with reduced viscosity may lead to some advective transport away from the waste package.

Should the type and rate of canister corrosion be affected by temperature, the failure and radionuclide release scenario may change and greatly determine the near-field source term, both in terms of magnitude, timing, and duration, with implications on the overall repository performance. Corrosion products may further lead to significant pressure changes and gas production, thus impacting the conditions and performance of the bentonite buffer. These effects are not considered in this preliminary analysis.

The functional relationships and magnitudes of these effects are not well known, and their overall impact on barrier and repository performance is difficult to evaluate because of the aforementioned coupling and feedback mechanisms. Section 5.2 is a preliminary attempt to examine coupled THMC effects in the bentonite under a high-temperature scenario, supported by the laboratory experimentations described in Section 5.4. These results are used as a conceptual basis for developing a performance assessment approach.

5.3.2.3 Temperature dependence of system state

Temperature not only (directly or indirectly) controls changes in the hydraulic, chemical, mechanical, and thermal properties of the bentonite, but it could also (directly or indirectly) affect the system state and its evolution. Specifically, in a high-temperature scenario, the emergence of two-phase conditions may drastically change the driving forces, resistances to fluid and heat flow, related property changes, and transport mechanisms. Whether the boiling point is reached not only depends on the thermal load and thermal properties of the near field, but also on the pressure conditions, which in turn are affected by repository depth, the rate of resaturation and pressure build-up. The latter can be partly controlled by the chosen emplacement and ventilation options. Again, the possibility of creating a steam phase is the result of a complex interplay of processes, properties, design decisions, and timing between temperature and pressure evolution.

5.3.2.4 Design impacts on temperature distribution

The thermal load as well as temperature distribution from the canister surface through the bentonite buffer to the adjacent host rock depends on the design details of the overall repository layout (depth, emplacement method, deposition tunnel spacing, waste inventory, cooling time in intermediate storage facilities, packing density, materials chosen for EBS components, etc.) as well as the details of the near-field elements (bentonite type, thickness, bentonite emplacement method, etc.). This dependency on design details implies that there is some opportunity for optimization and mitigation, should high temperature become a safety issue. For example, the heat output from a given canister can be adjusted by increasing the cooling time; heat dissipation away from the canister can be increased by considering an open-tunnel option with active or passive ventilation, or modified by adding heat-conducting materials (e.g., graphite) or insulating materials (e.g., sand) to the bentonite, affecting its thermal conductivity; loss

of sorption and swelling capacity can be partly compensated by installing a sacrificial bentonite layer; host-rock temperatures caused by deposition hole interference can be reduced by increasing the spacing between emplacement tunnels.

As with any optimization of engineering design elements, there are tradeoffs between multiple competing objectives that need to be understood and weighted against each other. Notably, reducing the temperature in the bentonite may lead to an increase in the temperature at the canister surface with its detrimental implications that have to be weighted against partial loss of the buffer's barrier function. All design alternatives must be evaluated against economic constraints (an analysis that is beyond the scope of this project).

5.3.3 Physical processes in near field

For these initial scenario evaluations, a simplified, computationally tractable model is developed, in which flow and transport of radionuclides and heat is considered, but no chemical reactions are explicitly accounted for. The chemical reactions that affect bentonite swelling and sorption properties are abstracted to simple temperature-dependent flow and transport properties, guided by the results of numerical laboratory studies described in Sections 5.2 and 5.4.

5.3.3.1 Mass transfer of radionuclide

In the porous media surrounding the canister, radionuclide movement is controlled by diffusion, sorption, and advection. Diffusive flow, which occurs in both aqueous and gas phases, is driven by a radionuclide concentration gradient and will be away from the canister. The key parameter is the effective diffusivity D, generally taken to be the product of the diffusivity the radionuclide would have in free water or air, D_{fw}, the porosity of the porous medium ϕ, the phase saturation S, and a tortuosity factor τ. For a sorbing radionuclide, aqueous-phase diffusive flow will be retarded as a portion of the radionuclides sorbs onto the mineral grains of the porous medium. The key parameter of a linear sorption model is Kd, the distribution coefficient between the sorbed and aqueous phases. If a pressure gradient develops outside the canister, either in response to increased temperature or phase changes, and permeability is high enough, radionuclides will be advected along with the resulting fluid flow. The key parameters are the porosity ϕ, intrinsic permeability k, and (if two-phase conditions develop) parameters of the relative permeability k_{rl} and k_{rg} and capillary pressure P_c functions.

5.3.3.2 Heat transfer

The primary mechanism for heat transfer is conduction, with key parameters thermal conductivity λ and heat capacity C. If the system remains single-phase liquid and permeability remains low, conduction is likely to be the only heat transfer mechanism. However, if fluid flow is significant, heat transfer by convection will occur, controlled by porosity and permeability. If phase changes occur, significant heat transfer effects associated with latent heat will exist, along with convection in both fluid phases.

5.3.4 Conceptual model

The waste canister is modeled as a heat source with time-varying strength; it has a constant concentration of radionuclide at the surface, to represent a small leak that does not introduce enough fluid into the system to create significant fluid flow. The depth of the canister is 500 m, and initial conditions are uniform pressure of 50 bars and uniform temperature of 30°C. The system is initially saturated with liquid water. At this pressure, the boiling temperature of water is greater than 250°C, so single-phase liquid conditions are expected to be maintained for a broad range of heat sources. (The assumption that the

system is fully saturated and repository pressure conditions are hydrostatic at the beginning of heat generation is not realistic and potentially significantly affecting the results of these initial analyses. We proceed with these simplifying assumptions for these preliminary analyses, because simulating two-phase and boiling conditions is conceptually and computationally much more demanding, but they do not add substantially to the discussion of the analysis approach, which is the focus of this section.)

We consider a one-dimensional (1D) radial geometry with the canister at the center, surrounded by backfill consisting of bentonite and possibly a sand mixture introduced to alter thermal conductivity, beyond which an excavation damaged zone (EDZ) of increased porosity and permeability exists, surrounded by the host rock, a low-permeability argillaceous (or clay-rich) formation (Figure 5-42). The temporal variation of a typical heat-source is shown in Figure 5-43. The decaying nature of the heat source means that throughout the system, temperatures will increase to some maximum value and then decline. The numerical simulations all run until temperatures throughout the model domain have declined to well below 100°C.

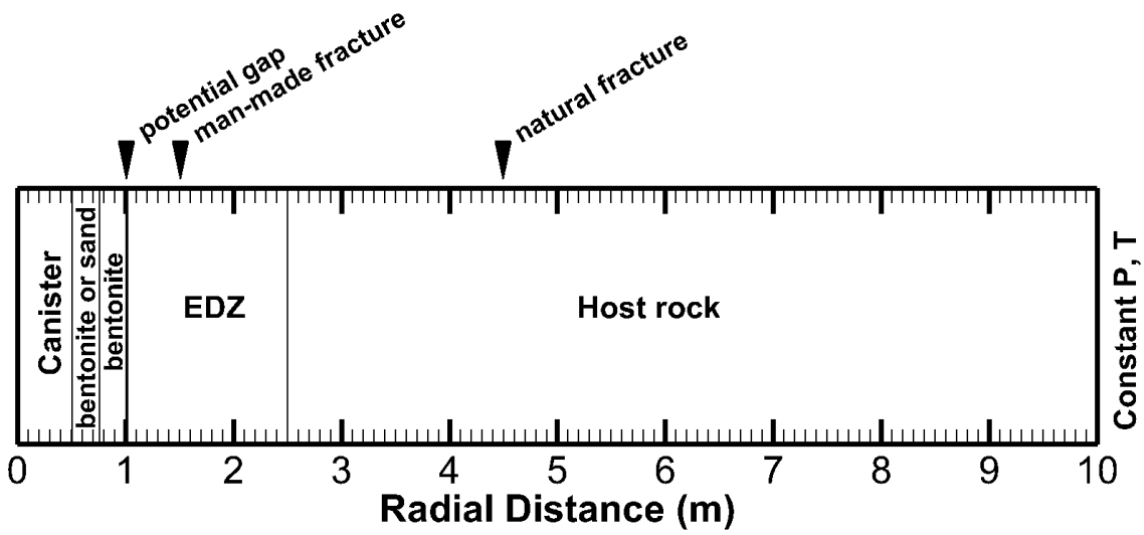

Figure 5-42. Schematic diagram of 1D radial model, showing different materials and locations of potential axial flow paths.

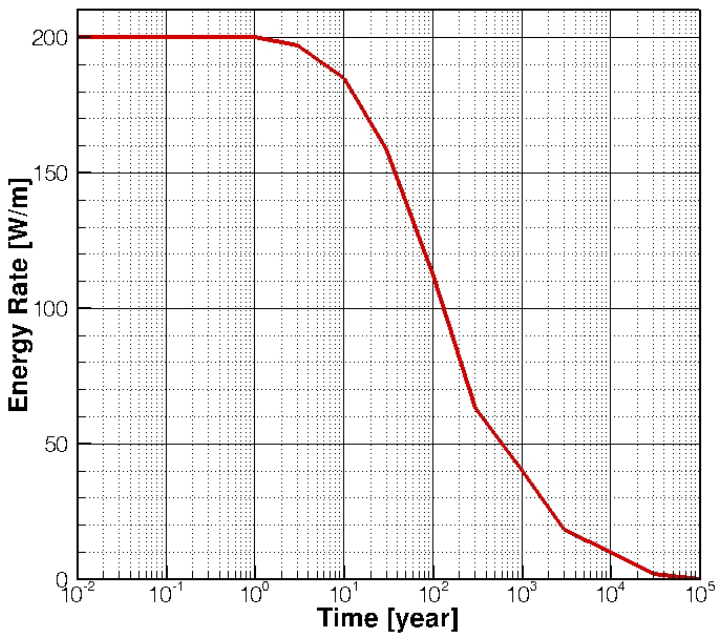

Figure 5-43. Heat source strength per meter of waste package as a function of time for the base case.

We hypothesize the existence of potential high-permeability axial flow paths at several radial distances (see Figure 5-42):

(1) at the bentonite/EDZ interface, representing a potential gap; such a gap likely exists after bentonite installation, is expected to close upon bentonite swelling during resaturation, but may persists if it is too large, if resaturation is heterogeneous, or if bentonite swelling properties are insufficient or have been changed (e.g., due to high temperatures). The permeability of this cylindrical flow path is highly uncertain and depends on the quality of the seal created at the bentonite-EDZ interface (r = 1 m)
(2) midway through the EDZ, to represent through-going damage in the EDZ (r = 1.5 m)
(3) in the host rock to represent a natural fracture (r = 4.5 m)

The time at which radionuclides reach these potential axial flow paths is a key performance metric however, the axial flow itself is not modeled, but only very approximately accounted for in the evaluated performance metric by multiplying radionuclide concentration with the permeability of the axial flow path. The radial permeabilities are shown in Table 5-10. The axial flow paths in the EDZ and host rock are always present, but the flow path at the bentonite/EDZ boundary is only present when temperature in the bentonite has been high enough to promote illitization, which hampers bentonite swelling, thus leading to permeability increase.

Our simplified representation of illitization includes three effects on the bentonite properties:

(1) decrease in swelling
(2) increase in permeability
(3) decrease in sorption

Specifically, we represent three material properties (which are usually assumed temperature-independent) as a function of temperature. The temperature dependence is included only for temperatures above a threshold temperature (assumed to be 100°C in the base case), where illitization is expected to occur. The property changes are assumed irreversible, i.e., the long-term properties at any given location are determined by the maximum temperature reached by the thermal pulse as it passed through that particular location. Three simple, parameterized functions are defined. They provide the desired property changes, as illustrated schematically in Figure 5-44. Figure 5-44a and Figure 5-44b, and show the effect on permeability and swelling, qualitatively consistent with results from laboratory experiments. Figure 5-44c, which shows the decline in sorption capacity as a function of temperature, is more conceptual in nature, and follows general principles, but not specific laboratory data. Note that each temperature effect is controlled by two or three parameters. These parameters are varied in the global sensitivity and uncertainty propagation analyses described in Sections 5.3.7 and 5.3.8, respectively.

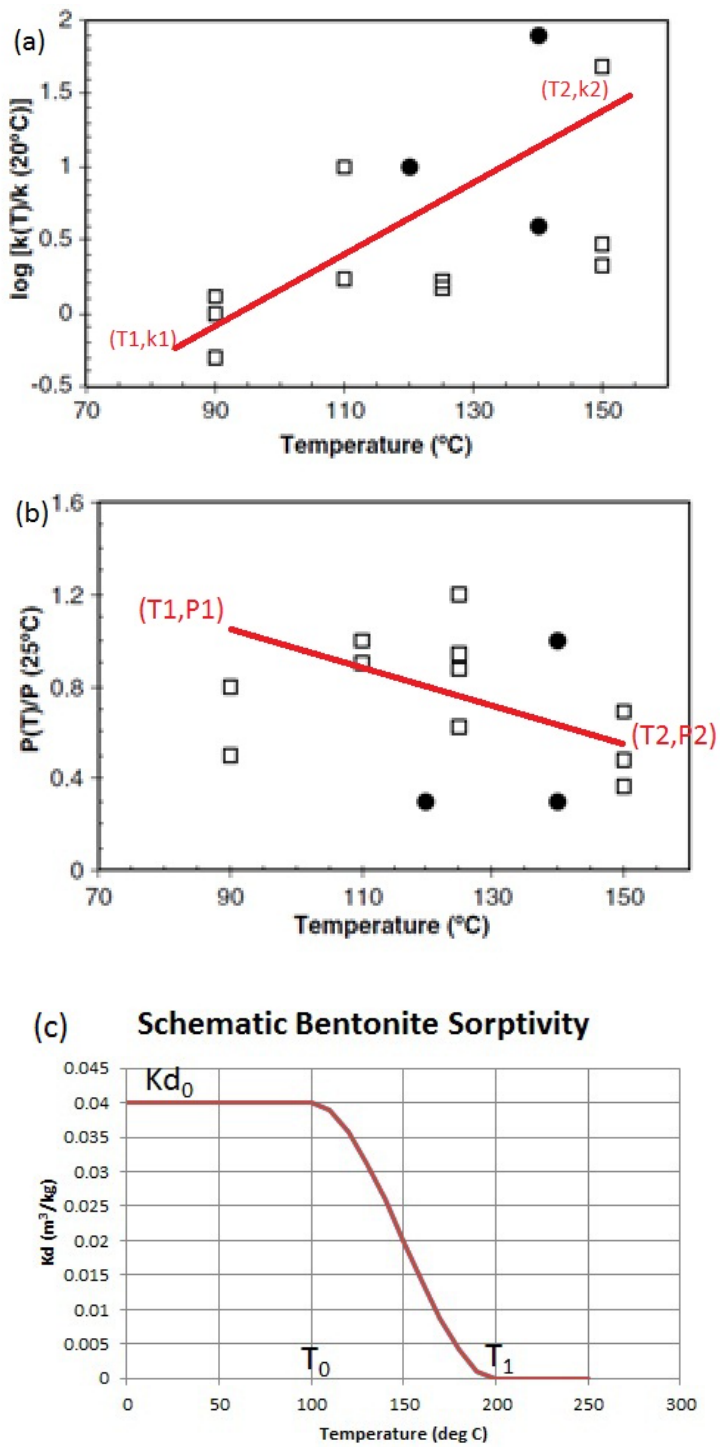

Figure 5-44. Simplified temperature-dependent properties to represent the effects of illitization: (a) permeability increases, (b) swelling ability decreases, and (c) sorptivity decreases.

5.3.5 Performance metrics

The overall system behavior and its sensitivity to changes in scenarios and model input parameters are evaluated by recording relevant state variables at specific points in the model domain and as a function of time. These performance metrics are:

1. The maximum temperature at key locations: at the canister surface (r = 0.5 m), at the (potential) sand/bentonite boundary (r = 0.75 m), at the bentonite/EDZ boundary (r = 1.0 m), in the middle of the EDZ (r = 1.5 m), at the EDZ/host rock boundary (r = 2.5 m), and at the axial fracture in the host rock (r = 4.5 m).
2. The maximum permeability and minimum sorption capacity of bentonite at the same key locations.
3. The time-integrated radionuclide concentration at a potential axial flow path, multiplied by this flow path's permeability. Multiplication by the temperature-dependent permeability is introduced as a very simple means to indicate that arrival of radionuclides at an axial flow path is only performance-relevant if this flow path has the potential to advectively carry the radionuclides to the accessible environment. (It is understood that this representation is highly simplified; a more realistic representation of radionuclide transport in radial and axial direction requires using a 2D or 3D model.)

Note that the third metric is the "bottom line" metric that describes how well the bentonite is performing to limit radionuclide escape from the near field; the first two are to help us better understand the system.

5.3.6 Base-case scenario and variations

The base-case simulation does not include a temperature dependence of bentonite permeability, swelling, or sorptivity. Heat source strength is taken from Figure 5-43. Material properties are given in Table 5-10 and are generally considered representative of typical repositories, but do not represent any particular site.

Table 5-10. Material properties used for the base case simulation (fluid remains single-phase liquid)

Property	Bentonite	EDZ	Host Rock	Units
Porosity ϕ	0.33	0.33	0.16	-
Permeability k	2E-21	2E-18	2E-20	m^2
Compressibility	5E-8	3.2E-8	3.2E-9	Pa^{-1}
Thermal conductivity λ	1	2	2	W/mK
Heat Capacity C	1000	1000	1000	J/kg
Sorptivity Kd	4E-2	$0^{\&}$	$0^{\&}$	m^3/kg
Diffusivity D_{fw}	2.35E-9	2.35E-9	2.35E-9	m^2/s
Tortuosity τ	$1^{\#}$	$1^{\#}$	$1^{\#}$	-

[&] Neglecting sorption in the host rock highlights the barrier role of the bentonite buffer; non-zero linear sorption coefficients are considered in the sensitivity and uncertainty analyses (see Table 5-11 below).

[#] A tortuosity of 1.0 is a conservative assumption regarding diffusive radionuclide transport; the impact of diffusion-related parameters on repository performance will be analyzed in future studies.

The buffer consists of pure bentonite (i.e., no sand mixture is included) and there is no gap between the bentonite and the EDZ. The radionuclide is assumed to be strongly sorbing and non-decaying.

Figure 5-45 shows the temperature as a function of time at key locations in the system for the base case (Figure 5-45a) and two cases with stronger heat sources. In Figure 5-45b, heat source strength is doubled and in Figure 5-45c, heat source strength is tripled compared to Figure 5-43. Another means of varying heat source strength would be to keep the same function, but assume different durations of above-ground storage, leading to different starting times. For the base case, temperature never exceeds 100°C anywhere in the system; for the doubled heat source strength, temperature exceeds 100°C in the inner half of the bentonite, and for the tripled heat source strength, temperature exceeds 100°C throughout the bentonite and beyond.

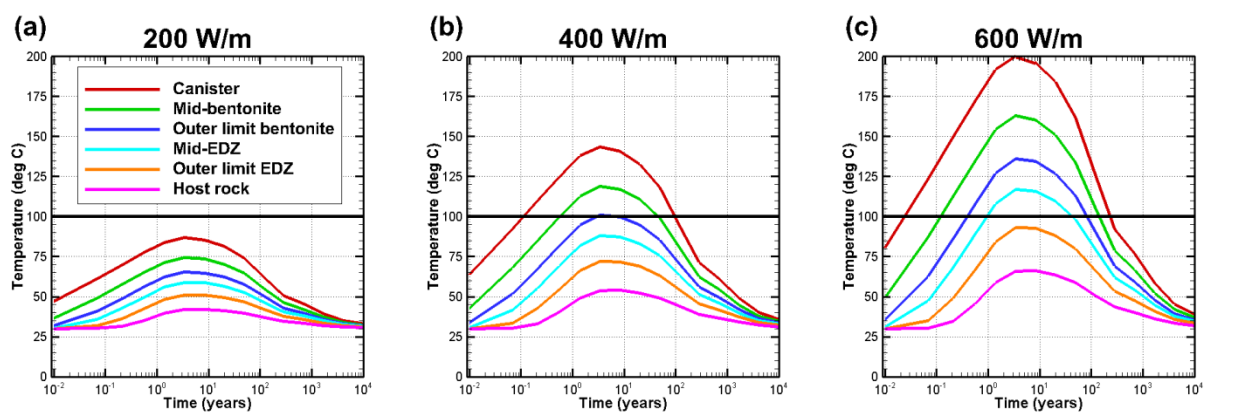

Figure 5-45. Temperature as a function of time at key locations for the base case (a) and cases in which the heat source strength shown in Figure 5.4.2 is doubled (b) and tripled (c).

The radionuclide concentration as a function of time at key locations is shown in Figure 5-46 for the base case (strongly sorbing radionuclide) and for a non-sorbing radionuclide. The concentration level of 10^{-7} is picked as the threshold level at which radionuclide "arrival" occurs. The units here are arbitrary, with 10^{-4} as the concentration at the canister and therefore the threshold being 1000 times smaller. Note that the arrival times differ greatly depending on the sorption strength of the bentonite. In particular, the arrival time at the bentonite/EDZ boundary (the first potential axial flow path) increases from 2 months to 22 years, the arrival time at the mid-EDZ location increases from 0.5 years to 28 years, and the arrival at the hypothetical fracture in the host rock increases from 9 years to 53 years. The materials beyond the bentonite (the EDZ and the host rock) are assumed to be non-sorbing in the base case shown here (but is included later during the sensitivity and uncertainty quantification analyses), so the delays are just due to sorption in the bentonite. Hence, when we consider temperature-dependent effects that may decrease bentonite sorptivity, we expect a large impact on arrival times.

Note that the assumption of radionuclides beginning to leak at time zero (as implemented by our constant-concentration boundary condition) is extremely unrealistic, and the arrival times should thus be considered as elapsed times since leakage began. For the base case and the variations that do not include temperature-dependent properties, shifting time this way poses no problems. However, when temperature-dependent properties are included, applying a boundary condition that initiates canister leakage at a non-

zero time will be important, so that heat transfer and radionuclide movement will be properly synchronized.

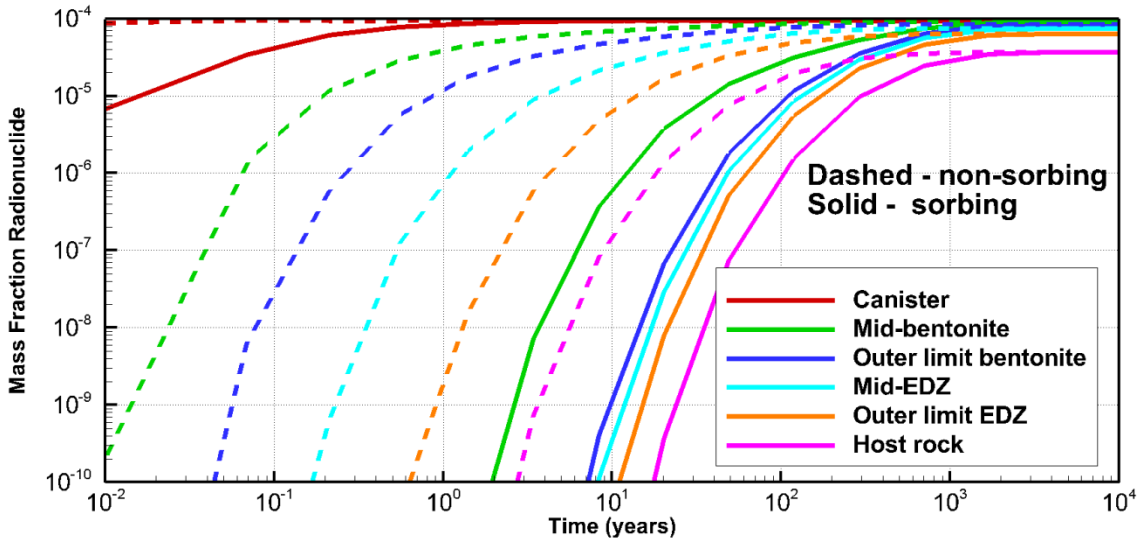

Figure 5-46. Radionuclide concentration as a function of time at key locations for the base case (strongly sorbing radionuclide) and for a non-sorbing radionuclide.

Several additional variations of the conceptual model using non-temperature-dependent properties help illustrate the range of thermal behavior we can expect.

The inner half of the bentonite backfill can be replaced with a bentonite/sand/graphite mixture that has a higher thermal conductivity, to promote heat transfer, and thereby limit maximum temperature. The temperature response when the mixture has double the bentonite thermal conductivity is shown in Figure 5-47. In contrast, a mixture with lower thermal conductivity has also been proposed, to effectively insulate the canister. The temperature response when the mixture has half the bentonite thermal conductivity is shown in Figure 5-48.

Figure 5-47 shows the temperature response when the inner half of the backfill is sand with a thermal conductivity of 2 W/mK, double that of the bentonite. Only the temperature response at the canister shows a decrease compared to Figure 5-45. This is because all the other locations are beyond where the thermal conductivity was changed. But temperature is lower throughout the region where sand replaces bentonite. Similarly, Figure 5-47 shows the temperature response when the inner half of the backfill is a material with half the thermal conductivity of bentonite. Now temperature is higher throughout the region with lower thermal conductivity.

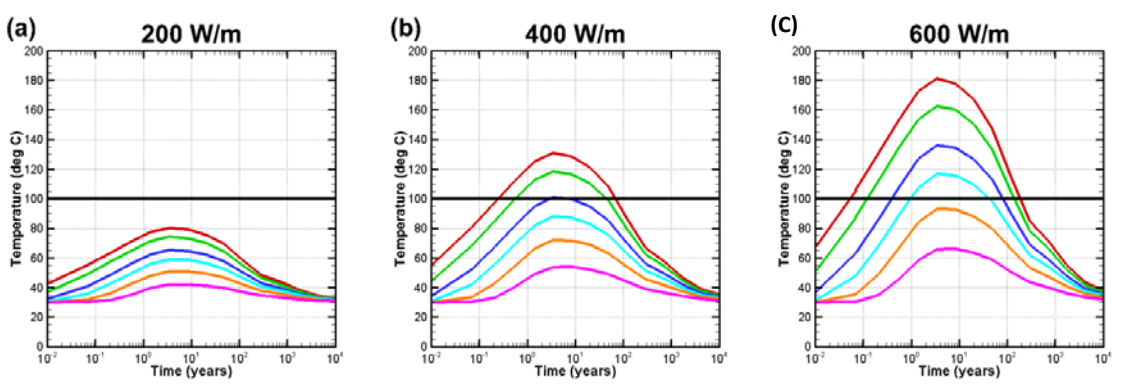

Figure 5-47. Temperature as a function of time at key locations for a case with high-thermal conductivity material in place of inner bentonite: (a) heat source strength as shown in Figure 5-43, (b) heat source strength is doubled, and (c) heat source strength is tripled.

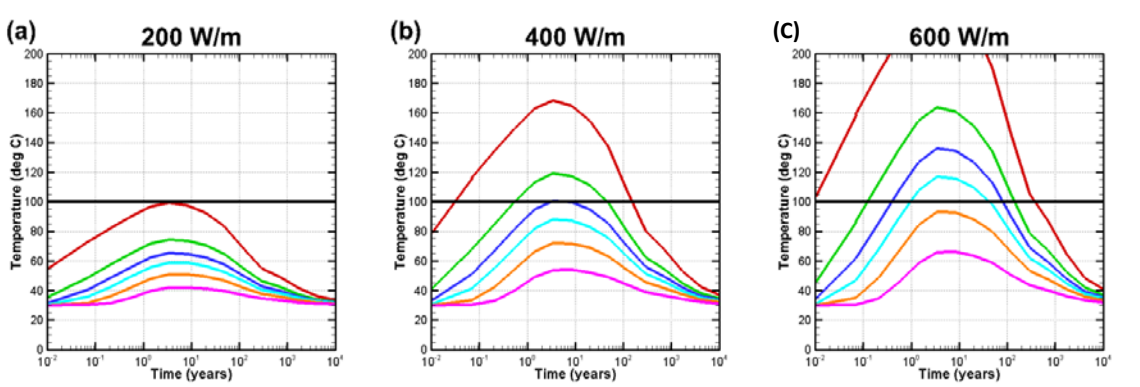

Figure 5-48. Temperature as a function of time at key locations for a case with low-thermal conductivity material in place of inner bentonite: (a) heat source strength as shown in Figure 5-43, (b) heat source strength is doubled, and (c) heat source strength is tripled.

5.3.7 Global sensitivity analysis

5.3.7.1 Analysis approach

In a probabilistic performance assessment calculation, the performance metrics are evaluated for a large number of parameter combinations to examine the expected system behavior and its uncertainty, and for eventual comparison to regulatory limits. The uncertainty and variability in these model predictions depend not only on the uncertainties of the input parameters, but also on the sensitivity of the performance measure to this input parameter. It is therefore essential to identify the relevant parameters in a comprehensive sensitivity analysis to help focus research and characterization on the parameters that most likely influence the repository performance.

An additional complication arises due to the fact that the sensitivity of the performance metric to a given parameter depends on the values of other parameters. For example, the parameters describing the temperature dependence of bentonite properties are only influential if temperature itself reaches a certain level, which in turn depends on the various coupling and feedback mechanisms described in Section 5.3.2. To account for the impact of nonlinearities and parameter interdependence on sensitivity measures, so-called global sensitivity analysis methods have been developed.

Global sensitivity analysis methods examine many combinations within the range of acceptable parameter values. Saltelli et al. (2008) describe available global sensitivity analysis approaches. Specifically, the method originally proposed by Morris (1991) serves the purpose of providing qualitative measures of relative parameter influence and nonlinearity with a manageable number of simulation runs. In this approach (which is commonly referred to as the Morris one-at-a-time (MOAT) elementary effects method), each axis of the parameter hypercube is subdivided into k-1 intervals for a total of k^n grid points, where n is the number of parameters. A perturbation Δ is then calculated for each parameter i:

$$\Delta_i = \frac{k}{2(k-1)} \cdot (p_{i,\max} - p_{i,\min}) \tag{5-10}$$

Next, a random grid point in the parameter space is selected, the model is run and the performance measure z is evaluated. Then—one at a time and in random order—each parameter p_i is perturbed by Δ_i, the model is run to recalculate z, and the corresponding impact (or elementary effect, EE_i) on the output is computed as

$$EE_i = \frac{z(p_1, p_2, \ldots, p_{i-1}, p_i + \Delta, \ldots, p_n) - z(p_1, p_2, \ldots, p_n)}{\Delta} \tag{5-11}$$

The procedure is repeated for multiple, randomly selected starting points of a path in the parameter space that consists of n steps and n+1 simulation runs for the evaluation of the elementary effect in the vicinity of this point. After completion of a number of such paths, which is mainly determined by computational limitations, the mean and standard deviation of the absolute elementary effects are calculated. The mean assesses the overall influence of the respective parameter on the output; the standard deviation indicates whether the effects are linear and additive or nonlinear, or whether interactions among the parameters are involved.

The iTOUGH2 code (Finsterle, 2004; http://esd.lbl.gov/iTOUGH2), which is the inverse modeling and uncertainty analysis tool for TOUGH2, is used to perform the TOUGH2 simulations of repository performance and to perform global sensitivity and uncertainty propagation analyses.

5.3.7.2 Morris global sensitivity analysis

For demonstration purposes, the Morris one-at-a-time global sensitivity analysis method described in the previous subsection is applied to the highly simplified conceptual model of Section 5.3.4 to identify the most influential parameters —with respect to the performance metrics listed in Section 5.3.5—among the 18 parameters shown in Table 5-11. The parameters include the heat load factor, permeabilities, thermal conductivities, sorption coefficients, and 5 parameters that describe the temperature dependence of sorptivity and permeability, specifically that of the gap between the bentonite buffer and the EDZ. Parameters #14 and #15 refer to the temperatures beyond which sorptivity starts to be affected, and when it reaches a value of zero, respectively (see Figure 5-45). Parameter #16 is the temperature at which permeability is increased due to reduced swelling. The slope of the relationship between temperature and

permeability increase is given by parameter #17. Finally, a special treatment is given to the gap between the bentonite and the EDZ: it is expected that the permeability of the gap increases much more strongly should swelling of the bentonite be affected by illitization; this effect is represented by parameter #18. It is also assumed that the boundary between these two materials may have increased permeability even if swelling is unaffected by temperature (parameter #4). Note that both the temperature-dependent reduction in sorptivity *Kd* and increase in permeability are assumed irreversible in the model, i.e., the respective values calculated for the highest temperature experienced at any given location is maintained also during the cooling period.

Table 5-11 shows the parameter ranges, which defines the hypercube for the global sensitivity analysis. The ranges also provide the lower and upper bounds for the Monte Carlo uncertainty propagation analysis discussed in Section 5.4.8, where parameters are sampled from the indicated probability distribution. If the distribution is normal or log-normal, the mean is the base-case value of Table 5-11, and the standard deviation is given in the fifth column of Table 5-11.

Within the parameter hypercube chosen here, no boiling conditions at the waste canister are reached, avoiding the complexity of two-phase flow, which would also greatly increase the number of parameters that are potentially influential. Emerging steam may greatly complicate the abstraction of the temperature dependencies and would require the inclusion of pathway dilation and other coupled effects.

Table 5-11. Parameters subjected to global sensitivity and uncertainty propagation analyses

#	Parameter	Range	Distribution	Std. Dev.	Units
1	Heat load factor	1 – 3	uniform	-	-
2	log(*k*) Sand	-21 – -16	uniform	-	log(m^2)
3	log(*k*) Bentonite	-22 – -19	normal	1.0	log(m^2)
4	log(*k*) Gap	-21 – -18	uniform	-	log(m^2)
5	log(*k*) EDZ	-19 – -16	normal	1.0	log(m^2)
6	log(*k*) Host rock	-21 – -18	normal	1.0	log(m^2)
7	Conductivity λ Sand	0.5 – 2.5	uniform	-	W/mK
8	Conductivity λ Bentonite	0.5 – 2.5	normal	0.5	W/mK
9	Conductivity λ EDZ	1.0 – 3.0	normal	0.5	W/mK
10	Conductivity λ Host rock	1.0 – 3.0	normal	0.5	W/mK
11	log(*Kd*) Sand	-3 – -1	normal	0.5	log(m^3/kg)
12	log(*Kd*) Bentonite	-3 – -1	normal	0.5	log(m^3/kg)
13	log(*Kd*) EDZ/Host rock	-4 – -2	uniform	-	log(m^3/kg)
14	T_0 for *Kd* reduction	90 – 140	uniform	-	°C
15	T_1 for *Kd* reduction	150 – 200	uniform	-	°C
16	T_0 for log(*k*) increase	90 – 140	uniform	-	°C
17	Δlog(*k*) at T = 200 °C	2 – 5	uniform	-	-
18	Δlog(*k*) at T = 200 °C Gap	2 – 10	uniform	-	-

The sensitivity analysis of the first performance metric, i.e., the maximum temperature encountered at certain control points, does not reveal any surprises, with the heat load being by far the most dominant factor, followed by the thermal conductivities. In this conceptual model, advective fluid and heat flow is essentially non-existent, because there is no natural pressure gradient or gravity, no capillary-driven resaturation of the bentonite, no development of a steam phase with associated expansion, pressure build-

up, and liquid displacement; convective heat flow is limited to water movement driven by the very small thermal expansivity of the liquid phase. As a result, the permeabilities have no influence on maximum temperatures, and —consequently—none of the parameters describing the temperature dependence of permeability (nor sorptivity) need to be considered to predict the temperature distribution. It is interesting to note that the maximal temperatures are significantly more sensitive to the thermal conductivities of the EDZ and host rock than to the thermal conductivity of the buffer material. Thermal diffusivity is large enough so that the thermal pulse travels through the bentonite within a short time (compared to the time of elevated temperatures); consequently, the ability of the formation to carry away the decay heat out of the EBS becomes the relevant process, which is determined by the thermal properties of the EDZ and host rock. Figure 5-49 shows the maximum temperature at (a) the canister surface and (b) the contact between the bentonite and the EDZ as a function of the buffer's and host formation's thermal conductivity. The gradient along each axis shows the respective parameter's influence on the maximum temperature, indicating that the host formation thermal conductivity is generally more influential than that of the bentonite, whose relative influence only increases if it becomes the limiting factor (i.e., low values for bentonite and high values for host formation); the impact of the bentonite thermal properties at the buffer-host rock interface is barely visible. This suggests that only limited thermal control can be exercised by modifying the thermal properties of the buffer materials for irreversible temperature effects and long-term radionuclide release. (This conclusion applies to a backfilled repository; it may be different for a ventilated repository, where a temperature at the outer buffer boundary is fixed during the ventilation period.)

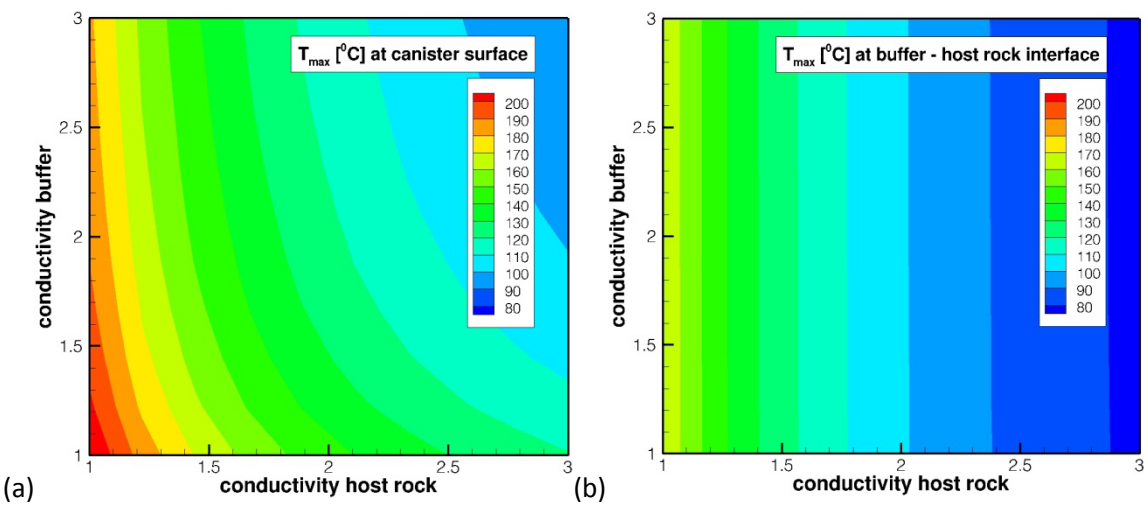

Figure 5-49. Maximum temperature at (a) canister surface and (b) interface between bentonite buffer and host formation as a function of thermal conductivity of the two materials (the heat load corresponds to the 400 W/m scenario).

The maximum permeability is foremost influenced by the parameters determining the maximum temperature (i.e., heat load factor and host rock thermal conductivity) as well as the parameters of the temperature-dependence model shown in Figure 5-44a, specifically the minimum temperature at which permeability increase is initiated (i.e., parameter #16). The reference permeabilities obviously also affect the maximum permeabilities. All the other parameters are non-influential, as expected.

Similarly, the minimum *Kd* is determined by the sorptivity values themselves (specifically that of the bentonite), the parameters determining the maximum temperature, as well as parameters #14 and #15 of the *Kd*-reduction model (Figure 5-44c).

As discussed in Section 5.4.5, the third performance metric (the radionuclide release to the axial flow paths, whose permeability might have been increased due to temperature effects) is the metric of interest for performance assessment. Figure 5-50 summarizes the results of the Morris global sensitivity analysis. The heat load factor is indeed the most influential factor among the parameters considered in the analysis, followed by the minimum temperature when permeability starts to increase, and the host formation's thermal conductivity, which influences the maximum temperature, as discussed above. The permeability of the interface between the buffer and the host rock as well as the slope of the permeability increase model come next, followed by sorptivity parameters, albeit all with significantly reduced impact.

The relative insensitivity of sorptivity parameters (or the relatively strong impact of permeability-related parameters) can be explained by the chosen performance metric, which includes the permeability of the axial flow path as a surrogate for capturing migration of radionuclides from the near field to the accessible environment. Changing maximum temperature and thus maximum permeability of these axial flow paths affects the performance metric in a multiplicative manner. On the other hand, the long-term concentration flux of a non-decaying radionuclide arriving at the axial flow paths is not that strongly affected by sorptivity, because the sorption capacity of the small-volume buffer is being asymptotically reached.

The coefficient of variation for all parameters is very high, indicating strong parameter interdependencies and nonlinearity effects. For example, a specific combination of parameters must be realized for the gap between the buffer and host rock to remain open, as high temperatures trigger illitization and reduce bentonite swelling. For many parameter combinations, the gap may be closed; however, once it remains open, its hydraulic properties increase dramatically, directly impacting the performance metric. It is such parameter interdependence and nonlinearity effects that would render a local sensitivity analysis almost useless, specifically if being concerned about conditions that occur, with a small probability. A detailed discussion of how to interpret variability in the elementary effect can be found in Morris (1991) and Wainwright et al. (2013).

These preliminary results of a global sensitivity analysis should not be taken as guidelines for performance assessment or mitigation measures to reduce the impact of high-temperature scenarios on repository performance. Instead, they highlight the importance of model conceptualization and the choice of a performance metrics used in an abstracted performance assessment model. For example, the existence of the gap is an important factor, and it is conceptualized by a dramatic permeability increase triggered by high temperatures that lead to illitization and thus loss of swelling capacity. This conceptualization is highly uncertain, and thus a wide range is given for gap-related model parameters, leading to its strong influence. While capturing the existence of a gap and its hydraulic properties is obviously important for performance assessment, its influence is exaggerated here because of an oversimplified performance metric, which gives increasing weight to transport along the gap as the permeability increases. In reality, however, release of radionuclides to the water flowing in the gap will be diffusion-limited, i.e., repository performance will not be further affected if the gap widens more. This highlights that the performance assessment model must be carefully built with appropriate abstraction of key features and processes. The details of the *Kd*-reduction model of Figure 5-44c are also influential, warranting further research into this key factor controlling radionuclide retardation in the bentonite for high-temperature scenarios. However, these factors only become influential if the maximum temperatures are high, giving temperature control its special significance.

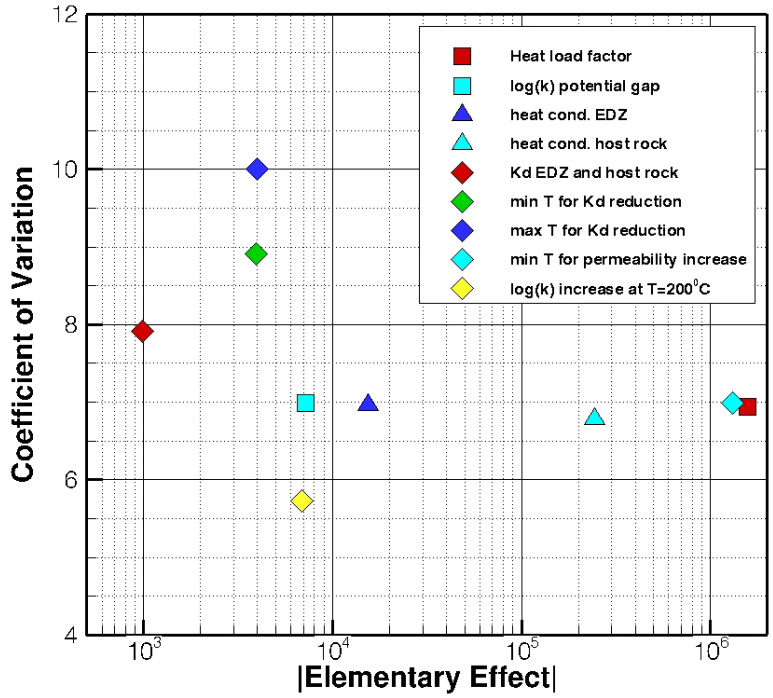

Figure 5-50. Morris global sensitivity analysis of surrogate repository performance metric: absolute elementary effect and coefficient of variation, indicating relative influence and effects of nonlinearity and parameter interdependence.

5.3.8 Uncertainty quantification

A preliminary Monte Carlo analysis was performed, using Latin hypercube sampling within the ranges and based on the distributions defined in Table 5-11. Sample size is 500. No correlations among the parameters are included, even though they are likely to exist (specifically between the initiation temperatures of permeability increase and *Kd* reduction, which are both related to illitization).

Figure 5-51 shows the maximum temperature reached at six locations within the EBS and host rock. The uncertainties in the predicted maximum temperatures are considerable. From the global sensitivity analysis it is clear that most of this variability is the result of the assumed range in the heat load factor and uncertainty in the EDZ and host rock thermal conductivities. The predicted temperature ranges are considerably reduced if the heat load is considered known and fixed at the 400 W/m scenario. Figure 5-52 shows the histograms of the maximum temperature at the canister surface, with and without accounting for uncertainty in the heat load factor. The histograms highlight the reduction in predicted canister temperature if the heat load is controlled; it also shows that the distribution is not normal, i.e., nonlinearity effects exist.

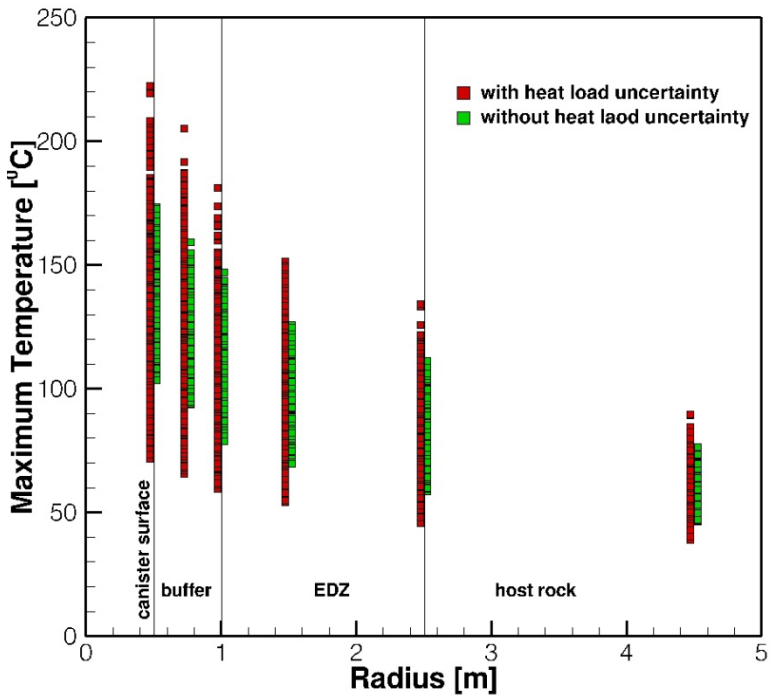

Figure 5-51. Range of predicted maximum temperature as a function of radial distance.

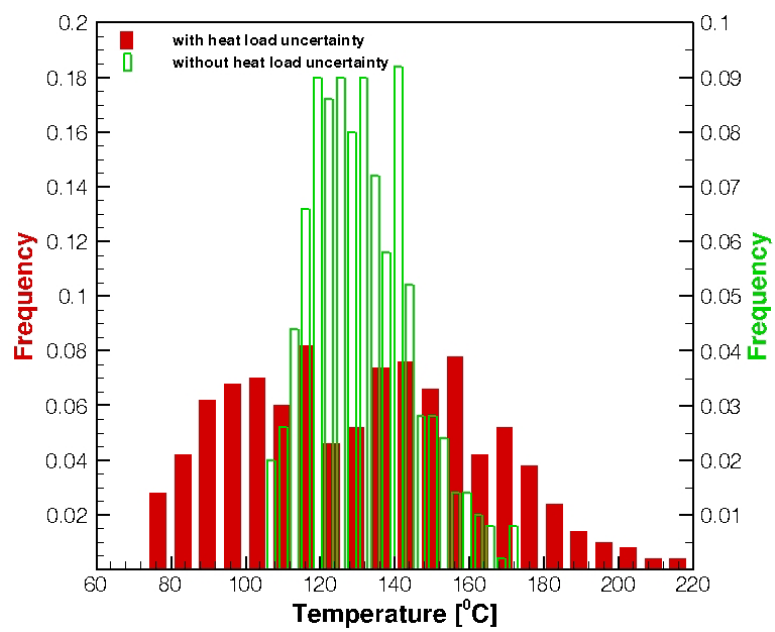

Figure 5-52. Histogram of maximum temperature at canister surface, with (red) and without (green) accounting for uncertainty in the heat load factor.

Figure 5-53 shows the uncertainty ranges of the repository performance metric (which is based on radionuclide releases along all three axial flow paths), again including and excluding uncertainty in the heat load factor. Three characteristics are noteworthy. First, the range of predicted permeability-weighted concentration fluxes at axial migration pathways is very large, with most of the realizations resulting in very small values, and a few leading to potentially very high impacts on repository performance. Second, the system reaches a quasi-steady state after about 1000 years, after which temperature-dependent effects and the prediction uncertainty do not change anymore. This is explained by the type of source term used (that of a non-decaying radionuclide released from a non-diminishing constant concentration boundary), and the fact that the heat pulse has passed and the maximum temperature (which determines the irreversible effects on permeability and sorptivity) has been established after about 1000 years. Third, the probability that very high values are obtained (reflecting problematic repository performance) is considerably reduced if the heat load of the emplaced waste is known and can be controlled.

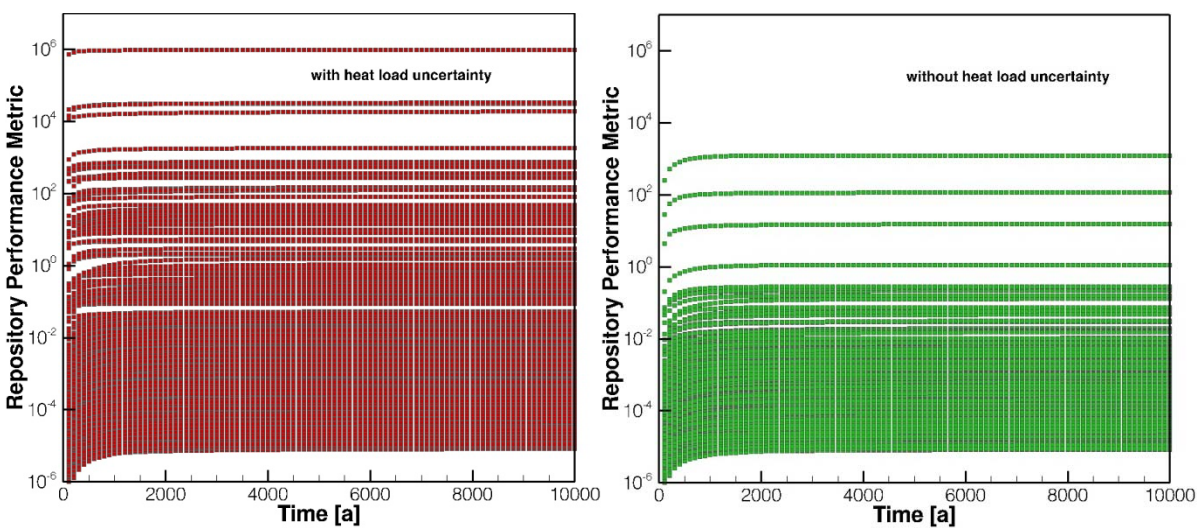

(a) (b)

Figure 5-53. Results of Monte Carlo uncertainty propagation analysis, showing spread of predicted repository performance metric due to uncertainties in select input parameters (see Table 5-11), (a) including, and (b) excluding uncertainty in heat load factor.

5.3.9 Summary and future work

This subtask presents an outline of a modeling approach that could be used to examine the impact of a variety of complex factors and interdependent processes on the performance of a clay-based high-temperature repository. In particular, our research activities performed in FY13 addressed the following issues:

(1) What potential scenarios may lead to elevated temperatures at the canister surface, within the bentonite buffer, or the host rock?

(2) How do elevated temperatures affect the state, properties, and behavior of the near-field repository system?
(3) How can complex temperature effects be abstracted and implemented into a model for efficient multi-query simulations as needed for global sensitivity analysis and uncertainty quantification?
(4) To what extent is the repository performance adversely affected by elevated temperatures?
(5) Which factors and parameters most critically affect repository performance?
(6) Which of these influential factors or parameters can be controlled (i.e., are repository design parameters), and which parameters are not controllable and have an unacceptably high estimation uncertainty?
(7) What methods are appropriate to reliably identify influential parameters and prediction uncertainty?
(8) Which aspects of alternative scenarios can be parameterized and thus subjected to formal sensitivity and uncertainty analysis?

In our preliminary analysis, we illustrated how some of the coupled THMC processes examined by mechanistic modeling (see, for example, those described in Section 5.2) can be incorporated into a simpler model suitable for performance assessment calculations. Influential parameters have been identified using global sensitivity analysis methods, and their uncertainties have been propagated through the model to evaluate the uncertainty ranges of the predicted repository performance.

These preliminary results should not be taken as guidelines for performance assessment or mitigation measures to reduce the impact of high-temperature scenarios on repository performance. Instead, they intend to highlight the importance of model conceptualization and the choice of performance metrics used in an abstracted performance assessment model.

The simulations describe here represent only an initial, simple case. Additional features that may be considered in future analyses include:

(1) A non-backfilled (ventilated) case, in which pressure is atmospheric, making boiling temperature within reach, and thereby introducing multi-phase flow effects;
(2) Canister integrity that is a function of time, temperature, or saturation conditions to represent corrosion or breach;
(3) The impact of nonuniform or partial resaturation of the bentonite;
(4) The type of radionuclides considered (half life and sorption coefficients);
(5) Any diffusion-related parameters as well as parameters describing non-equilibrium sorption effects;
(6) Effects of heterogeneity;
(7) Two-dimensional and three-dimensional models to capture end effects, and gravity effects, and multiple interacting canisters; and
(8) Inclusion of far-field fate of the released radionuclides.

5.4 Laboratory Tests

The primary objective of the laboratory experiments is to investigate the impact of high-T physical and chemical alterations of buffer and backfill materials (bentonite) and clay host rock on their geomechanical and hydrological properties, and on interaction between EBS and natural system (Note that this interaction is critical, because moisture and related chemicals needed for chemical alteration [e.g., K^+] are

mainly provided by the host rock). Our particular interest is the heat-induced chemical alteration—illitization of smectite and cementation—of buffer and backfill materials (bentonite) within the EBS, because it may compromise the mechanical and hydrological integrity and sealing efficiency of the EBS by reducing the clay's plasticity and swelling capability when moisture is introduced. The experiment conducted in this task aims to identify maximum allowable temperature of the clay repository. So far, clay and mudrock samples for the tests have been acquired and preliminary initial characterizations have been conducted. Additionally, an experimental setup for simultaneous heat treatment of multiple clay samples has been built. The details of these activities are described below.

5.4.1 Tested samples

For this experiment, we acquired two types of samples through collaborations with LANL and NAGRA. From LANL, raw (untreated) bentonite (Bara-Kade Bentonite chips, Bentonite Performance Minerals, LLC) was obtained. This particular batch of the clay has been undergoing extensive geochemical characterization by the NANL team. In addition, Opalinus Clay cores from Mont Terri were obtained from NAGRA.

Initial characterizations were conducted on two Mont Terri cores (Mont Teri 11_12 and 33_34 Cores, Figure 5-54). The cores are approximately 111 mm in diameter and 1 meter in length. Core 11_12 arrived in 2 pieces, while Core 33_34 in four large and one small piece. The mass of each core was estimated to be ~ 25 kg (mass of core + box ~ 27 kg, left in box for stability). Visually, the cores appeared to be hard and dry. Although they were in sealed plastic liners, no condensation was observed on the inside of the liners, as is often seen in samples even under mild temperature gradients observed in the laboratory.

Figure 5-54. Mont Terri clay cores acquired through collaboration with NAGRA

X-ray CT scans of both cores were performed to examine the internal structure. Both cores were similar and have the same general characteristics. CT data show density, with high density shown as light and low density shown as dark in Figure 5-55. Both cores had fractures (e.g., dark linear features in the Figure), which may have been caused by desiccation. The distance between these fractures was relatively uniform, with larger fracture spacing being ~1 cm and smaller spacing ~0.5 cm.

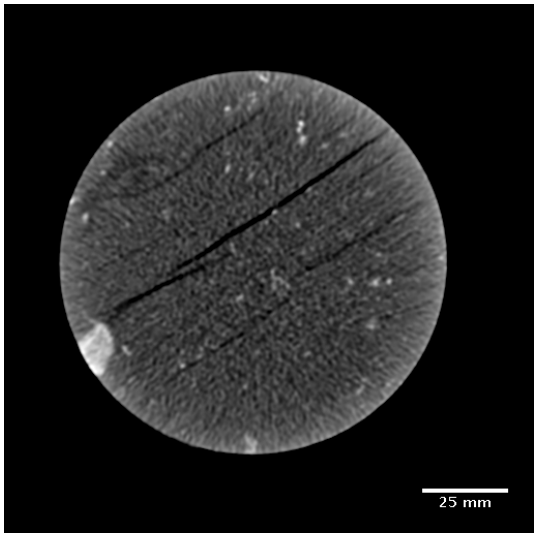

Figure 5-55. CT cross section of Core 11_12. Dark linear features appear to be desiccation fractures. Bright high density features are also present (discussed below).

CT images also revealed one-dimensional, sublinear high-density features pervading the clay. The orientation appeared to be random at first (Figure 5-56). However after examining the reconstructed 3D images from numerous angles, a predominant orientation was identified (Figure 5-57). Interestingly, the high-density features were oriented perpendicularly to the desiccation fractures which were most likely associated with the bedding planes of the rock. One possibility is that these high-density features are minerals such as calcite precipitating from the escaping pore fluid when the clay was consolidated at early stages of diagenesis. At this point, it is not clear how these features will impact water vapor or liquid transport in the clay, and also the mechanical properties. Therefore, our experiments will need to consider the anisotropy of the samples very carefully.

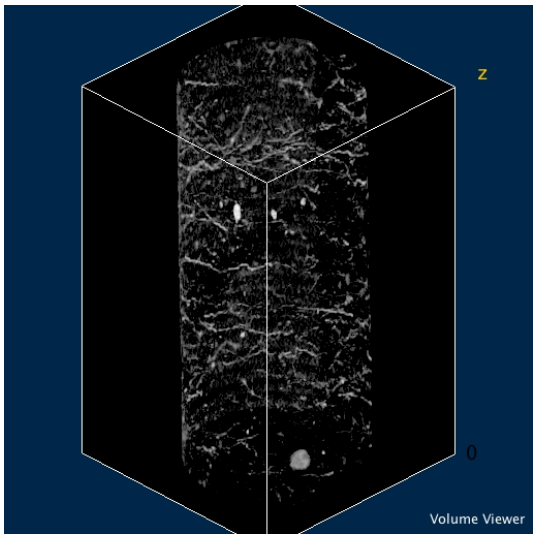

Figure 5-56. A 20 cm section of Core 11_12 with the one-dimensional high-density features highlighted.

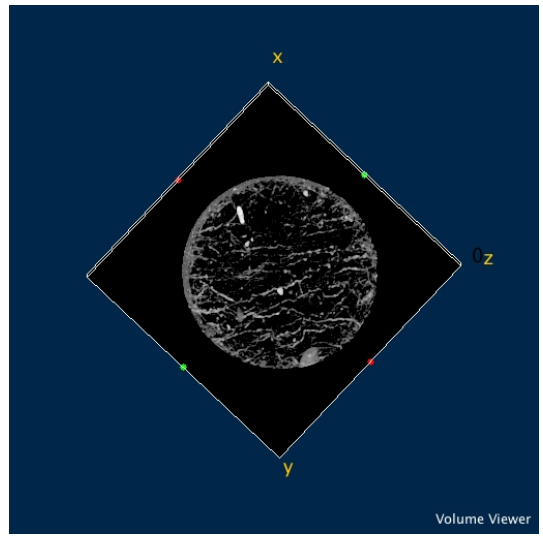

Figure 5-57. Same as Figure 5-56, but reoriented identifying the orientation of the high-density features.

5.4.2 Fabrication of miniature inert reaction vessels for clay heating tests

The experiment will heat bentonite and/or other rock samples of interest (Opalinus Clay) within sealed containers for varying durations (a few days to a month) and examine time-dependent changes in the mechanical and hydraulic properties. For this reason, multiple reactor vessels were fabricated to allow characterization of the samples for different heating durations (Figure 5-58). The vessels are rated for 7,000 psi at 204ºC (3,000 psi at 300ºC guaranteed by the manufacturer), fabricated by the High Pressure Equipment Co.

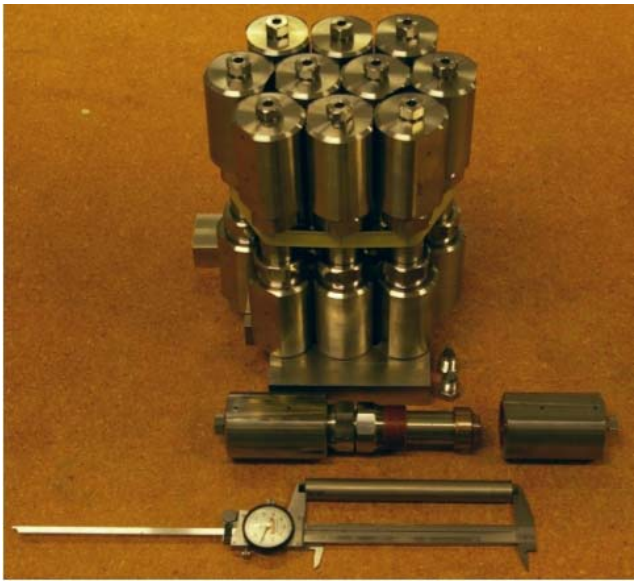

(a) Miniature reactor vessels

(b) Acid/heat treated vessel (left) and untreated vessel (right)

Figure 5-58. Miniature reactor vessels used for clay rock heat treatment

Because the metals in the experimental setup may react with the clay under elevated temperature and pressure, particularly in the presence of water, special care must be taken to avoid this unwanted effect. In our experiments, the miniature reactor vessels were fabricated from a corrosion-resisting material (commercially pure, grade-2 titanium). These vessels were first treated with acid (10% nitric acid at room temperature for 1 hour) to remove surface impurities. Subsequently, the vessels were heated up to 400ºC overnight (6-hour linear ramp up→12-hour hold at 400ºC →~12-hour natural cooling) to form a chemically inactive protective film of TiO_2.

To facilitate experiments conducted before and after the heat treatment of sample, an internal sample holder (tube insert) was also fabricated. The holder contains a mechanism for applying a small compression load to a small core sample (Figure 5-59), consisting of plugs, loading platen and springs, all made of chemically passivated titanium-2 alloy.

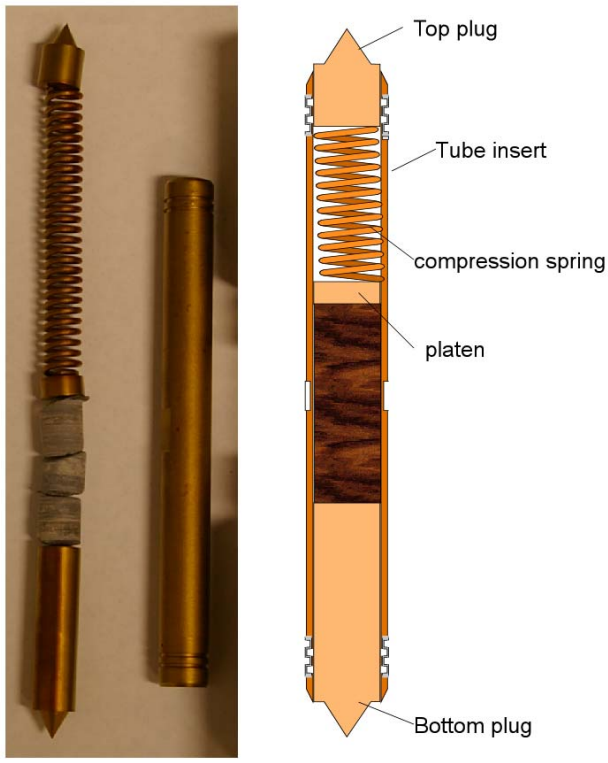

Figure 5-59. Sample holder with internal loading system which is inserted in the miniature reactor (sample diameter =1.40 cm)

The inner tube and the plugs were machined precisely to prevent extrusion of the samples during the experiment. Also, the support provided by the tube wall ensures the integrity of the clay sample during planned acoustic measurements and permeability tests. For further mechanical testing including the strength test (e.g., uniaxial compression test), the sample will be removed from this tube.

5.4.3 Summary and future work

The experimental work is still ongoing. Accomplishments so far are as follows:

- Clay samples (bentonite and Opalinus Clay from Mont Terri) for the laboratory geomechanical experiments were acquired. Initial sample characterization was conducted
- Special miniature pressure (reactor) vessels for high-temperature of heat treatment of clays were fabricated
- Internal mechanism of the pressure vessel was designed and built for facilitating sample preparation and planned material property characterization

Future work for the remaining months of FY13 and FY14 includes:

- Initial heating test of Opalinus Clay samples (Mont Terri) using the fabricated reactor vessels. Mechanical (strength, seismic velocity) and hydrological (flow permeability) property measurements will be conducted before and after the heating.
- Fabrication of more experimental parts required for the experiment. The design of the internal core holder may be slightly modified based upon the outcome of the initial test.
- Heating tests of bentonite/and or Opalinus Clay samples at various temperatures and the sample characterization before and after the heating.
- Development of miniature indentation experiment setup for elastic moduli and yield strength measurements of clay samples. Because of the limited size and quantity of the samples used in our experiment, the indentation test may provide more robust and useful data for characterizing the heat-induced changes in the mechanical properties of clay in both engineered and natural barriers.

5.5 Conclusions

Maximum allowable temperature is one of the most important design variables for a geological repository, because it determines waste package spacing, distance between disposal galleries, and therefore the overall size (and cost) of a repository for a given amount of waste. Up to now, almost all design concepts have chosen a maximum allowable temperature of 100 ^{o}C. However, such a choice is based on concerns that have not been addressed with rigorous scientific studies. Maximum allowable temperature and the detailed impacts of high temperature on repository performance are therefore still open questions for a clay repository. This chapter documents our attempt to systematically study the impact of higher temperature on a clay repository with a bentonite EBS using detailed mechanistic THMC modeling, uncertainty quantification based on the performance assessment level models, and a laboratory experiment.

The detailed mechanistic THMC simulations reveal that the major chemical alteration to EBS bentonite and clay formation is illitization (dissolution of smectite and precipitation of illite), accompanied by the dissolution of K-feldspar and calcite, and precipitation of quartz, chlorite and kaolinite. Higher temperature (about 200 ^{o}C) leads to more illitization in comparison with lower temperature (about 100 ^{o}C). However, the smectite volume fraction change is affected by many chemical factors and has to be evaluated with site-specific data. The most important chemical factors are the concentration of K and dissolution rate of K-feldspar; less important are the concentration of Na and quartz precipitation rate. A decrease in the smectite volume fraction in the bentonite ranges from 0.004 to a maximum of about 27% of the initial volume fraction of smectite. Higher temperature leads to much higher stress due to thermal pressurization. However, smectite dissolution causes only minimal changes in the stress. Even for the case with the maximum dissolution of smectite, smectite dissolution results in only about a 3% drop in stress, and therefore contributes very little to stress-induced porosity changes.

The coupled THMC processes examined by detailed mechanistic modeling were incorporated into a simpler model suitable for performance assessment calculations. Influential parameters have been identified using global sensitivity analysis methods, and their uncertainties have been propagated through the model to evaluate the uncertainty ranges of the predicted repository performance. These preliminary results should not be taken as guidelines for performance assessment or mitigation measures to reduce the impact of high-temperature scenarios on repository performance. Instead, they intend to highlight the importance of model conceptualization and the choice of performance metrics used in an abstracted performance assessment model.

Motivated by the fact that most laboratory studies have up to now been conducted at temperature < 100 ^{o}C, we are also working on a high temperature laboratory experiment for bentonite and Opalinus Clay from Mont Terri). Currently, we have finished the initial sample characterization and fabrication of special miniature pressure (reactor) vessels.

6. Overall Summary

This report has addressed the following items: (1) development and validation of constitutive relationships (Chapter 2); (2) development of a DFN model for investigating coupled processes in EDZ (Chapter 3); (3) development and validation of a THM model for FE tests at Mont Terri, Switzerland (Chapter 4); and (4) investigation of high-temperature impacts, including both laboratory and modeling studies (Chapter 5). The results of these efforts are summarized here:

(1) Development and validation of constitutive relationships(Chapter 2)

Coupled THM processes are critical for EDZ formation and evolution in a clay repository. The constitutive relationships are the key elements for modeling these coupled processes. Considerable progress has been made during FY13 in validating the new constitutive relationships (TPHM). Specific accomplishments are as follows:

- A three-dimensional model was developed for the mine-by (MB) test at the Mont Terri site.
- The usefulness and validity of the TPHM are demonstrated by the consistency between predicted results and field observations from the MB test. Note that use of model prediction in this study, rather than calibration, allows for a more convincing and transparent model evaluation.
- We found that the predicted results based on the traditional constitutive model (SPHM) considerably underestimate observed hydro-mechanical responses to the tunnel excavation for the MB test (including the EDZ size).

Future work for the remaining months of FY13 and FY14 includes:

- Development of the TPHM to include the bedding effects. The current version of the TPHM has been developed for an isotropic rock mass.
- Development of a TPHM-based dual-continuum approach to capture fracture effects with the EDZ.

(2) Discrete fracture network (DFN) approach for fractures in argillaceous rock (Chapter 3)

A three-dimensional computational method capable of addressing fracture initiation and propagation as a THM coupled process has been further developed and tested. The hydrogeologic model implemented using TOUGH2 considers a discrete fracture approach. Geomechanics and fracture damage are computed using the RBSN modeling method. Specific accomplishments include:

- A new approach for the RBSN method documented here addresses the problem of computing elastic geomechanical problems involving the Poisson effect. A demonstration of this new RBSN method is provided in which both global and local representations of the Poisson affect are captured.
- Two numerical methods, TOUGH2 for thermal hydrology and RBSN for geomechanics and fracture damage, have been effectively linked. A significant advantage for coupling TOUGH2 and RBSN to model THM and fracture-damage processes is that both codes utilize the same set of nodal points based on a Voronoi tessellation of the spatial domain.

- The capabilities of the linked TOUGH-RBSN simulator have been validated for a desiccation cracking processes through comparison with experimental results. The simulations provide excellent qualitative and reasonable quantitative agreement with experimental results.

- Initial scoping analyses for the HG-A test being conducted at the Mont Terri URL have shown that fracture damage in the EDZ is likely to be a result of both shear and tensile failure and that these failures are linked to anisotropic strength in the Opalinus Clay.

- An analytical model for transport in a single fracture through a porous and permeable rock matrix reported in Liu et al. (2012) has been extended to include additional process capability for longitudinal diffusion/dispersion. The model can simultaneously treat several processes not included previously in analytical treatments, in particular: (1) flow fields with general matrix advection in which the pressure gradient is not necessarily aligned with the fracture axis resulting in matrix flow across the fracture; (2) solute release points in the fracture and matrix; and (3) independent levels of longitudinal matrix diffusion and dispersion in the fracture. Transport processes in discrete fracture models, particularly those including solute exchange with the rock matrix, pose difficult computational challenges that require benchmarking against independent solutions such as the analytical model developed here.

- Solute transport cases analyzed with the analytical model show that matrix cross-flow has an increasing effect on solute transport as the orientation of the fracture relative to the hydraulic gradient goes from parallel to orthogonal. This is a result of increasing cross-flow and decreasing flow along the fracture. The effects of cross-flow result in reduced solute interaction with the fracture, such that a greater degree of longitudinal advance of solute occurs in the matrix. As the effects of cross-flow become stronger, more of the solute transport occurs in the matrix, and transport times approach the time for advection through the matrix. Significant delays in transport can also occur for cases in which solute is released into the matrix, with the main impact found on the early breakthrough behavior and secondary impact on the trailing portion of the breakthrough.

Future work for the remaining months of FY13 and FY14 includes:

- The proposed approach for capturing the Poisson effect in the RBSN method needs to be tested over a large range of material behavior with more complicated factors, such as multi-axial loading conditions, nonlinear behavior including fracturing, and 3-D unstructured grid.

- Future work will demonstrate capabilities for two-way coupling of THM processes, including abilities to simulate crack-assisted mass transport.

- Discrepancies in calculated observed crack spacing for desiccation cracking suggest needs for further work, including a study of the effects of material toughness on desiccation cracking.

- The TOUGH-RBSN model needs further development for application to the HG-A test being conducted at the Mont Terri URL. These improvements concern the modeling of shear fracture and the representation of anisotropic elastic and strength parameters.

- Comparisons of analytical and numerical results in Liu et al. (2012) showed that very fine gridding, on the order of the fracture aperture, is needed in numerical solutions of solute transport in discrete fracture models that also have solute transport exchange with the rock matrix. A

potential approach using an analytical treatment of fracture-matrix exchange is outlined here but requires development and testing for general applications.

(3) Development of a THM model for FE tests at Mont Terri, Switzerland, for the purpose of model validation (Chapter 4)

Fully coupled 3D TH and THM model simulations of the FE test at Mont Terri have been performed. The parameters used in the model are the best estimates based on site specific data for the rock and literature data for the bentonite. Specific accomplishments include:

- Compared to our previous 2D model analysis, we show that our new 3D analysis provides a much more accurate estimate of the temperature evolution near the heater and thereby should provide a better prediction of the peak temperature.
- TH modeling shows that the canister surface reaches the maximum temperature of 130°C, which is right within the indented targeted maximum temperature of 125 to 135°C. After the installation of the bentonite buffer, water is pulled from the host rock, and the resaturation of the bentonite buffer is slow because of the low permeability of the host rock. The buffer is still unsaturated after 30 years.
- We conducted for the first time a THM analysis involving the BBM in a full 3D field setting for modeling of the geomechanical behavior of the buffer. The analysis highlights the complex coupled geomechanical behavior in the buffer and its interaction with the surrounding rock.
- The adopted modeling approach is adequate for modeling the coupled THM processes at the FE heater, including all components of bentonite, concrete lining, and Opalinus Clay. We managed to discretize the 3D model using the inclined mesh discretization in both TOUGH2 and FLAC3D and the modeling results are reasonable.

Future work for the remaining months of FY13 and FY14 includes:

- Modeling laboratory scale experiments on MX-80 pellets of bentonite.
- Modeling of a benchmark test for code-to-code verification with other FE modeling teams.
- Final prediction of FE heater experiment (should be completed and reported before start of heating).

(4) Investigation of the maximum allowable temperature and detailed impacts of a high temperature on repository performance (Chapter 5):

Maximum allowable temperature is one of the most important design variables for a geological repository. Maximum allowable temperature and detailed impacts of a high temperature on repository performance are largely open questions for a clay repository. The impact of high temperatures on a clay disposal with bentonite EBS was investigated in FY13 using the detailed mechanistic THMC modeling, uncertainty quantification based on a system-level model, and a laboratory experiment. Specific accomplishments include:

- A fully coupled THMC model for a clay repository with a bentonite EBS was conducted with TOUGHREACT-FLAC3D.

- Within the scenarios explored in this study, we found that the major chemical alteration to EBS bentonite and clay formation is illitization (dissolution of smectite and precipitation of illite), along with dissolution of K-feldspar and calcite and precipitation of quartz.

- We also found that a higher temperature (about 200 ^{o}C) in general leads to more illitization in comparison with a lower temperature (about 100 ^{o}C). However, the smectite volume fraction change is affected by many chemical factors and has to be evaluated with site specific data. Smectite dissolution causes only minimal changes in the stress and porosity, even for the case with the maximum dissolution of smectite.

- The coupled THMC processes examined by detailed mechanistic modeling were incorporated into a simpler model suitable for performance assessment calculations. Influential parameters have been identified using global sensitivity analysis methods, and their uncertainties have been propagated through the model to evaluate the uncertainty ranges of the predicted repository performance.

- A high temperature laboratory experiment for bentonite and Opalinus Clay from Mont Terri is ongoing. Currently we have finished the initial sample characterization, and fabrication of special miniature pressure (reactor) vessels.

Future work for the remaining months of FY13 and FY14 includes:

- Further investigating of the chemical and mechanical alteration in bentonite and clay formation under different chemical and hydrological conditions at high temperatures.

- Refining current chemical model. In the current model, canisters serve only as a heat source and chemical changes in them are neglected for simplification. The model should consider the chemical changes in canisters, specifically the release of Fe^{+2} which might enhance the dissolution of smectite by forming chlorite.

- Incorporating more rigorous mechanical model for bentonite to more accurately calculate the stress and porosity change in bentonite, and more advanced mechanical-chemical coupling to perform more rigorous calculation of the impact of chemical changes on the mechanical behavior.

- Developing a constitutive relation that incorporates the chemical component in the mechanical model so that we can analyze the effect of chemical changes on the mechanical behavior in clay formations.

- Improving the system-level model by considering additional features such as a non-backfilled (ventilated) case, canister integrity, the impact of nonuniform or partial resaturation of the bentonite, the type of radionuclides considered, effects of the heterogeneity and far-field fate of the released radionuclides.

- Conducting heating tests of bentonite and/or Opalinus Clay samples at various temperatures and the sample characterization before and after the heating.

- Developing miniature indentation experiment setup for elastic moduli and yield strength measurements of clay samples. Because of the limited size and quantity of the samples used in our experiment, the indentation test may provide more robust and useful data for characterizing

the heat-induced changes in the mechanical properties of clay in both engineered and natural barrier systems.

Acknowledgment

Funding for this work was provided by the Used Fuel Disposition Campaign, Office of Nuclear Energy, of the U.S. Department of Energy under Contract Number DE-AC02-05CH11231 with Berkeley Lab.

References

Alonso, E.E., Gens A. and Josa A. (1990). A constitutive model for partially saturated soils. Géotechnique, 40(3), 405-430.

Aris, R. (1956). On the dispersion of a solute in a fluid flowing through a tube. Proc. R. Soc. London Ser. A, 235, 67-77.

Asahina, D., Landis, E.N. and Bolander, J.E. (2011). Modeling of phase interfaces during pre-critical crack growth in concrete. Cement & Concrete Composites, 33, 966-977.

Barnichon, J.D. and Volckaert, G. (2003). Observations and Predictions of Hydromechanical Coupling Effects in the Boom Clay, Mol Underground Research Laboratory, Belgium. Hydrogeology Journal, 11(1), 193-202.

Bear, J. (1972). "Dynamics of Fluids in Porous Media," Elsevier, New York, New York.

Berkowitz, B. (2002). Characterizing flow and transport in fractured geological media: A review. Advances in Water Resources, 25, 861-884.

Bianchi, M., Liu, H.-H. and Birkholzer, J.T. (2013). Diffusion Modeling in a Clay Repository: FY13 Report, Lawrence Berkeley National Laboratory, DOE Used Fuel Disposition Campaign, FCRD-UFD-2013-000228.

Biot, M.A. (1941). General theory of three dimensional consolidation. Journal of Applied Physics, 12, 155-164.

Biot, M.A. (1956). General Solutions of the equations of Elasticity and Consolidation for a Porous Material. J. Appl. Mech., Trans. ASME, 78, 91-96.

Biot, M.A. and Willis, D.G. (1957). The elastic coefficients of the theory of consolidation. Journal of Applied Mechanics, 24, 594-601.

Birkhö1zer, J., Rubin, H., Daniels, H. and Rouvé, G. (1993a). Contaminant advection and spreading in a fractured permeable formation: Part 1. Parametric evaluation and analytical solution. Journal of Hydrology, 144, 1-33.

Birkhö1zer, J., Rubin, H., Daniels, H. and Rouvé, G. (1993b). Contaminant advection and spreading in a fractured permeable formation: Part 2. Numerical simulation. Journal of Hydrology, 144, 35-58.

Birkhölzer, J. and Rouve, G. (1994). Dual-continuum modeling of contaminant transport in fractured formations. In X International Conference on Computational Methods in Water Resources, Heidelberg, Germany.

Bisschop, J. (2008). Size and boundary effects on desiccation cracking in hardened cement paste. International Journal of Fracture, 154, 211-224.

Blümling, P., Bernier, F., Lebon, P. and Martin, C.D. (2007). The excavation damaged zone in clay formations time-dependent behaviour and influence on performance assessment. Physics and Chemistry of the Earth, 32, 588-599.

Bock, H. (2001). RA Experiment Rock Mechanics Analyses and Synthesis: Data Report on Rock Mechanics, Mont Terri Project, Technical Report 2000-02.

Bock, H. (2009). RA Experiment: Updated Review of the Rock Mechanics Properties of the Opalinus Clay of the Mont Terri URL based on Laboratory and Field Testing. Technical Report 2008-04, Q+S Consult, Germany.

Bock, H., Dehandschutter, B. and Martin, CD. (2010). Self-sealing of fractures in argillaceous formations in the context of geological disposal of radioactive waste, Review and Synthesis. Nuclear Energy Agency, ISBN 978-92-64-99095-1.

Bodin, J., Delay, F. and de Marsily, G. (2003a). Solute transport in a single fracture with negligible matrix permeability: 1. fundamental mechanisms. Hydrogeology Journal, 11, 418-433, DOI 10.1007/s10040-003-0268-2.

Bodin, J., Delay, F. and de Marsily, G. (2003b). Solute transport in a single fracture with negligible matrix permeability: 2. mathematical formalism. Hydrogeology Journal, 11, 434-454, DOI 10.1007/s10040-003-0269-1

Bolander, J.E. and Saito, S. (1998). Fracture analyses using spring networks with random geometry. Eng Fract Mech, 61, 569-91.

Bolander, J.E., Moriizumi, K., Kunieda, M. and Yip, M. (2001). Rigid-Body-Spring Network modeling of cement-based composites. Fracture Mechanics of Concrete Structures, de Borst, J. Mazars, G. Pijaudier-Cabot and J. G. M. van Mier, Eds., Ia-FraMCos, pp. 773-780.

Bossart, P. (2011). Characteristics of the Opalinus Clay at Mont Terri, http://www.mont-terri.ch/internet/mont-terri/en/home/geology/key_characteristics.parsys.49924.DownloadFile.tmp/characteristicsofopa.pdf

Bossart, P. and Thury, M. (2008). Mont Terri Rock Laboratory. Project, Programme 1996 to 2007 and Results. Report No. 3 - Swiss Geological Survey, Wabern.

Bossart, P., Meier, P.M., Moeri, A., Trick, T. and Mayor, J.-C. (2002). Geological and hydraulic characterization of the excavation disturbed zone in the Opalinus Clay of the Mont Terri Rock Laboratory. Eng Geol, 66, 19-38.

Bossart, P., Meier, P.M., Moeri, A., Trick, T. and Mayor, J.-C. (2004). Structural and hydrogeological characterisation of the excavation-disturbed zone in the Opalinus Clay (Mont Terri Project, Switzerland). Applied Clay Science, 26, 429- 448.

Brady, B.T. (1969). The nonlinear mechanical behavior of brittle rock Part I-Stress-strain behavior during regions I and II. Int J Rock Mech Min Sci, 6, 211-225

Brown, E.T., Bray, J.W. and Santarelli, F.J. (1989). Influence of stress-dependent elastic moduli on stresses and strains around axisymmetric boreholes. Rock Mechanics and Rock Engineering, 22, 189-203.

Brusewitz, A.M. (1986). Chemical and physical properties of Paleozoic bentonites from Kinnekulle, Sweden. Clays & Clay Miner, 34, 442-454.

Bucher, F. and Müller-Vonmoos, M. (1989). Bentonite as a containment barrier for the disposal of highly radioactive waste. Applied Clay Science, 4(2), 157-177.

Caporuscio F.A., Cheshire, M.C. and McCarney, M. (2012). Bentonite Clay Evolution at Elevated Pressures and Temperatures: An experimental study for generic nuclear repositories. 2012 AGU fall meeting.

Carslaw, H.S. and Jaeger, J.C. (1959). Conduction of Heat in Solids, 2nd Edition, Oxford University Press Inc., New York, New York.

Casciello, E., Cosgrove, J.W., Cesarano, M., Romero, E., Queralt, I. and Vergés, J. (2011). Illite-smectite patterns in sheared Pleistocene mudstones of the Southern Apennines and their implications regarding the process of illitization: A multiscale analysis. Journal of Structural Geology, 33(11), 1699-1711.

Cazacu, O. (1999). On the choice of stress-dependent elastic moduli for transversely isotropic solids. Mech Res Commun, 26, 45-54.

Cheshire, M.C., Caporuscio, F.A., Jové-Colon, C. and McCarney, M.K. (2013). Alteration of clinoptilolite into high-silica analcime within a bentonite barrier system under used nuclear fuel repository conditions. International High-Level Radioactive Waste Management (2013 IHLRWM). Albuquerque, NM.

Cihan, A. and Tyner, J.S. (2011). 2-D radial analytical solutions for solute transport in a dual-porosity medium. Water Resources Research, 47, DOI:10.1029/2009WR008969.

Colina, H. and Acker, P. (2000). Drying cracks: kinematics and scale laws. Materials and Structures, 33, 101-107.

Colina, H. and Roux, S. (2000). Experimental model of cracking induced by drying shrinkage. European Physical Journal, E 1, 189-194.

Corkum, A.G. and Martin, CD. (2007). The mechanical behaviour of weak mudstone (Opalinus Clay). at low stresses. International Journal of Rock Mechanics & Mining Sciences, 44, 196-209.

Cortis, A. and Birkholzer, J. (2008). Continuous time random walk analysis of solute transport in fractured porous media. Water Resources Research, 44, DOI:10.1029/2007WR006596

Cosgrove, J.W. (2001). Hydraulic Fracturing during the Formation and Deformation of a Basin: A Factor in the Dewatering of Low-Permeability Sediments. AAPG Bulletin, 85(4), 737-748.

Couture, R.A. (1985). Steam rapidly reduces the swelling capacity of bentonite. Nature, 318(6041), 50-52.

Cuadros, J. (2006). Modeling of smectite illitization in burial diagenesis environments. Geochimica et Cosmochimica Acta, 70(16), 4181-4195.

Cuadros, J. and Linares, J. (1996). Experimental kinetic study of the smectite-to-illite transformation. Geochimica et Cosmochimica Acta, 60(3), 439-453.

Davis J., Rutqvist, J., Steefel, C., Tinnacher, R., Vilarrasa, V., Zheng, L., Bourg, I., Liu, H.-H. and Birkholzer, J.T. (2013). Investigation of Reactive Transport and Coupled THMC Processes in the EBS: FY13 Report, FCRD-UFD-2013-000216.

De Canniere, P. (1997). Measurements of Eh on slurries of Opalinus Clay, Mont Terri. SCKoCEN. Mont Terri Project, Technical Note TN 96-32 (internal unpublished report).

Dentz, M. and Carrera, J. (2007). Mixing and spreading in stratified flow. Physics of Fluids, 19, http://dx.doi.org/10.1063/1.2427089.

ENRESA (2000). Full-scale engineered barriers experiment for a deep geological repository in crystalline host rock FEBEX Project, European Commission, 403.

Ewing, J. and Senger, R. (2011). Evolution of Temperature, Pressure and Saturation in the Bentonite Buffer: Scoping Calculations in Support of the Design of the Full-Scale Emplacement Experiment at the Mont Terri URL. NAGRA NAB 10-38, September 2011.

Fernández, A.M., Turrero, M.J., Sánchez, D.M., Yllera, A., Melón, A.M., Sánchez, M., Peña, J., Garralón, A., Rivas, P., Bossart, P. and Hernán, P. (2007). On site measurements of the redox and carbonate system parameters in the low-permeability Opalinus Clay formation at the Mont Terri Rock Laboratory. Physics and Chemistry of the Earth, Parts A/B/C 32(1-7), 181-195.

Finsterle, S. (2004). Multiphase inversion modeling: Review and iTOUGH2 applications. Vadose Zone Journal, 3, 747-762.

Fouche, O., Wright, H., Cleach, J.L. and Pellenard, P. (2004). Fabric Control on Strain and Rupture of Heterogeneous Shale Samples by Using a Non-Conventional Mechanical Test. Applied Clay Science, 26, 367-387.

Freivogel, M. and Huggenberger, P. (2003). Modellierung bilanzierter Profile im Gebiet Mont Terri - La Croix (Kanton Jura), in: Geology, Paleohydrology and Stress Field, Heitzmann & Tripet (eds.), Reports of the Federal Office for Water and Geology (FOWG), Geology Series 4, Switzerland.

Garitte, B. and Gens, A. (2012). TH and THM Scoping computations for the definition of an optimal instrumentation layout in the Full-scale Emplacement (FE). experiment NAGRA NIB 10-34, March 2012.

Garitte, B., Bond, A., Millard, A., Zhang, C., English, M., Nakama, A. and Gens, A. (2013). Analysis of hydro-mechanical processes in a ventilated tunnel in an argillaceous rock on the basis of different modelling approaches. Journal of Rock Mechanics and Geotechnical Engineering, 5, 1-17.

Geiger, S., Cortis, A. and Birkholzer, J.T. (2010). Upscaling solute transport in naturally fractured porous media with the continuous time random walk method. Water Resources Research, 46, DOI:10.1029/2010WR009133.

Gens, A., Sanchez, M., Guimaraes, L.D.N., Alonso, E.E., Lloret, A., Olivella, S., Villar, M.V. and Huertas, F. (2009). A full-scale in situ heating test for high-level nuclear waste disposal: observations, analysis and interpretation. Geotechnique, 59:377-399.

Ghezzehei, T.A., Trautz, R.C., Finsterle, S., Cook, P.J. and Ahlers, C.F. (2004). Modeling coupled evaporation and seepage in ventilated cavities. Vadose Zone Journal, 3, 806-818.

Gonzales, S. and Johnson, K.S. (1984). Shale and other argillaceous strata in the United States. Oak Ridge National Laboratory. ORNL/Sub/84-64794/1.

Gräsle, W. and Plischke, I. (2010). Laboratory Testing (LT). Experiment: Mechanical Behavior of Opalinus Clay, Final report from Phases 6 - 14. Technical Report 2009-07, BGR, Germany.

Griffiths, D.V. and Mustoe, G.G.W. (2001). Modelling of elastic continua using a grillage of structural elements based on discrete element concepts. International Journal for Numerical Methods in Engineering, 50(7), 1759-1775.

Grisak, G.E. and Pickens, J.F. (1980). Solute Transport Through Fractured Media 1. The Effect of Matrix Diffusion. Water Resources Research, 16(4), 719-730.

Hicks, T.W., White M.J. and Hooker, P.J. (2009). Role of Bentonite in Determination of Thermal Limits on Geological Disposal Facility Design, Report 0883-1, Version 2, Falson Sciences Ltd., Rutland, UK.

Hooker, J.N., Laubach, S.E. and Marrett R. (2013). Fracture-aperture size-frequency, spatial distribution and growth processes in strata-bounded and non-strata-bounded fractures, Cambrian Mesón Group, NW Argentina, Journal of Structural Geology, DOI:10.1016/j.jsg.2013.06.011.

Horseman, S.T. and McEwen, T.J. (1996). Thermal constrains on disposal of heat-emitting waste in argillaceous rocks. Engineering Geology, 41, 5-16.

Houseworth, J. (2012). Disposal System Material Properties, Lawrence Berkeley National Laboratory, DOE Used Fuel Disposition Campaign, FCRD-UFD-2012-000207.

Houseworth, J.E. (2006). An analytical model for solute transport in unsaturated flow through a single fracture and porous rock matrix. Water Resources Research, 42, DOI:10.1029/2004WR003770.

Hughes, T.J. (2000). The Finite Element Method - Linear Static and Dynamic Finite Element Analysis. Dover Publications, Inc.

Itasca Consulting Group (2005). FLAC3D: Fast Lagrangian Analysis of Continua in 3 Dimensions. Itasca Consulting Group, Minneapolis ‹http://www.itascacg.com/flac3d/index.php›.

Jaeger, J.C., Cook, N.G.W. and Zimmerman, R.W. (2007). Fundamentals of rock mechanics. 4th ed. Oxford: Blackwell.

Jaeggi, D., Nussbaum, C. and Vietor, T. (2012). MB Experiment: visualization of EDZ-fractures around the MB niche by using the in-situ resin impregnation technique. Mont Terri Project TN 2010-56.

Jagota, A. and Bennison, S.J. (1994). Spring-network and finite-element models for elasticity and fracture. Non-linearity and Breakdown in Soft Condensed Matter. Spring Lecture Notes in Physics, 437, 187-201.

JNC (Japan Nuclear Cycle Development Institute) (2000). H12: Project to Establish the Scientific and Technical Basis for HLW Disposal in Japan. Second Progress Report on Research and Development for the Geological Disposal of HLW in Japan. Supporting Report 2: Repository Design and Engineering Technology. JNC TN1410, 2000-003.

JNC, (Japan Nuclear Cycle Development Institute) (1999). H12: project to establish the scientific and technical basis for HLW disposal in Japan: supporting report 2 (respiratory design and engineering Technology). Japan Nuclear Cycle Development Institute, Tokyo.

Jobmann, M., Wilsnack, T.h. and Voigt, H.D. (2010). Investigation of damage-induced permeability of Opalinus clay. International Journal of Rock Mechanics & Mining Sciences, 47, 279-285.

Johnson, P.A. and Rasolofosaon P.N.J. (1996). Nonlinear elasticity and stress induced anisotropy in rock. J Geophys Res, 101, 3113-3124.

Kamei, G., Mitsui, M.S., Futakuchi, K., Hashimoto S. and Sakuramoto, Y. (2005). Kinetics of long-term illitization of montmorillonite-a natural analogue of thermal alteration of bentonite in the radioactive waste disposal system. Journal of Physics and Chemistry of Solids, 66(2-4), 612-614.

Karnland, O., Olsson, S. and Nilsson, U. (2006). Mineralogy and sealing properties of various bentonites and smectite-rich clay materials. SKB Technical Report TR-06-30.

Kawai, T. (1978). New Discrete Models and their Application to Seismic Response Analysis of Structures. Nuclear Engineering and Design, 48, 207-229.

Kirsch, G. (1898). Die Theorie der Elastizität und die Bedürfnisse der Festigkeitslehre. Zeitschrift des Vereines deutscher Ingenieure, 42, 797-807.

Kitsunezaki, S. (2011). Crack growth in drying paste. Advanced Powder Technology, 22, 311-318.

Komine, H. and Ogata, N. (1996). Prediction for swelling characteristics of compacted bentonite. Canadian Geotechnical Journal, 33, 11-22.

Konrad, J.-M. and Ayad, R. (1997). Desiccation of a sensitive clay: field experimental observations. Canadian Geotechnical Journal, 34, 929-942.

Lakshmikantha, M.R., Prat, P.C. and Ledesma, A. (2012). Experimental evidence of size effect in soil cracking. Canadian Geotechnical Journal, 49, 264-284.

Lanyon, G.W., Marschall, P., Trick,T., de La Vaissière, R., Shao, H. and Leung, H. (2009). Hydromechanical Evolution and Self-Sealing of Damage Zones around a Microtunnel in a Claystone Formation of the Swiss Jura Mountains. American Rock Mechanics Association, ARMA 09-333.

Laredj, N., Missoum, H. and Bendani, K. (2010). Modeling the effect of osmotic potential changes on deformation behavior of swelling clays. Journal of Porous Media, 13(8), 743-748.

Lauber, M., Baeyens, B. and Bradbury, M.H. (2000). Physico-Chemical Characterisation and Sorption Measurements of Cs, Sr, Ni, Eu, Th, Sn and Se on Opalinus Clay from Mont Terri. PSI Bericht Nr. 00-10 December 2000 ISSN 1019-0643.

Lionco, A. and Assis, A. (2000). Behaviour of Deep Shafts in Rock Considering Nonlinear Elastic Models. Tunneling and Underground Space Technology, 15(4), 445-451.

Liu H.-H., Houseworth, J., Rutqvist, J., Li, L., Asahina, D., Chen, F. and Birkholzer, J. (2012). Report on Modeling Coupled Processes in the Near Field of a Clay Repository, Lawrence Berkeley National Laboratory, DOE Used Fuel Disposition Campaign, FCRD-UFD-2012-000223.

Liu, H.-H., Bodvarsson, G.S. and Finsterle, S. (2002). A note on unsaturated flow in two-dimensional fracture networks. Water Resources Research, 38(9), 1176, DOI:10.1029/2001WR000977.

Liu, H.-H., Bodvarsson, G.S. and Zhang, G. (2004). Scale Dependency of the Effective Matrix Diffusion Coefficient. Vadose Zone Journal, 3, 312-315.

Liu, H.-H., Houseworth, J., Rutqvist, J., Li, L., Asahina, D., Chen, F. and Birkholzer, J. (2012). Report on Modeling Coupled Processes in the Near Field of a Clay Repository. Report in Lawrence Berkeley National Laboratory, Berkeley, US.

Liu, H.-H., Rutqvist, J. and Berryman, J.C. (2009). On the relationship between stress and elastic strain for porous and fractured rock. International Journal of Rock Mechanics & Mining Sciences, 46, 289-296.

Lloret, A. and Villar, M.V. (2007). Advances on the knowledge of the thermo-hydro-mechanical behaviour of heavily compacted "FEBEX" bentonite. Physics and Chemistry of the Earth, 32, 701-715.

Maloszewski, P. and Zuber, A. (1990), Mathematical modeling of tracer behavior in short-term experiments in fissured rocks. Water Resour. Res., 26(7), 1517-1528.

Maloszewski, P. and Zuber, A. (1985). On the theory of tracer experiments in fissured rocks with a porous matrix. J. Hydrol., 79, 333-358.

Marschall, P., Distinguin, M., Shao, H., Bossart, P., Enachescu, C. and Trick, T. (2006). Creation and Evolution of Damage Zones Around a Microtunnel in a Claystone Formation of the Swiss Jura Mountains. Society of Petroleum Engineers, SPE-98537-PP.

Marschall, P., Trick, T., Lanyon, G.W., Delay, J. and Shao, H. (2008). Hydro-Mechanical Evolution of Damaged Zones around a Microtunnel in a Claystone Formation of the Swiss Jura Mountains. American Rock Mechanics Association, ARMA 08-193.

Martin, C.D. and Lanyon, G.W. (2003). Measurement of In-Situ Stress in Weak Rocks at Mont Terri Rock Laboratory, Switzerland. International Journal of Rock Mechanics & Mining Sciences, 40, 1077-1088.

Martin, P.L. and Barcala, J.M. (2005). Effects of over-heating on the performance of the engineering clayed barriers of the mock-up test. In: Advances in Understanding Bentonite Thermal Limits Engineered Clay Barriers (E.E. Alonso and A. Ledesma, eds), pp. 391-412. Taylor & Francis Group, London, ISBN 04 1536 544 9.

Marty, N.C.M., Fritz, B., Clément, A. and Michau, N. (2010). Modelling the long term alteration of the engineered bentonite barrier in an underground radioactive waste repository. Applied Clay Science, 47(1-2), 82-90.

Matthäi, S.K., Nick, H.M., Pain, C. and Neuweiler, I. (2009). Simulation of Solute Transport Through Fractured Rock: A Higher-Order Accurate Finite-Element Finite-Volume Method Permitting Large Time Steps. Transport in Porous Media, DOI:10.1007/s11242-009-9440-z, on line access 08/12/2013.

Mavko, G.M. and Nur, A. (1978). The effect of nonelliptical cracks on the compressibility of rocks. J Geophys Res, 83, 4459-4468.

Mazurek, M., Pearson, F.J., Volckaert, G. and Bock, H. (2003). Features, Events and Processes Evaluation Catalogue for Argillaceous Media, OECD, Nuclear Energy Agency Organisation for Economic Co-Operation and Development. http://www.oecd-nea.org/rwm/reports/2003/nea4437-FEP.pdf.

Meier, O., Nussbaum, C. and Bossart, P. (2005). HG-A experiment: Drilling of the microtunnel (BHG-A0 and BHG-A1), Mont Terri Project, TN 2005-55.

Meier, P., Trick, T., Blumling, P. and Volckaert, G. (2000). Self-Healing of Fractures within the EDZ at the Mont Terri Rock Laboratory: Results after One Year of Experimental Work. In: Proceedings of the International Workshop on Geomechanics, hydromechanical and Thermomechanical Behavior of deep argillaceous Rocks: Theory and Experiments, Paris, October11-12, 2000.

Mont Terri Consortium (2009). Geotechnisches Institut AG. Characterisation of the dry shotcrete sprayed in MB niche for modelling works-Final Report, Bern.

Montes-H., G., Fritz, B., Clement, A. and Michau, N. (2005a). Modelling of geochemical reactions and experimental cation exchange in MX80 bentonite. Journal of Environmental Management, 77(1), 35-46.

Montes-H., G., Fritz, B., Clement, A. and Michau, N. (2005b). A simplified method to evaluate the swelling capacity evolution of a bentonite barrier related to geochemical transformations. Applied Geochemistry, 20(2), 409-422.

Montes-H., G., Marty, N.C.M., Fritz, B., Clement, A. and Michau, N. (2005c). Modelling of long-term diffusion-reaction in a bentonite barrier for radioactive waste confinement. Applied Clay Science, 30, 181-198.

Morris, M.D. (1991). Factorial sampling plans for preliminary computational experiments. Technometrics, 33(2), 161-174.

Mosser-Ruck, R., Cathelineau, M., Baronnet, A. and Trouiller, A. (1999). Hydrothermal reactivity of K-smectite at 300C and 100 bar: dissolution-crystallization process and non-expandable dehydrated smectite formation. Clay Minerals, 34(2), 275-290.

Nagra (2002). Projekt Opalinuston - Synthese der geowissenschaftlichen Untersuchungsergebnisse. Entsorgungsnachweis für abgebrannte Brennelemente, verglaste hochaktive sowie langlebige mittelaktive Abfälle. Nagra Technical Report NTB 02-03, Nagra, Wettingen, Switzerland.

NAGRA (2003). Geosynthese. Nagra Technical Report NTB 02-03. Nagra, Wettingen, Switzerland.

Nater, P. (2012). Mont Terri / FE-Experiment Geomechanische Modellierung des Vortriebs. NAGRA AN 12-184.

Nelson, R.A. (1985). Geologic Analysis of Naturally Fractured Reservoirs, 2nd ed., Gulf Professional Publishing, Boston, Massachusetts.

Neretnieks, I. (1980). Diffusion in the rock matrix: An important factor in radionuclide retardation. J. Geophys. Res., 85, 4379- 4397.

NRC (National Research Council) (1996). Rock Fractures and Fluid Flow: Contemporary Understanding and Applications, National Academy of Sciences.

Nur, A. (1971). Effects of stress on velocity anisotropy in rocks with cracks. Journal of Geophysical Research, 76, 2022-2034.

Nussbaum, C. and Bossart P. (2006). HG-A experiment: Mapping of new breakouts developed in the HG-A microtunnel about 11 months after the excavation, Mont Terri Project, TN 2006-31.

Nutt, M. (2011). Used Fuel Disposition Campaign Disposal Research and Development Roadmap (FCR&D-USED-2011-000065 REV0), U.S. DOE Used Fuel Disposition Campaign.

Ochs, M., Lothenbach, B., Shibata, M. and Yui, M. (2004). Thermodynamic modeling and sensitivity analysis of porewater chemistry in compacted bentonite. Physics and Chemistry of the Earth, Parts A/B/C 29(1), 129-136.

Odling, N.E. and Roden, J.E. (1997). Contaminant transport in fractured rocks with significant matrix permeability, using natural fracture geometries. Journal of Contaminant Hydrology, 27, 263-283.

Okabe, A., Boots, B., Sugihara, K. and Chiu, S.N. (2000). Spatial tessellations: Concepts and applications of Voronoi diagrams, 2nd ed. Probability and Statistics. Wiley, NYC. 671 pages.

Oldenburg, C.M. and Pruess, K. (1995). EOS7R: Radionuclide Transport for TOUGH2, Lawrence Berkeley National Laboratory, LBL-34868.

Pacovsky, J., Svoboda, J., Zapletal, L. (2005). Saturation development in the bentonite barrier of the mock-up CZ geotechnical experiment. Clay in Natural and Engineered Barriers for Radioactive Waste Confinement-Part 2. Physics and Chemistry of the Earth, vol. 32/8-14. Elsevier, Amsterdam, pp. 767-779.

Painter, S., Cvetkovic, V., Mancillas, J. and Pensado, O. (2008). Time domain particle tracking methods for simulating transport with retention and first-order transformation. Water Resources Research, 44, W01406, DOI:10.1029/2007WR005944.

Patriarche, D., Ledoux, E., Simon-Coincon, R., Michelot, J. and Cabrera, J. (2004). Characterization and Modeling of Diffusive Process for Mass Transport through the Tournemire Argillites Aveyron, France. Applied Clay Science, 26, 109-122.

Pollard, D.D. and Fletcher, R.C. (2005). Fundamentals of Structural Geology, Cambridge University Press, Cambridge, U.K.

Pruess, K., Oldenburg, C.M. and Moridis, G. (1999). TOUGH2 User's Guide, Version 2.0, Lawrence Berkeley National Laboratory, Berkeley, CA.

Pruess, K., Oldenburg, C.M. and Moridis, G. (2011). TOUGH2 User's Guide, Version 2.1, LBNL-43134 (revised), Lawrence Berkeley National Laboratory, Berkeley, California.

Pusch, R. (2000). On the effect of hot water vapor on MX-80 clay, Technical Report TR-00-16, SKB, Swedish Nuclear Fuel and Waste Management Co, October 2000, 36 pp.

Pusch, R. and Karnland, O. (1988). Geological evidence of smectite longevity. The Sardinian and Gotland cases. SKB Technical Report 88-26, Stockholm, Sweden, 60 pp.

Pusch, R. and Karnland, O. (1996). Physico/chemical stability of smectite clays. Engineering Geology, 41, 73-85.

Pusch, R. and Madsen, F.T. (1995). Aspects on the illitization of the kinnekulle bentonites. Clays and Clay Minerals, 43(3), 261-270.

Pusch, R., Bluemling, P. and Johnson, L. (2003). Performance of strongly compressed MX-80 pellets under repository-like conditions. Applied Clay Science, 23, 239- 244.

Pusch, R., Karnland, O., Hökmark, H., Sandén, T. and Börgesson, L. (1991). Final report of the Rock Sealing Project-sealing properties and longevity of smectitic clay grouts. Stripa Project Technical Report 91-30. SKB, Stockholm.

Pusch, R., Kasbohm, J. and Thao, H.T.M. (2010). Chemical stability of montmorillonite buffer clay under repository-like conditions-A synthesis of relevant experimental data. Applied Clay Science, 47(1-2), 113-119.

Pyrak-Nolte, L.J. and Morris, J.P. (2000). Single fractures under normal stress: The relation between fracture specific stiffness and fluid flow. International Journal of Rock Mechanics and Mining Sciences, 37, 245-262.

Robinson, N.I., Sharp Jr., J.M. and Kreisel, I. (1998). Contaminant transport in sets of parallel finite fractures with fracture skins. Journal of Contaminant Hydrology, 31, 83-109.

Rodríguez, R., Sánchez, M., Ledesma, A. and Lloret, A. (2007). Experimental and numerical analysis of desiccation of a mining waste. Canadian Geotechnical Journal, 44, 644-658.

Roubinet, D., de Dreuzy, J.-R. and Tartakovsky, D.M. (2012). Semi-analytical solutions for solute transport and exchange in fractured porous media. Water Resources Research, 48, DOI:10.1029/2011WR011168.

Rubin, H., Dveyrin, D., Birkhö1zer, J. and Rouvé G. (1997). Advection and dispersion of contaminant in a permeable medium embedding fractures in which advection velocity is comparatively slow. Journal of Hydrology, 199, 135-162.

Rubin, H., Soliman, A.M., Birkhölzer, J. and Rouvé G. (1996). Transport of a tracer slug in a fractured permeable formation. Journal of Hydrology, 176, 153-180.

Rutqvist J. and Tsang C.-F. (2002). A study of caprock hydromechanical changes associated with CO2-injection into a brine formation. Environmental Geology, 42, 296-305.

Rutqvist, J. (2011). Status of the TOUGH-FLAC simulator and recent applications related to coupled fluid flow and crustal deformations. Computers & Geosciences, 37(6), 739-750.

Rutqvist, J., Ijiri, Y. and Yamamoto, H. (2011). Implementation of the Barcelona Basic Model into TOUGH-FLAC for simulations of the geomechanical behavior of unsaturated soils. Computers &Geosciences, 37, 751-762.

Rutqvist, J., Wu, Y.-S., Tsang, C.-F. and Bodvarsson, G. (2002). A modeling approach for analysis of coupled multiphase fluid flow, heat transfer and deformation in fractured porous rock. International Journal of Rock Mechanics & Mining Sciences, 39, 429-442.

Rutqvist, J., Zheng, L., Chen, F., Liu, H.-H. and Birkholzer, J.T. (2013). Modeling of Coupled Thermo-Hydro-Mechanical Processes with Links to Geochemistry Associated with Bentonite-Backfilled Repository Tunnels in Clay Formations. Rock Mechanics and Rock Engineering, (In Press).

Saltelli, A., Ratto, M., Andres, T., Campolongo, F., Cariboni, J., Gatelli, D., Saisana, M. and Tarantola, S. (2008). Global Sensitivity Analysis, the Primer. John Wiley & Sons Ltd., West Sussex, England, 292 pp.

Sánchez, M., Gens, A., Guimarães, L.J.D.N. and Olivella, S. (2005). A double structure generalized plasticity model for expansive materials. International Journal for numerical and analytical methods in geomechanics, 29, 751-787.

Sharifi Haddad, A., Hassanzadeh, H. and Abedi, J. (2012). Advective-diffusive mass transfer in fractured porous media with variable rock matrix block size, Journal of Contaminant Hydrology, 133, 94-107, doi:10.1016/j.jconhyd.2012.02.008.

Soler, J.M. (2001). The effect of coupled transport phenomena in the Opalinus Clay and implications for radionuclide transport. Journal of Contaminant Hydrology, 53(1-2), 63-84.

Sonnenthal, E. Chapter 5 in: Birkholzer, J., Rutqvist, J., Sonnenthal, E. and Barr, D. (2008). Long-Term Permeability/Porosity Changes in the EDZ and Near Field due to THM and THC Processes in Volcanic and Crystalline-Bentonite Systems, DECOVALEX-THMC Project Task D Final Report.

Sonnenthal, E., Ito, A., Spycher, N., Yui, M., Apps, J., Sugita, Y., Conrad M. and Kawakami, S. (2005). Approaches to modeling coupled thermal, hydrological and chemical processes in the Drift Scale Heater Test at Yucca Mountain. Int. J. Rock Mech. Min. Sci., 42, 6987-6719.

Stríček, I., Šucha, V., Uhlík, P., Madejová J. and Galko, I. (2009). Mineral stability of Fe-rich bentonite in the Mock-Up-CZ experiment, Geologica Carpathica, 60(5), 431-436.

Sudicky, E.A. and Frind, E.O. (1982). Contaminant transport in fractured porous media: Analytical solutions for a system of parallel fractures. Water Resour. Res., 18(6), 1634-1642.

Tang, D.H., Frind, E.O. and Sudicky, E.A. (1981), Contaminant transport in fractured porous media: Analytical solution for a single fracture. Water Resour. Res., 17(3), 555- 564.

Taylor, G.I. (1953). Dispersion of soluble matter in solvent flowing slowly through a tube. Proc. R. Soc. London Ser A, 219, 186-203.

Taylor, G.I. (1954). The dispersion of matter in turbulent flow through a pipe. Proc. R. Soc. London Ser A, 223, 446-468.

Thacker, W.C. (1976). A Solvable Model of "Shear Dispersion." Journal of Physical Oceanography, 6, 66-75.

Thury, M. (2002). The characteristics of the Opalinus Clay investigated in the Mont Terri underground rock laboratory in Switzerland. Comptes Rendus Physique, 3(7-8), 923-933.

Thury, M. and Bossart, P. (1999). Results of the hydrogeological, geochemical and geotechnical experiments performed in the Opalinus Clay (1996-1997). Chapter 6.4 Organic Matter Characterisation of Rocks and Pore Waters. Geological report No. 23. Swiss Geological Survey.

Tonon, F. and Amadei, B. (2003). Stresses in anisotropic rock masses: an engineering perspective building on geological knowledge. International Journal of Rock Mechanics & Mining Sciences, 40, 1099-1120.

Towhata, I., Kuntiwattanakul, P., Ohishi, K. and Takeuchi, N. (1998). Effect of Elevated Temperature on Mechanical Behaviour of Clays. Journal of the Japanese Geotechnical Society, 46(10) 27-30 (in Japanese).

Tsang, C.-F., Bernier, F. and Davies C. (2005). Geohydromechanical processes in the Excavation Damaged Zone in crystalline rock, rock salt and indurated and plastic clays-in the context of radioactive waste disposal. International Journal of Rock Mechanics & Mining Sciences, 42, 109-125.

van Genuchten, M.T. (1980). A closed-form equation for predicting the hydraulic conductivity of unsaturated soils. Soil Science Society of America Journal, 44, 892-898.

Vietor, T. (2011). Mine-by test in Mont Terri rock laboratory-MB Experiment. Report- MB Experiment: Data base for the predictive model. Nagra, Switzerland.

Vietor, T. (2012). Mont Terri Project - FE Experiment Modelling Kick-off Meeting. February 9, 2012, Mont Terri, Switzerland. NAGRA Technical Discussion TD-217,

Villar, M.V. and Lloret, A. (2004). Influence of temperature on the hydro-mechanical behaviour of a compacted bentonite. Applied Clay Science, 26(1-4), 337-350.

Volckaert, G., Bernier, F., Sillen, X., Van Geet, M., Mayor, J.-C., Göbel, I., Blümling, P., Frieg, B. and Su, K. (2004). Similarities and Differences in the Behaviour of Plastic and Indurated Clays, The Sixth European Commission Conference on 'The Management and Disposal of Radioactive Waste: Euradwaste '04', held on 29-31 March 2004 in Luxembourg.

Waber, H.N., Mazurek, M. and Pearson, F.J. (1998). Opalinus Clay: reference porewater, mineralogy and porosity. Nagra Internal Report.

Wainwright, H., Finsterle, S., Jung, Y., Zhou, Q. and Birkholzer, J.T. (2013). Making sense of global sensitivity analyses, Computers & Geosciences, DOI:10.1016/j.cageo.2013.06.006.

Walsh, J.B. (1965). The effect of cracks on the compressibility of rock. Journal of Geophysical Research, 70, 381-389.

Wang, Y. (2011). Research & Development (R&D). Plan for Used Fuel Disposition Campaign (UFDC). Natural System Evaluation and Tool Development, U.S. DOE Used Fuel Disposition Campaign.

Weatherhill, D., Graf, T., Simmons, C.T., Cook, P.G., Therrien, R., Reynolds, D.A. (2008). Discretizing the Fracture-Matrix Interface to Simulate Solute Transport. Ground Water, 46(4), 606-615.

Wersin P., Johnson, L.H. and McKinley, I.G. (2007). Performance of the bentonite barrier at temperature beyond 100°C: A critical review. Physics and Chemistry of the Earth, 32, 780-788.

Wooding, R.A. (1960). Instability of a viscous liquid of variable density in a vertical Hele Shaw cell. Journal of Fluid Mechanics, 7, 501-515, DOI:10.1017/S0022112060000256.

Wu, Y.-S. and Pruess, K. (2000). Numerical simulation of non-isothermal multiphase tracer transport in heterogeneous fractured porous media. Advances in Water Resources, 23, 699-723.

Xu, T., Sonnenthal, E., Spycher, N. and Pruess, K. (2006). TOUGHREACT: A simulation program for non-isothermal multiphase reactive geochemical transport in variably saturated geologic media. Computers and Geosciences 32, 145-165.

Xu, T., Spycher, N., Sonnenthal, E., Zhang, G., Zheng, L. and Pruess, K. (2011). TOUGHREACT Version 2.0: A simulator for subsurface reactive transport under non-isothermal multiphase flow conditions. Computers & Geosciences, 37(6), 763-774.

Yang, Y. and Aplin, A.C. (2010). A permeability-porosity relationship for mudstones. Marine and Petroleum Geology, 27, 1692-1697.

Yip, M., Mohle, J. and Bolander, J. (2005). Automated modeling of three-dimensional structural components using irregular lattices. Computer-Aided Civil and Infrastructure Engineering, 20, 393-407.

Zhan, H., Wen, Z., Huang, G. and Sun, D. (2009). Analytical solution of two-dimensional solute transport in an aquifer-aquitard system. Journal of Contaminant Hydrology, 107, 162-174, DOI:10.1016/j.jconhyd.2009.04.010.

Zhang, C.L., Rothfuchs, T., Dittrich, J. and Muller. J. (2008). Investigations on self-sealing of indurated clay. -GRS Report, GRS-230, 1-67, ISBN 978-3-939355-04-5.

Zhao, Y. and Liu, H.-H. (2012). An elastic strain-stress relationship for porous rock under anisotropic stress conditions. Rock Mechanics & Rock Engineering, 45(3), 389-399.

Zheng, L., Li, L., Rutqvist, J., Liu, H.-H. and Birkholzer, J.T. (2012). Modeling Radionuclide Transport in Clays. Lawrence Berkeley National Laboratory. FCRD-UFD-2012-000128

Zheng, L., Rutqvist, J., Houseworth, J., Davis, J., Tinnacher, R., Li, L. and Liu, H.-H. (2011). Investigation of near-field THMC coupled processes, milestone report in UFD, Work Package number 1.02.08.03.

Zhou, Q., Liu, H.-H., Molz, F.J., Zhang, Y. and Bodvarsson, G.S. (2007). Field-scale effective matrix diffusion coefficient for fractured rock: Results from literature survey. Journal of Contaminant Hydrology, 93, 161-187, DOI:10.1016/j.jconhyd.2007.02.002.

Zhu, C. (2005). In situ feldspar dissolution rates in an aquifer. Geochimica et Cosmochimica Acta, 69(6), 1435-1453.

Zimmerman, R.W., Chen, G., Hadgu, T. and Bodvarsson, G.S. (1993). A Numerical Dual-Porosity Model with Semianalytical Treatment of Fracture/Matrix Flow. Water Resources Research, 29(7), 2127-2137.